Separation of Local and Regional Information in Geomagnetic Response Functions using Hypothetical Event Analysis

Patricia Ritter
University of Edinburgh
Dept. of Geology and Geophysics

Ph.D. Thesis

1996

Declaration

This thesis has been composed by me and has not been submitted for any other degree. Except where acknowledgement is made, the work is original.

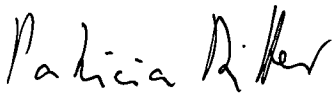

Patricia Ritter

Abstract

Electromagnetic investigations are usually intended to examine regional structures where induction takes place at a given period range. However, the regional information is often distorted by galvanic effects at local boundaries. Bahr (1985) and Groom & Bailey (1989) developed a physical distortion model for decomposing the MT impedance tensor, based upon local galvanic distortion of a regional 2D electromagnetic field. I have extended their method to predicting the magnetic variation fields created at an array of sites. The magnetic response functions at periods around 1000s may be distorted by large scale inhomogeneities in the upper or middle crust. In this period range, the data measured by a magnetometer array contains common regional information, which can be extracted if the dataset is treated as a unit, e.g. by using hypothetical event analysis.

Magnetic fields of galvanic or inductive origin can be distinguished by their phase behaviour. Pure distortion fields are in-phase with the regional electric field. Hence the magnetic phase of the galvanic response approaches the regional impedance phase, as distortion effects outweigh the inductive response of an anomaly with increasing period. Hypothetical event analysis is suited extremely well to examining the common phase content of a magnetic response function array. This technique can recover the regional strike direction as well as the regional impedance phases. I have tested its application extensively by a series of 3D modelling studies, which incorporate regional 2D and local 3D structures.

The approach has also been used to investigate two datasets. For the Iapetus array, which covers an area of 200 km $\times$ 300 km in N-England/S-Scotland, the technique revealed a common regional strike azimuth of ca. N125°E in the period range 500s - 2000s. This direction differs from the strike indicated by the induction arrows, which seem influenced mainly by local current concentration along the east-west striking Northumberland Trough and the northeast striking Southern Upland Fault. Both impedance phases are positive and differ by ca. 10°, which supports the assumption of distortion fields in the dataset and that the regional structure is 2D.

In the case of the BC87 profile data from British Columbia (Canada), a regional strike direction of N60°E could be recovered at long periods, which is in agreement with the results derived from earlier magnetotelluric decomposition procedures. The negative phase angle, however, indicates that the local fields are of inductive origin. Hence we do not obtain any information on the regional impedance phase.

The modelling studies confirm, that with hypothetical event analysis it is always possible to recover the regional strike direction from distorted data, even if a strong regional vertical field is present in the dataset or if the local fields are generated by induction processes rather than distortion. The determination of the regional impedance phases, on the other hand, is far more sensitive to deviations from the physical distortion model.

Acknowledgements

I wish to thank Dr. R.J. Banks for initiating and supporting my studies with most valuable advice and expertise. He provided me with the comprehensive Iapetus database, that he compiled from numerous data archives, papers and theses. I also thank him for reading thoroughly through the various versions of the manuscript. I am very grateful to Drs. R.J. Banks and R.V.S. Hutton, G.J.K. Dawes and in particular Prof. V. Haak for motivating me to apply for this project.

I thank the former and recent members of the EM group at the Department for Geology and Geophysics in Edinburgh, D. Bailey, G. Balasis, Dr. R.J. Banks, G.J.K. Dawes, C. Dumitrescu, Dr. B.A. Hobbs, Dr. R.V.S. Hutton, Dr. D.W. Livelybrooks, K. MacDonnald, D. Nascimiento, Dr. O. Ritter, T. Volti, Prof. K. Whaler, A. Vickery, A.J.K. Wilson, and in particular Prof. A. Junge for many stimulating discussions during our regular meetings.

Furthermore, I wish to thank sincerely the many colleagues who collected and processed the time series of the Iapetus dataset and the BC87 dataset. Their excellent work made an essential contribution to my studies.

I should also like to thank the GeoForschungsZentrum Potsdam, in particular Dr. M. Eisel, for their effort to make Geotools available at European universities.

Our departmental computing staff S. Voss and Dr. I. Chisholm are thanked for maintaining the departmental computer network and for their patience with us users. Many thanks also to G. Waugh for his help in administrative matters.

My very special thanks go to Oliver for his great motivation and help during the past years. Without his continuous support and strong commitment for the care of our children I could not have accomplished this thesis. He also helped to set up the computing facilities, and he patiently had a first reading of all manuscripts. I thank him, Iannis and Muriel for keeping up my spirits during a time, which was not always easy for us all.

I am also thankful to the families of our colleagues and friends who made us very welcome in Edinburgh and Scotland.

This thesis was accomplished with the financial support of the EEC Grant Nr. B/Joug 900017 (Research Programme in the Field of Non-Nuclear Energies). I wish to thank M^{me} E. Staroste for her helpful support to get through the bureaucratic maze in Brussels.

Contents

List of Figures

List of Symbols

symbol	*description*
x, y, z	cartesian coordinates, z positive downwards
x', y'	regional strike coordinates
x'', y''	local strike coordinates
i	imaginary number $\sqrt{-1} := i$
Re, Im	real part, imaginary part of a complex number: $\mathcal{C} = Re + iIm$
$\mathcal{C}^*$	conjugate complex of C; $\mathcal{C}^* = Re - iIm$
$\mathbf{B}$	magnetic induction vector; $\mathbf{B}^o$ regional field, $\mathbf{B}^a$ anomalous local field; [Tesla] = $[\frac{\mathrm{Vs}}{\mathrm{m}^2}]$
$\mathbf{E}$	electric field vector; $\mathbf{E}^o$ regional field, $\mathbf{E}^a$ local electrostat. field; $[\frac{\mathrm{V}}{\mathrm{m}}]$
$\mathbf{j}$	electric current density $[\frac{\mathrm{A}}{\mathrm{m}^2}]$
$\mathbf{D}$	electric displacement $[\frac{\mathrm{As}}{\mathrm{m}^2}]$
$\dot{\mathbf{D}}$	displacement current
$g(\mathbf{r}, \mathbf{r}')$	scalar Green's function
$\mathbf{G}(\mathbf{r}, \mathbf{r}')$	dyadic Green's function (tensor)
$\underline{\mathbf{\Gamma}}(\mathbf{r}')$	depolarisation tensor
$\mathbf{r}$	field vector to observation point
$\mathbf{r}'$	field vector to source point
T	period [s]; $T^{-1} = f$ frequency $[\mathrm{s}^{-1}]$
T_o	period of sign change of the magnetic phase φ_m
ω	angular frequency $\omega = \frac{2\pi}{T}$; $[\mathrm{s}^{-1}]$
k	wavenumber $[\mathrm{m}^{-1}]$; $\mathrm{k_o} = \sqrt{\mathrm{i}\omega\mu_o\sigma_o}$
$Q(\mathbf{r})$	material variation $k^2(\Delta\sigma(\mathbf{r}))$ $[\mathrm{m}^{-2}]$; with$\Delta\sigma(\mathbf{r}) = \sigma(\mathbf{r}) - \sigma_o$
σ	electrical conductivity $\sigma = \rho^{-1}$; $[\frac{\mathrm{S}}{\mathrm{m}}]$
τ	electrical conductance [S] = $[\Omega^{-1}]$; $[\frac{\mathrm{A}}{\mathrm{V}}]$
q	volume density of charge $[\frac{\mathrm{As}}{\mathrm{m}^3}] = [\frac{\mathrm{C}}{\mathrm{m}^3}]$
μ_o	magnetic permeability $\mu_o = 4\pi 10^{-7} \frac{\mathrm{Vs}}{\mathrm{Am}}$; $[\frac{\mathrm{H}}{\mathrm{m}}]$
	μ_r: relative permeability; $\mu = \mu_r \mu_o$
ε	dielectric constant (electrical permittivity) $\varepsilon_o = \frac{1}{36\pi} 10^{-9} \frac{\mathrm{As}}{\mathrm{Vm}}$; $[\frac{\mathrm{F}}{\mathrm{m}}]$
	ε_r: relative permittivity; $\varepsilon = \varepsilon_r \varepsilon_o$
ρ	electrical resistivity $\rho = \sigma^{-1}$; $[\Omega\mathrm{m}]$
ρ_a	apparent resistivity $[\Omega\mathrm{m}]$
c	Schmucker's c - response: $c(\omega) = \frac{1}{i\omega} Z(\omega)$
$\underline{\mathbf{I}}$	unity matrix
$\underline{\mathbf{Z}}$	magnetotelluric impedance tensor with complex components $Z_{xx}, Z_{xy}, Z_{yx}, Z_{yy}$; $[\frac{\mathrm{m}}{\mathrm{s}}]$
$\underline{\mathbf{Z}}^{\mathbf{o}}$	regional impedance tensor in strike coordinates (x', y') with
Z_E, Z_B	principal impedances; $Z_{\tilde{E}}, Z_{\tilde{B}}$ distorted principal impedances
φ_E, φ_B	phases of the principal impedances
$\underline{\mathbf{C}}$	electric distortion tensor with real components $C_{xx}, C_{xy}, C_{yx}, C_{yy}$
$\underline{\mathbf{D}}$	magnetic distortion tensor with real components D_{xx}, D_{xy}, D_{yx}, D_{yy}; D_{zx}, D_{zy}; $[\frac{\mathrm{s}}{\mathrm{m}}]$

symbol	*description*
S_1, S_2, D_1, D_2	modified impedances; sums and differences of the observed impedances
D', D''	'unknown' static shift factors
μ	Bahr's measure of phase difference
η	Bahr's phase sensitive skew
δ	Bahr's phase deviation angle
β_1, β_2	Bahr's 'skew parameters' (also Zhang's proportionality parameters for off-diagonal impedances (θ_r))
α	Zhang's proportionality parameter for diagonal impedances (θ_ℓ)
$\mathcal{Q}(\beta_1, \beta_2)$	target function for least squares fitting of parameters β_1, β_2 (Zhang)
T_{zx}, T_{zy}	prediction coefficients (Zhang)
λ	Lagrangian multiplier (Zhang)
g	scalar factor; g' normalised factor (Groom & Bailey)
$\underline{\mathbf{A}}, s$	anisotropy tensor, anisotropy parameter (Groom & Bailey)
$\underline{\mathbf{T}}, \phi_t$	twist tensor, twist angle (Groom & Bailey)
$\underline{\mathbf{S}}, \phi_e$	shear tensor, shear angle (Groom & Bailey)
$\alpha_0, \ldots \alpha_3$	complex nonlinear equations (Groom & Bailey)
$\zeta_0, \ldots \zeta_5$	complex nonlinear equations (Chave & Smith)
κ	normalizing factor for the extended equation system (Chave & Smith)
$(\mathcal{A}, \mathcal{B})$	magnetic response function: $\mathcal{A}$, $\mathcal{B}$ in x, y directions, respectively; $(\mathcal{A}^o, \mathcal{B}^o)$ regional response function, $(\tilde{\mathcal{A}}^o, \tilde{\mathcal{B}}^o)$ distorted regional response function, $(\mathcal{A}^\ell, \mathcal{B}^\ell)$ local response function
φ_m	magnetic phase: phase of the magnetic response function (of $\mathcal{B}'$ in strike coordinates x')
$\mathbf{P}$, $\mathbf{Q}$	induction arrows, real and imaginary; L_P, L_Q: lengths; θ_P, θ_Q: directions
$\underline{\mathbf{W}}$	magnetic perturbation tensor with complex components $W_{xx}, W_{xy}, W_{yx}, W_{yy}$
θ_r, θ_ℓ	regional, local strike azimuth (pos. from north), respectively. $\theta_\ell - \theta_r = \alpha$
$\underline{\mathbf{R}}_\theta$	rotation matrix for anti-clockwise rotation ($\theta > 0$) with $\underline{\mathbf{R}}_\theta = \begin{pmatrix} \cos\theta & -\sin\theta & 0 \\ \sin\theta & \cos\theta & 0 \\ 0 & 0 & 1 \end{pmatrix}$ or only $\begin{pmatrix} \cos\theta & -\sin\theta \\ \sin\theta & \cos\theta \end{pmatrix}$
$\mathbf{B}^\star$	hypothetical horizontal magnetic field
$\vartheta^\star$	polarisation azimuth of the hypothetical event
B_z^p	predicted vertical magnetic field
r	linear correlation coefficient
r_{max}	maximized linear correlation coefficient
∇	Nabla operator; $\nabla A = gradA$, $\nabla \cdot \mathbf{A} = div\mathbf{A}$, $\nabla \times \mathbf{A} = curl\mathbf{A}$, $\nabla^2\mathbf{A} =$ Laplacian of $\mathbf{A}$, $\nabla^2\mathbf{A} := \nabla(\nabla \cdot \mathbf{A}) - \nabla \times (\nabla \times \mathbf{A})$

1 Introduction

Electromagnetic methods are used in geophysics to determine the properties of crustal structures in terms of electrical conductivity and strike direction. The time variations of the electric and magnetic fields measured at the surface provide the basic data, as they are related by induction processes in the interior of the Earth. The input to this causal system is the uniform, time-varying magnetic field of current systems in the ionosphere and magnetosphere. The magnetic source field diffuses through the conductive Earth as a plane wave and induces an electric field. This electric field, in turn, generates an internal magnetic field, which is uniform if the conductivity varies only with depth. The spatial variations of the horizontal and vertical magnetic field are caused by lateral boundaries in the crust. Both the electric field and the internal magnetic field can be regarded as the output of the system. The ratio of the horizontal components of the electric to the magnetic field is used in the magnetotelluric method (MT) to compute the impedance (Tichonov, 1950; Cagniard, 1953) and the strike (Swift, 1967) of conductivity structures. The geomagnetic deep sounding method (GDS) uses the ratio of the vertical to the horizontal magnetic field to estimate the strike direction and the lateral conductivity distribution (Chapman, 1919; Lahiri & Price, 1939; Parkinson, 1962; Wiese, 1962; Schmucker, 1970).

MT and GDS surveys are usually applied to examine *regional* structures, where induction takes place at a given period range. However, it is a well-known difficulty that galvanic effects due to near-surface inhomogeneities can modify the regional MT impedance tensor and the magnetic response function in such a way that a two-dimensional interpretation becomes misleading (e. g. Jones, 1983). The term galvanic distortion is usually employed for non-inductive processes at *local* structures, that are typically too small or too shallow to be involved in the induction process at the relevant period range. Instead, they are responsible for the deflection of regional currents induced in much larger, deeper or remote structures. This effect is thought to be caused by electrostatic fields due to surface charges on the local boundaries. The important factor governing these two processes is the ratio of the scale length of the local anomaly to the skin depth of the host material at the investigated period.

The effect of distortion on the electric field is frequency-independent, causing shift and rotation of the MT impedances at long periods. Several techniques to eliminate electric distortion have been developed in recent years; some of these are based on purely mathematical approaches, while others are based upon the physical model of distortion. The physical decomposition methods (Zhang et al. 1987; Bahr, 1988; Groom & Bailey, 1989) are now being applied widely and almost standard procedures in MT interpretations. The spatial deflection of regional currents, however, also generates a local anomalous magnetic field that is superimposed on the regional magnetic field. As a consequence, distortion of the vertical magnetic response functions in GDS must also be considered. Its effects on single GDS sites and on the MT impedances have been examined recently with respect to decomposition methods by Zhang et al. (1993, 1995), and Chave & Smith (1994).

Magnetic distortion - as opposed to electric distortion - is frequency-dependent because it is closely coupled to the regional impedance. Since its effects fall off with increasing period, it has been argued that data in the MT- and especially in the GDS period range are not affected (Zhang et al. 1987, Groom & Bailey, 1989). This argument is based on the assumption that galvanic distortion is produced only by very small-scale, near-surface structures. Groom & Bailey (1991), for example, examine the effects of a conductive hemisphere, that is located at the surface and has a radius of just 100 m. As a consequence, magnetic distortion appears in the short period range at $T < 10^{-2}$s and is irrelevant at longer periods. However, at periods > 100s, upper- and mid-crustal structures with an extent of 10 km or more are smaller than the skin-depth and the major influence in this period range may take the form of scattering rather than induction (Chave & Smith, 1994). Thus, conductivity anomalies of different scales may be responsible for a sequence of induction and distortion effects in different period ranges (Zhang et al. 1993).

Magnetic response functions are usually presented as induction arrows. However, in the period range where distortion dominates, their lengths and azimuths may be controlled entirely by the anomalous magnetic field of locally deflected regional currents. Nevertheless, the response functions also contain information about the regional geology. This information is common to all sites in a certain area depending on the period range. Hence the magnetic distortion problem can be formulated as a combination of site-dependent distortion parameters and contributions from site-independent regional induction processes. Zhang et al. (1993, 1995) and Chave & Smith (1994) proposed techniques for the elimination of magnetic distortion. These use the MT impedances and are based on the analysis of observations at single sites. They are explained alongside with the decomposition methods in chapter 3.

In contrast to these single site investigations, it is the purpose of my studies to use the data from a spatially distributed array of GDS sites in order to extract the common regional information. Hypothetical event analysis (HEA) of magnetometer array data treats the dataset as a unit, and therefore provides a very effective way of recovering such common information. If the results from HEA are presented in Argand diagrams, the regional and site-dependent parts of the vertical magnetic field can be separated without the need for complex inversion techniques. I show in the theory presented in chapter 4, and in a series of full 3D modelling studies in chapter 7, that with HEA it is possible to determine the regional strike direction and the regional impedance phases from distorted magnetic response functions.

In chapter 5, I apply the method to real data. The Iapetus dataset is a good example of an array where magnetic distortion is suspected. It comprises vertical magnetic response functions in the period range 10s - 7000s from relatively densely spaced sites (10 km - 20 km) in N-England and S-Scotland. The data are clearly influenced by current concentrations associated with the Northumberland Trough, causing strong anomalous vertical fields. Hypothetical event analysis, however, reveals that the data at these periods contain additional information that is common to all sites. This common information suggests a different strike azimuth which I conclude is the strike direction of the regional structure.

I investigate a second dataset, the BC87 profile, in chapter 6. Earlier MT results suggest that the crustal structure is strongly 3D at all levels. Although the data are relatively noisy at long periods and the local distortion field may be dominated by inductive processes rather than purely galvanic effects, a common strike direction can be recovered with HEA, which is close to the regional strike determined by MT decomposition. All results are summarized in the final conclusions section.

2 General Theoretical Background

It is a consequence of Faraday's Law that any time-varying, external part of the geomagnetic field, such as that originating with the variable electric currents flowing in the ionosphere, will necessarily induce electric currents within the earth which to some extent is electrically conducting.

Weaver, 1994

2.1 Maxwell's equations

The electromagnetic fields in a source-free, isotropic medium of uniform permittivity ε and permeability μ are fully described by Maxwell's equations:

$$\nabla \times \mathbf{E} = -\frac{\partial \mathbf{B}}{\partial t} \tag{1}$$

$$\nabla \times \mathbf{B} = \mu \left(\mathbf{j} + \frac{\partial \mathbf{D}}{\partial t}\right) \tag{2}$$

$$\nabla \cdot \mathbf{E} = \frac{q}{\varepsilon} \tag{3}$$

$$\nabla \cdot \mathbf{B} = 0 \tag{4}$$

In this context, the physical material parameters μ $[\frac{\mathrm{Vs}}{\mathrm{Am}}]$, ε $[\frac{\mathrm{As}}{\mathrm{Vm}}]$, and the electrical conductivity σ $[\frac{\mathrm{S}}{\mathrm{m}}]$ are assumed isotropic, frequency-independent constants; q $[\frac{\mathrm{As}}{\mathrm{m}^3}]$ is the volume density of charge. The material parameters relate the magnetic field $\mathbf{H}$ $[\frac{\mathrm{A}}{\mathrm{m}}]$ to the magnetic induction $\mathbf{B}$ $[\frac{\mathrm{Vs}}{\mathrm{m}^2}]$, the electric field $\mathbf{E}$ $[\frac{\mathrm{V}}{\mathrm{m}}]$ to the displacement $\mathbf{D}$ $[\frac{\mathrm{As}}{\mathrm{m}^2}]$, and furthermore to the electric current density $\mathbf{j}$ $[\frac{\mathrm{A}}{\mathrm{m}^2}]$ (generalized Ohm's law, eqn. 5).

$$\mathbf{j} = \sigma \mathbf{E} \tag{5}$$

$$\mathbf{B} = \mu \mathbf{H} \qquad (\text{with } \mu = \mu_r \mu_o) \tag{6}$$

$$\mathbf{D} = \varepsilon \mathbf{E} \qquad (\text{with } \varepsilon = \varepsilon_r \varepsilon_o) \tag{7}$$

Both μ and ε do not differ appreciably from their free space values which are: $\mu_o = 4\pi 10^{-7} \frac{\mathrm{Vs}}{\mathrm{Am}}$ and $\varepsilon_o = \frac{1}{\mu_o c^2} = 8.85 \cdot 10^{-12} \frac{\mathrm{As}}{\mathrm{Vm}}$. For most materials in the Earth we can assume the relative permeability and permittivity as: $\mu_r \approx 1$ and $\varepsilon_r < 80$ (water), for most materials $\varepsilon_r \approx 20$ (Beblo, 1982).

All field quantities are functions of position $\mathbf{r}$ (or in cartesian coordinates x, y, z; with z positive downwards) and time t. The wave properties of the fields may be expressed by a harmonic term of the form

$$E, B \sim e^{i(\omega t + \mathbf{k}\mathbf{r})} \tag{8}$$

where ω is the angular frequency ($\omega = 2\pi f$) and $\mathbf{k}$ is the wave vector (k_x, k_y) for plane waves along the direction of propagation.

With this notation, the two Maxwell equations (1 and 2) take the form:

$$\nabla \times \mathbf{E} = -i\omega \mathbf{B} \tag{9a}$$

$$\nabla \times \mathbf{B} = \mu_o \sigma \left(1 + i \frac{\varepsilon\omega}{\sigma}\right) \mathbf{E} \tag{9b}$$

From Maxwell's equations we obtain two second order differential equations, the induction equations for homogenous media ($\nabla\sigma = 0$):

$$\nabla \times \nabla \times \mathbf{E} = -\mu_o \left(\sigma \frac{\partial \mathbf{E}}{\partial t} + \varepsilon \frac{\partial^2 \mathbf{E}}{\partial t^2}\right) = -i\omega\mu_o\sigma \left(1 + i \frac{\varepsilon\omega}{\sigma}\right) \mathbf{E} \tag{10a}$$

$$\nabla \times \nabla \times \mathbf{B} = -\mu_o \left(\sigma \frac{\partial \mathbf{B}}{\partial t} + \varepsilon \frac{\partial^2 \mathbf{B}}{\partial t^2}\right) = -i\omega\mu_o\sigma \left(1 + i \frac{\varepsilon\omega}{\sigma}\right) \mathbf{B} \tag{10b}$$

The last terms on the right sides of eqn. 9b, 10a and 10b represent the contribution due to the displacement current $\mathbf{j}_D$. Since the conductivity of the crust and mantle takes values in the range 10^{-6}S/m to 4 S/m and we restrict our investigations to periods > 0.001s, we can assume $\omega\varepsilon/\sigma \ll 1$. The effects of the displacement current can therefore be neglected when discussing geo-electromagnetic induction (Weaver, 1994). As a result, eqn. 9b reduces to:

$$\nabla \times \mathbf{B} = \mu_o \mathbf{j} \,, \tag{11}$$

which implies that $\nabla \cdot \mathbf{j} = 0$, i.e. the normal component of current density is continuous across interfaces. However, charges can accumulate in regions where $\nabla\sigma \neq 0$ if an electric field component is parallel to the gradient of conductivity, since

$$\nabla \cdot \mathbf{E} = -\nabla\sigma \cdot \mathbf{E}/\sigma \qquad \text{and therefore} \qquad q = -\frac{\varepsilon}{\sigma} \nabla\sigma \cdot \mathbf{E}. \tag{12}$$

Introducing the vector Laplacian operator[1] we can write the quasi-static induction equations (10a and 10b without displacement terms) for both fields in a general form for non-homogenous media: [2]

$$\nabla^2 \mathbf{E} = i\omega\mu_o\sigma\mathbf{E} - \nabla \left(\nabla\sigma \cdot \frac{\mathbf{E}}{\sigma}\right) \tag{13a}$$

$$\nabla^2 \mathbf{B} = i\omega\mu_o\sigma\mathbf{B} - \frac{1}{\sigma}\nabla\sigma \times \left(\nabla \times \mathbf{B}\right) \tag{13b}$$

For homogenous regions, where $\sigma = constant$, the last terms in both equations may be dropped since $\nabla\sigma = 0$ and therefore $\nabla \cdot \mathbf{E} = 0$. Now, the quasi-static induction equations describe the penetration of the fields into the earth as a process of diffusion:

$$\nabla^2 \mathbf{E} = i\omega\mu_o\sigma\,\mathbf{E} = k_o^2\,\mathbf{E} \tag{14a}$$

$$\nabla^2 \mathbf{B} = i\omega\mu_o\sigma\,\mathbf{B} = k_o^2\,\mathbf{B} \tag{14b}$$

These equations are also applicable for a layered earth model with both electrical components parallel to the interface ($\nabla\sigma \cdot \mathbf{E} = 0$), and furthermore for a 2D case if the electric field is parallel to the lateral interface and the magnetic field is parallel to the gradient of conductivity ($\frac{1}{\sigma}\nabla\sigma \times (\nabla \times \mathbf{B}) = 0$; *E-polarisation*).

---

[1] $\nabla^2 := \nabla(\nabla\cdot) - \nabla \times (\nabla\times)$

[2] using: $\nabla \times \sigma\mathbf{E} = \sigma\nabla \times \mathbf{E} - \mathbf{E} \times \nabla\sigma$ and $\mathbf{a} \times \mathbf{b} = -\mathbf{b} \times \mathbf{a}$ and $\nabla \cdot (\nabla\times) = 0$

2.2 1D Structures

k_o is the complex wave number of the medium: $k_o = \sqrt{i\omega\mu_o\sigma}$. Together with the magnitude of the horizontal wave vector of the source field $|k| = \sqrt{k_x^2 + k_y^2}$, it defines the solution for the diffusion equations 14a and 14b for the case of a **uniform halfspace**. The variations of the fields with position and time $\mathbf{F}(\mathbf{r}, t)$ depend on the frequency (ω), the source field geometry ($\mathbf{k}$), and on the depth (z) inside the medium of a certain conductivity σ:

$$\mathbf{F}(\mathbf{r}, t) = F_o(z) \cdot e^{i\omega t + i\mathbf{k}\mathbf{r}} \tag{15}$$

This dependency may be described by an attenuation term in the z - direction:

$$F_o(z) = F_o(z = 0) \cdot e^{-\frac{z}{c}} \tag{16}$$

The so-called $c - response$ defines the complex depth of penetration or *inductive scale length* (Schmucker, 1987): [3]

$$c(\omega, |k|) = \frac{\mathbf{F}(\omega)}{-\frac{\partial}{\partial z}\mathbf{F}(\omega)}\bigg|_{z=0} = \frac{1}{\sqrt{k_o^2 + |k|^2}} \tag{17}$$

Clearly, $c(\omega, |k|)$ depends strongly on the lateral modulations of the source field. Only for very small $|k|$ is the c - response determined predominantly by the conductivity of the subsurface. Since setting $|k| = 0$ (uniform source field) does not lead to a correct solution of the induction problem (Weaver, 1973; Schmucker & Weidelt, 1975), the source field is usually assumed *quasi-uniform* with $|k| \longrightarrow 0$. The c - response is then determined by the material parameters and the frequency alone:

$$c(\omega) = \frac{1}{\sqrt{i\omega\mu_o\sigma}} \tag{18}$$

The skin depth p is the depth at which the penetrating field is attenuated by a factor e^{-1}; it is the real part of twice the complex inductive scale length:

$$p = \sqrt{\frac{2}{\omega\mu_o\sigma}} = \frac{2\,c(\omega)}{1 - i} \tag{19}$$

For a rough estimation of the skin depth we can use the approximation $p \approx 0.5\sqrt{\rho T}$, with $\rho = 1/\sigma$. Using eqn. 18, the resistivity of the uniform halfspace ρ_o can be obtained from its c - response c_o:

$$\rho_o = \omega\mu_o\,|c_o|^2 \tag{20}$$

---

[3] Example:
Let $\mathbf{E} = (E_x, 0, 0)$ and the variations of E_x with y be due to an external, non-uniform magnetic field: $E_x(y, z, t) = E_x(z) \cdot e^{i\omega t} \cdot e^{ik_y\hat{y}}$
The diffusion equation (14a) yields:

$$\frac{\partial^2 E_x}{\partial y^2} + \frac{\partial^2 E_x}{\partial z^2} = -k_y^2\,Ex + \frac{\partial^2 E_x}{\partial z^2} = i\omega\mu_o\sigma\,Ex$$

$$\frac{\partial^2 E_x}{\partial z^2} = (i\omega\mu_o\sigma + k_y^2)Ex = (k_o^2 + k_y^2)Ex$$

The resistivity can also be estimated from the the impedance Z which is defined as the ratio of the electric and the magnetic surface fields[4]. The amplitude and phase of the impedance are used in the **magnetotelluric method** (MT) to determine the electrical properties of the subsurface (Tikhonov, 1950; Cagniard, 1953):

$$\frac{E(\omega)}{B(\omega)} = \frac{1}{\mu_o}\hat{Z}(\omega) = Z(\omega)\,, \qquad E(\omega) \perp B(\omega) \tag{21}$$

Considering all horizontal field components, we can write the impedance as a tensor:

$$\begin{pmatrix} E_x \\ E_y \end{pmatrix} = \begin{pmatrix} 0 & Z \\ -Z & 0 \end{pmatrix} \begin{pmatrix} B_x \\ B_y \end{pmatrix} \tag{22}$$

Z is related to Schmucker's c - response by Maxwell's equations through

$$Z(\omega) = i\omega\, c(\omega). \tag{23}$$

The resistivity ρ_o can therefore also be obtained from

$$\rho_o = \frac{\mu_o}{\omega}|Z_o|^2 \tag{24}$$

If the resistivity of the subsurface varies with depth (**layered earth model**, $\sigma = \sigma(z)$), the resistivity determined from the surface fields depends on the skin depth of the observed period range. We obtain an average value which is the resistivity of an equivalent homogenous halfspace (Cagniard, 1953); it is therefore called *apparent resistivity* $\rho_a(\omega)$.

2.3 2D Structures

For two-dimensional structures with a strike direction chosen along the x - axis and $\sigma = \sigma(y,z)$, Maxwell's equations may be grouped into two sets of de-coupled equations: The so-called E-polarisation set describes the electric field parallel to the strike direction (E_x), caused by the variations of the perpendicular magnetic field ($-B_y$). The B-polarisation set contains equations for the perpendicular electric field (E_y) due to a magnetic excitation which is parallel to the strike (B_x) .

E-polarisation

$$\begin{aligned} \frac{\partial B_z}{\partial y} - \frac{\partial B_y}{\partial z} &= \mu_o\sigma E_x \\ \frac{\partial E_x}{\partial z} &= -i\omega B_y \\ \frac{\partial E_x}{\partial y} &= i\omega B_z \end{aligned} \tag{25}$$

B-polarisation

$$\begin{aligned} \frac{\partial E_y}{\partial z} - \frac{\partial E_z}{\partial y} &= i\omega B_x \\ \frac{\partial B_x}{\partial z} &= \mu_o\sigma E_y \\ \frac{\partial B_x}{\partial y} &= -\mu_o\sigma E_z \end{aligned} \tag{26}$$

[4] Z is defined as $Z = E/H$ in [V/A]=[Ω] (see paper on standards in EM studies by Hobbs, 1992). For better readability of the sometimes very long equations in the following chapters, I use Z like many other authors as $Z = E/\mu_o H = E/B$ in units of velocity [m/s].

2.3.1 Magnetotellurics

In the 2D case the magnetotelluric impedance tensor $\underline{\mathbf{Z}}$ contains two independent components, the two principal impedances Z_E (E-polarisation) and Z_B (B-polarisation):

$$\begin{pmatrix} E_{x'} \\ E_{y'} \end{pmatrix} = \begin{pmatrix} 0 & Z_E \\ Z_B & 0 \end{pmatrix} \begin{pmatrix} B_{x'} \\ B_{y'} \end{pmatrix} \tag{27}$$

The primes denote the coordinate system of the strike direction (x', y'). If the coordinate system of the magnetotelluric fields does not coincide with the strike direction of the structure ($x' \neq x$), the impedance tensor contains four non-zero elements[5]. For a purely two-dimensional conductivity distribution, the strike direction ϑ can be determined by minimizing the sum of the diagonal elements of the impedance tensor $|Z_{xx}^2 + Z_{yy}^2| \longrightarrow 0$ (Swift, 1967):

$$\vartheta = \frac{1}{4} \arctan \frac{2Re[(Z_{xx} - Z_{yy})(Z_{xy} + Z_{yx})]}{|Z_{xx} - Z_{yy}|^2 - |Z_{xy} + Z_{yx}|^2} \pm \frac{\pi}{2} \tag{28}$$

To differentiate a possibly rotated 2D impedance tensor from a full 3D tensor, which also consists of four non-zero components, Swift (1967) introduced the rotationally invariant *skew* parameter:

$$skew = \frac{|Z_{xx} + Z_{yy}|}{|Z_{xy} - Z_{yx}|} \tag{29}$$

We can expect values close to zero (< 0.2 for real data) for one- and two-dimensional structures. For three-dimensional conductivity distributions, the *skew* can be distinctly non-zero (> 0.3 for real data), but it may still be close to zero for symmetric structures (e.g. sphere).

Note that both the strike and skew as proposed by Swift can be interpreted in terms of regional strike and dimensionality only for impedances of a purely inductive response. If galvanic processes at conductivity inhomogeneities, that are smaller than the skin depth of the investigated period range, distort the strength and direction of the induced fields, these parameters may be strongly affected and misleading. I shall give an overview of alternative treatments of the magnetotelluric impedance tensor (decomposition methods) in chapter 3.

The respective diffusion equations for E - polarisation and B - polarisation (see equations 25 and 26) are (e.g. Haak, 1978):

$$\frac{\partial^2 E_x}{\partial y^2} + \frac{\partial^2 E_x}{\partial z^2} = i\omega\mu_o\sigma E_x \tag{30a}$$

$$\frac{\partial^2 B_x}{\partial y^2} + \frac{\partial^2 B_x}{\partial z^2} = i\omega\mu_o\sigma B_x \tag{30b}$$

---

[5]The rotated 2D impedance tensor is (rotation angle $\vartheta = \angle(\vartheta_{x'} - \vartheta_x)$; positive from N over E):

$$\begin{pmatrix} Z_{xx} & Z_{xy} \\ Z_{yx} & Z_{yy} \end{pmatrix} = \underline{\mathbf{R}}_\vartheta \begin{pmatrix} 0 & Z_E \\ Z_B & 0 \end{pmatrix} \underline{\mathbf{R}}_\vartheta^T \quad \text{with } \underline{\mathbf{R}}_\vartheta = \begin{pmatrix} \cos\vartheta & -\sin\vartheta \\ \sin\vartheta & \cos\vartheta \end{pmatrix}$$

Only for some simple 2-D cases can the solutions for these differential equations be obtained analytically. For more complex situations, the solutions can be found by using finite element methods (e.g. Coggon, 1971; Reddy & Rankin, 1971; Wannamaker et al. 1987), finite differences (e.g. Jones & Price, 1970; Jones, 1973; Brewitt-Taylor & Weaver, 1977), or a combination of the latter and integral equations (Schmucker, 1986).

For three-dimensional conductivity distributions with $\sigma = \sigma(x, y, z)$, the distinction of E- and B - polarisation is no longer applicable and the problem is approached by integral equation solutions (e.g. Hobbs, 1971; Weidelt, 1975; Hohmann 1975, Xiong et al. 1986).

2.3.2 Geomagnetic Deep Sounding Method

The geomagnetic deep sounding method (GDS) is based on the interpretation of the spatial variations of the magnetic field components due to lateral conductivity boundaries. The directed current flow inside and near a two-dimensional conductive structure generates two perpendicular anomalous magnetic components, as expressed by the equations of the E-polarisation case in eqn. 25: one in horizontal and one in vertical direction. The anomalous horizontal component is directed perpendicular to the strike direction and superimposed on the horizontal source field of the same direction. It is largest directly above the current concentration at the edge of a conductive structure (Banks et al. 1993), and decreases rapidly with increasing distance from the boundary. The vertical component, on the other hand, reaches its maximum values above the more resistive side of the contact. It falls off rapidly only in a close distance to the boundary, but slowly further away.

The mapping of all three components of the magnetic field is therefore a widely used method to investigate multi-dimensional structures. Special attention is paid to the relation between the vertical and the horizontal field components, which is contained in the vertical magnetic response function:

$$B_z = (\mathcal{A}, \mathcal{B})\,\mathbf{B}_h = \mathcal{A}B_x + \mathcal{B}B_y \tag{31}$$

Since the two components of the magnetic response function ($\mathcal{A}$, $\mathcal{B}$) are each linked to one of the horizontal components, they bear information on the lateral conductivity distribution. They are used to construct the induction arrows, which are a projection of the magnetic field on the x, y -plane (Schmucker, 1970). They are usually presented as real and imaginary arrows:

$$\mathbf{P}(\omega) = Re\mathcal{A}(\omega)\hat{\mathbf{x}} + Re\mathcal{B}(\omega)\hat{\mathbf{y}} \tag{32a}$$

$$\mathbf{Q}(\omega) = Im\mathcal{A}(\omega)\hat{\mathbf{x}} + Im\mathcal{B}(\omega)\hat{\mathbf{y}} \tag{32b}$$

In this thesis, the induction arrows are always presented in the *Wiese*[6] - convention, i.e. the real arrows point away from a conductive region[7]. Although the arrows $\mathbf{P}$ and $\mathbf{Q}$ are written here in vector notation, arrows of different conductivity anomalies

[6]Wiese (1962) constructed the induction arrows from single events in the time domain.

[7]Parkinson (1959) defined his arrows pointing towards a conductive region.

cannot be added as vectors in the case of inductive coupling (Weaver, 1990; Siemon, 1991). The lengths and directions of the induction arrows are given by:

$$L_{\mathbf{P}} = \sqrt{Re\mathcal{A}^2 + Re\mathcal{B}^2}, \qquad \theta_{\mathbf{P}} = \arctan\left(\frac{Re\mathcal{B}}{Re\mathcal{A}}\right) \tag{33a}$$

$$L_{\mathbf{Q}} = \sqrt{Im\mathcal{A}^2 + Im\mathcal{B}^2}, \qquad \theta_{\mathbf{Q}} = \arctan\left(\frac{Im\mathcal{B}}{Im\mathcal{A}}\right) \tag{33b}$$

The directions of the induction arrows allow assumptions on the strike direction of a lateral conductivity contrast. They point perpendicular to the direction of current flow, i.e. the lateral boundary. The lengths can be interpreted as a measure of the lateral conductivity gradient. If the coordinate system of observation coincides with the strike direction ϑ, the magnetic response function contains only one component: $\mathcal{B}'$ perpendicular to the strike direction x':

$$(\mathcal{A}, \mathcal{B}) = (0, \mathcal{B}') \quad \text{for} \quad x' = x \tag{34}$$

Consequently, in this case the induction arrows point strictly 90° (y).

Since a vertical magnetic component can be produced by an induced time-varying electric field *or* by spatial deflections due to galvanic distortion of the induced currents, the induction arrows may be misleading if small-scale conductivity inhomogeneities are present in or near the surveyed area (Jones, 1983). This problem is investigated further in chapters 3 and 4, with the aim of revealing information on the inductive process from distorted magnetic response functions.

The induction arrows are usually calculated from the magnetic response functions of the total fields at each site (also called *single site* response functions, eqn. 31). They may be biased if the horizontal field is spatially non-uniform. If the time-series have been recorded synchronously to a common (remote) reference site, *relative* vertical response functions using the horizontal field of the reference site can be computed, and from these the *relative* induction arrows can be determined. This method rules out local contributions from horizontal anomalous fields due to lateral conductivity boundaries. Banks (1986) proposes to eliminate the effects of spatial variations of the horizontal fields in single site magnetic response functions by using the horizontal inter-station transfer functions (perturbation tensor, eqn.35) at each site and the magnetic response function at a reference site. If data have not been recorded time-synchronously to a reference site, the anomalous horizontal magnetic fields at each site can be computed from the potentials of the vertical magnetic components in the wavenumber domain (Banks et al. 1993).

The anomalous parts of the horizontal magnetic field can also be used to determine the strike direction of a two-dimensional structure. They are obtained by subtracting the reference magnetic field from the total field at each site: $\mathbf{B}_i^a = \mathbf{B}_i - \mathbf{B}^r$. The relations between the normal reference field and these local difference fields are contained in the magnetic *perturbation tensor* $\underline{\mathbf{W}}$:

$$\begin{pmatrix} B_x^a \\ B_y^a \end{pmatrix} = \begin{pmatrix} W_{xx} & W_{xy} \\ W_{yx} & W_{yy} \end{pmatrix} \begin{pmatrix} B_x^r \\ B_y^r \end{pmatrix} \tag{35}$$

Like the impedance tensor, the amplitudes of the perturbation tensor elements allow conclusions on the dimensionality and the strike direction of the conductivity structure. In a 1D case, all elements are zero. For a 2D conductivity distribution, only the one diagonal component which accounts for the perpendicular magnetic field (E - polarisation) is non-zero in the coordinate system of the strike direction (e.g. W_{yy} for $\vartheta \parallel x$). If the observation coordinates differ from the strike direction, the strike may be found by minimizing the off-diagonal elements (Fluche, 1983). In a 3D case, all four tensor components are distinctly non-zero and independent.

The spatial variations of the anomalous magnetic field components (horizontal and vertical) over the area of investigation allow us to make assumptions on the lateral conductivity structure. In magnetometer array interpretations, hypothetical event analysis is often used to investigate such variations with respect to the polarisation azimuth of the horizontal magnetic field (Bailey et al. 1974; Gough & Ingham, 1983; Banks & Beamish, 1984; Banks et al. 1993). This technique can also be used effectively to separate local and regional information in magnetic response functions, that are influenced by multiple structures of different sizes and depths, as will be shown in chapter 4 (theory) and chapter 7 (3D modelling).

3 Galvanic Distortion and Decomposition Methods:

It is a well-known difficulty in electromagnetic methods that galvanic distortion due to near surface inhomogeneities can modify regional 2D MT tensors and the magnetic response function in such a way that 2D interpretation becomes very misleading. Bodies causing this problem are typically too small or too shallow to be involved in the induction process at the relevant period range, and thus produce no true two- or three-dimensional inductive response. They are therefore referred to as 'local' inhomogeneities, as opposed to 'regional' structures, that do have an electromagnetic response originating from induction within them.

Local anomalies can act as current channels if their resistivity is less than that of the surrounding host medium. Or they can appear more like an obstacle and force the regionally induced currents to flow around them if their resistivity is higher. To understand the redirection of regional currents we have to examine the problem in a microscopic way as described for example by Price (1973). In both cases the current distribution is controlled by a buildup of boundary charges on the body's interface, generated by the component of the regional E-field that is perpendicular to the conductivity gradient. The surface charge density on the interface is minute, and so is the displacement current $\dot{\mathbf{D}}$ and hence the difference $\dot{\mathbf{D}}_1 - \dot{\mathbf{D}}_2$ that builds up these charges (indexes 1 and 2 refer to two media with resistivities ρ_1, ρ_2). For geological media, and in the quasistatic approximation ($\sigma >> \omega\varepsilon$), its inductive effects can therefore be neglected. However, the secondary *electrostatic* field of the boundary charges $\mathbf{E}^a$ is quite large on both sides, since the dielectric constants ε involved are in the range of 10^{-10}.

$$\mathbf{E}_1^a = \frac{\mathbf{D}_1}{\varepsilon_1} \quad \text{in } \rho_1, \qquad \text{and} \qquad \mathbf{E}_2^a = \frac{\mathbf{D}_2}{\varepsilon_2} \quad \text{in } \rho_2 \tag{36}$$

In fact, the local 'anomalous' field $\mathbf{E}^a$ is of the same order as the regional field $\mathbf{E}^o$ that is driving the whole process. $\mathbf{E}^a$ is directed opposite to the regional field component on the less resistive side of the boundary (ρ_1), and in the same direction as the regional field on the more resistive side (ρ_2). Due to the different skin depths of the regional current in the two media the distribution of boundary charges has also a vertical gradient, generating a vertical component of the electrostatic field. The currents arising from this secondary E-field are, unlike the displacement currents, of considerable strengths. They can either enhance or decrease the regional current density.

Since we are dealing with a confined body, the buildup of surface charges causes polarisation of the material inside. This process generates an electric dipole field, as shown in fig. 1, (a) and (b). The graphs can be seen as sections through horizontal or vertical planes. The dipole field is strongest, but directed reversely inside the conductive anomaly (a). The electrostatic field inside a resistive structure (b) is weaker compared to the latter case, and is polarised in the direction of the regional E-field. However, it is strong outside the body, close to its sides parallel to the regional field direction.

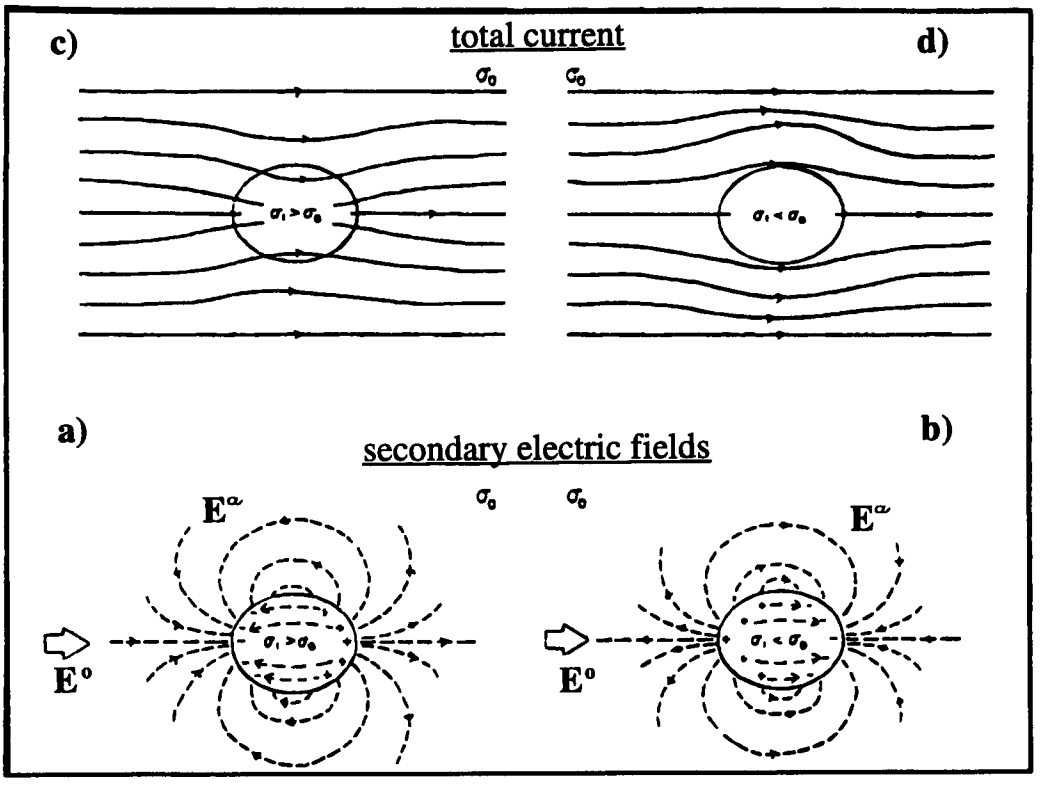

Figure 1: *Galvanic effect: Dipole fields* $\mathbf{E}^a$ *of a conductive (a) and a resistive (b) body. Total fields resulting in 'current channelling' (c) and 'current deflection' (d) (from Jiracek, 1990).*

The total field (graphs (c) and (d)) can be regarded as a vector sum of secondary local and primary regional E-fields. It is therefore decreased over the conductive body (c), but the overall current density is increased inside it. In the case of the resistive anomaly the total field is increased above the anomaly, but the currents split up and flow around its sides (d).

The spatial deviation of regional currents involves all three components of the E-field. Therefore galvanic distortion also produces a local anomalous magnetic field that in turn leads to local distortion of the regional magnetic field. Since these two processes are linked closely, I shall introduce their theoretical formulation together in this chapter. Having already started to approach the problem from a physical point of view, the following sections will present methods to correct electromagnetic data for galvanic distortion effects that are based on a physical model of the earth: the *decomposition* methods, developed by Larsen (1977), Bahr (1985, 1988, 1991), Groom (1988), Groom & Bailey (1989, 1991), Zhang et al. (1987, 1993), and Chave & Smith (1994).

A more mathematically based treatment of the distorted MT impedance tensor (considering electrical distortion only) has been pursued by methods like *eigenstate analysis* by Eggers (1982), and *eigenvalue decompositions* by Spitz (1885), Cevallos (1986), LaTorraca et al. (1986), and Yee & Paulson (1987). A compilation of these methods can be found in Weaver(1994) and Groom & Bailey (1991).

3.1 Physical model of the Earth

The scattering of the electric and magnetic field over a resistivity inhomogeneity may be derived from the solution of the differential wave equation for the electric field under the quasistatic approximation (Habashy et al. 1993; Chave & Smith, 1994). The induction equation (see eqn.10a) for non-magnetic media is given at an observation point ($\mathbf{r}$) by:

$$\nabla \times \nabla \times \mathbf{E}(\mathbf{r}) + k_o^2 \mathbf{E}(\mathbf{r}) \;=\; -i\omega\mu_o \Delta\sigma(\mathbf{r})\, \mathbf{E}(\mathbf{r}) \;=\; Q(\mathbf{r})\, \mathbf{E}(\mathbf{r}) \qquad (37)$$

k_o is the wavenumber of the background medium with conductivity σ_o, hence $k_o^2 = i\omega\mu_o\sigma_o$, and $Q(\mathbf{r})$ marks the change of the material properties from the background medium, with $\Delta\sigma(\mathbf{r}) = \sigma(\mathbf{r}) - \sigma_o$. Eqn.37 can be solved using a dyadic Green function $\underline{\mathbf{G}}(\mathbf{r}, \mathbf{r}')$. The total field outside the anomaly $\mathbf{E}(\mathbf{r})$ can then be expressed as a sum of the regional background field $\mathbf{E}^o(\mathbf{r})$ and the scattered field (integral term):

$$\mathbf{E}(\mathbf{r}) = \mathbf{E}^o(\mathbf{r}) + \int_{V_s} d\mathbf{r}'\, \underline{\mathbf{G}}(\mathbf{r}, \mathbf{r}')\, Q(\mathbf{r}')\, \mathbf{E}(\mathbf{r}') \qquad (38)$$

V_s is the volume of the scattering body and $\mathbf{E}(\mathbf{r}')$ is the electric field inside it (the vector of position $\mathbf{r}'$ marks a point inside the anomaly). Replacing the tensor function by the scalar Green function $g(\mathbf{r}, \mathbf{r}')$ in such a way that

$$\underline{\mathbf{G}}(\mathbf{r}, \mathbf{r}') = [\, \underline{\mathbf{I}} + \frac{1}{k_o^2} \nabla\nabla \,]\, g(\mathbf{r}, \mathbf{r}') \qquad with \quad g(\mathbf{r}, \mathbf{r}') = \frac{e^{ik_o|\mathbf{r}-\mathbf{r}'|}}{4\pi|\mathbf{r}-\mathbf{r}'|} \qquad (39)$$

yields the basic integral equation for electromagnetic scattering:

$$\begin{aligned} \mathbf{E}(\mathbf{r}) \;=\; & \mathbf{E}^o(\mathbf{r}) + \int_{V_s} d\mathbf{r}'\, g(\mathbf{r}, \mathbf{r}')\, Q(\mathbf{r}')\, \mathbf{E}(\mathbf{r}') \\ & + \frac{1}{k_o^2} \nabla\nabla \cdot \int_{V_s} d\mathbf{r}'\, g(\mathbf{r}, \mathbf{r}')\, Q(\mathbf{r}')\, \mathbf{E}(\mathbf{r}') \end{aligned} \qquad (40)$$

The first integral term represents the inductive component since it contains the vector potential. Its contribution to the total scattering vanishes for long periods ($\omega \to 0$) or for small conductivity contrasts ($\Delta\sigma(\mathbf{r}') \to 0$). The second integral term represents the galvanic distortion since it contains the scalar potential. Its contribution is not frequency-dependent, it is based on the conductivity contrast $\Delta\sigma(\mathbf{r}')$ and the volume of the body instead.

Similarly we can express the distortion of the magnetic field (Habashy et al. 1993; Chave & Smith, 1994) :

$$\mathbf{B}(\mathbf{r}) \;=\; -\frac{1}{i\omega}\nabla \times \mathbf{E}(\mathbf{r}) \;=\; \mathbf{B}^o(\mathbf{r}) - \frac{1}{i\omega}\, \nabla \times \int_{V_s} d\mathbf{r}'\, g(\mathbf{r}, \mathbf{r}')\, Q(\mathbf{r}')\, \mathbf{E}(\mathbf{r}') \qquad (41)$$

Again, the scattering term is purely dependent on material and volume. The secondary anomalous magnetic field is in phase with the background electric field, since it is generated by spatial variations only ($\nabla \times \mathbf{E}$). Note that eqn.40 and eqn.41 both contain the internal electric field $\mathbf{E}(\mathbf{r}')$ in their integral parts. Solutions may be obtained using the Born approximation that simply replaces this internal field by

the background electric field $\mathbf{E}^o(\mathbf{r})$. However, this simplification is justified only for smaller bodies and longer periods (Born & Wolf, 1980). Habashi et al. (1993) suggest to use the localized non-linear (LN) approximation, that allows the internal field to vary inside the inhomogeneity, while the background field is assumed to be uniform around it:

$$\mathbf{E}(\mathbf{r}') \;=\; \underline{\Gamma}(\mathbf{r}')\,\mathbf{E}^o(\mathbf{r}') \;\approx\; \underline{\Gamma}(\mathbf{r}')\,\mathbf{E}^o(\mathbf{r}) \tag{42}$$

The depolarisation tensor $\underline{\Gamma}(\mathbf{r}')$ in turn reflects the form of this solution:

$$\underline{\Gamma}(\mathbf{r}') = \left[\,\underline{\mathbf{I}} - \left(\,\underline{\mathbf{I}} + \frac{1}{k_o^2}\nabla\nabla\,\right)\int_{V_s} d\mathbf{r}'\; g(\mathbf{r},\mathbf{r}')\;Q(\mathbf{r}')\,\right]^{-1} \tag{43}$$

Keeping in mind the assumptions made in the previous formulations, eqn.40 and eqn.41 can be rewritten in tensor form:

$$\mathbf{E}(\mathbf{r}) \;=\; \underline{\mathbf{C}}\cdot\mathbf{E}^o(\mathbf{r}) \tag{44}$$

$$\text{and}\qquad \mathbf{B}(\mathbf{r}) \;=\; \mathbf{B}^o(\mathbf{r}) + \underline{\mathbf{D}}\cdot\mathbf{E}^o(\mathbf{r}) \tag{45}$$

with (40 and 41)

$$\underline{\mathbf{C}} \;=\; \underline{\mathbf{I}} \;+\; \left(\,\underline{\mathbf{I}} + \frac{1}{k_o^2}\nabla\nabla\,\right)\int_{V_s} d\mathbf{r}'\; g(\mathbf{r},\mathbf{r}')\;Q(\mathbf{r}')\;\underline{\Gamma}(\mathbf{r}') \tag{46}$$

$$\underline{\mathbf{D}} \;=\; -\,\frac{1}{i\omega}\,\nabla\times\int_{V_s} d\mathbf{r}'\; g(\mathbf{r},\mathbf{r}')\;Q(\mathbf{r}')\;\underline{\Gamma}(\mathbf{r}') \tag{47}$$

At periods where the inhomogeneity produces an inductive response, the elements of the distortion tensor $\underline{\mathbf{C}}$ are complex quantities. Only at long enough periods, when the size of the body becomes small compared to the skin depth of the penetrating fields, both tensors $\underline{\mathbf{C}}$ and $\underline{\mathbf{D}}$ contain purely real components. The galvanic distortion tensor elements are then functions of position, depending also on the geometry of the inhomogeneity. This implies that the distortion tensor components are not inherently interesting, but rather serve as an avenue for estimating the undistorted electromagnetic response (Chave & Smith, 1994).

3.2 The galvanic distortion tensors C and D

Theoretically, both distortion tensors can have up to 9 real components, since both regional fields may contain a vertical component (Zhang, 1987): For the MT approach, the electric and magnetic fields are assumed to have only horizontal components (see eqn.22). The distortion tensors are therefore 2×2 matrices :

$$\underline{\mathbf{C}} = \begin{pmatrix} C_{xx} & C_{xy} \\ C_{yx} & C_{yy} \end{pmatrix} \qquad \text{and} \qquad \underline{\mathbf{D}} = \begin{pmatrix} D_{xx} & D_{xy} \\ D_{yx} & D_{yy} \end{pmatrix} \tag{48}$$

Note that the electric distortion tensor is non-dimensional, whereas the components of the magnetic distortion tensor have the units of the admittance $[\frac{\mathrm{s}}{\mathrm{m}}]$.

Galvanic distortion has two principal effects on the MT impedance tensor $\underline{\mathbf{Z}}$:
a) purely real, frequency-independent distortion due to distortion of the electric

field; b) a mixture of real and complex, frequency-dependent distortion if magnetic distortion is involved, because the magnetic distortion operator contains the purely regional impedance tensor $\underline{\mathbf{Z}}^{\circ}$: This can be shown by rewriting the basic relation $\mathbf{E} = \underline{\mathbf{Z}} \cdot \mathbf{B}$ (see eqn. 21) using the expressions that allow for distortion of the electric and magnetic fields (equations 44 and 45):

$$\begin{aligned} \underline{\mathbf{C}}\,\mathbf{E}^{\circ} &= \underline{\mathbf{Z}} \cdot (\mathbf{B}^{\circ} + \underline{\mathbf{D}}\,\mathbf{E}^{\circ}) \\ &= \underline{\mathbf{Z}} \cdot (\underline{\mathbf{I}} + \underline{\mathbf{D}}\,\underline{\mathbf{Z}}^{\circ})\,\mathbf{B}^{\circ} \end{aligned} \tag{49}$$

Here, the regional electric field was replaced by the product of the regional impedance and the magnetic field. This step enables us to link the purely regional impedance tensor $\underline{\mathbf{Z}}^{\circ}$ to the observed, distorted impedances in $\underline{\mathbf{Z}}$:

$$\mathbf{E}^{o} = \underbrace{\underline{\mathbf{C}}^{-1}\,\underline{\mathbf{Z}} \cdot (\underline{\mathbf{I}} + \underline{\mathbf{D}}\,\underline{\mathbf{Z}}^{\circ})}_{\underline{\mathbf{Z}}^{\circ}}\,\mathbf{B}^{o} \tag{50}$$

Consequently, the measured impedance tensor is:

$$\underline{\mathbf{Z}} = \underline{\mathbf{C}}\,\underline{\mathbf{Z}}^{\circ} \cdot (\underline{\mathbf{I}} + \underline{\mathbf{D}}\,\underline{\mathbf{Z}}^{\circ})^{-1} \tag{51a}$$

$$\text{or} \quad \underline{\mathbf{Z}} = \underline{\mathbf{R}}_{\theta_r}\,\underline{\mathbf{C}}\,\underline{\mathbf{Z}}^{\circ} \cdot (\underline{\mathbf{I}} + \underline{\mathbf{D}}\,\underline{\mathbf{Z}}^{\circ})^{-1}\underline{\mathbf{R}}_{\theta_r}^{T} \quad \text{for regional strike } \theta_r \tag{51b}$$

Decomposition methods are aimed at revealing the two undistorted principal impedances, the undistorted strike direction and a trustworthy, undistorted dimensionality parameter (skew). Since the magnetic distortion operator decays with $\sqrt{\omega}$, its effects are usually assumed to be much smaller than those of the electric distortion tensor. Therefore and because usually the extension of the distorting inhomogeneities are assumed to be of the order of 10 to 100 m, most methods treat the distortion of the impedance tensor as an electric distortion problem only: $\underline{\mathbf{Z}} = \underline{\mathbf{C}}\,\underline{\mathbf{Z}}^{\circ}$ or $\underline{\mathbf{Z}} = \underline{\mathbf{R}}_{\theta_r}\,\underline{\mathbf{C}}\,\underline{\mathbf{Z}}^{\circ}\,\underline{\mathbf{R}}_{\theta_r}^{T}$ if measurement coordinates do not coincide with the direction of regional strike. Only recently has magnetic distortion been included into MT tensor decomposition by Chave & Smith (1994).

The consequences of distortion for the magnetic response function in GDS are more significant, because current concentrations due to conductivity heterogeneities can produce a large anomalous vertical magnetic field. Induction arrows can be contaminated strongly by these local effects; they can even be produced entirely by a near surface heterogeneity, or for longer periods by a body of considerable extension. If their origin is not recognized properly the arrows can erroneously be interpreted as resulting from regional structures.

Now the magnetic distortion matrix consists of 6 real components, two of them referring to the vertical field. Eqn.45 can be rewritten proceeding similarly as in eqn.49: The regional electric field is replaced by the regional impedance and the magnetic field.

$$\mathbf{B} = \mathbf{B}^{o} + \mathbf{B}^{a} = \mathbf{B}^{o} + \underline{\mathbf{D}}\,\underline{\mathbf{Z}}^{\circ}\,\mathbf{B}_{h}^{o} \tag{52}$$

$$\begin{pmatrix} B_x \\ B_y \\ B_z \end{pmatrix} = \begin{pmatrix} B_x^o \\ B_y^o \\ B_z^o \end{pmatrix} + \begin{pmatrix} D_{xx} & D_{xy} \\ D_{yx} & D_{yy} \\ D_{zx} & D_{zy} \end{pmatrix} \begin{pmatrix} 0 & Z_E \\ -Z_B & 0 \end{pmatrix} \begin{pmatrix} B_x^o \\ B_y^o \end{pmatrix} \tag{53}$$

This expression can be split into horizontal and vertical parts $\mathbf{B}_h$ and B_z:

$$\mathbf{B}_h = \mathbf{B}_h^o + \mathbf{B}_h^a = (\underline{\mathbf{I}} + \underline{\mathbf{D}}_h \underline{\mathbf{Z}}^o)\,\mathbf{B}_h^o \tag{54a}$$

$$B_z = B_z^o + B_z^a = [(\mathcal{A}^o, \mathcal{B}^o) + (D_{zx}, D_{zy})\underline{\mathbf{Z}}^o]\,\mathbf{B}_h^o \tag{54b}$$

$(\mathcal{A}^o, \mathcal{B}^o)$ is the regional magnetic response function, obtained from the the regional field contributions: $B_z^o = (\mathcal{A}^o, \mathcal{B}^o)\,\mathbf{B}_h^o$. From the observed field components, however, we get a distorted response:

$$B_z = (\mathcal{A}, \mathcal{B})\,\mathbf{B}_h = \mathcal{A}\,B_x + \mathcal{B}\,B_y \tag{55}$$

Using Eqn.54b we can now separate local and regional parts of the response function:

$$(\mathcal{A}, \mathcal{B}) = \underbrace{(\mathcal{A}^o, \mathcal{B}^o)\,(\underline{\mathbf{I}} + \underline{\mathbf{D}}_h \underline{\mathbf{Z}}^o)^{-1}}_{\tilde{\mathcal{A}}^o, \tilde{\mathcal{B}}^o)} + \underbrace{(D_{zx}, D_{zy})\underline{\mathbf{Z}}^o\,(\underline{\mathbf{I}} + \underline{\mathbf{D}}_h \underline{\mathbf{Z}}^o)^{-1}}_{(\mathcal{A}^\ell, \mathcal{B}^\ell)} \tag{56}$$

$(\tilde{\mathcal{A}}^o, \tilde{\mathcal{B}}^o)$ is the regional response function which still contains contributions from distortion processes at the scattering structure. $(\mathcal{A}^\ell, \mathcal{B}^\ell)$ is the local response valid at periods sufficiently long that the local anomaly can be considered free of induction (Zhang et al. 1993). In this context, the scatterer may be much larger than a mere near-surface inhomogeneity. Magnetic distortion will then affect GDS data at periods that are usually considered distortion-free. Note that the distortion terms are additive and multiplicative to the regional response in GDS, whereas the MT impedance tensor is distorted only by a multiplicative term (Chave & Smith, 1994). Hence it is impossible to solve the problem in GDS for all parameters involved and we can only obtain combinations as done by Zhang et al. (1993) and Chave & Smith (1994). Or else, we can concentrate on situations, where the regional field has no or only a small, spatially non-varying, vertical component, either because the regional structure is 1D, or the body is sufficiently removed from vertical boundaries. This approach has been pursued in chapter 4.

3.3 Physical decomposition methods

MT decomposition is usually done for electric distortion only (with the exception of Chave and Smith's method (1994)), where the impedance tensor is described by 9 parameters: 2 complex regional impedances, 4 real distortion parameters and the regional strike angle θ_r. Since the observed impedance tensor provides only 4 complex quantities, it is obvious that the problem cannot be solved exactly. Thus the principal impedances determined by decomposition still may contain distortion in the form of two different 'anisotropy' or 'shift' factors (see sections 3.3.1 and 3.3.2). Only if the distortion matrix is known to be caused by a two-dimensional anomaly, distortion may be described by two independent parameters. In this case the number of parameters is smaller than the number of input quantities, and therefore the true principal impedances may be recovered (see sections 3.3.4; Zhang et al. 1987).

However, it is impossible to decide the dimensionality of the scattering body from the measured impedance tensor, because a 3D distortion matrix can always be

turned into a two-dimensional one. This is done simply by absorbing some matrix elements into the unknown shift parameters of the principal impedances (Smith, 1995). Consequently, the determined impedances are contaminated even more badly by distortion which is the opposite of what was intended, when considering a two-dimensional distortion matrix. Methods for the removal of magnetic distortion in MT and at single GDS sites suffer also from the problem of indeterminacy (see sections 3.3.3 and 3.3.4).

3.3.1 Bahr's decomposition

Larsen (1977) described galvanic distortion of a local 3D anomaly over a 1D layered earth using the real electric distortion matrix. Bahr (1985) introduced a combination of local 3D scattering of 2D regional fields in his 'superimposition model'. He put special emphasis on the investigation of the phases of the observed impedance tensor elements. Since he considers electric distortion only, both elements of the two columns of the impedance tensor must contain the same phase information, respectively:

$$\underline{\mathbf{Z}} = \underline{\mathbf{C}}\,\underline{\mathbf{Z}}^{\circ} = \begin{pmatrix} -C_{xy}Z_B & C_{xx}Z_E \\ -C_{yy}Z_B & C_{yx}Z_E \end{pmatrix} \quad with \quad \underline{\mathbf{Z}}^{\circ} = \begin{pmatrix} 0 & Z_E \\ -Z_B & 0 \end{pmatrix} \tag{57}$$

This assumption forms the basis for the extraction of 3 parameters, that are not elements of the distortion tensor itself. They rather describe the extent to which electric distortion affects the principal impedances Z_E and Z_B.

a) A rotationally invariant 'measure of the phase difference' of all four elements[8] of the observed impedance tensor (also an indication for one-dimensionality) is given by[9]:

$$\mu = \sqrt{|[D_1, S_2] + [S_1, D_2]|}\,/D_2 \tag{58}$$

b) The 'phase sensitive skew' measures whether the assumed model is appropriate:

$$\eta = \sqrt{|[D_1, S_2] - [S_1, D_2]|}\,/D_2 \tag{59}$$

c) Deviations of the above model result in phase differences between the two elements of one column. Small differences can be tolerated within the given framework by introducing a 'phase deviation angle' as an additional model parameter (Bahr, 1991):

$$\underline{\mathbf{Z}} = \begin{pmatrix} -C_{xy}Z_B e^{i\delta} & C_{xx}Z_E \\ -C_{yy}Z_B & C_{yx}Z_E e^{-i\delta} \end{pmatrix} \tag{60}$$

After determining the properties of the impedance tensor, the undistorted regional strike angle can be determined analytically by minimizing the phase differences within the columns:

$$\tan 2\theta_r = ([S_1, S_2] - [D_1, D_2]) \;/\; ([S_1, D_1] + [S_2, D_2]) \tag{61}$$

---

[8] with $S_1 = Z_{xx} + Z_{yy}$, $S_2 = Z_{xy} + Z_{yx}$, $D_1 = Z_{xx} - Z_{yy}$, $D_2 = Z_{xy} - Z_{yx}$

[9] and $[S_1, D_2] = ReS_1 ImD_2 - ImS_1 ReD_2$; S_1, D_2 are rotationally invariant

Rotation into the strike coordinate system yields the undistorted principal impedance phases ϕ_E and ϕ_B. The magnitudes of the principal impedances, however, still contain the 'two unknown shift parameters' D' and D'':

$$Z_{\tilde{E}} = D' Z_E = \sqrt{C_{xy}^2 + C_{yy}^2}\, Z_E \tag{62a}$$

$$\text{and} \quad Z_{\tilde{B}} = D'' Z_B = \sqrt{C_{xx}^2 + C_{yx}^2}\, Z_B \tag{62b}$$

Since the column elements of the impedance tensor in strike coordinates are proportional, the distortion contained may equally well be expressed by one parameter per column. These parameters are given by the ratios of the column elements which is equal to the ratios of the linked distortion parameters. Since these coefficients must describe the spatial deviation of the regional electric currents, they can be defined as two angles of rotation. Then Eqn.60 becomes:

$$\underline{\mathbf{C}}\,\underline{\mathbf{Z}}^{\circ} = \begin{pmatrix} \tan\beta_1 Z_{\tilde{B}} & Z_{\tilde{E}} \\ Z_{\tilde{B}} & -\tan\beta_2 Z_{\tilde{E}} \end{pmatrix} \tag{63}$$

It follows that the distortion matrix must have the form:

$$\underline{\mathbf{C}} = \begin{pmatrix} D'' \cos\beta_2 & -D' \sin\beta_1 \\ D'' \sin\beta_2 & D' \cos\beta_1 \end{pmatrix} \tag{64}$$

β_1 and β_2 are referred to as 'skew angles' and describe how much the regional electric fields associated with E- and B-polarisation are rotated out of their normal directions (Groom & Bahr, 1992). In this notation, β_1 and β_2 rotate the E'_y and E'_x component, respectively, while D' and D'' denote their gains. At this point, it becomes clear that one cannot decide from the data whether the distortion matrix is two- or three-dimensional. The distortion tensor given above can be transformed into a two-dimensional matrix simply by absorbing $\sin^{-1}\beta_1$ and $\sin^{-1}\beta_2$ into D' and D''. The distortion parameters describe only the rotation of the electric components out of their 'normal' directions, they do not describe the scattering body.

From the ratios of rotated impedances one can determine β_1 and β_2 and from these, the (still) shifted principal impedances $Z_{\tilde{B}}$ and $Z_{\tilde{E}}$.

3.3.2 Groom & Bailey's decomposition

Groom & Bailey (1989) introduced a factorisation of the electric distortion tensor into 3 matrices. Each one describes a different effect on the MT impedance tensor:

$$\underline{\mathbf{C}} = g\,\underline{\mathbf{T}}\,\underline{\mathbf{S}}\,\underline{\mathbf{A}} \tag{65}$$

The scalar factor g ('site gain') and the anisotropy tensor $\underline{\mathbf{A}}$ (containing anisotropy parameter s) correspond to Bahr's unknown shift factors, and are inseparably linked to the principal impedances, since $g\underline{\mathbf{A}}\,\underline{\mathbf{Z}}^{\circ}$ still looks like an ideal 2D impedance tensor (Groom & Bailey, 1989). Shear tensor $\underline{\mathbf{S}}$ and twist tensor $\underline{\mathbf{T}}$ are defined as:

$$\underline{\mathbf{T}} = \frac{1}{\sqrt{1+t^2}} \begin{pmatrix} 1 & -t \\ t & 1 \end{pmatrix} \quad \text{and} \quad \underline{\mathbf{S}} = \frac{1}{\sqrt{1+e^2}} \begin{pmatrix} 1 & e \\ e & 1 \end{pmatrix} \tag{66}$$

The factors preceding the matrices are usually absorbed into the site gain factor g, but their purpose is, to define twist and shear as rotation matrices, using:

$$\frac{1}{\sqrt{1+t^2}} = \cos\varphi_t \qquad \text{and} \qquad \frac{t}{\sqrt{1+t^2}} = \sin\varphi_t \tag{67}$$

With these two definitions (e.g. Bronstein, 1981), the twist and shear operators describe two different effects that distortion has on the electric field components: The twist tensor rotates both components clockwise through twist angle φ_t, whereas the shear tensor causes rotation of the components relative to each other by shear angle φ_e:

$$\underline{\mathbf{T}} = \begin{pmatrix} \cos\varphi_t & -\sin\varphi_t \\ \sin\varphi_t & \cos\varphi_t \end{pmatrix} \qquad \text{and} \qquad \underline{\mathbf{S}} = \begin{pmatrix} \cos\varphi_e & \sin\varphi_e \\ \sin\varphi_e & \cos\varphi_e \end{pmatrix} \tag{68}$$

The product of both matrices yields exactly the same form for the distortion matrix, as Bahr's approach did by using the skew angles β_1 and β_2:

$$\underline{\mathbf{T}}\,\underline{\mathbf{S}} = \begin{pmatrix} \cos(\varphi_t+\varphi_e) & -\sin(\varphi_t-\varphi_e) \\ \sin(\underbrace{\varphi_t+\varphi_e}_{\beta_2}) & \cos(\underbrace{\varphi_t-\varphi_e}_{\beta_1}) \end{pmatrix} \tag{69}$$

For their decomposition, Groom & Bailey (1989) chose to solve a nonlinear equation system, using the same sums and differences of the observed impedances as defined in Bahr's method[10]

$$\begin{aligned}
\alpha_0 &= [(e+t)\,\tilde{Z_E} - (e-t)\,\tilde{Z_B} \\
\alpha_1 &= [(1-et)\,\tilde{Z_E} - (1+et)\,\tilde{Z_B}]\cos 2\theta_r - [(e+t)\,\tilde{Z_E} + (e-t)\,\tilde{Z_B}]\sin 2\theta_r \\
\alpha_2 &= -[(1-et)\,\tilde{Z_E} + (1+et)\,\tilde{Z_B}] \\
\alpha_3 &= -[(1-et)\,\tilde{Z_E} - (1+et)\,\tilde{Z_B}]\sin 2\theta_r - [(e+t)\,\tilde{Z_E} + (e-t)\,\tilde{Z_B}]\cos 2\theta_r
\end{aligned} \tag{70}$$

After linearisation (P.Ritter, 1988), these 4 complex equations can be solved simultaneously for all 7 parameters (i.e. two complex shifted regional impedances, shear, twist, and regional strike angle) by least squares fitting. A χ^2 - like error estimate is used to monitor the fit of the data over the period range with respect to the strike angle. The regional strike is usually fixed to an azimuth of relatively low error over the whole period range. Twist and shear angles may then be constrained to those values that were found to be most constant over the whole period range.

Bahr's and Groom/Bailey's decomposition methods differ basically in the sequence in which the model parameters are derived; the latter procedure seems to give more stable results with real data, i.e. slight deviations from the ideal model (Bahr, 1991). Groom (1988) and Groom & Bailey (1991) point out that a more complete decomposition of the MT impedance tensor may be achieved by incorporating magnetic distortion into the decomposition. This can only be done by increasing the number of degrees of freedom, i.e. solving the equation system for a whole band of periods or for several sites simultaneously. These ideas have led to an extension of the Groom/Bailey method by Chave & Smith (1994).

---

[10] with $\alpha_0 = S_1$, $\alpha_1 = S_2$, $\alpha_2 = D_2$, $\alpha_3 = D_1$.

3.3.3 Chave & Smith's decomposition

The full electric and magnetic decomposition of the MT impedance tensor suffers from an even greater indeterminacy than results from electric decomposition alone (Chave & Smith, 1994). The antidiagonal elements D_{xy} and D_{yx} of the magnetic distortion tensor $\underline{\mathbf{D}}$ are absorbed into the regional impedance tensor (see eqn.51b) without changing its 2D form (similar to g and s in the Groom/Bailey factorisation). Thus only the diagonal components D_{xx} and D_{yy} can be determined from the observed impedances. The equation system derived for MT decomposition consists of 4 complex nonlinear expressions. They contain Groom & Bailey's equations $\alpha_o \ldots \alpha_3$:

$$\begin{aligned}
\zeta_0 &= \kappa\,[\,\alpha_o + [\,(1-et)D_{yy} + (1+et)D_{xx}]\; Z_E Z_B\,] \\
\zeta_1 &= \kappa\,[\,\alpha_1 + [\,((e+t)D_{yy} + (e-t)D_{xx})\;\cos 2\theta_r \\
&\qquad + ((1-et)D_{yy} - (1+et)D_{xx})\;\sin 2\theta_r]\; Z_E Z_B\,] \\
\zeta_2 &= \kappa\,[\,\alpha_2 + [\,(e+t)D_{yy} - (e-t)D_{xx}]\; Z_E Z_B\,] \\
\zeta_3 &= \kappa\,[\,\alpha_3 + [\,((e+t)D_{yy} + (e-t)D_{xx})\;\sin 2\theta_r \\
&\qquad + ((1-et)D_{yy} - (1+et)D_{xx})\;\cos 2\theta_r]\; Z_E Z_B\,]
\end{aligned} \tag{71}$$

with $\kappa = (1 + D_{xx}D_{yy}Z_E Z_B)^{-1}$. The system can be solved for all 9 parameters involved only if it is fitted for more than two frequencies simultaneously. This makes sense because all distortion parameters involved should be frequency independent. The number of degrees of freedom can also be increased by including the magnetic response function into the equation system. This step provides 2 more complex equations. Then the whole system consists of 12 real equations and it can be solved for 12 parameters: 2 regional impedances, 1 magnetic response $(0, \tilde{\mathcal{B}}^o)$ (with $D_{zx} \cdot Z_E$ subsumed into $\tilde{\mathcal{B}}^o$), shear, twist, regional strike, and 3 magnetic distortion parameters D_{xx}, D_{yy} and D_{zy}:

$$\begin{aligned}
\zeta_4 &= \mathcal{A} = \kappa\,[\,-\tilde{\mathcal{B}}^o(\sin\theta_r - D_{yy}Z_B\cos\theta_r) \;-\; D_{zy}Z_B(\cos\theta_r + D_{xx}Z_E\sin\theta_r)\,] \\
\zeta_5 &= \mathcal{B} = \kappa\,[\,\tilde{\mathcal{B}}^o(\cos\theta_r + D_{yy}Z_B\sin\theta_r) \;-\; D_{zy}Z_B(\sin\theta_r - D_{xx}Z_E\cos\theta_r)\,]
\end{aligned} \tag{72}$$

With this extension a simultaneous fitting gives an exact solution of the decomposition at each frequency. The procedure for the magnetic response function can also be carried out as a separate step following MT decomposition and using these results. Chave & Smith (1994) use a modified Levenberg-Marquard algorithm to solve the equation system, and they suggest the non-parametric jacknife method for the computation of more realistic confidence intervals for the estimates.

3.3.4 Zhang's decomposition

The idea underlying Zhang's approach is very similar to Bahr's phase concept. In the principal model the scattering body is two-dimensional with a local strike θ_ℓ and related coordinate system (x'', y''), different from the regional strike θ_r with (x', y'). In this case the local structure is fully described by 2 real parameters: C''_{yy} and θ_ℓ if the body strikes in the x'' direction (Zhang et al. 1987). The distortion tensor in

measurement coordinates then takes the form:

$$\underline{\mathbf{C}} = \underline{\mathbf{R}}_{\theta_\ell}\,\underline{\mathbf{C}}^o\,\underline{\mathbf{R}}^T_{\theta_\ell} \qquad \text{with} \quad \underline{\mathbf{C}}^o = \begin{pmatrix} 0 & 0 \\ 0 & C''_{yy} \end{pmatrix} \tag{73}$$

Rotated into the local coordinate system, the 2D impedance tensor has a particular form: the diagonal elements are proportional. They are related by a real, frequency-independent factor α. The regional strike direction, however, is characterized by that direction for which the elements of the columns of the impedance tensor are proportional:

$$\underline{\mathbf{Z}}(\theta_\ell) = \begin{pmatrix} \alpha Z_{yy} & Z_{xy} \\ Z_{yx} & Z_{yy} \end{pmatrix} \qquad \text{and} \qquad \underline{\mathbf{Z}}(\theta_r) = \begin{pmatrix} \beta_1 Z_{yx} & Z_{xy} \\ Z_{yx} & \beta_2 Z_{xy} \end{pmatrix} \tag{74}$$

The two real and frequency-independent proportionality constants (β_1 and β_2) correspond to Bahr's skew parameters. While Bahr (1985) gives analytic solutions for the determination of the principal impedances and θ_r, Zhang et al. (1987) use the least-squares method to estimate the five parameters $(\alpha, \beta_1, \beta_2, \theta_r, \theta_\ell)$ from the proportionality relations:

$$\begin{aligned} Z_{xx}(\theta_\ell) &= \alpha Z_{yy}(\theta_\ell) \qquad \text{and} \qquad Z_{xx}(\theta_r) = \beta_1 Z_{yx}(\theta_r) \\ & \qquad\qquad\qquad\quad\;\; Z_{yy}(\theta_r) = \beta_2 Z_{xy}(\theta_r) \end{aligned} \tag{75}$$

where Z_{xy} and Z_{yx} are assumed to be noise-free compared to Z_{xx} and Z_{yy}. The noise level of the two diagonal elements is equal. In this procedure the following equations are minimized for impedance values of a specific period interval (a decade):

$$\begin{aligned} \mathcal{Q}(\beta_1, \beta_2, \theta) &= |Z_{xx} - \beta_1 Z_{yx}|^2 + |Z_{yy} - \beta_2 Z_{xy}|^2 \\ \mathcal{Q}(\alpha, \theta) &= |\alpha_1 Z_{xx} + \alpha_2 Z_{yy}|^2 + \lambda(1 - \alpha_1^2 - \alpha_2^2) \quad \text{with} \quad \alpha = -\alpha_2/\alpha_1 \end{aligned} \tag{76}$$

The impedances are weighted by the standard errors of $Z_{xx}(\theta)$, and λ is a Lagrangian multiplier[11]. At any rotation angle θ the parameters are obtained from the complex conjugates of the impedances:

$$\begin{aligned} \beta_1 &= \frac{Z^*_{xx} Z^*_{yx}}{|Z^*_{yx}|} & \alpha_1 &= \left[1 + \left(\frac{|Z^*_{xx}| - \lambda^{\pm}}{Re(Z^*_{xx} Z^*_{yy})}\right)^2\right]^{-\frac{1}{2}} \\ \beta_2 &= \frac{Z^*_{yy} Z^*_{xy}}{|Z^*_{xy}|} & \alpha_2 &= -\alpha_1 \frac{|Z^*_{xx}|^2 - \lambda^{\pm}}{Re(Z^*_{xx} Z^*_{yy})} \end{aligned} \tag{77}$$

The global minima for the target functions $\mathcal{Q}(\beta_1, \beta_2, \theta)$ and $\mathcal{Q}(\alpha, \theta)$ may be found by varying the rotation angle θ from 0° to 90° in small steps. Now the distortion parameter can be determined from β_1 and β_2. Both should yield the same value for C''_{yy}. Then the (still distorted) principal impedances can be estimated, and in contrast to all other methods described before, even the undistorted regional impedances Z_E and Z_B can be determined, since we know C''_{yy} (Zhang et al. 1987). This is a consequence of the assumed principal model.

---

[11] with solutions $\lambda^{\pm} = \frac{1}{2}\left[\, |Z^*_{xx}| + |Z^*_{yy}| \pm \sqrt{(\,|Z^*_{xx}| - |Z^*_{yy}|\,)^2 + 4Re^2(Z^*_{xx} Z^*_{yy})}\,\right]$

For the treatment of the distorted magnetic response function, Zhang et al (1993) replace the regional impedance tensor in eqn.56 by the observed one using eqn.51a: $\underline{\mathbf{C}}^{-1}\underline{\mathbf{Z}} = \underline{\mathbf{Z}}^{o} \cdot (\underline{\mathbf{I}} + \underline{\mathbf{D}}_h \underline{\mathbf{Z}}^{o})^{-1}$. This change enables all further calculations to be made directly from data in field coordinates (x, y):

$$\begin{aligned}(\mathcal{A}, \mathcal{B}) &= (\mathcal{A}^o, \mathcal{B}^o)\,[\underline{\mathbf{I}} + \underline{\mathbf{D}}_h\,\underline{\mathbf{Z}}^o]^{-1} + \underbrace{(D_{zx}, D_{zy})\underline{\mathbf{C}}^{-1}\,\underline{\mathbf{Z}}}_{(T_{zx}, T_{zy})} \\ &= (\tilde{\mathcal{A}}^o, \tilde{\mathcal{B}}^o) + (\mathcal{A}^\ell, \mathcal{B}^\ell)\end{aligned} \tag{78}$$

Since $\underline{\mathbf{Z}}$ never increases faster than period on a logarithmic scale, the period range where magnetic distortion occurs is restricted to non-increasing induction arrows. Instead their lengths will be constant at long periods, at which skin depths are significantly larger than crustal conductivity structures (Zhang et al. 1993). The real, frequency-independent prediction coefficients T_{zx} and T_{zy} can be found by minimizing the target function:

$$\mathcal{Q}(T_{zx}, T_{zy}) = |\mathcal{A} - T_{zx}Z_{xx} - T_{zy}Z_{yx}|^2 + |\mathcal{B} - T_{zx}Z_{xy} - T_{zy}Z_{yy}|^2 \tag{79}$$

This condition yields the following two linear equations, where the impedances are assumed to be noise-free compared to the measured regional response components $\mathcal{A}$ and $\mathcal{B}$:

$$Re(Z^*_{xx}\mathcal{A} + Z^*_{xy}\mathcal{B}) = (|Z_{xx}|^2 + |Z_{xy}|^2)T_{zx} + Re(Z^*_{xx}Z_{yx} + Z^*_{xy}Z_{yy})T_{zy} \tag{80a}$$

$$Re(Z^*_{yx}\mathcal{A} + Z^*_{yy}\mathcal{B}) = (|Z_{yx}|^2 + |Z_{yy}|^2)T_{zy} + Re(Z^*_{xx}Z_{yx} + Z^*_{xy}Z_{yy})T_{zx} \tag{80b}$$

Impedances and magnetic response functions are realisations over a period band, normalized by the standard deviations of $\mathcal{A}$ and $\mathcal{B}$. The prediction coefficients are used to identify period bands where galvanic distortion is affecting the data, and furthermore to estimate the contribution of the local response to the total magnetic response function.

3.4 Discussion

All decomposition methods aim at explaining 3D data at longer periods in terms of simplified, regional 2D structures without conducting full 3D model calculations. This approach is certainly justified by the considerable computing time that 3D modelling, even thinsheet modelling, still requires, not to mention the time needed to design and adopt the appropriate model. Often models cannot be calculated over the full period range to include induction as well as galvanic distortion.

As a consequence one wishes to extract as much information as possible from the observed electromagnetic response functions directly. Obviously, as all approaches show, information on the regional 2D structure is contained in distorted data. However, great care should be taken to choose the appropriate method for every survey and every single site, since the regional/local situation may vary and demand different procedures. Automatic data processing could rather cause damage than benefit in this context: *'No one method is a panacea and the user must be wary of their*

effects on the data so as not to be misled' (Jiracek, 1990). To allow a correct choice of method, Bahr (1991) suggested a classification of telluric distortion into 7 subdivisions, starting with the simplest model and proceeding to the more complex settings.

On the other hand, all we need to extract from our data is the correct regional strike angle in order to determine the undistorted phases of the principal impedances. Their amplitudes are still shifted, and it has been shown that static shift cannot be eliminated by decomposition methods, nor can distortion parameters be interpreted in terms of the local inhomogeneity. The strike angle, however, may as well be determined without using any of the presented equations and inversion methods, simply by rotating the impedance tensor and monitoring the phases of the column elements at each period (Junge, 1994a). A reliable angle is found as soon as the phases within each of the columns overlap within their error bars. This procedure is most straight foreward and probably the most effective off all, because it focusses on the most important parameter, θ_r, and also takes into account data errors.

If no corresponding angles for both columns of the impedance tensor can be found within the confidence limits, the only conclusion can be that the galvanic distortion model is not appropriate for the dataset in the investigated period range. Or, as this approach (like most of the widely applied techniques) is based on electric distortion only, the scattering inhomogeneity is big enough that magnetic distortion affect the impedance phases. For the same reason, GDS data at longer periods cannot always be assumed distortion-free, if large-scale conductive structures are responsible for the deviation of regional currents. An example for this case is given in chapter (5) with magnetic response functions from the 'Iapetus' dataset.

Since the separation of local from regional effects depends very much on the geometrical relation of the structures involved and on their extensions in respect to the surveyed area, it seems insufficient to solve the problem for single stations alone. Hence it is most important to consider the spatial distribution of the data, either by comparing results to those from neighbouring sites, or more efficiently, by inverting sites that represent the same regional geology jointly by any of the above methods.

In the following chapter I will present a method to reveal regional information from distorted magnetic response functions, that was developed entirely on this idea. It seemed natural to use a whole array of data and process it as a unit, in order to extract common information. Hypothetical event analysis has always been a tool to help us visualize and interpret spatial distributions of magnetic fields. It can be shown that magnetic distortion of the vertical magnetic field may be eliminated by applying this procedure.

4 Separation of Local and Regional Information

Magnetic distortion is caused by the local superposition of an anomalous magnetic field $\mathbf{B}^a$ on the regional magnetic field $\mathbf{B}^o$. The observed field $\mathbf{B}$ equals therefore the sum $\mathbf{B}^o + \mathbf{B}^a$. The anomalous field (B_x^a, B_y^a, B_z^a) is generated by the spatial deviation of uniform regional currents through or around a local anomaly, which is assumed to be much smaller than the skin depth of the investigated period range (see also section 7.1.1). $\mathbf{B}^a$ is therefore *in phase* with the regional electric field $\mathbf{E}^o$:

$$\mathbf{B}^a = \underline{\mathbf{D}} \cdot \mathbf{E}^o \qquad \Longrightarrow \varphi(\mathbf{B}^a) = \varphi(\mathbf{E}^o) \tag{81}$$

The magnetic distortion matrix $\underline{\mathbf{D}}$ consists of 6 real, frequency-independent parameters (Zhang et al. 1987). As shown in the previous chapter, the regional electric field $\mathbf{E}^o$ can be replaced by the product of the regional MT impedance tensor $\underline{\mathbf{Z}}^o$ and the horizontal magnetic field $\mathbf{B}^o$:

$$\mathbf{B}^a = \underline{\mathbf{D}}\,\mathbf{Z}^o \cdot \mathbf{B}^o \tag{82}$$

This replacement is based on the assumption that the regional fields are uniform over the area of interest, which implies that the local anomaly is sufficiently removed either horizontally or vertically from the regional lateral conductivity boundaries. In particular, the regional vertical magnetic field B_z^o is assumed to be spatially uniform over an area A (see fig. 2), and possibly small or of zero magnitude:

$$B_z^o = const.$$

This means, that the spatial variation of the observed vertical component is due to local distortion only ($B_z - B_z^o = B_z^a$). Furthermore it follows, that the phase shift between the anomalous and the regional magnetic field equals the phase of the regional impedance: $\varphi(\mathbf{B}^a, \mathbf{B}^o) = \varphi(\underline{\mathbf{Z}}^o)$.

Figure 2 is a sketch of a possible scenario of conductivity distributions in the crust. The contributions of induction and distortion response in the data strongly depend on the ratio of the length scale L of an inhomogeneity to the skin depth δ of the investigated period range.

4.1 The magnetic distortion parameters

For the vertical component of the anomalous magnetic field, eqn. 82 contains two magnetic distortion parameters:

$$B_z^a = (D_{zx}, D_{zy})\,\underline{\mathbf{Z}}^o \begin{pmatrix} B_x^o \\ B_y^o \end{pmatrix} \tag{83}$$

This expression is similar to the definition of the magnetic response function for two-dimensional induction: $B_z^o = (\mathcal{A}^o, \mathcal{B}^o)\mathbf{B}_h$, see eqn. 31, which relates the vertical to the horizontal magnetic field. Obviously, even in the absence of a regional vertical component, the magnetic response function contains information on the regional structure, if magnetic distortion is involved:

$$(\mathcal{A}, \mathcal{B}) \;=\; (\mathcal{A}^\ell, \mathcal{B}^\ell) \;=\; (D_{zx}, D_{zy})\,\underline{\mathbf{Z}}^o \tag{84}$$

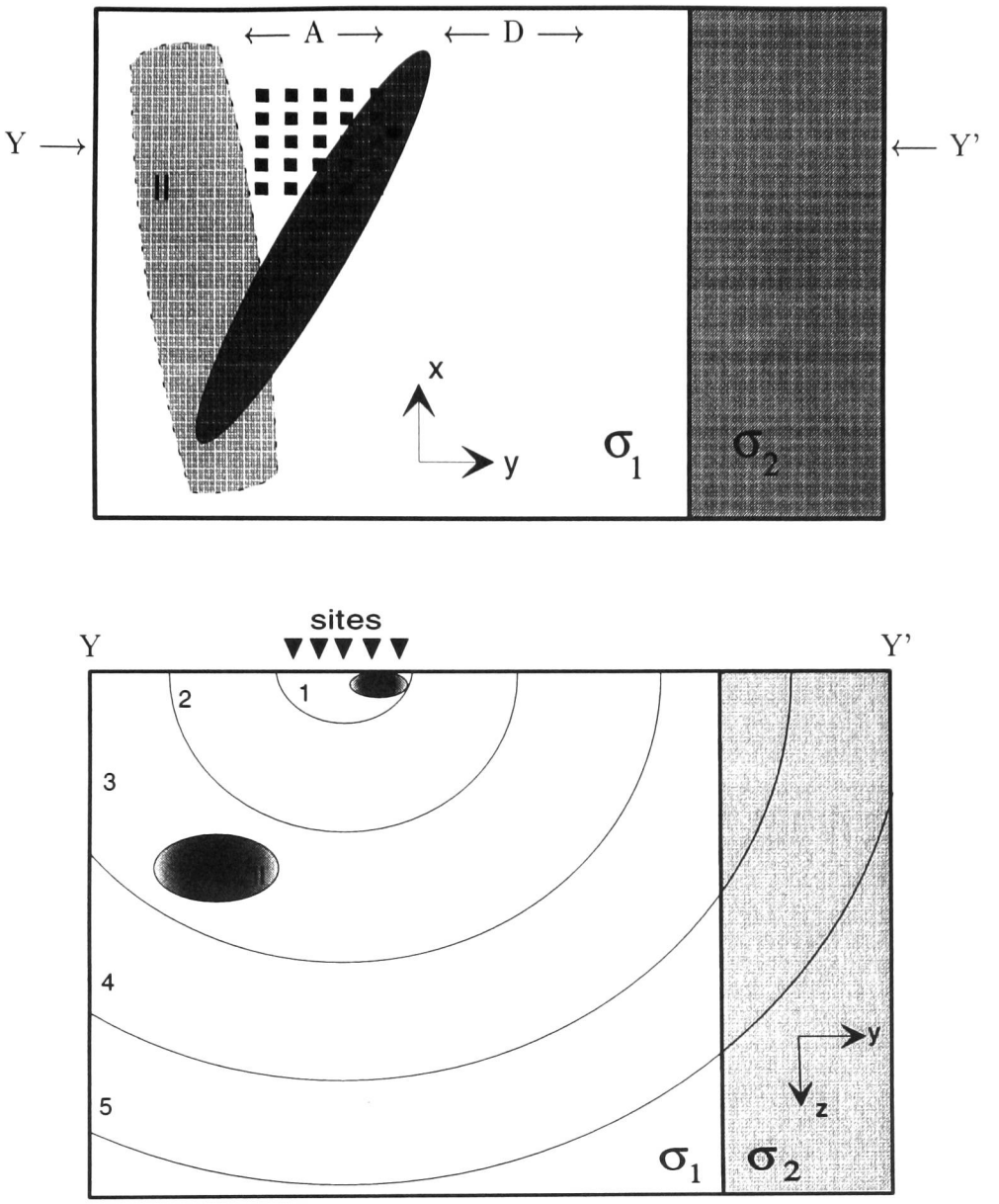

Figure 2: *Induction and distortion processes (sketch):*
The top figure is a plan view showing the location of a sensor array in relation to two local 3D anomalies and a large scale regional structure. The regional 2D structure is represented by the vertical boundary of the two quarterspaces with $\sigma_1 < \sigma_2$.
The lower figure is a section along a profile YY'. The radii of the circles indicate the change in skin depth in the host (σ_1) *with increasing period* ($1 \longrightarrow 5$).

1.) At the shortest period, the shallow body (I) lies fully within the induction range.
2.) Body I causes galvanic distortion of the regional 1D response.
3.) Induction in body II; electric distortion due to body I may still be present.
4.) Body II causes galvanic distortion of the regional 2D response at long periods.
5.) Magnetic distortion may have already vanished, while electric distortion is still present in the MT response functions at longest periods.

For sites at a certain distance to the regional 2D contact (area A), the regional vertical component B_z^o *is relatively small and presumably uniform. Within that distance (area D), we must expect large and spatially varying amplitudes of* B_z^o.

Hence we call $(\mathcal{A}^\ell, \mathcal{B}^\ell)$ the local magnetic response function. Since the distortion parameters are real quantities, it is clear that the complex phase information contained in the local response function is solely related to the regional MT impedance tensor. This regional phase must be contained in all response functions of a whole array of sites at a given period, if all these sites represent the same regional geology. The phases of the vertical magnetic field components observed at these sites must also be the same over the whole area, as the phase of the anomalous field is equal to the phase of the regional electric current.

Suppose the local heterogeneity is embedded in a 1D earth and is elongated in the x'' - direction at an angle θ_ℓ to the measurement coordinates. It can then be regarded as a *quasi* - two-dimensional structure. In that case the anomaly is fully described by two parameters: D''_{zx} and θ_ℓ. The vertical field is generated by the electrical field component in strike direction:

$$B_z^a = (D''_{zx},\ 0) \begin{pmatrix} \mathbf{E}_x^{o\prime\prime} \\ \mathbf{E}_y^{o\prime\prime} \end{pmatrix} \tag{85}$$

where double-primed quantities denote the quantities in local (x'', y'') coordinates. In observation coordinates (x, y), this expression yields[12]:

$$\begin{aligned} B_z^a &= (D''_{zx},\ 0)\ \underline{\mathbf{R}}^T_{\theta_\ell} \begin{pmatrix} E_x^o \\ E_y^o \end{pmatrix} \\ &= (D''_{zx}, 0)\ \underline{\mathbf{R}}^T_{\theta_\ell}\ \underline{\mathbf{Z}}^o \begin{pmatrix} B_x^o \\ B_y^o \end{pmatrix} \end{aligned} \tag{86}$$

For the local magnetic response function we obtain:

$$\begin{aligned} (\mathcal{A}^\ell, \mathcal{B}^\ell) &= (D''_{zx},\ 0)\ \underline{\mathbf{R}}^T_{\theta_\ell}\ \underline{\mathbf{Z}}^o \\ &= (D''_{zx} \cos\theta_\ell,\ D''_{zx} \sin\theta_\ell)\ \underline{\mathbf{Z}}^o \end{aligned} \tag{87}$$

It follows, that the magnetic distortion parameters in observation coordinates may be defined as:

$$(D_{zx}, D_{zy}) = (D''_{zx} \cos\theta_\ell,\ D''_{zx} \sin\theta_\ell) \tag{88}$$

They are functions of position and of the geometry of the anomaly: D''_{zx} varies as the observation point is moved relative to the body; the local strike may vary, if inhomogeneities of different strike directions are involved.

In the following sections the influence of distortion on the magnetic response function will be investigated for one- and two-dimensional regional conductivity distributions. Special attention will be given to phase behaviour, variation with period and spatial variations.

---

[12] rotation matrix for angle θ : $\underline{\mathbf{R}}_\theta = \begin{pmatrix} \cos\theta & -\sin\theta \\ \sin\theta & \cos\theta \end{pmatrix}$; $\underline{\mathbf{R}}^T_\theta = \begin{pmatrix} \cos\theta & \sin\theta \\ -\sin\theta & \cos\theta \end{pmatrix}$; $\theta > 0$

4.1.1 Distortion effects for a 1D regional model

The MT impedance tensor for a one-dimensional conductivity distribution ($\sigma = \sigma(z)$) takes the form:

$$\underline{\mathbf{Z}}^o = \begin{pmatrix} 0 & Z \\ -Z & 0 \end{pmatrix} \tag{89}$$

As the regional vertical component B_z^o equals 0, we may assume that $B_z = B_z^a$. Eqn. 83 becomes then:

$$B_z = \underbrace{-D_{zy}\, Z}_{\mathcal{A}^\ell} B_x^o + \underbrace{D_{zx}\, Z}_{\mathcal{B}^\ell} B_y^o \tag{90}$$

$$\text{with} \quad \begin{aligned} \mathcal{A}^\ell &= -D''_{zx} Z \sin\theta_\ell \\ \mathcal{B}^\ell &= D''_{zx} Z \cos\theta_\ell \end{aligned} \tag{91}$$

Phase: The components of the local magnetic response function $\mathcal{A}^\ell$ and $\mathcal{B}^\ell$ differ only by real, frequency-independent parameters. However, both components contain the same 1D impedance, and therefore the same phase information:

$$\varphi(\mathcal{A}_i^\ell) = \varphi(\mathcal{B}_i^\ell) = \varphi(Z) \tag{92}$$

This phase information must be the same at all sites (index i) representing the same regional geology. Consequently, in the complex plane, the real and imaginary parts of all $\mathcal{A}_i$ and $\mathcal{B}_i$ values at a given period will fall on a line through the origin. The gradient of this line indicates the regional impedance phase angle at that period (fig. 3 a,b). The phase of the vertical magnetic component B_{z_i} is also the same for all sites. It is equal to the phase of the regional electric field at a given period: $\varphi(B_{z_i}) = \varphi(\mathbf{E}^o)$.

Variation over period: Another consequence of the fact, that $\mathcal{A}^\ell(T)$ and $\mathcal{B}^\ell(T)$ differ only by real parameters is, that the components show the same period dependency, differing only by $-\tan\theta_\ell$:

$$\frac{\mathcal{A}_i^\ell(T)}{\mathcal{B}_i^\ell(T)} = -\tan\theta_{\ell_i} \tag{93}$$

For the same reason, the components of different sites ($\mathbf{r}_{j,j}$) will plot as parallel curves over the period range where magnetic distortion occurs:

$$\frac{\mathcal{A}_i^\ell(T)}{\mathcal{A}_j^\ell(T)} = \frac{D_{zy}(\mathbf{r}_i)}{D_{zy}(\mathbf{r}_j)} \quad \text{and} \quad \frac{\mathcal{B}_i^\ell(T)}{\mathcal{B}_j^\ell(T)} = \frac{D_{zx}(\mathbf{r}_i)}{D_{zx}(\mathbf{r}_j)} \tag{94}$$

The form of the curves at different sites is determined entirely by the 1D impedance $Z(T)$ (see fig. 3d). The components are shifted up or down relative to each other according to the ratios of their distortion parameters.

Induction arrows: The direction Θ of induction arrows is calculated by the ratio of the two components of the magnetic response function (Wiese convention). For a one-dimensional regional conductivity distribution, induction arrows do not

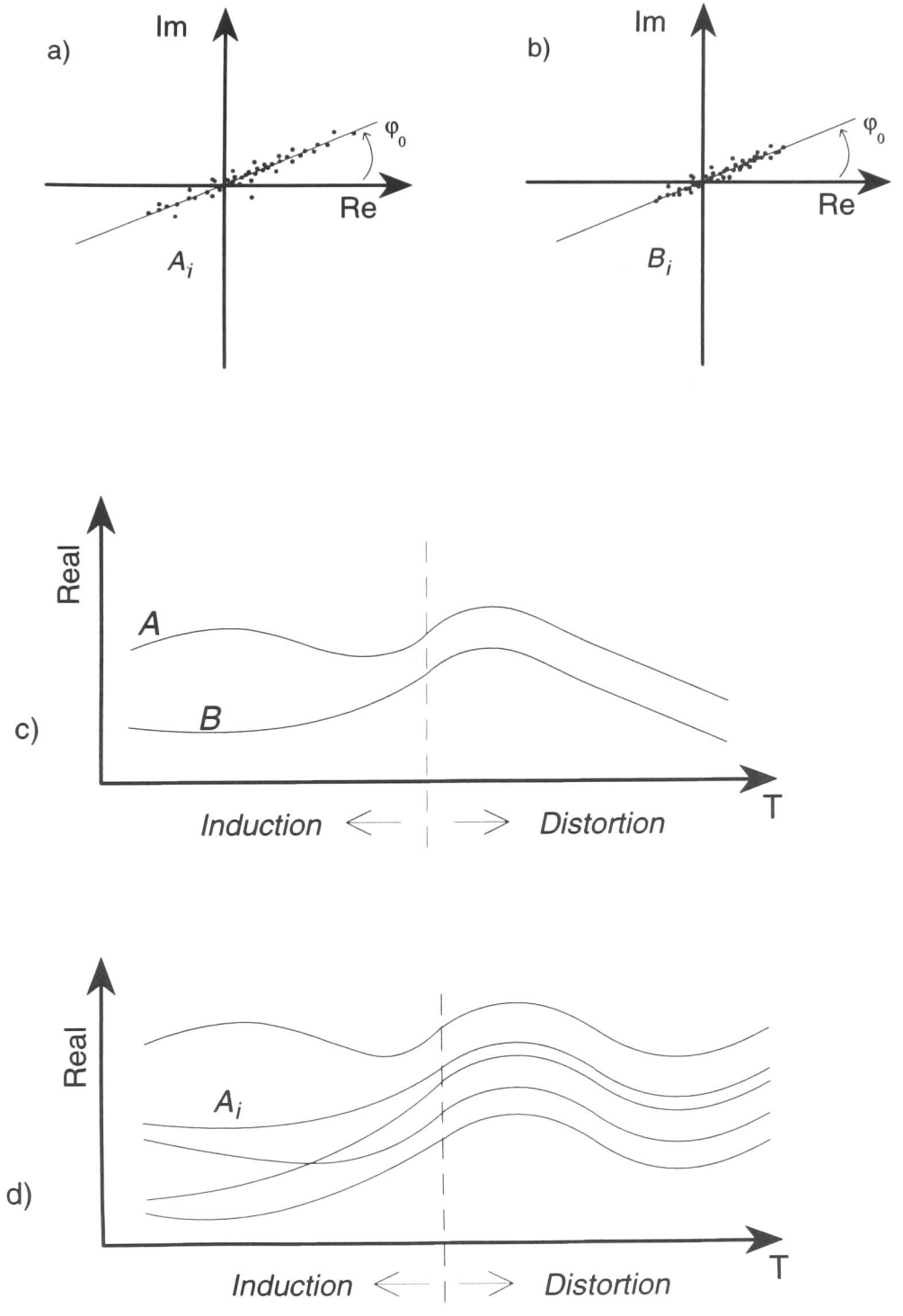

Figure 3: *Behaviour of the magnetic response functions* $(\mathcal{A}, \mathcal{B})$ *when the regional structure is 1D (sketches):*
a) and b) Argand diagrams of $\mathcal{A}$ *and* $\mathcal{B}$ *at one period. The same phase* φ_o *is exhibited by all sites in both* $\mathcal{A}$ *and* $\mathcal{B}$.
c) Variations with period of $\mathcal{A}(T)$ *and* $\mathcal{B}(T)$ *at one site.*
d) Variations with period of $\mathcal{A}(T)$ *at five different sites.*

exist, because the vertical component is zero. In the presence of galvanic distortion, however, real and imaginary arrows (**P**, **Q**) can be computed and they point perpendicular to the strike direction of the local anomaly:

$$\theta_{P,Q} = \arctan \frac{Re\mathcal{B}^\ell}{Re\mathcal{A}^\ell} = \arctan \frac{Im\mathcal{B}^\ell}{Im\mathcal{A}^\ell} = \arctan \frac{\cos\theta_\ell}{-\sin\theta_\ell} = \theta_\ell - 90° \qquad (95)$$

Over the period range of distortion, this direction is constant for all sites located along the long axis of the same local anomaly. Sites positioned at the ends of an elongated anomaly will show directions depending on the particular form of the body. The lengths of the arrows vary according to the frequency-dependence of the real and imaginary parts of Z and according to their position. For example, sites located directly above a conducting body will have smaller arrows than those above the resistive host:

$$\begin{aligned} \text{real arrow:} \quad & L_P = \sqrt{(Re\mathcal{A}^\ell)^2 + (Re\mathcal{B}^\ell)^2} = |D''_{zx}(\mathbf{r})\, ReZ(T)| \\ \text{imaginary arrow:} \quad & L_Q = \sqrt{(Im\mathcal{A}^\ell)^2 + (Im\mathcal{B}^\ell)^2} = |D''_{zx}(\mathbf{r})\, ImZ(T)| \end{aligned} \qquad (96)$$

Lengths at different sites only depend only on the parameters of position $D''_{zx}(\mathbf{r}_i)$. The relative lengths of the real and imaginary arrows depend on the variation of conductivity with depth:

a) Homogenous halfspace: Phase: $\varphi(Z) = 45°$; $L_P = L_Q$
b) Resistor at depth: Phase: $\varphi(Z) < 45°$; $L_P > L_Q$
c) Conductor at depth: Phase: $\varphi(Z) > 45°$; $L_P < L_Q$

4.1.2 Distortion effects for a 2D regional model

For a two-dimensional conductivity distribution ($\sigma = \sigma(x', z)$), the MT impedance tensor in the coordinate system (x', y') of the regional strike θ_r takes the form:

$$\underline{\mathbf{Z}}^o = \begin{pmatrix} 0 & Z_E \\ Z_B & 0 \end{pmatrix} \qquad (97)$$

Consequently, in *measurement coordinates*, we obtain for the vertical anomalous magnetic field component (eqn. 83) the following expression:

$$\begin{aligned} B^a_z &= (D_{zx}, D_{zy})\, \underline{\mathbf{R}}_{\theta_r} \begin{pmatrix} 0 & Z_E \\ Z_B & 0 \end{pmatrix} \underline{\mathbf{R}}^T_{\theta_r} \begin{pmatrix} B^o_x \\ B^o_y \end{pmatrix} \\ &= \mathcal{A}^\ell\, B^o_x + \mathcal{B}^\ell\, B^o_y \end{aligned} \qquad (98)$$

Using the local magnetic distortion parameters, eqn. 98 becomes:

$$\begin{aligned} B^a_z &= (D''_{zx},\ 0)\, \underline{\mathbf{R}}^T_{\theta_\ell}\, \underline{\mathbf{R}}_{\theta_r}\, \underline{\mathbf{Z}}^o\, \underline{\mathbf{R}}^T_{\theta_r}\, \mathbf{B}^o \\ &= (D''_{zx},\ 0)\, \underline{\mathbf{R}}^T_{\alpha}\, \underline{\mathbf{Z}}^o\, \underline{\mathbf{R}}^T_{\theta_r}\, \mathbf{B}^o \qquad \text{with } \alpha = \theta_\ell - \theta_r \end{aligned} \qquad (99)$$

As before, double primes denote local coordinates (x'', y''). The observation coordinates (x, y) are in north/east directions at (0°, 90°), respectively. θ_r and θ_ℓ are the regional and local strike directions, relative to the observation coordinates (x). The

angle difference α denotes the local strike direction relative to the regional coordinate system. With this notation, we obtain for the components of the local magnetic response function the following expressions:

$$\mathcal{A}^{\ell} = D_{zx''} \cdot [-Z_E \sin\theta_r \cos\alpha + Z_B \cos\theta_r \sin\alpha] \quad (100a)$$

$$\mathcal{B}^{\ell} = D_{zx''} \cdot [\, Z_E \cos\theta_r \cos\alpha + Z_B \sin\theta_r \sin\alpha] \quad (100b)$$

Both components contain mixtures of the two principal impedances and of the local and regional strike directions. Interpretation of phase behaviour, variation over period and induction arrows is therefore difficult, especially if the regional vertical component B_z^o is non-zero. In this case, the regional response function $(\mathcal{A}^o, \mathcal{B}^o)$ is added to the local response function:

$$\begin{aligned} B_z = B_z^o + B_z^a &= (\mathcal{A}, \mathcal{B})\, \mathbf{B}^o \\ &= [(\mathcal{A}^o, \mathcal{B}^o) + (\mathcal{A}^{\ell}, \mathcal{B}^{\ell})]\, \mathbf{B}^o \end{aligned} \quad (101)$$

Hence, the total magnetic response function becomes:

$$(\mathcal{A}, \mathcal{B}) = \left[(0, \mathcal{B}^{o'})\, \underline{\mathbf{R}}_{\theta_r}^T + (D''_{zx},\, 0)\, \underline{\mathbf{R}}_{\alpha}^T\, \underline{\mathbf{Z}}^o\, \underline{\mathbf{R}}_{\theta_r}^T\right] \quad (102)$$

In *coordinates of the regional strike direction* (x', y'), the basic equation eqn. 98 for the vertical anomalous magnetic field simplifies considerably:

$$B_z^a = \underbrace{D'_{zy}\, Z_B}_{\mathcal{A}^{\ell'}}\, B_x^{o'} + \underbrace{D'_{zx}\, Z_E}_{\mathcal{B}^{\ell'}}\, B_y^{o'} \quad (103)$$

For the total magnetic response function with contributions from a regional vertical component (eqn.100a,b and 102) we obtain in strike coordinates

$$(\mathcal{A}', \mathcal{B}') = \left[\; (0, \mathcal{B}^{o'}) + (D''_{zx}, 0)\, \underline{\mathbf{R}}_{\alpha}^T \underline{\mathbf{Z}}^o\right] \quad (104)$$

hence:

$$\mathcal{A}' = D''_{zx} Z'_{yx} \sin\alpha \quad (105)$$

$$\mathcal{B}' = D''_{zx} Z'_{xy} \cos\alpha + \mathcal{B}^{o'} \quad (106)$$

The fact that each one of the local response function components contains only one of the principal impedances, has the following consequences for the phase and frequency dependence:

Phase: The phases of $\mathcal{A}_i^{\ell'}$ and $\mathcal{B}_i^{\ell'}$ are solely determined by the phase of one principal impedance, Z_B and Z_E, respectively. All sites representing the same regional geology will produce the same phases for the local response function components at a given period, regardless of position and local strike direction (fig. 4a,b):

$$\varphi(\mathcal{A}_i^{\ell'}) = \varphi(Z_B) \quad \text{and} \quad \varphi(\mathcal{B}_i^{\ell'}) = \varphi(Z_E) \quad (107)$$

If the components $\mathcal{A}_i'$ and $\mathcal{B}_i'$ are displayed in Argand diagrams, they will fall on lines indicating the regional impedance phases of Z_B and Z_E, respectively. If a spatially uniform, regional vertical component B_z^o exists, the phase for components $\mathcal{B}'$ will

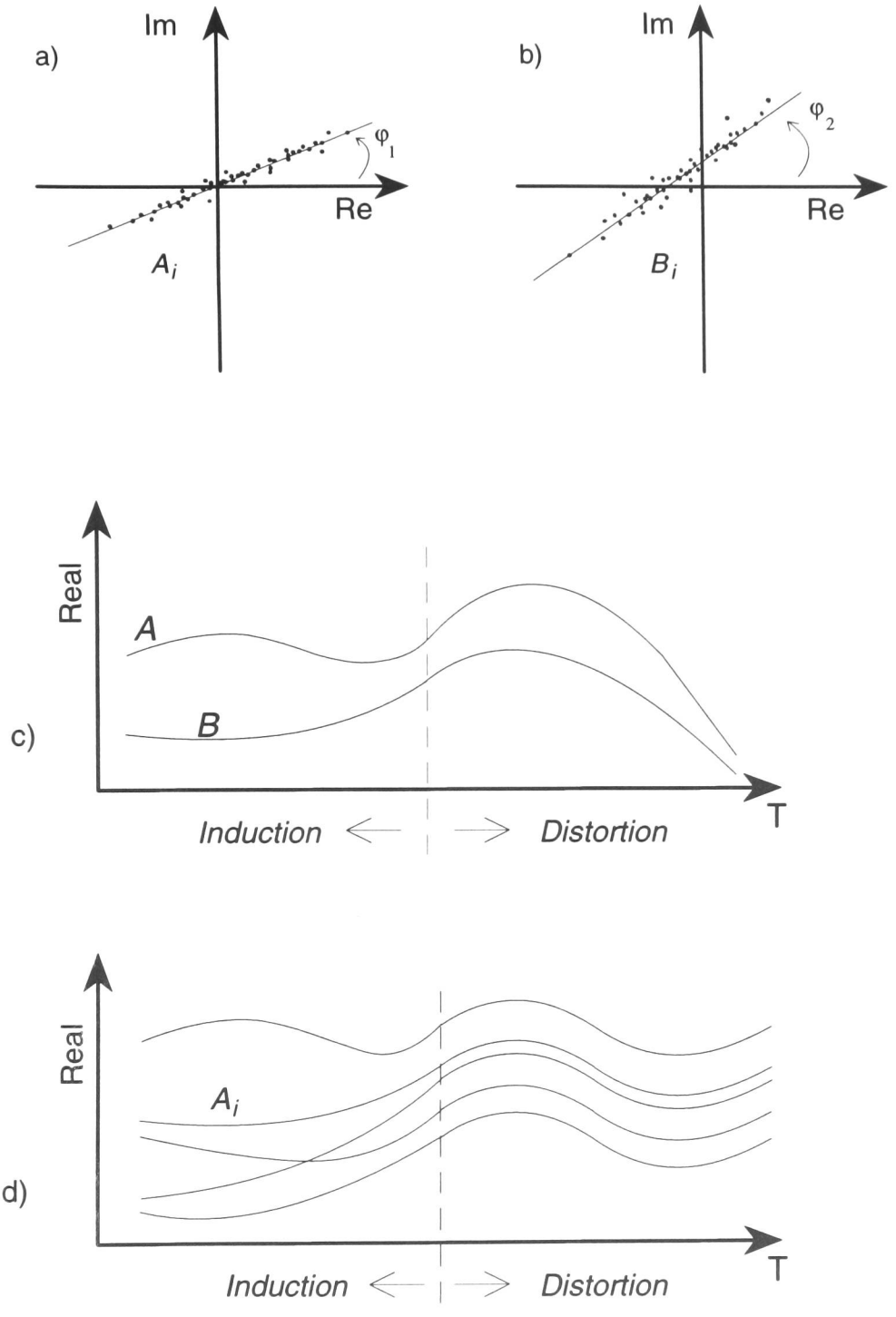

Figure 4: *Behaviour of the magnetic response functions* $(\mathcal{A}, \mathcal{B})$ *when the regional structure is 2D and strikes in y-direction (sketches):*
a) and b) Argand diagrams of $\mathcal{A}$ *and* $\mathcal{B}$ *at one period. The components display different phases as they contain different impedances:* $\varphi_1(Z_B)$, $\varphi_2(Z_E)$. *The line indicated by* $\mathcal{B}_i$ *is shifted due the regional vertical magnetic field.*
c) Variations with period of $\mathcal{A}(T)$ *and* $\mathcal{B}(T)$ *at one site.*
d) Variations with period of $\mathcal{A}(T)$ *at five different sites.*

be shifted by $\mathcal{B}^{o'}$. However, since the values at every site are shifted by the same amount, the inclination of the phase line is not affected and it indicates the correct impedance phase angle. Only if the regional magnetic field is non-uniform, because the sites are located close to the regional structure, will the distribution of $\mathcal{B}'_i$ in the Argand diagrams become less linear. Component $\mathcal{A}'$ is not affected, because the regional contribution $\mathcal{A}^{o'}$ equals zero for a strike direction along x'.

Variation over period: As the components $\mathcal{A}^{\ell'}(T)$ and $\mathcal{B}^{\ell'}(T)$ each contain only one of the principal impedances, the curves at different sites are parallel over the period range of magnetic distortion (fig. 4d).

$$\frac{\mathcal{A}_i^{\ell'}(T)}{\mathcal{A}_j^{\ell'}(T)} = \frac{D'_{zy}(\mathbf{r}_i)}{D'_{zy}(\mathbf{r}_j)} \quad \text{and} \quad \frac{\mathcal{B}_i^{\ell'}(T)}{\mathcal{B}_j^{\ell'}(T)} = \frac{D'_{zx}(\mathbf{r}_i)}{D'_{zx}(\mathbf{r}_j)} \tag{108}$$

The forms of the curves are determined entirely by either Z_E or Z_B. Therefore, the frequency response curves of $\mathcal{A}'$ and $\mathcal{B}'$ of one site are not parallel to each other (fig. 4c). The addition of a regional vertical component, as long as it is spatially uniform, still results in parallel curves at different sites. But, since it reflects a frequency-dependent induction process, it will certainly alter the shape of the curve of the component $\mathcal{B}'$.

Induction arrows: The direction of induction arrows is determined by the ratio of the two principal impedances, and the relative local strike θ_α:

$$\theta_{P,Q} = \arctan \frac{\mathcal{B}_i^{\ell'}}{\mathcal{A}_i^{\ell'}} = \arctan \frac{Z_E}{Z_B} \cdot \cot \theta_{\alpha_i} \tag{109}$$

For the real and imaginary arrows (**P** and **Q**), the real and imaginary parts of the principal impedances apply. The presence of a spatially uniform regional component B_z^o affects the arrows considerably, but equally at all sites:

$$\frac{\mathcal{B}'_i}{\mathcal{A}'_i} = \frac{Z_E \cos \alpha_i + \mathcal{B}^{o'}}{Z_B \sin \alpha_i} \tag{110}$$

The lengths of the arrows vary according to the frequency-dependence of the real and imaginary parts of Z_E and Z_E and, if present, $\mathcal{B}^{o'}$:

$$\begin{aligned} L_P &= \sqrt{D''^2_{zx}((ReZ_B)^2 + (ReZ_B)^2) + (Re\mathcal{B}^{o'})^2} \\ L_Q &= \sqrt{D''^2_{zx}(ImZ_B)^2 + (ImZ_B)^2) + (Im\mathcal{B}^{o'})^2} \end{aligned} \tag{111}$$

Lengths at different sites vary only depending on the parameter of position $D''_{zx}(\mathbf{r}_i)$ (or by a spatially non-uniform $\mathcal{B}^{o'}$, if applicable).

4.1.3 Special cases

To complete this section, the following special cases are examined in more detail:

a) 1D Earth: $\theta_\ell = 0°$ or $\theta_\ell = 90°$, local strike north or east
b) 2D Earth: $\theta_\ell = 0°$ or $\theta_\ell = 90°$, local strike north or east
c) 2D Earth: $\theta_r = 0°$ or $\theta_r = 90°$, regional strike north or east
d) 2D Earth: $\alpha = 0°$ or $\alpha = 90°$, local strike $\parallel$ or $\perp$ regional strike

a) 1D Earth: $\theta_\ell = 0°$ (north) **or** $\theta_\ell = 90°$ (east):
If the local anomaly strikes exactly north or east, one of the distortion parameters equals zero, and therefore only one of the components $\mathcal{A}^\ell$ or $\mathcal{B}^\ell$ exists:

$$\theta_\ell = 0° : \quad D_{zy} = 0; \quad \mathcal{A}^\ell = 0; \quad \mathcal{B}^\ell = D''_{zx} Z \tag{112a}$$

$$\theta_\ell = 90° : \quad D_{zx} = 0; \quad \mathcal{A}^\ell = D''_{zx} Z; \quad \mathcal{B}^\ell = 0 \tag{112b}$$

The non-zero components are the same for north- or eastward strike direction.

b) 2D Earth: $\theta_\ell = 0°$ (north) **or** $\theta_\ell = 90°$ (east):
If the local anomaly strikes exactly north or east, one of the distortion parameters equals zero, and the angle difference α is identical to θ_r or $90° - \theta_r$.

$$\theta_\ell = 0° : \quad \begin{aligned} \mathcal{A}^\ell &= D_{zx''} \cdot [-Z_E \sin\theta_r \cos\theta_r - Z_B \sin\theta_r \cos\theta_r] \\ \mathcal{B}^\ell &= D_{zx''} \cdot [\, Z_E \cos^2\theta_r - Z_B \sin^2\theta_r] \end{aligned} \tag{113a}$$

$$\theta_\ell = 90° : \quad \begin{aligned} \mathcal{A}^\ell &= D_{zx''} \cdot [-Z_E \sin^2\theta_r + Z_B \cos^2\theta_r] \\ \mathcal{B}^\ell &= D_{zx''} \cdot [\, Z_E \sin\theta_r \cos\theta_r + Z_B \sin\theta_r \cos\theta_r] = -\mathcal{A}^\ell(0°) \end{aligned} \tag{113b}$$

As the components $\mathcal{A}^\ell$ and $\mathcal{B}^\ell$ contain only θ_r, they are slightly simplified (compared to eqn.100a,b); however, they still represent mixtures of the principal impedances.

c) 2D Earth: $\theta_r = 0°$ (north) **or** $\theta_r = 90°$ (east):
If the regional structure strikes exactly north or east, the expressions describing the local magnetic response function reduce to the form in strike coordinates (eqn. 105) given in the previous section (4.1.2). For an eastward strike direction, the components $\mathcal{A}^\ell$ and $\mathcal{B}^\ell$ have to be exchanged: $\mathcal{A}^\ell(90°) = -\mathcal{B}^\ell(0°)$ and $\mathcal{B}^\ell(90°) = \mathcal{A}^\ell(0°)$.

d) 2D Earth $\alpha = 0°$ ($\theta_\ell \parallel \theta_r$) **or** $\alpha = 90°$ ($\theta_\ell \perp \theta_r$):
If the local strike direction is parallel or perpendicular to the regional structure, we find the local magnetic response function simplified in a way, that both components contain the same principal impedance:

$$\underline{\alpha = 0° :} \quad \begin{aligned} \mathcal{A}^\ell &= -D''_{zx} Z_E \sin\theta_r \\ \mathcal{B}^\ell &= D''_{zx} Z_E \cos\theta_r \end{aligned} \qquad \underline{\alpha = 90° :} \quad \begin{aligned} \mathcal{A}^\ell &= D''_{zx} Z_B \cos\theta_r \quad (114a) \\ \mathcal{B}^\ell &= D''_{zx} Z_B \cos\theta_r \quad (114b) \end{aligned}$$

Since $\mathcal{A}^\ell$ and $\mathcal{B}^\ell$ differ only by the term concerning the regional strike in both cases, their properties in measurement coordinates are similar to those described for the 1D - earth. Both components contain the same phase information at each site of the area which is the phase of only one of the principal impedances (Z_E or Z_B). Obviously, in regional coordinates, either $\mathcal{A}^{\ell'}$ ($\alpha = 0°$) or $\mathcal{B}^{\ell'}$ ($\alpha = 90°$) equal zero.

4.2 Hypothetical event analysis

An alternative way of interpreting the magnetic response function is to apply hypothetical event analysis to the data. *'The purpose of this method is to calculate the vertical field B_z^p, at all stations, that would be associated with a hypothetical event which has a uniform external horizontal field $\mathbf{B}_h^\star$ of specified polarisation. Since the hypothetical external field is uniform, all variations in B_z from station to station must be of internal origin, the result of local channelling or induction'* (Bailey et al. 1974). In practice, a predicted vertical field B_z^p is estimated from the observed magnetic response function by assuming a horizontal magnetic field of unit amplitude and polarisation $\vartheta^\star$:

$$B_z^p = (\mathcal{A}, \mathcal{B})\,\mathbf{B}_h^\star = (\mathcal{A}, \mathcal{B}) \cdot \begin{pmatrix} 1 \cdot \cos\vartheta^\star \\ 1 \cdot \sin\vartheta^\star \end{pmatrix} \tag{115}$$

$\mathbf{B}_h^\star$ may also be phase-shifted relative to the measured response function. The uniformity of the hypothetical event is realized by assuming the same amplitude of the horizontal field at each site of the area under investigation. Obviously, this assumption is only justified if the observed horizontal field is uniform across the area. That implies that the anomalous fields may only be a small fraction of the total magnetic field, i.e. less than 20 % (Banks & Beamish, 1984) to 30 % (Bailey et al. 1974). In order to make sure that this condition is met in a dataset, inter-station transfer functions between some sites across the array and a distant reference site may be computed from simultaneous recordings (if available).

The interpretation of the magnetic response function by hypothetical event analysis was inferred by Schmucker (1970). He suggested to *'predict'* the anomalous behaviour of the magnetic field components from the magnetic response function by using the Fourier transforms of the horizontal magnetic field of one particular event. Bailey et al. (1974) presented and applied the technique described above for the first time on data from Eastern Canada. It has been used by numerous authors for the interpretation of magnetometer arrays ever since (e.g. Gough & Ingham, 1983; Banks & Beamish, 1984; Banks et al. 1993).

Apart from being a procedure that is easily applicable to the data, hypothetical event analysis has two main advantages that make it most suitable for the correction of magnetic distortion in the data:
a) The technique is usually applied to data from arrays of magnetometers. Spatial variations can be visualized by plotting the predicted fields as contour maps. From the pattern of the spatial distributions of these values one can infer current concentrations, whether channelled or induced, in areas of strong gradients of the predicted vertical field.
b) Secondly, the imaginary parts of the magnetic response functions are included, whereas the standard interpretation of induction arrows is often based only on variations of the real arrows. Since imaginary parts are often much smaller than real parts, they are best interpreted by presenting them together with their corresponding real parts in the complex plane. Such diagrams provide an excellent tool to examine the phase information contained in a whole array of data.

4.2.1 Elimination of magnetic distortion

For the purpose of revealing regional information from distorted magnetic response functions, we investigate the expression for the predicted vertical field in the presence of magnetic distortion:

$$B_z^p = (\mathcal{A},\mathcal{B})\,\mathbf{B}_h^\star = [(\mathcal{A}^o,\mathcal{B}^o)+(D_{zx},D_{zy})\,\underline{\mathbf{Z}}^o]\begin{pmatrix}1\cdot\cos\vartheta^\star\\1\cdot\sin\vartheta^\star\end{pmatrix} \tag{116}$$

Obviously, if the hypothetical event is polarized in north- or eastward direction and has zero phase, the predicted value B_z^p is simply the corresponding component of the magnetic response function:

$$B_z^p = \mathcal{A} \quad \text{for} \quad \vartheta^\star = 0° \tag{117a}$$

$$B_z^p = \mathcal{B} \quad \text{for} \quad \vartheta^\star = 90° \tag{117b}$$

In what follows, the information content of the predicted vertical field of hypothetical event analysis (HEA) will be investigated for regional 1D and 2D settings.

HEA for a regional 1D model:
Again, for a regional one-dimensional conductivity distribution the expression in eqn.116 simplifies and we obtain for the predicted vertical field:

$$\begin{aligned} B_z^p &= -D_{zy}Z\cos\vartheta^\star + D_{zx}Z\sin\vartheta^\star \\ &= Z\,(D_{zx}\sin\vartheta^\star - D_{zy}\cos\vartheta^\star) \end{aligned} \tag{118}$$

Because the distortion parameters D_{zx} and D_{zy} are real, The phase of B_z^p is the phase of Z. It follows, that the phases of the predicted values at all sites must be equal to the phase of the one-dimensional impedance, irrespective of the polarisation azimuth of the hypothetical event. If the real and imaginary parts of $B_{z_i}^p$ for all sites representing the same regional 1D structure are plotted in the complex plane (Argand diagrams), they arrange along a line through the origin which indicates the regional 1D phase. The slope of this line will be unaltered by changes in the polarisation azimuth $\vartheta^\star$ of the hypothetical event.

Inclusion of the local strike direction into eqn. 118 shows, that B_z^p must become very small, if the polarisation azimuth approximates the local strike direction. If, on the other hand, a polarisation perpendicular to the local structure is approached, the predicted value reaches a maximum:

$$\begin{aligned} B_z^p &= -D''_{zx}Z\sin\theta_\ell\cos\vartheta^\star + D''_{zx}Z\cos\theta_\ell\sin\vartheta^\star \\ &= -D''_{zx}Z\sin(\theta_\ell-\vartheta^\star) \end{aligned} \tag{119}$$

hence:

$$B_z^p = 0 \quad \text{for} \quad \vartheta^\star = \theta_\ell \tag{120}$$

$$B_z^p = D''_{zx}Z \quad \text{for} \quad \vartheta^\star = \theta_\ell + 90°$$

In order to find the local strike direction, the data of all sites can be examined for minimum/maximum amplitudes in the Argand diagrams by gradually changing the polarisation angle.

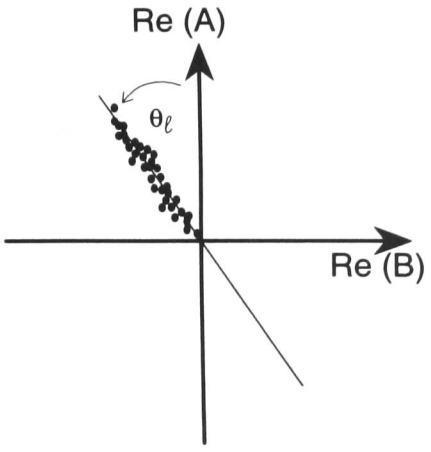

Figure 5: *$\mathcal{A}$ over $\mathcal{B}$ diagram for a regional 1D model: The predicted vertical fields $ReB^p_{z_i}$ at perpendicular polarisations (0° and 90°) form a line indicating the local strike azimuth θ_ℓ (sketch).*

A more straightforward way to determine the local strike direction is from the ratio of the predicted values for perpendicular polarisations at each site:

$$\frac{B^p_{z_i}(0°)}{B^p_{z_i}(90°)} = \frac{\mathcal{A}^\ell_i}{\mathcal{B}^\ell_i} = -\tan\theta_{\ell_i} \tag{121}$$

ϑ_ℓ may also be determined graphically by plotting the real parts of the $B^p_{z_i}$ in an '$\mathcal{A}$ over $\mathcal{B}$' diagram (see fig. 5). If several anomalies are present in the dataset, the data will plot on different lines for different local strike directions.

HEA for a regional 2D model:
For a two-dimensional regional structure, the predicted value for the vertical magnetic field contains the principal impedances and the regional strike. In observation coordinates, we obtain:

$$B^p_z = [(0, \mathcal{B}^{o'})\,\underline{\mathbf{R}}^T_{\theta_r} + (\mathcal{A}^{\ell'}, \mathcal{B}^{\ell'})\,\underline{\mathbf{R}}^T_{\theta_r}]\,\mathbf{B}^\star_h \tag{122a}$$

$$= [(0, \mathcal{B}^{o'})\,\underline{\mathbf{R}}^T_{\theta_r} + (D_{zx}, D_{zy})\,\underline{\mathbf{R}}_{\theta_r}\underline{\mathbf{Z}}^{\circ}\underline{\mathbf{R}}^T_{\theta_r}]\begin{pmatrix} 1\cdot\cos\vartheta^\star \\ 1\cdot\sin\vartheta^\star \end{pmatrix} \tag{122b}$$

Explicitly, this general expression yields:

$$\begin{aligned} B^p_z(\vartheta^\star) = {} & D_{zx}\cdot[Z_E\cos\theta_r\sin(\vartheta^\star-\theta_r) - Z_B\sin\theta_r\cos(\vartheta^\star-\theta_r)] \\ & + D_{zy}\cdot[Z_E\sin\theta_r\sin(\vartheta^\star-\theta_r) + Z_B\cos\theta_r\cos(\vartheta^\star-\theta_r)] \\ & + \mathcal{B}^{o'}\sin(\vartheta^\star-\theta_r) \end{aligned} \tag{123}$$

For a perpendicular polarisation azimuth we obtain a similar expression:

$$\begin{aligned} B^p_z(\vartheta^\star+90°) = {} & D_{zx}\cdot[Z_E\cos\theta_r\cos(\vartheta^\star-\theta_r) + Z_B\sin\theta_r\sin(\vartheta^\star-\theta_r)] \\ & + D_{zy}\cdot[Z_E\sin\theta_r\cos(\vartheta^\star-\theta_r) - Z_B\cos\theta_r\sin(\vartheta^\star-\theta_r)] \\ & + \mathcal{B}^{o'}\cos(\vartheta^\star-\theta_r) \end{aligned} \tag{124}$$

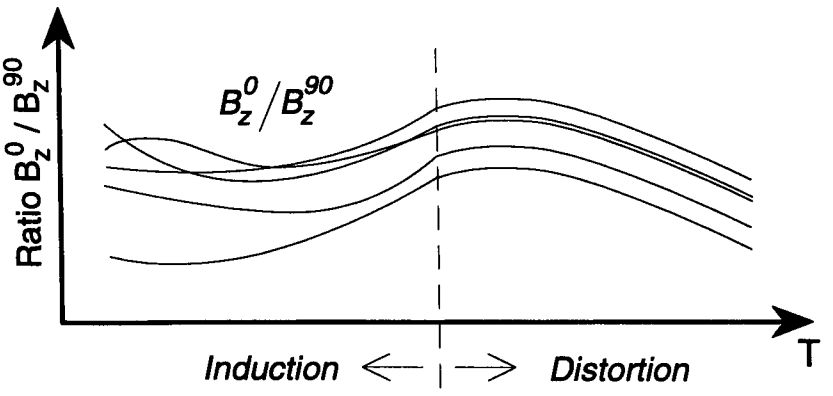

Figure 6: *Ratios of the predicted vertical fields at perpendicular polarisations* $B_{z_i}^p(0°)$ / $B_{z_i}^p(90°)$ *at five sites for a regional 2D model.*

These equations simplify considerably for the special cases, when the polarisation $\vartheta^\star$ is parallel to the regional strike direction θ_r and perpendicular to it.

$$\begin{aligned} \vartheta^\star = \theta_r : \qquad B_z^p &= Z_B[D_{zx}\sin\theta_r + D_{zy}\cos\theta_r] \\ \vartheta^\star \perp \theta_r : \qquad B_z^p &= Z_E[\ D_{zx}\cos\theta_r + D_{zy}\sin\theta_r] + \mathcal{B}^{o'} \end{aligned} \tag{125}$$

Note that in both cases the predicted value contains only one of the principal impedances. If we include the local strike direction into the distortion parameters, we find relations that are familiar from the previous chapter:

$$\begin{aligned} \vartheta^\star = \theta_r : \qquad B_z^p &= D''_{zx} Z_B \sin\alpha &&= \mathcal{A}' \\ \vartheta^\star = \theta_r + 90° : \qquad B_z^p &= D''_{zx} Z_E \cos\alpha + \mathcal{B}^{o'} &&= \mathcal{B}' \end{aligned} \tag{126}$$

In fact, the expressions for the predicted B_z^p for these cases are the same as for the response function components in *regional strike coordinates* (eqn.105). Hence, the characteristics described in the previous section (4.1.2) can be used to recover the common regional strike azimuth from the observed data array. By gradually varying the polarisation azimuth $\vartheta^\star$ and monitoring the predicted vertical fields of all sites simultaneously at one given period in an Argand diagram, we can find the regional strike direction, when the data points fall on a line through the origin. The gradient of this line indicates the phase angle of one of the regional impedances (Z_B). The line can be observed when the hypothetical event is polarised in the strike direction of the regional 2D structure.

If a polarisation perpendicular to the regional strike is selected, the values will scatter along the phase line of the orthogonal principal impedance. Its phase line, however, might not pass through the origin, but have a certain offset $\mathcal{B}^{o'}$, if the regional vertical field is non-zero. Therefore, a shift away from the origin is an indication for the presence of a uniform regional vertical component. It would occur

close to a significant vertical conductivity boundary, and results in a distortion of the phase line. In that case, no uniform horizontal field or impedance can be expected either, and the distortion model inappropriate.

If the regional vertical field is close to zero, or if difference-field transfer functions are available (where the regional vertical field is eliminated), the computed response functions represent the local response functions. Then, with reliable predictions of the local strike from surface geology or high frequency data, the ratio of the principal impedances may be estimated from the ratio of the predicted values at polarisations azimuths parallel and perpendicular to the regional strike:

$$\frac{B_z^p(\vartheta^\star)}{B_z^p(\vartheta^\star + 90)} = \frac{\mathcal{A}^{\ell'}}{\mathcal{B}^{\ell'}} = \frac{Z_B}{Z_E} \cdot \tan\alpha \tag{127}$$

The frequency dependency of this ratio can be expected the same for all sites representing the same regional geology (fig. 6).

Although we are not able to determine the individual values of the principal impedances from the distorted magnetic response function, hypothetical event analysis enables us to extract their frequency variations, their phases, their ratio, and the strike direction of the regional structure, in which the currents are induced.

4.2.2 Determination of the phase line

The common phase angle is determined from N data points in the complex plane by the least squares method. In order to determine the degree of linearity of the data distribution, the correlation coefficient is estimated from the real (x) and imaginary (y) parts of all sites (Bronstein, 1981):

$$r = \frac{\sum(x-\bar{x})(y-\bar{y})}{\sqrt{\sum(y-\bar{y})\sum(y-\bar{y})}} \tag{128}$$

where, in our case, $\bar{x}$ and $\bar{y}$ correspond to the mean values of all *real* and *imaginary* parts, respectively. If $|r|$ is found close to 1, the data are strongly correlated, whereas values close to 0 indicate weak or no linear relation. Hence this parameter can be used in HEA to find the range of polarisation azimuths, in which the data are correlated the most.

Since the estimation of the linear correlation coefficient depends on the chosen coordinate system and therefore on the inclination of the phase line, we will not get an objective idea of the degree of linearity if we calculate the coefficient from the data in a fixed system (e.g. in geographic coordinate). For example, points scattering along one of the axes (phases 0° or 90°) will deliver a correlation coefficient close to zero, even if they fall on a perfect line. However, points grouping closely along a diagonal line (phase 45°) yield a maximum coefficient close to |1|, which is a more realistic value for their correlation. Thus, in order to obtain an objective correlation coefficient, it is necessary to rotate all data through a quadrant (0° to 90°) and compare only maximum values. Data with low linear correlation will then still produce a low coefficient.

In practice, data distributions with $r > 0.7$ may be approximated well by linear regression lines with gradient m and intercept c for x- and y- distributions:

$$x_i = m_x y_i + c_x \qquad \text{and} \qquad y_i = m_y x_i + c_y \tag{129}$$

If the linear correlation is perfect ($|r| = 1$), both lines are equal. For relatively good correlation ($|r| > 0.8$), the lines differ only little. However, the smaller the correlation coefficient, the more the lines will differ. The two lines cross at $(\bar{x}, \bar{y})$, the centre of gravity of the data (Spiegel, 1961). Standard deviations for the slope and intercept are obtained from the related derivatives and standard deviations of the data, S_x or S_y, respectively for the two lines (Baird, 1962). In the case of non-perfect linear correlation, the line with the smaller error will be chosen to represent the regional phase.

The data distribution can also be fitted with one single regression line allowing for scattering of both the x- and y- components. However, I chose to compute the lines separately for x- and y- distributions for my datasets in order to obtain an instant impression of the linear correlation of the data. In most cases the data distribution is approximated best by the y- line, because the real parts are generally larger than the imaginary parts (see e.g. fig. 25). The y-lines also show the smaller standard deviations and less dramatic fluctuations with changing polarisation azimuths (see e.g. fig. 26).

Obviously, the same methods can be used to determine the local strike azimuth from an $\mathcal{A}$ over $\mathcal{B}$ diagram.

4.2.3 Is the regional setting 1D or 2D ?

From the findings in the previous sections, we can design the following tests for the dimensionality of the data:

a:) single site:
If we compute the ratio of the components of the magnetic response function (or the ratio of the predicted values for the vertical field at perpendicular polarisations), we should be able to distinguish one-dimensional from two-dimensional data: In the 1D case, the ratio is real and constant over the period range of distortion, because all complex frequency-dependent information is contained in the regional impedance, which is eliminated when calculating the ratio. We are left with the constant strike azimuth of the structure that is responsible for distortion at that site:

$$\text{1D Earth:} \qquad \frac{\mathcal{A}^\ell}{\mathcal{B}^\ell} = \frac{B_z^p(\vartheta^\star)}{B_z^p(\vartheta^\star + 90)} = -\tan\theta_\ell = \text{const.} \tag{130}$$

If the regional structure is 2D , however, the ratios contain both principal impedances in the numerator and in the denominator. Thus the ratios are clearly complex and frequency dependent.

b:) array:
If we visualize the real and imaginary parts of predicted values for the vertical field at gradually varying polarisation angles in the complex plane ('Argand diagram'),

one-dimensional data will plot along a line indicating the phase of the regional impedance. The resulting 1D phase must be independent of the polarisation azimuth.

$$\text{1D Earth:} \qquad \frac{ImB^p_{z_i}(\vartheta^*)}{ReB^p_{z_i}(\vartheta^*)} = \frac{ImZ}{ReZ} \tag{131}$$

In the case of a regional 2D structure, the distribution of the values in the complex plane is highly dependent on the azimuth of polarisation. One should be able to determine an angle, where the $B^p_{z_i}(\vartheta^*)$ and $B^p_{z_i}(\vartheta^* + 90°)$ collapse on distinct phase lines. If the phase line is shifted away from the origin, we must assume that a regional vertical magnetic component is present in the data. The shift can be eliminated by changing the polarisation azimuth: it vanishes if the hypothetical horizontal field is polarised parallel to the regional strike direction. This case corresponds to B-polarisation, where no vertical magnetic component is generated. On the other hand, the shift can be maximized by choosing a polarisation of the magnetic field that is perpendicular to the regional strike, corresponding to E-polarisation.

The existence of a shift of the phase line in the complex plane and the feasibility to remove it is therefore a good indication for regional two-dimensionality of the data. Only then can a spatially uniform vertical component be present. If no phase line or strike direction can be found with this technique (i.e. the shift is not removable), one must either assume a more complex regional structure, or the distortion model is not appropriate at all.

4.2.4 The period range of distortion

The features used above to determine the dimensionality of the regional structure can be applied equally well for the recognition of distortion in the data, especially with respect to the variation with period. A more straight-forward way to identify the period range, over which current deviation is the cause for a strong vertical magnetic field component, is to investigate the variation of the magnetic response function components of different sites. The curves for the component $\mathcal{A}_i(T)$, for example, will have different shapes in the period range of induction ($\mathcal{A}_i(T) = \mathcal{A}_i^o(T)$), whereas they run parallel over the periods, where galvanic distortion is the dominant process ($\mathcal{A}_i(T) \approx \mathcal{A}_i^\ell(T)$). That implies that the ratios of components at different sites ($\mathcal{A}_i/\mathcal{A}_j$) are real, frequency-independent numbers (see fig. 7) in the period range of distortion, regardless of the dimensionality of the regional geological setting.

If the magnetic data have been recorded simultaneously to a reference site, magnetic response functions estimated by common reference processing can be used to detect distortion. If the spatial variations of the vertical magnetic field are caused by galvanic effects, the hypothetical event analysis of the difference field data clearly reveals two common phases. For polarisations parallel and perpendicular to the regional strike, the data distributions will be highly linear, and regression lines at both polarisations will pass through the origin of the complex plane. In this case, the distortion model described in this thesis is valid and the data can be interpreted in the proposed way. However, if induction at a nearby regional boundary produces a spatially non-uniform magnetic field, the magnetic data at each site of an array are affected individually. This results in a strong scattering of the predicted vertical

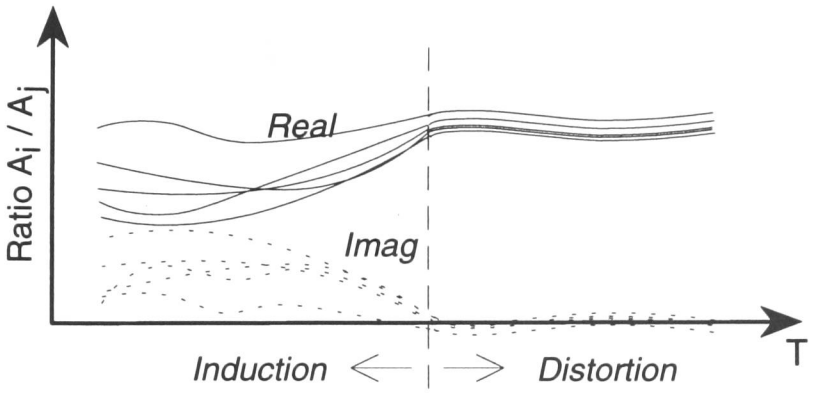

Figure 7: *Ratios of the components $\mathcal{A}_i/\mathcal{A}_j$ of five different sites (sketch). Solid lines are real parts, dotted lines are imaginary parts.*

fields in the Argand diagrams at all polarisation angles, execept close to the regional strike azimuth. If both effects are superimposed, and the galvanic contribution has the smaller amplitudes, it will be difficult to fit regression lines for a polarisation azimuth, that is perpendicular to the regional strike.

4.2.5 Error of the recovered regional strike azimuth

As already mentioned in section 4.2.2, we can determine an error for the common phase from the standard deviation of the slope of the regression line. However it is not possible to estimate a statistical error for the strike direction. Obviously, we cannot be sure that the assumptions underlying the theory of this approach are always met exactly, neither by the data nor by the geological setting. The strike angle is not calculated directly from the data, but determined by criteria which depend on the linear correlation of the data distribution and whether the common phase line passes through the origin. Hence we cannot derive an error estimate for the polarisation azimuth that we recognize as the regional strike direction. However, it seems reasonable to assume a general error of the strike azimuth of $\pm 5°$, as this reflects the azimuth range, where the phase line lies very close to the origin.

It is the purpose of this investigation to point out that common information is detectable consistently over the period range, where local distortion effects influence the data. I found that if the data are erroneous (as e.g. for the long periods > 1000s of the BC87 dataset in chapter 6), their predicted vertical fields scatter in a strongly non-linear way in the Argand diagrams, and it is impossible to derive a strike direction. Hence, we can take it as a strong case for the applicability of the method if the data are distributed linearly and we are able to find a regional strike angle.

5 The Iapetus Dataset

The ideas discussed in the previous chapter about the elimination of magnetic distortion and recovery of hidden regional information were tested against the vertical magnetic response functions of the 'Iapetus' database. The dataset was compiled by Banks (see Banks et al. (1993) for references to sources) and comprises 127 sites in an area which extends 200 km E/W × 300 km N/S in northern England and southern/central Scotland. They give a reasonably dense coverage (average spacing 10 - 20 km) of a region associated with an ancient plate boundary, the Iapetus suture zone. From the surface down to the mantle, the crustal structure is of a complex nature. Galvanic distortion due to current deviations is therefore a very likely phenomenon to occur in all levels of the crust, and problems like static shift have been discussed for interpretations of electromagnetic data in the whole region. Depending on the length scale of the distorting conductivity inhomogeneities, the effects on the electric and magnetic fields have to be expected to affect GDS response functions, even down to long periods around 1000s – 2000s. In addition, current concentrations in the shallow and deep seas and seafloors around the British Isles may create even more distortion problems (*ocean effects*). The availability of a large dataset of probably distorted magnetic response functions was the incentive and motivation for the detailed studies in the following sections. As an introduction, I shall give a short overview of the general geological situation and the geophysical research carried out in the region covered by the data array.

5.1 Crustal structure: tectonic development and recent geophysical results

The Iapetus suture marks the join of two formerly separated continental plates, welded by the closure of the Palaeozoic 'protoatlantic', called the Iapetus ocean. The crustal convergence of (North American) Laurentia and (South European) Avalonia & Gondwana and (North European) Baltica began in the Cambrian and lasted until the Devonian. In the process, oceanic crustal material was subducted under the Laurentian crust comprising present-day Scotland, Northern Ireland, Greenland, parts of Scandinavia, and parts of Northern Canada. Subduction possibly also took place under the Avalonian microplate to the south (Legget et al. 1983; Hutton, 1987), comprising Newfoundland, Wales, England, and the Ardennes.

Scraped-off material of the descending ocean plate was upthrust into the southern margin of the Laurentian crust and formed the Southern Uplands of Scotland (McKerrow & Cocks, 1986). After subduction had come to a halt in the early Devonian, the Caledonian orogenesis continued and the Southern Uplands were subjected to further metamorphism and folding, while the oceanic sediments were exposed to erosion. At the same time, during this late phase of the closure, numerous granitic intrusions were emplaced on both sites of the suture: namely the Weardale granite underlying the Alston Block, the Wensleydale granite underneath the Askrigg Block, the Cheviot granite beneath the volcanic Cheviot Hills, the Shap, Skiddaw and Eskdale granites beneath the Lake District, and the Doon, Criffel and Cairnsmoore of Fleet granites in Dumfries & Galloway (Leeder, 1982; Livelybrooks et al. 1993).

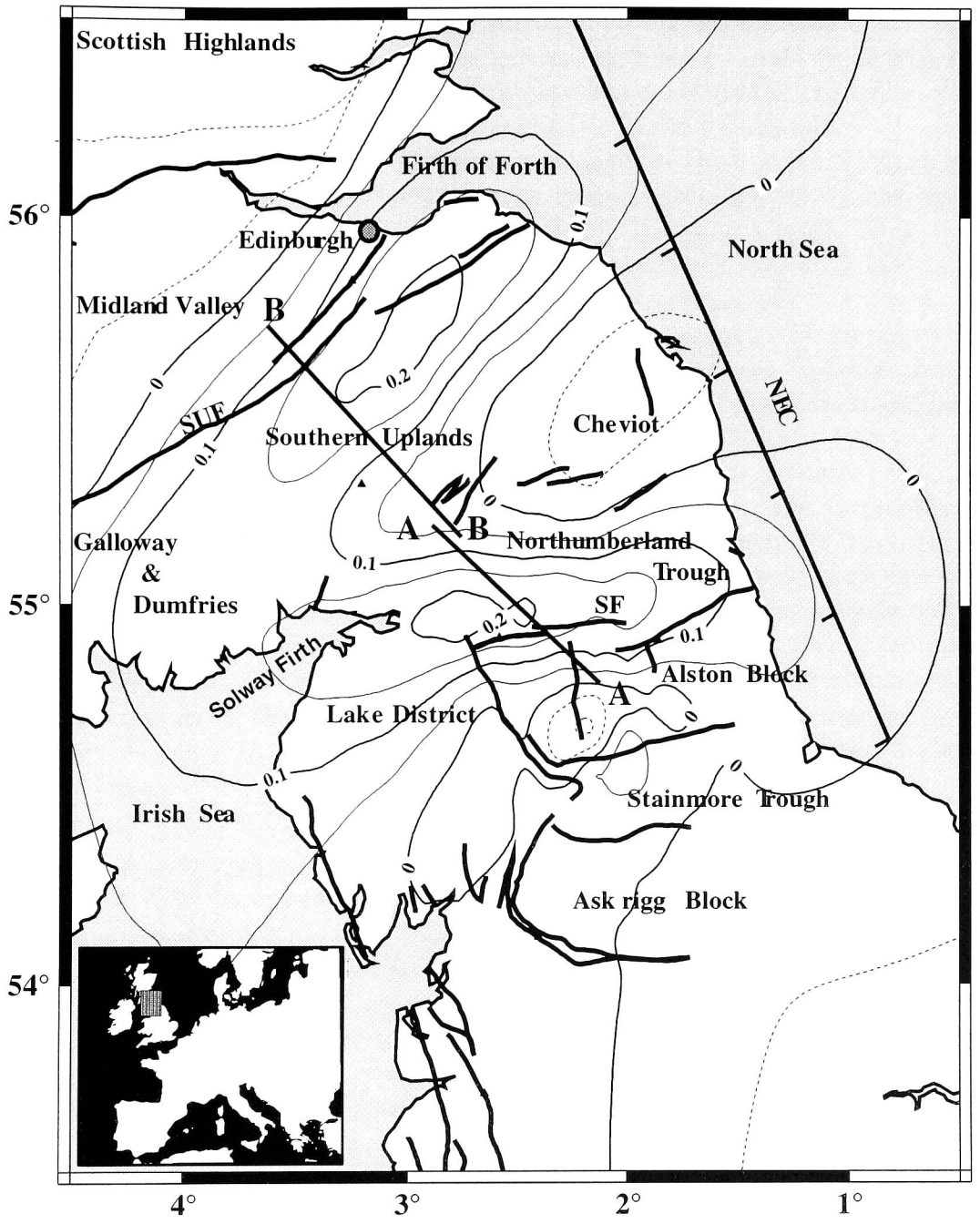

Figure 8: *Summary map of the Iapetus Suture Zone (based on Banks et al. 1996). The major faults are marked by heavy lines: SUF - Southern Upland Fault, KF - Kingledores Fault, SF - Stublick Fault. The contours show the horizontal component of the magnetic variation anomaly at a period of 250s, and delineate the crustal conductors. BB', AA' is the existing MT profile by Banks et al. (1996). NEC is the seismic reflection profile.*

Their locations are displayed in fig. 8.

These granite batholiths formed relatively buoyant blocks in the upper crust and have tended to rise relative to the surrounding region, whereas the crust in the intervening areas has tended to subside, creating a *block - and - basin* structure (Bott, 1967). As a consequence, major fault systems developed at the edges of the Devonian batholiths and various sedimentary basins were filled during the Upper Devonian, Carboniferous and later. The most prominent of them is the E/W-striking Northumberland Trough in northern England, which is thought to conceal the assumed Iapetus suture zone along the 'Solway line'. Reaching a width of up to 30 km, the trough stretches on land over 100 km from the North Sea in the east to the Solway Firth and Irish Sea, in the west. Its marine continuations to the east and west are thicker and more extensive than the sediments on land. To the north and south, the Northumberland Trough is bounded by the Southern Uplands and the Alston Block, respectively. On its southern edge, along the Stublick fault just north of the Alston Block, the sediments reach a thickness of up to 4 km.

South of the Northumberland Trough, the Alston Block is separated from the granites of the Lake District in the east by the Permo-Triassic and Carboniferous sediments of the N/S-striking Vale of Eden with a thickness of 2.5 km. To the south, the Carboniferous sediments of the Stainmore Trough extend in an east-west direction between the Alston and Askrigg Blocks. Here, the sediments also reach a thickness of 2.5 km. The Askrigg Block, in turn, is followed to the south by sediments of Carboniferous age which are up to 4 km thick. To the north, the Northumberland Trough is followed by the Southern Uplands. Their northern edge is marked by the prominent NE-striking Southern Upland Fault, separating the Southern Uplands from the Upper Palaeozoic sediments of the Midland Valley.

The crust of the whole region has been investigated intensively over the past decades by geophysical methods. Since the subject of this thesis is more concerned with the development of methods than with the study of the lithosphere, I shall give only a brief summary of the main aspects of the numerous surveys, with emphasize on electromagnetic results. A more detailed and up-to-date overview can be found in Livelybrooks et al. (1993) or Banks et al. (1996).

a) **Gravity** surveys show that the Devonian blocks are underlain by exposed or buried granites and that the troughs formed in between them (Bott et al. 1984). These blocks are all correlated with distinctive Bouguer anomalies (minima) and Bott (1967) stated their extensions to the depth to the order of 8 km. A gravity low was also found running parallel to and immediately south of the Southern Upland Fault, suggesting the presence of a concealed granite batholith beneath this area (Lagios & Hipkin, 1979). However, recent electromagnetic interpretations associate the middle to upper crust of the Southern Uplands with quarzo-feldspathic gneisses which contain abundant graphite (Banks et al. 1996).

b) Reinterpretation of the earliest **Seismic refraction** experiment (Bamford et al. 1978) by Bott et al. (1985) and numerous **seismic reflection** surveys (Hall et al. 1984; Beamish & Smithe, 1986; Klemperer & Mathews, 1987) revealed a northward dipping contact ($25° - 40°$) between Avalonian mid- and lower-crust, and upper crustal rocks of Laurentian affinity at a depth of 15-30 km, beginning under the Northumberland Trough. Klemperer & Mathews (1987) identified this feature

on a reflection profile in the North Sea (NEC) as the Iapetus Suture. Reflection seismics (NEC) also revealed a southward-dipping feature in the middle crust just south of the Solway line, interpreted as a low angle thrust (Freeman et al. 1988). An updated seismic velocity model based on the LISPB refraction data is given in Barton (1992). It features a discontinuity of the Moho beneath the Southern Upland Fault, inferring a thicker crust underneath the Midland Valley.

c) A number of **magnetotelluric** surveys have been carried out in order to investigate the crust in terms of conductivity anomalies. Parr (1991) reprocessed earlier MT data from Jones & Hutton (1979) and Harinarayana (1987), added some new measurements, and found a northward-dipping conductor by 1D inversion and 2D forward modelling in agreement with the seismic results. He also detected the southward-dipping thrust which appeared as a conductive feature in the middle crust beneath the Northumberland Trough (Parr & Hutton, 1993). 2D inversions of some of these data with the inclusion of GDS results from Beamish & Banks (1983) confirmed the presence of a southward-dipping mid-crustal conductor beneath the Northumberland Trough (Livelybrooks et al. 1993). However, there is no evidence for the presence of a northward dipping feature in the lower crust (Iapetus Suture). In the upper crust, the Weardale granite could be isolated as a resistive structure underneath the Alston block, reaching to a depth of 10 km. The sediments of the Northumberland Trough were well resolved as a shallow conductive feature. Further north, a mid/deep-crustal conductor was found beneath the Southern Uplands. This conductor seems to reach deeper beneath the Midland Valley (Livelybrooks et al. 1993), in agreement to the assumption of a thickened crust in this region from seismic refraction results (Barton, 1992). Junge (1995) confirmed the presence of the mid-crustal conductor in this region with new measurements. It is not clear, however, whether it is the continuation of the mid-crustal conductive structure beneath the Northumberland Trough further south (Banks et al. 1996). Fig. 9 shows a resistivity section of the region.

Recent 2D interpretations including new observations by Livelybrooks & Banks (Banks, 1994; Banks et al. 1996) found this conductor striking obliquely (NNE) to the previously assumed Southern Uplands Fault (striking NE). This strike direction confirmed earlier interpretations from GDS response functions, which detected a prominent conductivity anomaly crossing the geographic boundary of the Midland Valley (Banks et al. 1983). A recent, very dense mapping of the vertical magnetic field in the AMT frequency range (100Hz - 100s) across the Lammermuir Fault (often labelled as the eastward continuation of the Southern Upland Fault) revealed that this fault is electromagnetically not significant, even at shorter periods (O. Ritter, 1995). However, there is a strong indication for a 3-dimensional structure of the upper to middle crust. The more likely continuation of the Southern Upland Fault is now assumed to be in parallel to the Pentlands/Firth of Forth Fault (Floyd, 1994; Banks et al. 1996). Further south, Banks et al. (1996) correlated the top of the mid-crustal conductor beneath the Northumberland Trough with the southward dipping reflective thrust sheet, and the position of the assumed Iapetus Suture with the most conductive part of the lower crust. The boundary separating the mid- or lower crustal conductor from the more resistive basement was inferred from low impedance phases in the period range 400s - 2000s (Banks et al. 1993, 1996; Junge, 1995).

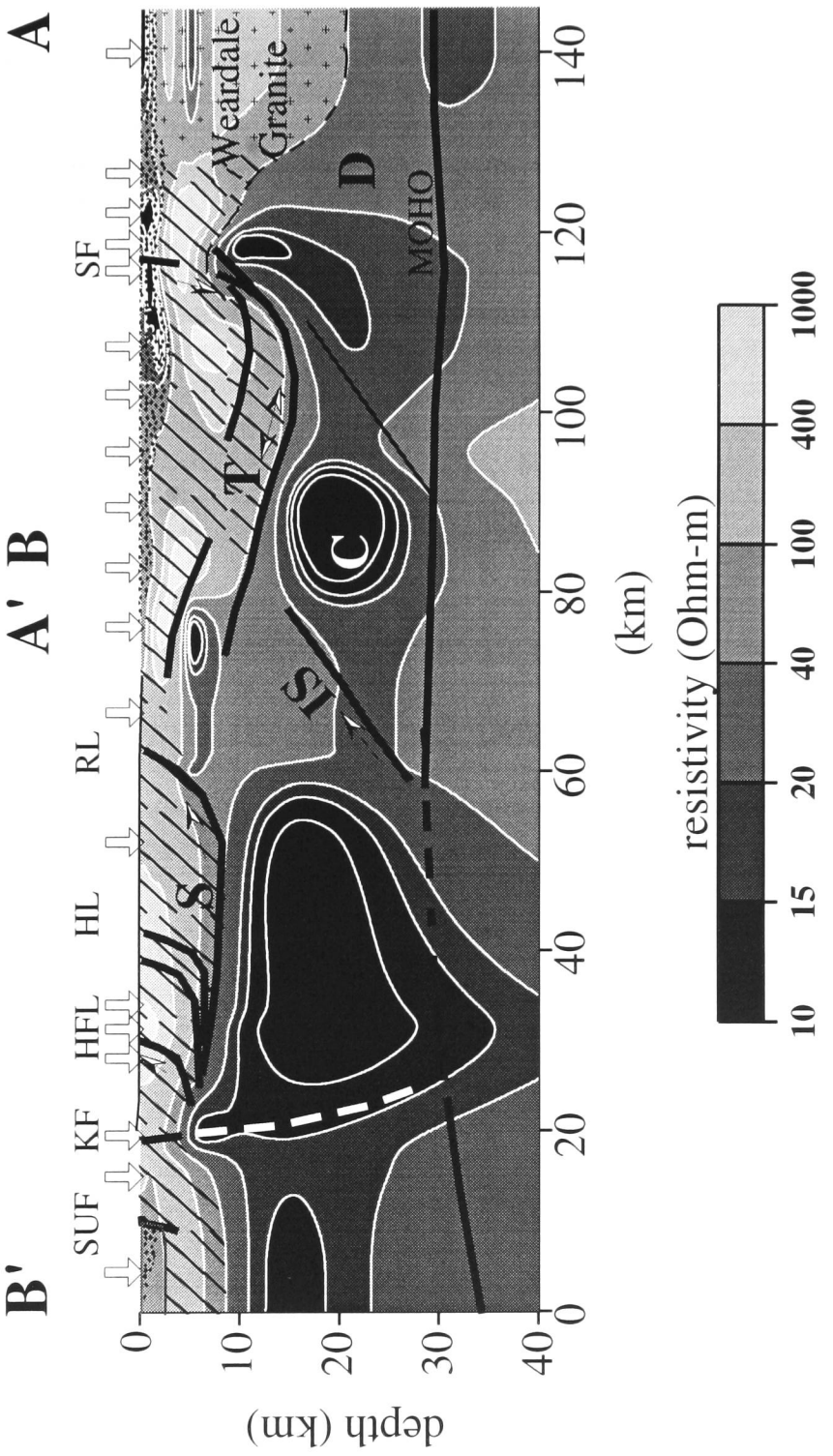

Figure 9: *A resistivity image of the Iapetus Suture Zone (from Banks et al. 1996). The profile (see fig. 8) runs from the Midland Valley of Scotland (B'), crosses the Southern Upland Fault (SUF), the Southern Uplands (SUF to RL), the Northumberland Trough (RL to SF), and ends on the Alston Block (A). Diagonal shading marks the resistive upper crust of Lower Palaeozoic metasedimentary rocks, stippling the conductive Upper Palaeozoic sediments. Heavy lines are faults, shears and thrusts identified with the aid of surface structure and offshore seismic reflection profiling; KF - Kingledores Fault, RL - Riccarton Line, SF - Stublick Fault; C and D zones of lower crust (seismic reflection), IS - Iapetus Suture, T - reflection zone from Freeman et al. (1988). The arrows mark MT sites.*

d) Results of various **Geomagnetic Deep Sounding** surveys (references are given at the beginning of the next section 5.2) indicate two lateral conductive features. The one in the north trends obliquely (NNE) to the Southern Upland Fault (see above), the southern one is correlated with the E/W-extension of the Northumberland Trough (see also fig. 8). The junction of the two anomalies is near Dumfries (SW of Scotland). Beamish & Banks (1983), Banks (1986) and Banks et al. (1993, 1996) pointed out that the anomaly associated with the Northumberland Trough is produced in part by current concentrations in the surface sediments but mainly in the mid-crustal conductor. From hypothetical event maps of magnetometer arrays they concluded that at long periods around 1000s, current channelling rather than induction is the ruling physical process in these structures. As a consequence, the vertical magnetic field component is strong in the surrounding region and induction arrows over a wide period range indicate clearly the east-west striking conductor. However, the arrows do not give information on the structure of the host, where these currents are actually induced (within a region delimited by the skin depth δ, see eqn. 19 in chapter 2). At long periods > 2000s, the induction arrows indicate current flow in the deep Atlantic Ocean to the west (Beamish & Banks, 1983).

Galvanic distortion: In a block-and-basin structure as described here for the Iapetus suture region, with lateral alterations of conductive and resistive features in the upper crust, large scale deflections of the electric currents are likely to occur at different depths. Consequently, galvanic distortion has to be considered for all electromagnetic data at any period range. Recent MT interpretations have therefore included correction for electric distortion effects (Harinarayana et al. 1993; Sule et al. 1993; Banks et al. 1996; Junge, 1995). In GDS, information on the regional structure may not be detected if the magnetic response functions are discussed only by conventional means such as induction arrows. Distortion of the magnetic field, as seen in the previous chapter, should equally well be included in the interpretation, even at long periods.

The fact that distorted magnetic response functions from GDS may contain more information than the obvious strike of the channelling structure was recognized by Banks & Beamish (1984). Applying hypothetical event analysis they detected a different direction that was commonly supported by most of the data of the array under investigation (53 sites). This direction (WSW) was associated with the strike of a *regional* two-dimensional structure, where the currents are induced in the long period range. As a consequence, the blocks and troughs of the upper crust are described as *local* features, despite their considerable extensions.

In the previous chapter 4, I have developed a theory to understand the effects of magnetic distortion on the vertical magnetic response functions. I shall examine in the following how GDS data of a large array of presumably distorted response functions respond to the proposed techniques (section 4.2) which are aiming to eliminate distortion effects. The data array studied is an extension of the one examined by Banks & Beamish (1984).

5.2 Vertical magnetic response functions

The data of 127 sites have been collected by various research teams during the past 20 years, the period range stretches from 20s - 7000s. A list of all site names, coordinates and period ranges is given in the appendix (section A.1). References for the various surveys are:

ELW71: Edwards, Law & White (1971)
EDU73: Hutton, Sikh & Gough (1977), Sik & Hutton (1977), Kirkwood, Hutton & Sikh (1981), Sikh, Hutton, Dawes & Kirkwood (1981)
LAN75: Grimes (1977)
JON75: Jones (1977), Hutton & Jones (1980)
LAN79: M. Geake, 1980
GMU79, LAN80, GMU80, GMU81: Beamish & Banks (1983)
ING81: Ingham (1981)
NOV81: Novak (1981)
LAN85: S. Thatcher, 1985

The data are grouped into 18 period bands in order to facilitate comparison of data originating from different processing schemes:

Data Base band	Central period (s)	Bandwidth (s)
18	27	20 - 40
17	37	30 - 50
16	48	40 - 60
15	58	50 - 70
14	68	60 - 80
13	82	70 - 100
12	125	90 - 200
11	185	150 - 250
10	263	200 - 400
9	400	300 - 500
8	500	400 - 600
7	750	600 - 1000
6	1000	800 - 1500
5	1428	1000 - 2000
4	2000	1000 - 3000
3	2727	2000 - 4000
2	4000	3000 - 5000
1	5454	4000 - 7200

Fig. 10 shows the station locations, for which single site vertical response functions are available. Additionally, 35 sites (filled squares) covering an area of approximately 40×40 km were recorded simultaneously to a reference station (DM) and their *local* response functions (i.e. difference field response functions) could be computed by

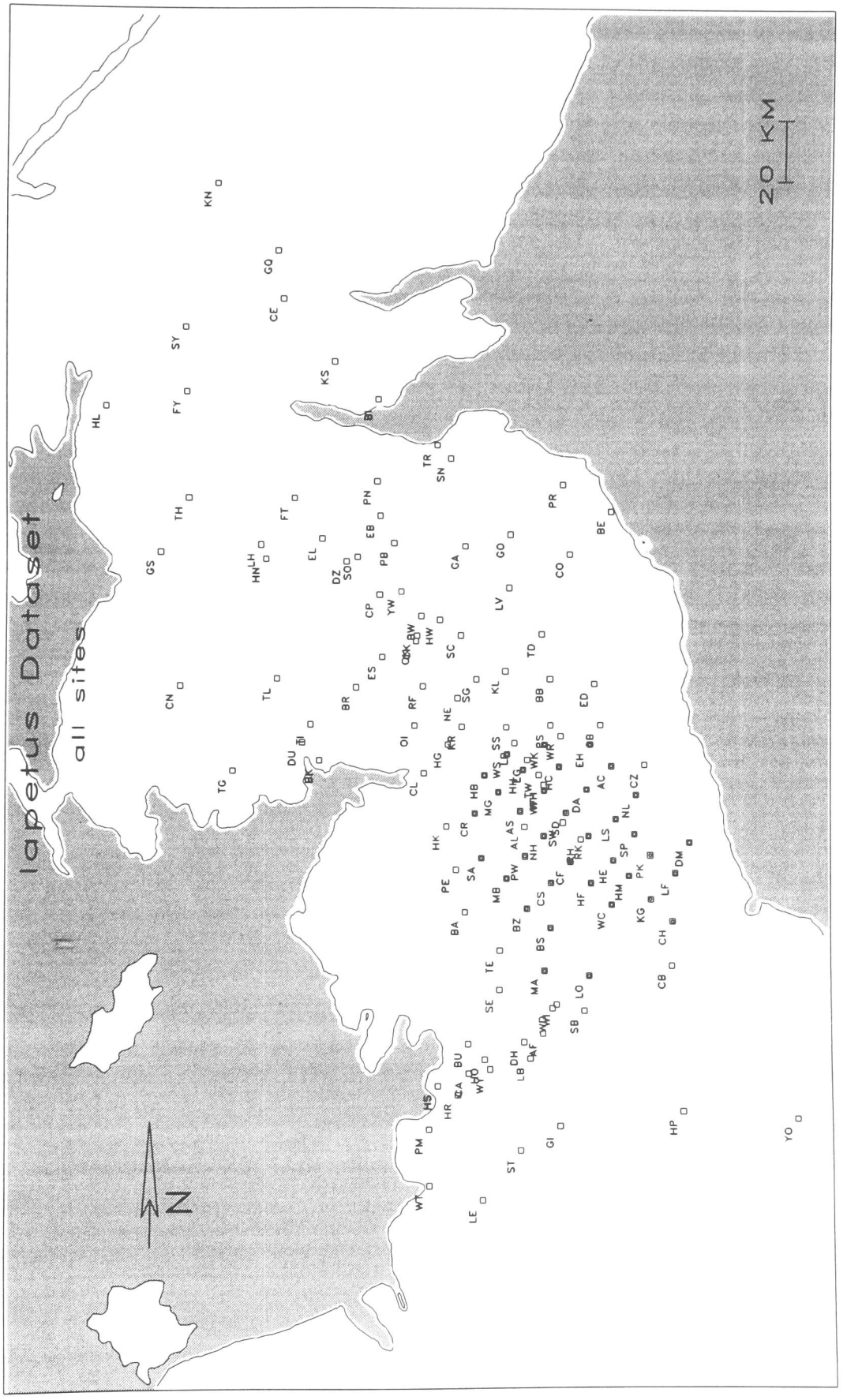

Figure 10: *The Iapetus Dataset: Locations of all sites; filled squares: sites recorded simultaneously with reference site* DM *on the eastern edge of the Alston Block.*

common reference processing (Beamish & Banks, 1983). These sites (see appendix A.2) are situated on dense profiles across the Alston Block in the central area. The reference site is on the eastern edge of this array. In the following, if not stated otherwise, 'magnetic response functions' are always single site response functions, whereas *local* response functions are labeled as such.

5.2.1 Induction arrows

To get a first impression of the data, figures 11 to 14 show real and imaginary induction arrows (single site, Wiese convention[13]) at different periods. Because not all sites provide data at all periods, the number of sites plotted varies between figures. The datafile for period band 7 at 750s contains the greatest number of sites. I chose the periods 70s, 260s, 750s, and 2700s (periods bands 14, 10, 7, 3, respectively) not only because they are approximately evenly spaced on a logarithmic scale, but also because each one is a representative of the neighbouring period bands. Since most of the data were known to be stored in magnetic coordinates (9° west of geographic north), all arrows were rotated into geographic coordinates (0° N).

In view of the huge amount of information, real and imaginary arrows are plotted in separate graphs for clarity. For the same reason error ellipses and site names are omitted. In order to emphasize trends of spatial variations, imaginary arrows are plotted on a larger scale than real arrows. All sites can be identified on the location map in fig. 10. Unfortunately, some sites have incomplete datasets, e.g. error estimates or parts of the response function components are not available. For the latter reason some sites had to be omitted from the datafiles. They are listed in the appendix (section A.3). Additionally, the imaginary arrows of sites LH (band 7, 10) and TH (band 3) were ruled out because they are totally inconsistent with the arrows of the neighbouring sites.

The induction arrow maps can be subdivided roughly into 6 areas, each of which can be identified by the characteristic behaviour of the induction arrows. The areas are (from south to north, see fig. 16): Askrigg Block & South - Alston Block & Stainmore Trough - Northumberland Trough - Southern Uplands - Midland Valley - The North. Fig. 15 shows typical induction arrows at all periods of sites from each of the areas. The major directions of the arrows in the different areas are:

a) Askrigg Block & South: The real arrows are small and turn from NE directions at 70s to mainly SSW directions at 2700s. They almost disappear at ca. 150s and grow larger towards longer periods. The imaginary arrows turn from NE at 70s (parallel to real arrows) over NNE at 750s (anti-parallel) to NW at 2700s. Their lengths are fairly constant up for periods to 500s; they decrease slightly at the longest periods

b) Alston Block & Stainmore Trough: The real arrows point consistently southwards, growing larger with increasing periods. Their maximum lengths are 0.4 - 0.5 at 400s - 2000s. For periods above 2000s they turn SE and decrease slightly. The imaginary arrows point approximately southwards at short periods (parallel to real arrows) and again at long periods. In between (at ca. 200s - 800s) they almost

[13] real arrows tend to point away from a conductor.

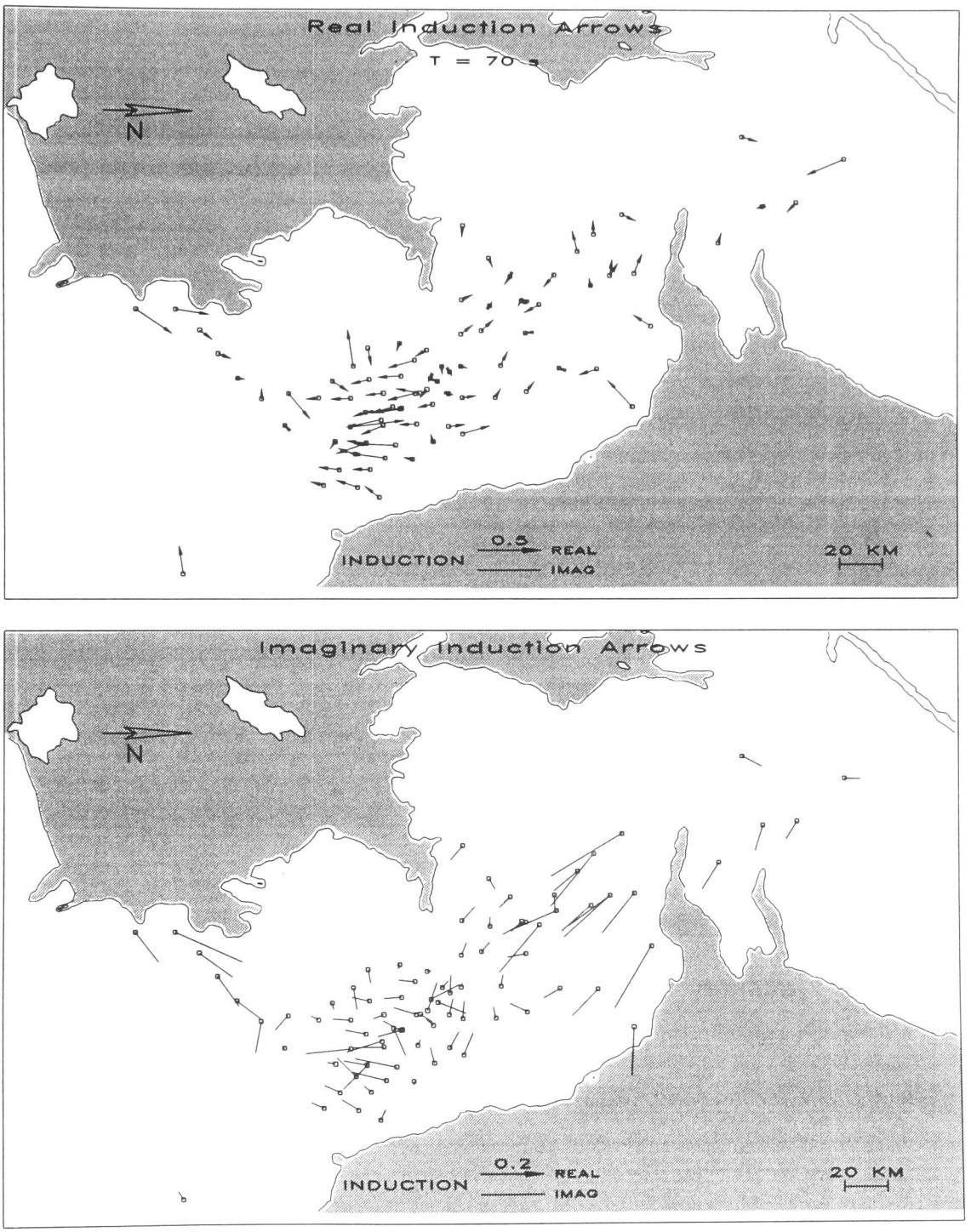

Figure 11: *The Iapetus Dataset: Induction arrows of period band 14: $T = 70s$. Note the different scales for real and imaginary arrows on these and subsequent diagrams.*

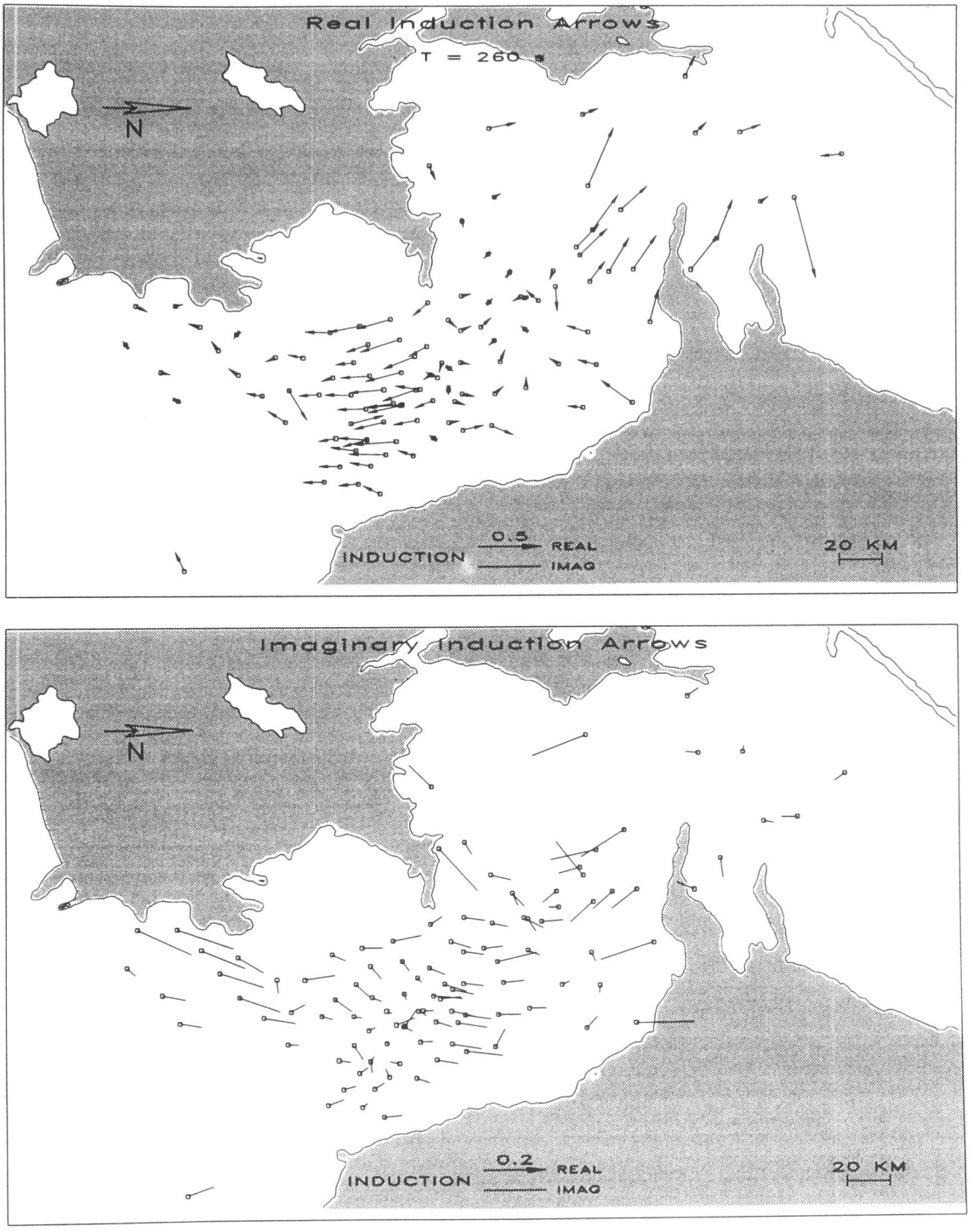

Figure 12: *The Iapetus Dataset: Induction arrows of period band 10:* $T = 260s$

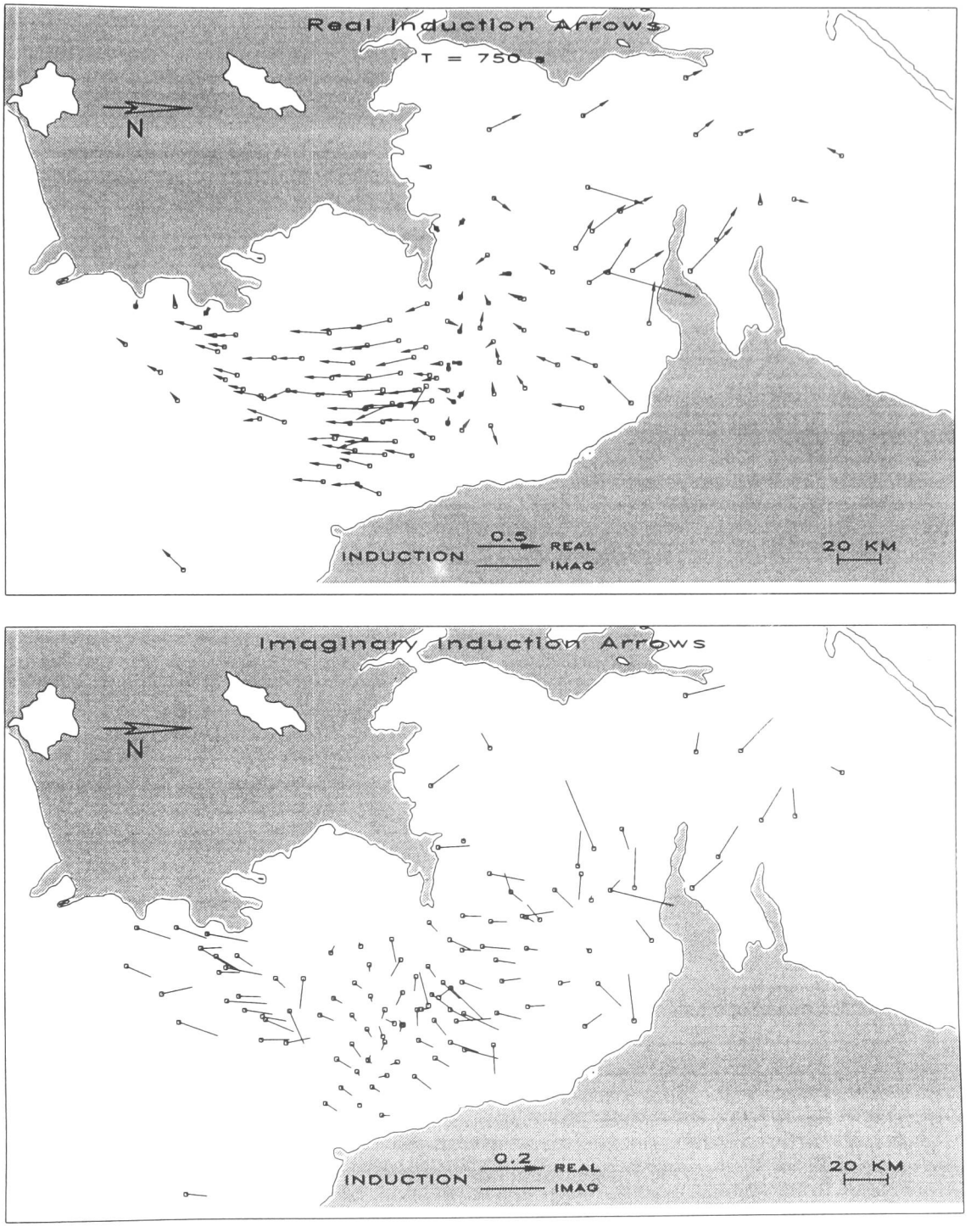

Figure 13: *The Iapetus Dataset: Induction arrows of period band 7: $T = 750s$*

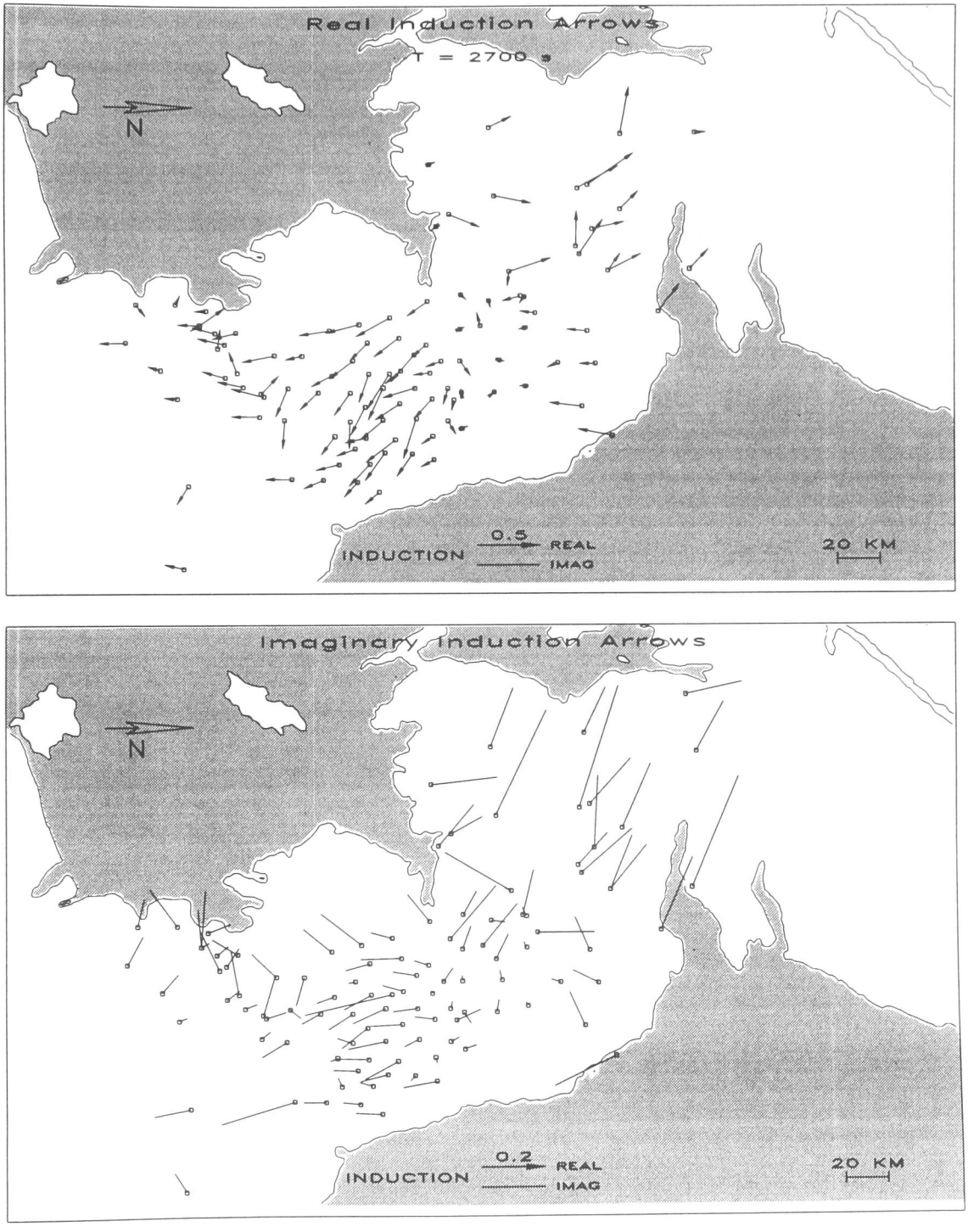

Figure 14: *The Iapetus Dataset: Induction arrows of period band 3:* $T = 2700s$

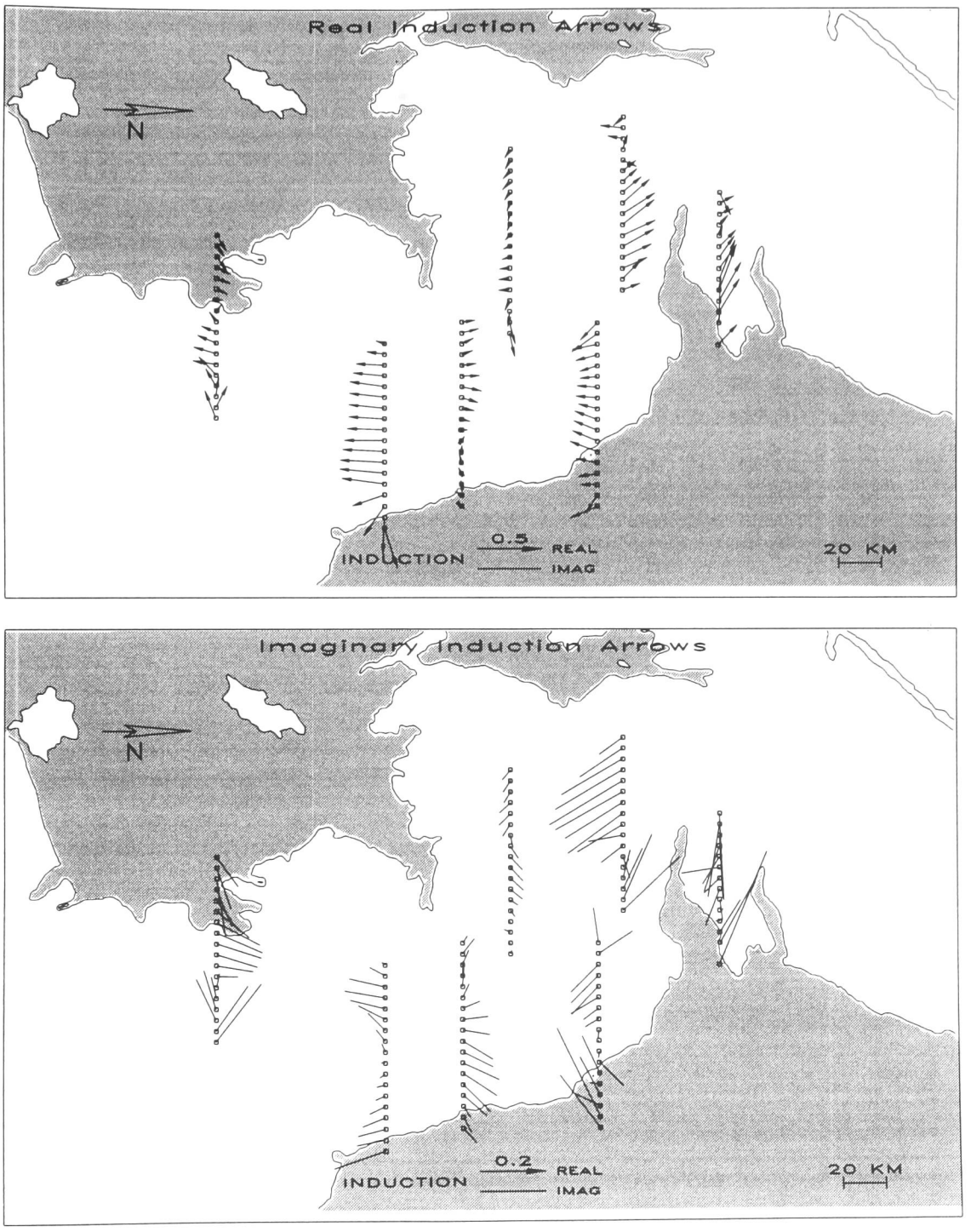

Figure 15: *The Iapetus Dataset: Induction arrows for all periods of 6 different areas. Sites from south to north are:* WY *(southwest of Askrigg Block),* SP *(Alston Block),* PS *(Northumberland Trough),* ES & GO *(Southern Uplands),* FT *(Midland Valley),* KS *(Kinross, North). For locations see fig. 10. Periods increase from left (west) to right (east).*

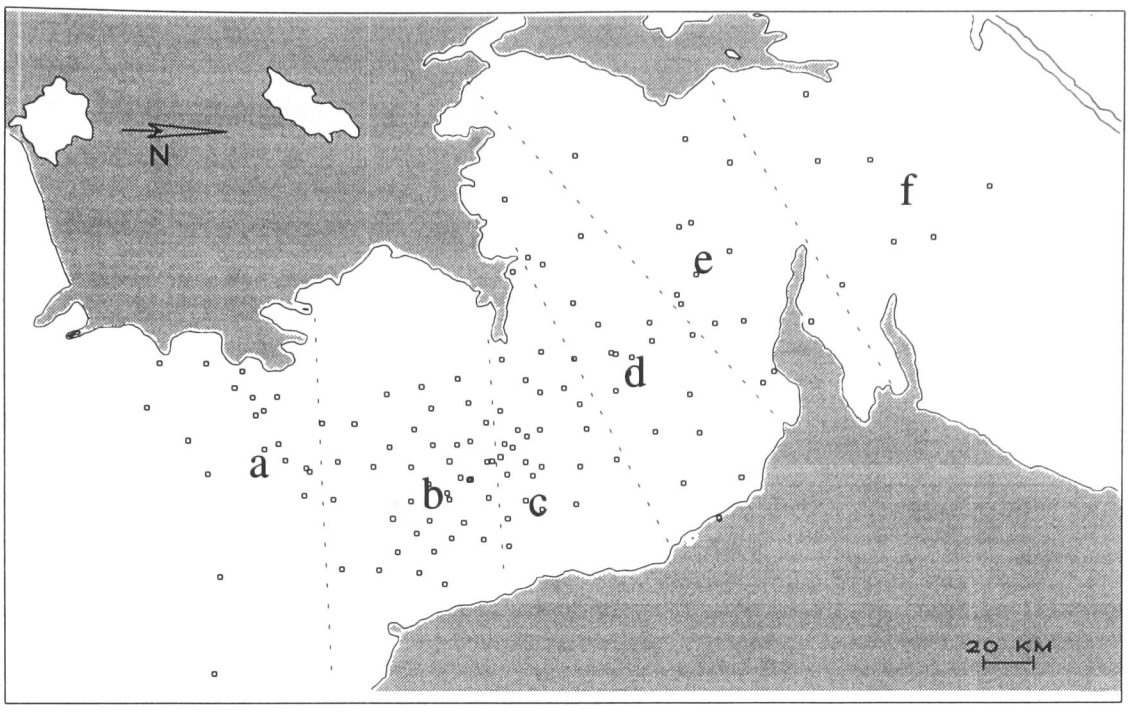

Figure 16: *The Iapetus Dataset: The induction arrow maps can be subdivided roughly into 6 areas. The areas from south to north are: (a) Askrigg Block & South - (b) Alston Block & Stainmore Trough - (c) Northumberland Trough - (d) Southern Uplands - (e) Midland Valley - (f) The North. Fig. 15 shows typical induction arrows at all periods of sites from each of the areas.*

vanish, and their direction (mainly NE) is not well determined. This period range corresponds to the range where the real arrows take their maximum values.

c) Northumberland Trough: The real arrows show 3 different regions within this area. On the southern edge, they are very small over the short and intermediate period range, their directions are undetermined. They are increased and tend to point towards SE at the longest periods; consistent with sites on the Alston Block. Those in the centre are still small, but point mainly northwards between 70s and 260s. The real arrows on the northern edge are larger and point towards NW at short periods and westwards at intermediate periods. They are very small and undetermined at the longest periods. The general directions of the imaginary arrows turn from NW at short periods (parallel to northern real arrows) to NNE at intermediate to longer periods. At the same time they grow longer until, above 2000s, the lengths decrease again, with undetermined directions at most sites. The arrows at the northwestern sites decrease only slightly and return to mainly NW directions at the longest periods.

d) Southern Uplands: The real arrows are generally small, only arrows at western sites are larger. A predominant SSW direction can only be established at intermediate periods (260s, 750s). At the longest periods, most arrows are still small but point consistently southwards. The imaginary arrows are roughly pointing SE at short periods (70s, 260s), but show no uniform trend for longer periods. They

are, however, relatively large (0.2) over the whole period range at most sites of the area.

e) Midland Valley: The real arrows point westwards at 70s and show a strong NW tendency throughout the rest of the period range (lengths up to 0.4). The imaginary arrows are also large (0.4) and rotate from SE to NW directions (i.e. from anti-parallel to parallel directions) with increasing periods. At 750s they cross the zero amplitude line.

f) The North (Grampian): Here, most of the real arrows > 100s point also in NW direction. The imaginary arrows rotate from mainly SE at short periods to roughly NW at longer periods. After having disappeared at ca. 500s, they are all relatively large (0.3) at the longest periods.

In accordance with the complexity of the geological structure of the whole region, the data of these sub-areas show very different characteristics, not only at short and intermediate periods, but even in the long period range. For these longest periods, which correspond to the lower crust and upper mantle, one would expect to find a more homogenous behaviour of the induction arrows. Therefore it seems very likely that the long period data in this region may be affected by local conductivity inhomogeneities of the upper and middle crust.

This is particularly evident in the areas of the Alston Block (b) and the Midland Valley (e). Both areas are associated with mid-crustal high conductivity features. The relatively large real arrows and parallel imaginary arrows indicate induction in the range 100s - 500 s for the Midland valley data, and in the range 50s - 100s for the Alston Block data. This correlates well with MT inversion results, which attribute different thicknesses to the mid-crustal conductor. The real arrows, however, remain large for considerably longer period bands, still indicating the approximate strike of the respective mid-crustal conductor (E/W for the Northumberland Trough and NE for the Southern Upland Fault). At the same time, the imaginary arrows, vanish and recover towards longer periods. This behaviour is a strong indication that galvanic distortion is affecting the data in the period range where the imaginary arrows are very small or recovering, i.e. at T> 200s for sites in the vicinity of the Northumberland Trough and at T > 800s for data north of the Southern Upland Fault. At these periods, information gained from the real induction arrows refers to properties of the scattering inhomogeneity rather than to the strike direction of the regional structure where the currents are actually induced.

At long periods T > 2000s (fig. 14), there are indications that the data are still affected by current flow in the conductive parts of the crust. In this period range, the real arrows south of the Northumberland Trough depart from their constant southward direction and point towards the southeast. In a wide area northwest of the Northumberland Trough, the imaginary arrows at 2700s point uniformly in a NW direction. This azimuth is parallel to the real and imaginary arrows in the region further north of the Southern Uplands, and approximately anti-parallel to real arrows of sites directly south of the Northumberland Trough (Alston Block & Stainmore Trough). Most of the imaginary arrows in this latter area are directed slightly more southwards, pointing SSE. However, imaginary and real arrows across the Northumberland Trough and parts of the Southern Uplands are very small and their directions are undetermined. This behaviour is typical for induction arrows

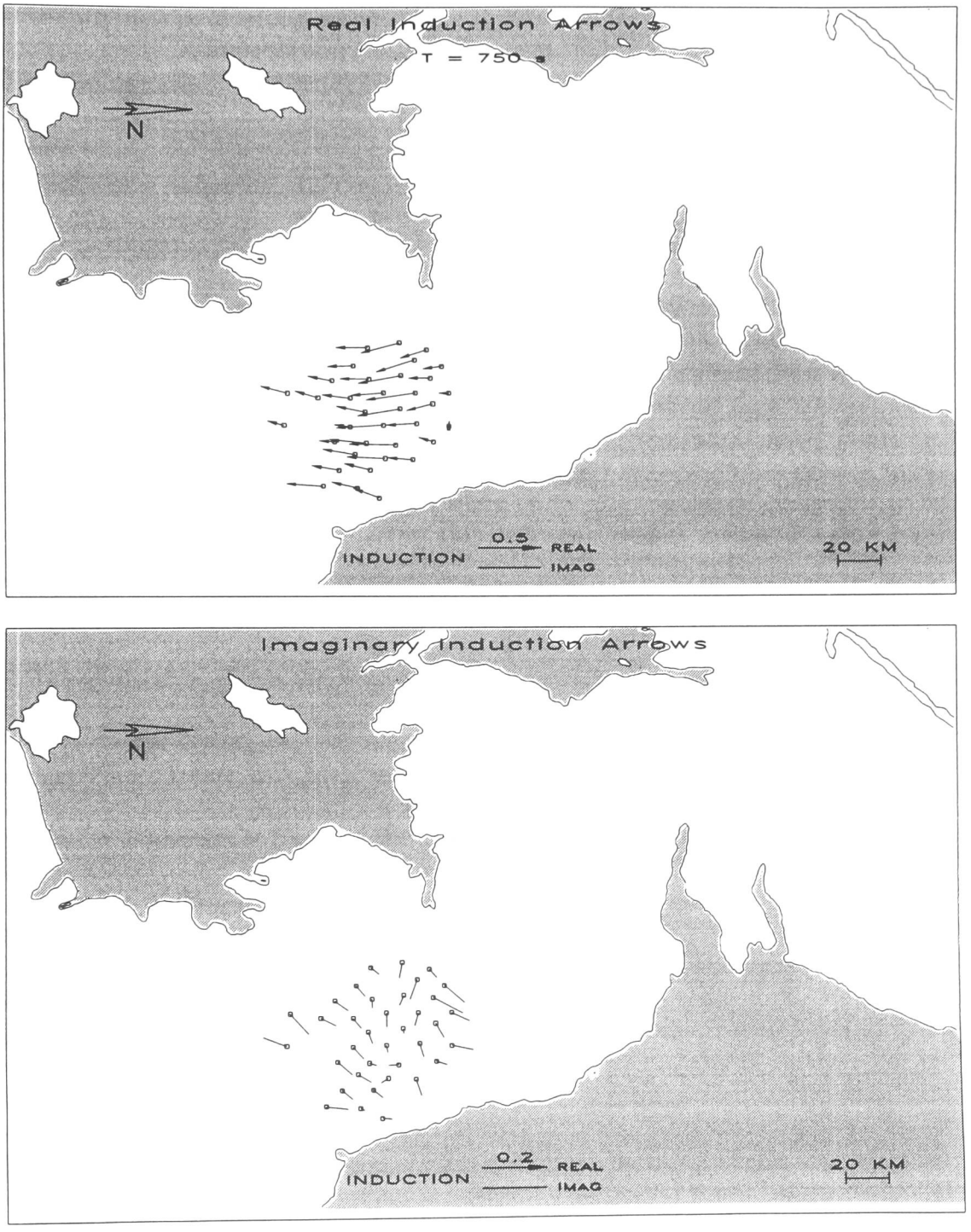

Figure 17: *The Iapetus Dataset: Relative induction arrows of a limited set of sites on the Alston Block for period band 7: $T = 750$s. Common reference site is* DM *at the eastern edge of the Alston Block. Although the arrows are slightly longer, their directions are very similar to those computed from single site response function estimates (fig. 13). The spatial variations of the horizontal magnetic field can therefore be assumed small across the area covered by these 35 sites.*

across a structure of strong current flow. In this case the zone of current concentration appears to be directed north-eastwards. Real arrows of sites in the southernmost area (Askrigg Block and further south (a)) do not repeat this long period feature, but indicate current flow in E/W direction to the north (similar to the imaginary arrows across the Alston block). Most of the imaginary arrows, however, point in north-westerly directions, approximately parallel to the real arrows across the Alston Block and to the arrows further north.

Edwards et al. (1971) and Beamish & Banks (1983) assumed induced current flow at long periods in the deep Atlantic Ocean to the west of the British Isles. The induction arrows of our extended dataset, however, agree only partly with this direction. While the imaginary arrows of most areas at very long periods support a WNW or NW direction, only the real arrows across the Alston Block indicate a north-easterly striking structure to the northwest. It is more likely, however, that the directions inferred by induction arrows at these long periods do not reflect solely induction processes but are again affected by current deviations in the complex crustal structure. At these longest periods, the direction of current concentrations seems to be predominantly NE-directed, i.e. along the Southern Uplands conductivity anomaly.

Apart from distortion of the vertical magnetic field, the significance of induction arrows computed from single site response functions (i.e. from total measured fields at each site) might not be ensured, if the horizontal magnetic field is spatially non-uniform. This problem arises near vertical conductivity boundaries due to galvanic distortion or secondary induction effects. For that reason it is safer to compare induction arrows estimated from *relative* response functions. These are obtained by relating the total vertical field at each site to a reference horizontal field. *Relative* response functions are only available at 35 sites across the Alston Block area (Beamish & Banks, 1983). Fig. 17 shows the *relative* induction arrows of these sites at period 750s. Fig. 13 shows the corresponding single site arrows at the same period for comparison. The *relative* induction arrows are slightly larger, but they point consistently in the same directions as the single site arrows. From this observation, we may conclude that the requirement of quasi-uniform fields is met and that single site induction arrows are reliable at least in this area. Beamish & Banks (1984) have stated less than 20 % variations of the horizontal fields to these sites. Unfortunately, there are no common reference data available for the other areas and we cannot be absolutely sure whether the conditions of quasi-uniformity are met over the whole region covered by the large dataset. We are also not able to use Banks' method to correct for effects of the anomalous horizontal fields (Banks, 1986) since the database does not contain the relevant horizontal perturbation tensors of each site.

5.2.2 Period dependency of the magnetic response functions

Figures 18, 19, and 20 show the variations of the magnetic response functions $(\mathcal{A}_i, \mathcal{B}_i)$ (see eqn. 31, chapter 2) grouped in 6 areas, as established from the induction arrow maps in the previous section. Apart from their geographic location, the sites could easily be classified to the appropriate areas by the shapes of their curves. A list of the sites used for each area is given in the appendix (A.4).

In each area, the curves of different sites are relatively uniform over the whole period range. Deviations occur mainly at the shortest and longest periods. At the shortest periods, the magnetometers work at their technical limits. At the longest periods, the data are less well determined due to smaller numbers of degrees of freedom. In this range, possibly source field effects need to be considered, too. In the intermediate period range, the curves run quite smoothly, with some exceptions probably caused by individual difficulties during measurements. Without going into the details of individual sites, the best data quality can be found at the sites on the Alston Block (area (b) in bottom fig. 18) and across the Northumberland Trough (area (c) in top fig. 19). The data quality seems to deteriorate in the areas further north (areas d - f).

The most important observation regarding the real parts is that curves in areas located south of the Southern Uplands Fault (areas a - d in figures 18 and 19), have basically the same shape in the period range 400s - 2000s. Although the amplitudes vary between sites and areas, the curves are all slightly descending with increasing periods. This is true for both components $\mathcal{A}_i$ and $\mathcal{B}_i$ of the response functions, although their curves differ in the adjacent period ranges, especially at the longest periods. At most sites, the maximum negative amplitudes of $\mathcal{B}_i$ in the intermediate period range are smaller than those of the corresponding $\mathcal{A}_i$. Since the $\mathcal{A}$ component represents the contribution of the response function in the geographic x - direction, the larger $\mathcal{A}_i$ values produce the strong real induction arrows pointing in southward directions.

Generally, the curves descend smoothly over the whole period range up to approximately 1000s. For even longer periods they either hold their level or ascend. The $\mathcal{B}$ curves rise later and more steeply than the $\mathcal{A}$ curves. At these long periods, they reach larger amplitudes than the $\mathcal{A}$ components, indicating a change of the inherent coordinate system (i.e. strike direction). Often, curves of different areas and also of individual sites have very similar shapes, but seem to be shifted up or down. For example, curves across the Northumberland Trough (area b) show the largest negative values at sites situated at the southern edge, while the curves at the northern edge are shifted (not reversed!) to positive values.

At short periods around 60s, a small negative peak can be detected in the real and imaginary parts of many sites (mainly area b, bottom fig. 18), indicating an inductive response in this range. Depending on the assumptions made for the resistivity of the crust, a structure causing this effect in the response functions would be situated in the middle crust (skin depth is ca. 12 km for 10 Ωm). In the intermediate period range, the curves of the imaginary parts lie in narrow bands mostly close to zero amplitude (areas b + c in figures 18 and 19); they are slightly larger in the southernmost area (a) (top fig. 18). Apart from the small negative peak around 60s, the imaginary amplitudes tend to rise slightly towards the longest periods. In this period range currents are presumably induced in the upper mantle (skin depth: 150 km for 50 Ωm at 2000s) or possibly in the deep ocean and underlying oceanic crust and mantle to the west and southwest of the British Isles.

North of the Southern Upland Fault (areas e+f of fig. 20), the curves of the real and imaginary parts of the components $\mathcal{A}$ and $\mathcal{B}$ change dramatically. The general pattern is reversed, as far as $Re\mathcal{A}_i$ is concerned: curves ascend with increasing

a) Askrigg Block & South

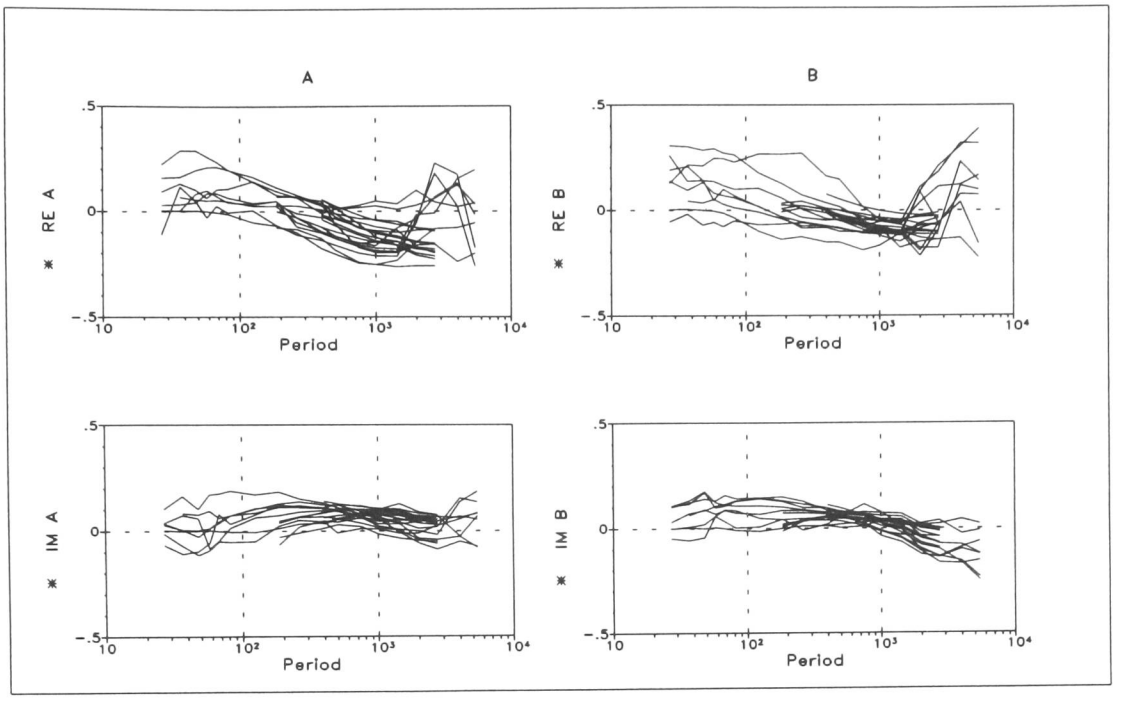

b) Alston Block & Stainmore Trough

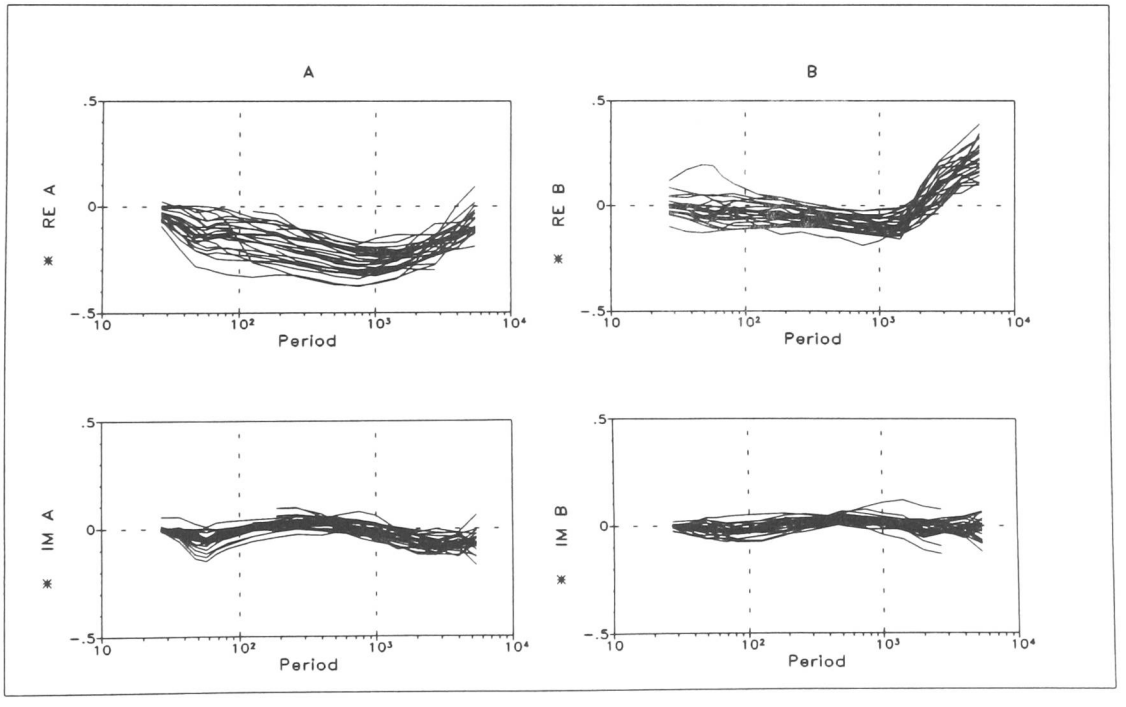

Figure 18: *The Iapetus Dataset:*
Real and imaginary parts of the magnetic response functions (Rotation: 0° N*)*
top figure: area a) Askrigg Block & South
bottom figure: area b) Alston Block & Stainmore Trough

c) Northumberland Trough

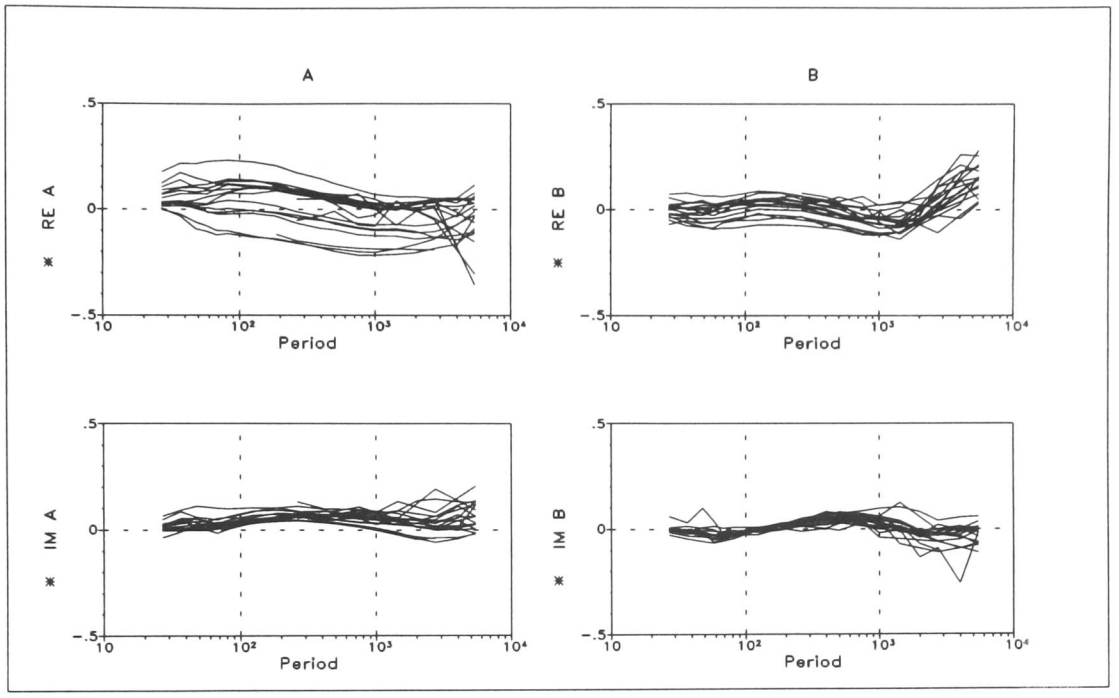

d) Southern Uplands

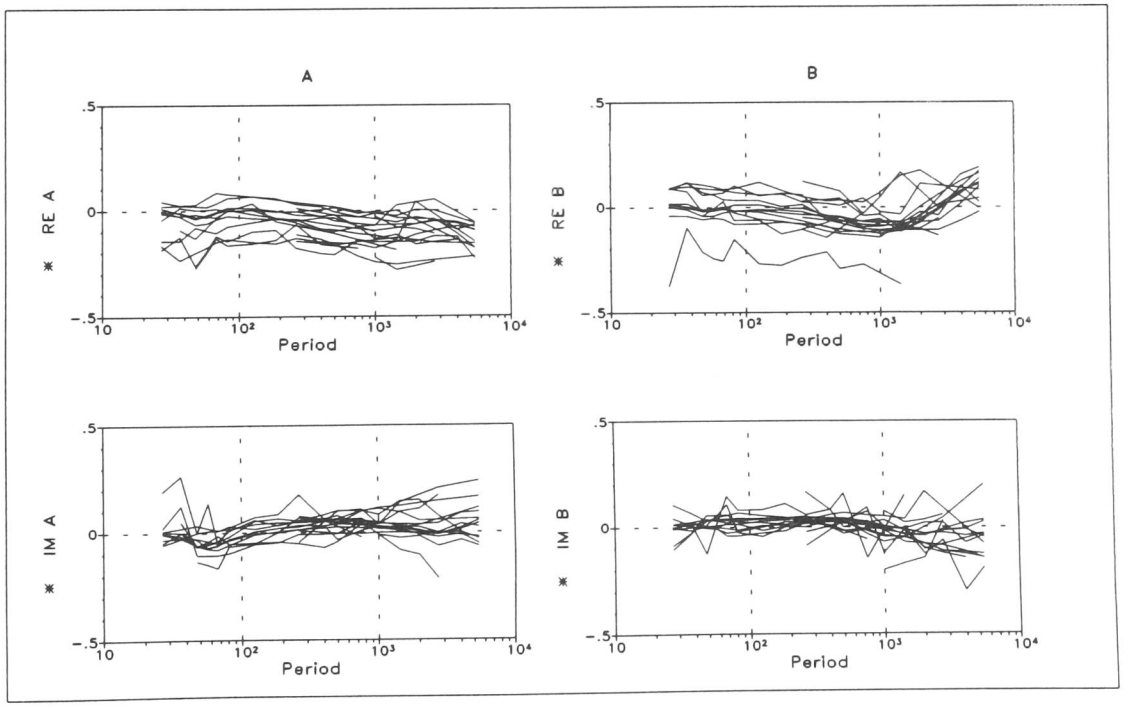

Figure 19: *The Iapetus Dataset:*
Real and imaginary parts of the magnetic response functions (Rotation: 0° N*)*
top figure: area c) Northumberland Trough
bottom figure: area d) Southern Uplands. The lowest curve of $Re\mathcal{B}_i$ *would fit perfectly into the band of curves* $Re\mathcal{B}_i$ *of area (e).*

e) Midland Valley

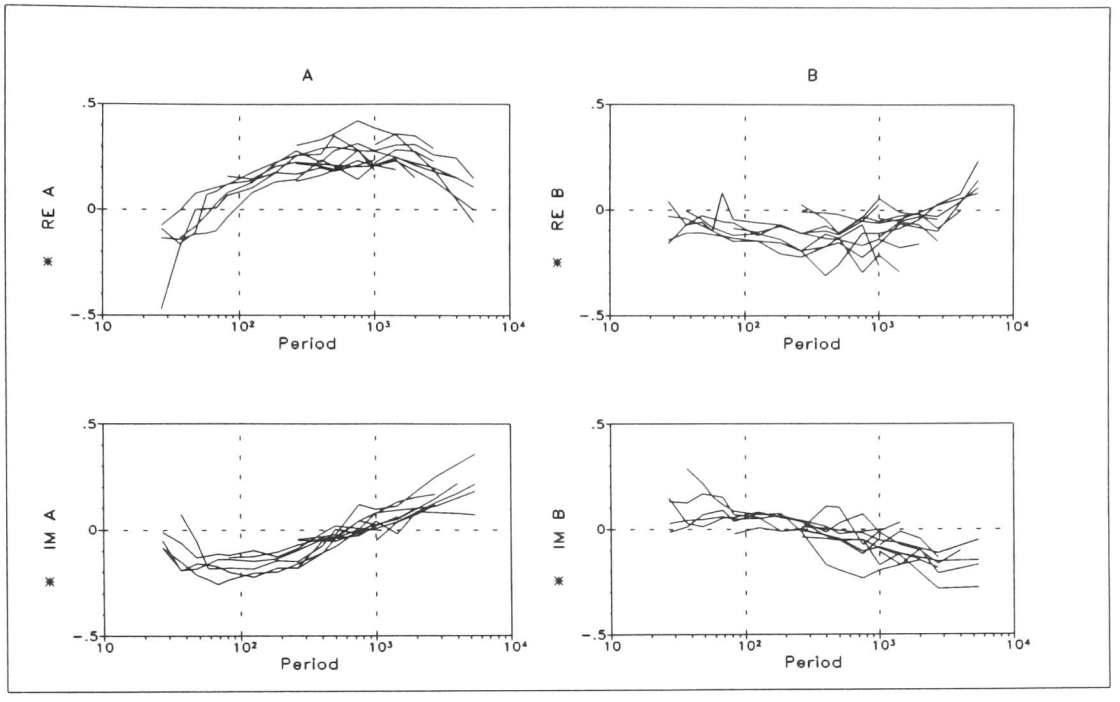

f) The North - Grampian

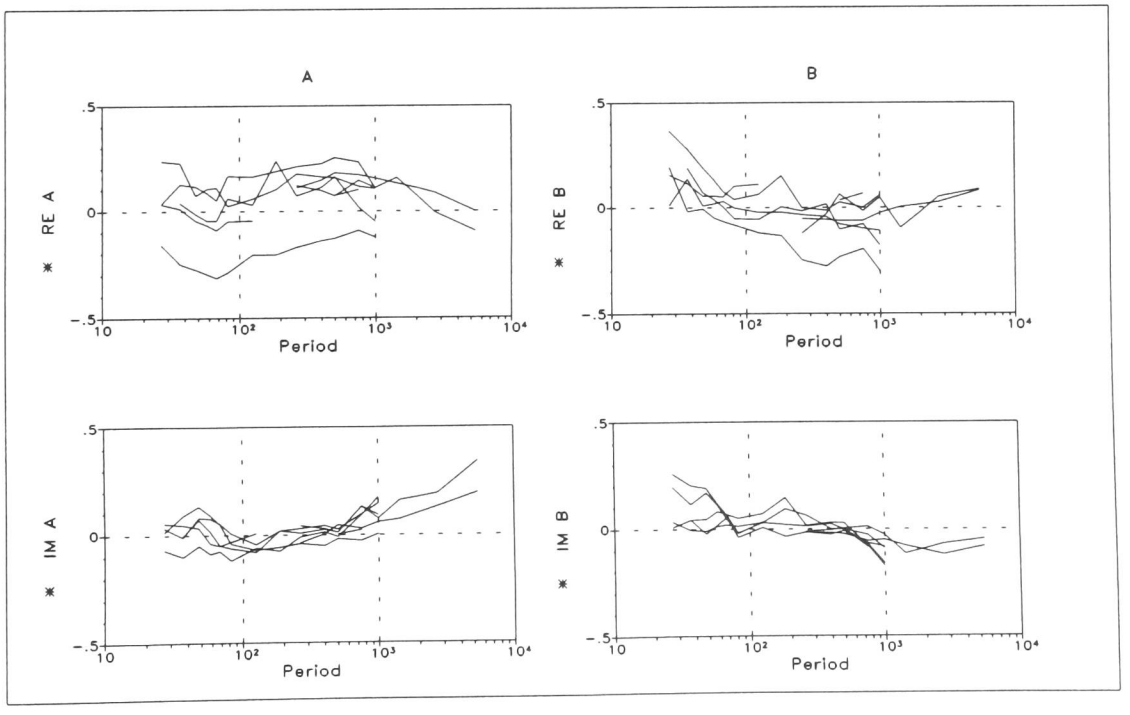

Figure 20: *The Iapetus Dataset:*
Real and imaginary parts of the magnetic response functions (Rotation: 0° N*)*
top figure: area e) Midland Valley
bottom figure: area f) The North

periods, go through maximum positive values around 1000s and descend towards the longest periods. The shapes of the $Re\mathcal{B}_i$ curves of area (e) are now similar to the shapes of the $Re\mathcal{A}_i$ curves south of the Southern Upland Fault, indicating a rotation of the inherent coordinate direction towards more westerly directions. They have a maximum negative amplitude at 400 s - 1000s. The maximum absolute values of the $\mathcal{A}_i$ are still larger than those of $\mathcal{B}_i$. Hence, the resulting real induction arrows point in NW directions. The imaginary parts of both components are distinctly larger at short and very long periods than south of the Southern Upland Fault. They are zero at periods just before the corresponding real parts take their maximum values (at ca. 800s). At the northernmost sites (area f), these characteristics are less distinctive, but still detectable. Unfortunately, for the areas north of the Southern Upland Fault, we have fewer sites available, especially in the long period range, and in addition, problems with noise seem to become more severe in these datasets.

One site in area (d) (fig. 19, site PR) shows ambiguous characteristics: component $\mathcal{A}$ fits well into the curve band $\mathcal{A}_i$ of the Southern Uplands sites (d), whereas component $\mathcal{B}$, although very disturbed, clearly parallels curves $\mathcal{B}_i$ of the region further north (e) (fig. 20). This site, however, can be regarded as an exception due to its location close to the fault line (see fig. 10).

The differences of real and imaginary parts of the magnetic transfer functions between sites located south and north of the Southern Upland Fault indicate two different structures of the crust and two different processes responsible for current flow reflected in the data:

1.) Sites of the southern area (south of Askrigg Block to Southern Uplands: areas a - d) have very similar curves of the real parts, with a negative maximum around 1000s. Although the shapes of $Re\mathcal{A}_i$ and $Re\mathcal{B}_i$ at the shortest and longest periods differ considerably, they run in parallel in the range ca. 400s - 2000s. The small peak of the real and imaginary curves at T = 60s and the very small amplitudes of the imaginary parts in the following intermediate period range suggest that we observe an induction process at short periods beneath the areas of Alston Block and Northumberland Trough. On the other hand, bigger amplitudes towards the longest periods reflect an inductive response for (T > 2000s). These two period ranges correspond to the depths of the middle crust and the upper mantle or a distant deep ocean, respectively. The amplitude ratios of $\mathcal{A}$ and $\mathcal{B}$ indicate that different strike directions may be attributed to these two depths: E-W for the mid-crustal and NE for the upper mantle / oceanic structure. In the intermediate period range, the real parts especially of the $\mathcal{A}$ component have large values. They run in smooth parallel curves and are likely to be produced by channelling of regional currents through the midcrustal conductor. As already mentioned in the previous section, the corresponding induction arrows may reflect only the strike direction of the local body where the regional currents are concentrated, but not of the regional structure where these currents are actually induced.

2.) North of the Southern Upland Fault, the $\mathcal{A}_i$ curves are reversed to positive values. Increased $\mathcal{B}_i$ values in the intermediate period range require a more NE - directed current flow. Large amplitudes of the imaginary parts and a distinct change from negative to positive values at the period of maximum real parts suggest an inductive response in the period range T < 500s. This indicates conductive structures reaching

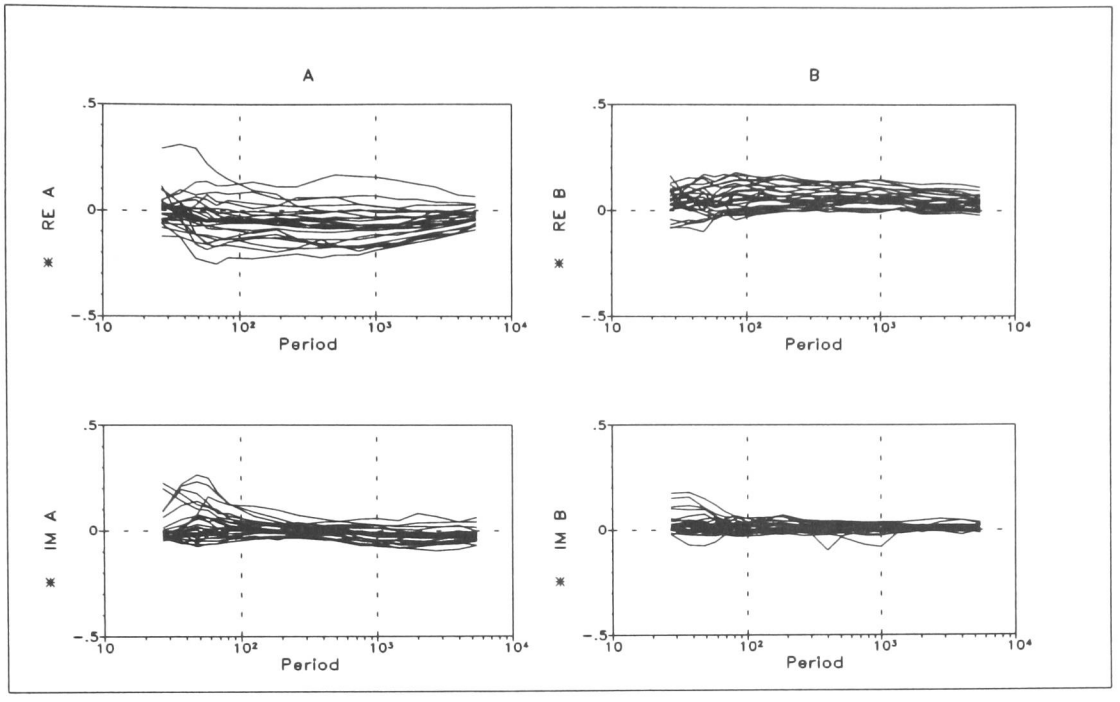

Figure 21: *The Iapetus Dataset:*
Real and imaginary parts of the local magnetic response functions calculated from difference fields (Rotation: 0° N*) of area (b) Alston Block & Stainmore Trough. Apart from shortest periods, the curves of different sites are parallel. They appear less structured than those of single site response functions, because the contribution of the regional vertical component is eliminated.*

to lower crustal depths. Possibly, the mid-crustal conductor is much thicker beneath the Midland Valley than underneath the Northumberland Trough, as also claimed by Livelybrooks et al. (1993) and Banks et al. (1996). Due to a low number of sites and high noise levels, in this area, the curves do not give a clear impression of magnetic distortion at longer periods. However, since the imaginary parts have zero amplitudes between 500s - 1000s, in the northern areas (e - f), current deviations due to this conductor are likely to occur at higher periods, i.e. ca. at T > 800s.

For sites across the Alston Block area, the variations of the single site response functions (bottom fig. 18) may be compared with the *local* vertical magnetic response functions in fig. 21. The *local* response functions were obtained, relating the difference of total and reference vertical field at each site ($B^l_{z_i} = B_{z_i} - B^r_z$) to the horizontal field at the common reference site DM (Beamish & Banks, 1983). Under the assumption that the anomalous vertical field at the reference site is small, this procedure should eliminate any contribution of the regional vertical magnetic field and reveal the *local* anomalous vertical field at each site $B^l_{z_i} \approx B^a_{z_i}$.

The variations of the *local* response functions ($\mathcal{A}^l_i, \mathcal{B}^l_i$) give a very different impression from the single site response functions. The maxima at short periods around 60s are still present in the data (mainly in $\mathcal{A}_i$), those of the imaginary parts $Im\mathcal{A}_i$ have even larger amplitudes. At long periods (T > 1000s), $Re\mathcal{A}_i$ seem to converge towards zero amplitudes. However, the negative maximum of $Re\mathcal{A}_i$ stretching over

the intermediate period range and the steep rise of the $Re\mathcal{B}_i$ have disappeared altogether. The remaining smooth and parallel curves in the period range 200s - 1000s are produced by the anomalous magnetic field due to galvanic distortion. According to the theory presented in the previous chapter, $\mathcal{A}_i^l$ and $\mathcal{B}_i^l$ represent the two principal impedances, Z_B and Z_E, in the case of a two-dimensional regional conductivity distribution. They may be shifted up or down by real factors of position. If the data are not given in the coordinate system of the regional strike direction, $\mathcal{A}_i^l$ and $\mathcal{B}_i^l$ contain mixtures of the two impedances.

Since we do not have information on the strike direction of the structure where the regional currents are actually induced in the period range of distortion, we do not know for sure whether the regional structure is really two-dimensional. Fig. 21 shows, that $\mathcal{A}_i^l$ and $\mathcal{B}_i^l$ are not altogether parallel, but their slopes differ slightly towards long periods. In the case of a one-dimensional regional structure, the curves of the two components are exactly parallel. Hence, we may conclude that the regional structure is likely to be two-dimensional. Furthermore, the obvious difference of *local* and single site magnetic response functions requires the presence of a regional vertical component B_z^o. This, in turn, can only be produced by a significant multi-dimensional structure.

5.2.3 Distortion test

In the induction arrow maps and frequency response diagrams we could already see indications for galvanic distortion of the magnetic response functions in the intermediate period range. It is now interesting to investigate whether the data of different sites behave in the way as described for the distortion test in section 4.2.4. We expect the ratios of the *local* response function components of different sites to be constant over the period range of distortion. The amplitude of the ratio may vary between sites due to the site-dependent distortion parameters. Period-dependency, however, as well as differences between the components (i.e. their ratios) should be eliminated in the distortion range. Because we cannot be sure whether the response functions determined at each site are purely local or whether they contain contributions from a regional vertical field component (affecting in turn the ratio), the distortion test was limited to investigating the *local* response functions determined from difference fields across the Alston Block. Given the large number of sites available in the complete dataset, it would not be feasible to assess all 8001 possible ratios.

Fig. 22 shows the ratios of $Re\mathcal{A}_i/Re\mathcal{A}_j$ and $Im\mathcal{A}_i/Im\mathcal{A}_j$ on the left side and those of $Re\mathcal{B}_i/Re\mathcal{B}_j$ and $Im\mathcal{B}_i/Im\mathcal{B}_j$ on the right side. For the test, the index i denotes one site (HM) for all ratios, whereas j represents all other sites in the Alston Block dataset. Note that the amplitudes are plotted logarithmically. Most of the real parts are parallel over the period range, while the imaginary parts show more diverging curves. The ratios of the $Re\mathcal{A}$ components decrease from values between 1 and 10 in the short period range up to 100s, but run in fairly constant and parallel curves from ca. 200s up to the longest periods. In this range, they mostly take on values between 0.4 and 2. The ratios of $Im\mathcal{A}$, however, tend to fall to values below 1 or even below 0.1 with increasing periods up to 500s. They are almost constant between 500s - 1500s, and diverge at the longest periods. Most ratios of the $Re\mathcal{B}$

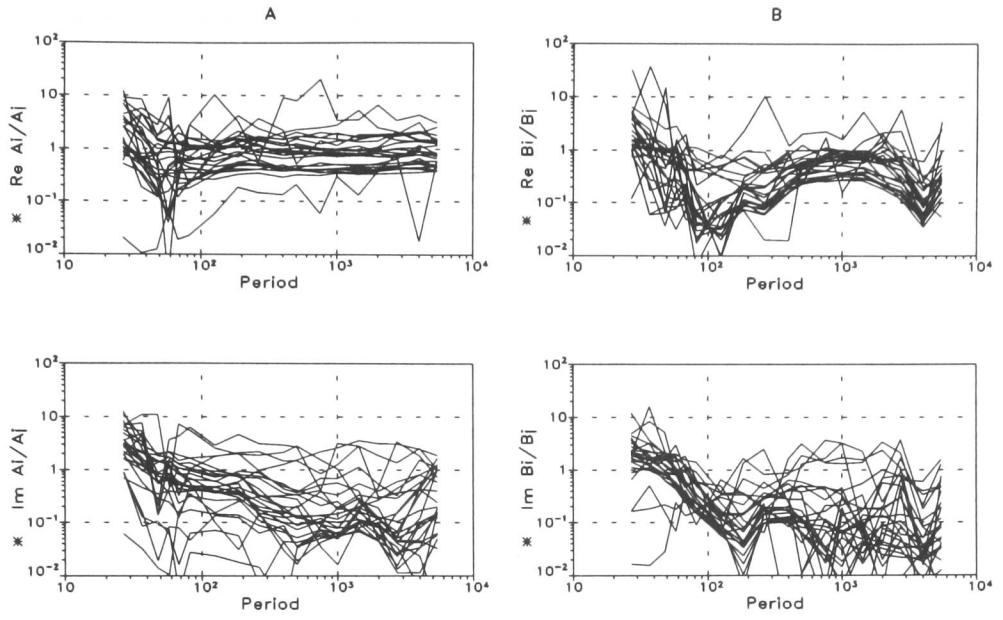

Figure 22: *The Iapetus Dataset:*
Ratios of the local magnetic response functions of all sites of area (b) Alston Block & Stainmore Trough (index j) with respect to site HM *(index i), Rotation:* 0° N. *At periods 400s - 1500s, the ratios of the real parts of both components have a constant value, suggesting distortion in this period range.*

components drop to values around 0.05 at periods 70s - 200s, then rise to run in parallel and constant curves in the range 500s - 1500s, with values between 0.25 and 1. In this range, they behave very similar to the ratios of the $\mathcal{A}$ components. At the longest periods, the $Re\mathcal{B}$ ratios drop again to smaller values. The ratios of $Im\mathcal{B}$ descend steeply at short periods up to 200s and diverge for longer periods.

From the uniform ratios of the $Re\mathcal{A}$ component alone, one can not derive distinct limits of the period range of distortion. But the constancy of the ratios of its imaginary parts and those of the $Re\mathcal{B}$ component clearly indicate that galvanic effects are occurring in the restricted range 400s - 1500s. In this range, the ratios of the real parts of both components are equally constant, run in parallel and have similar amplitudes. The resulting constrains agree with assumptions on the limits of the distortion range made in the previous two sections. It is therefore representative for all sites south of the Southern Upland Fault.

5.3 Hypothetical event analysis

The theoretical analysis of the vertical magnetic response function in chapter 4 showed that in the case of galvanic distortion, the phase content of the predicted values of the vertical magnetic field B_z^p, obtained by applying hypothetical event analysis, will be that of the regional impedances. Assuming quasi-uniform fields over the area under investigation, this information should be retrievable when the predicted values of all GDS stations are visualized in the complex plane (Argand diagram).

For a regional one-dimensional conductivity distribution, the predicted vertical fields will plot along one line indicating the regional impedance phase, regardless of the polarisation of the hypothetical magnetic field. For a regional two-dimensional distribution, the data points will fall on the phase lines of the principal impedances, provided that the polarisation of the hypothetical field parallels the regional strike direction or is perpendicular to it. If a spatially non-varying regional vertical field component is present in the dataset, one of the phase lines might not pass through the origin. In this case, B_z^o is added to each point in the complex plane, shifting each one by the same amount. The regional strike direction can be found by gradually varying the polarisation angle until this offset is eliminated.

The following sections describe the investigation of the magnetic response functions of the Iapetus dataset with respect to these features. The complete dataset and several subsets will be examined in order to assess the common information content, i.e. regional impedance phases and regional strike direction.

5.3.1 All sites at 4 chosen periods

To start with, fig. 23 (a - d) shows the predicted vertical fields of all sites at two perpendicular polarisations at the same four periods that were used in the induction arrow maps (70s, 260s, 750s, 2700s; see figures 11 - 14). In the left column, the hypothetical horizontal magnetic field is polarised northwards (0°), whereas the values of the right column were calculated assuming an eastward directed field (90°). At these two polarisations the predicted values correspond to the $\mathcal{A}$ and $\mathcal{B}$ components of the magnetic response function, if the hypothetical magnetic field has unit amplitude (1 nT). All diagrams are repeated in appendix B with site names (fig. 65 - 70) to identify the outliers.

As mentioned, we would expect the datapoints to arrange along lines. However, this is not always obvious. Instead, the data scatter strongly, forming clouds of points which in places do have certain orientations. Generally, the clouds seem more elongated in the left column of fig. 23, while in the right column the predicted values are rather focused on patches close to the origin. For northward polarisation, at periods 260s (b) and 750s (c), data points with real parts less than ca. 0.1 quite clearly scatter around a line with a positive slope of ca. 15° - 20°. The conceived line does not pass through the origin, but is slightly shifted towards the upper left quadrant. A vague linear trend is also visible at shorter periods (a); here it has no offset. Although most predicted vertical fields are smaller for eastward than for northward polarisation, linear trends can also be recognized at 260s and at 750s. The gradient at 750s is steeper, but less focused.

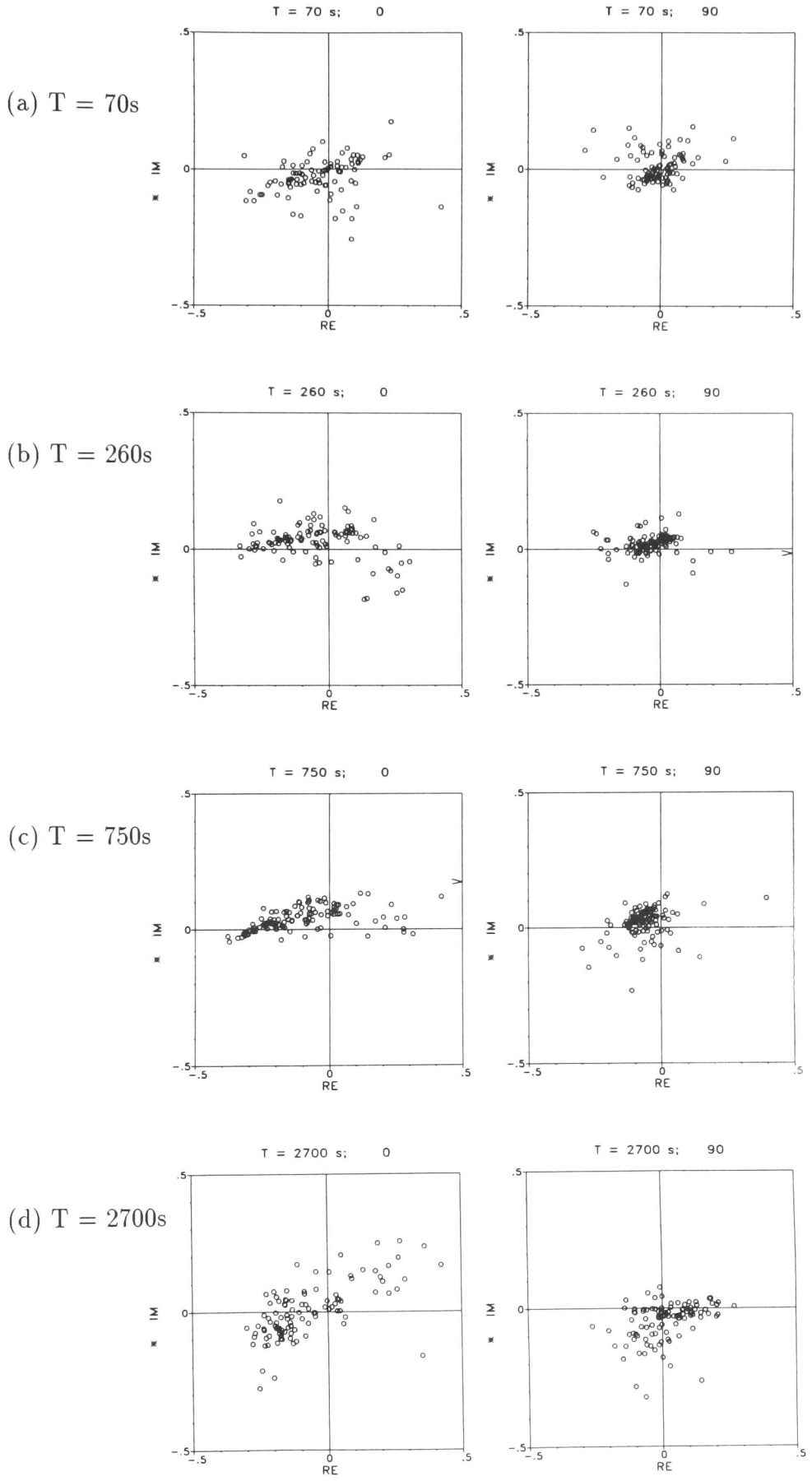

Figure 23: *The Iapetus Dataset: Hypothetical event analysis, all sites, 4 periods. Argand diagrams of predicted values $B^p_{z_i}$ of period bands 14, 10, 7, 3, estimated for northward polarisation ($\vartheta^\star = 0°$, left column) and eastward polarisation ($\vartheta^\star = 90°$, right column) of the hypothetical horizontal magnetic field. For northward polarisation the points plot roughly along lines indicating the regional impedance phase (except for the longest periods).*

At all four periods, the outliers (i.e. data points that scatter away from those linear trends), are limited to a fairly restricted area in the complex plane (see figures 65 - 68 in appendix B) . Most of them belong to the same geographic region: the affiliated sites are situated north of the Southern Uplands (BI, DZ, EB, EL, FT, FY, KN, KS, PB, PN, PR, SN, SO, SY; see fig. 10). At 70s the outliers are restricted mainly to the Midland Valley area, while at longer periods, more sites further north are involved. Some single outliers belong to sites south of the Alston Block (MA, PM, WT, WY), a few are scattered more widely over the remaining region.

5.3.2 All sites at period T = 750s

The next step of the data analysis is to examine the period range where distortion is suspected. In section 5.2, the curves of the components $\mathcal{A}$ and $\mathcal{B}$ of the magnetic response functions were found to run in parallel at periods < 2000s, particularly in the range 400s - 2000s. In the distortion test (section 5.2.3, fig. 22), the ratios of the *local* response functions of different sites are fairly constant over approximately the same period range. This behaviour of the data was attributed to anomalous magnetic fields caused by local channelling of regional currents in shallow and mid-crustal conductive structures. Therefore, and because the phase line in the Argand diagram is most distinct, I chose 750s as a representative period of the distortion range.

Fig. 24 shows the results of hypothetical event analysis with respect to varying polarisation angles of the horizontal magnetic field. The predicted vertical fields of all sites are plotted for polarisations 0°, 30°, 60° and 90° from top to bottom (a - d) in the left column and at perpendicular polarisations (90°, 120°, 150°, 180°) in the right column. Again, some of the diagrams (fig. 24 b,c) are repeated with station identifiers in appendix B (fig. 69 & 70)

With gradually changing polarisation angles, the data points move on elliptical curves in the complex plane, always forming one coherent cloud of points. This cloud stretches to an elongated form along a conceived line at most polarisations, and wanders diagonally from the upper left quadrant through the origin to the lower right quadrant. The polarisation, at which the imagined line actually passes through the origin, seems to be at $\vartheta^* = 120°$. At this polarisation azimuth, most points plot densely on a short line with a gradient of ca. 10°. At 90°, just before passing the origin, the cloud contracts to a small, almost round patch. The linear distribution seems to be best at north/southward polarisation. The variable form of the cloud indicates that the common information content originates from a regional structure that is at least two-dimensional. In the case of a regional 1D earth, the data would always plot along the same phase line, regardless of the polarisation azimuth.

The fact that the offset of the line from the origin can be eliminated by choosing an appropriate polarisation angle, strongly suggests that a regional vertical component B_z^o is present in the data. As a consequence, the azimuth range where the line passes through the origin and the range perpendicular to that may be interpreted in terms of a regional strike direction (section 4.2.1, 2D) and thus demands more detailed investigation. The gradients of the line at these polarisations provide the phase angles of the two principal impedances.

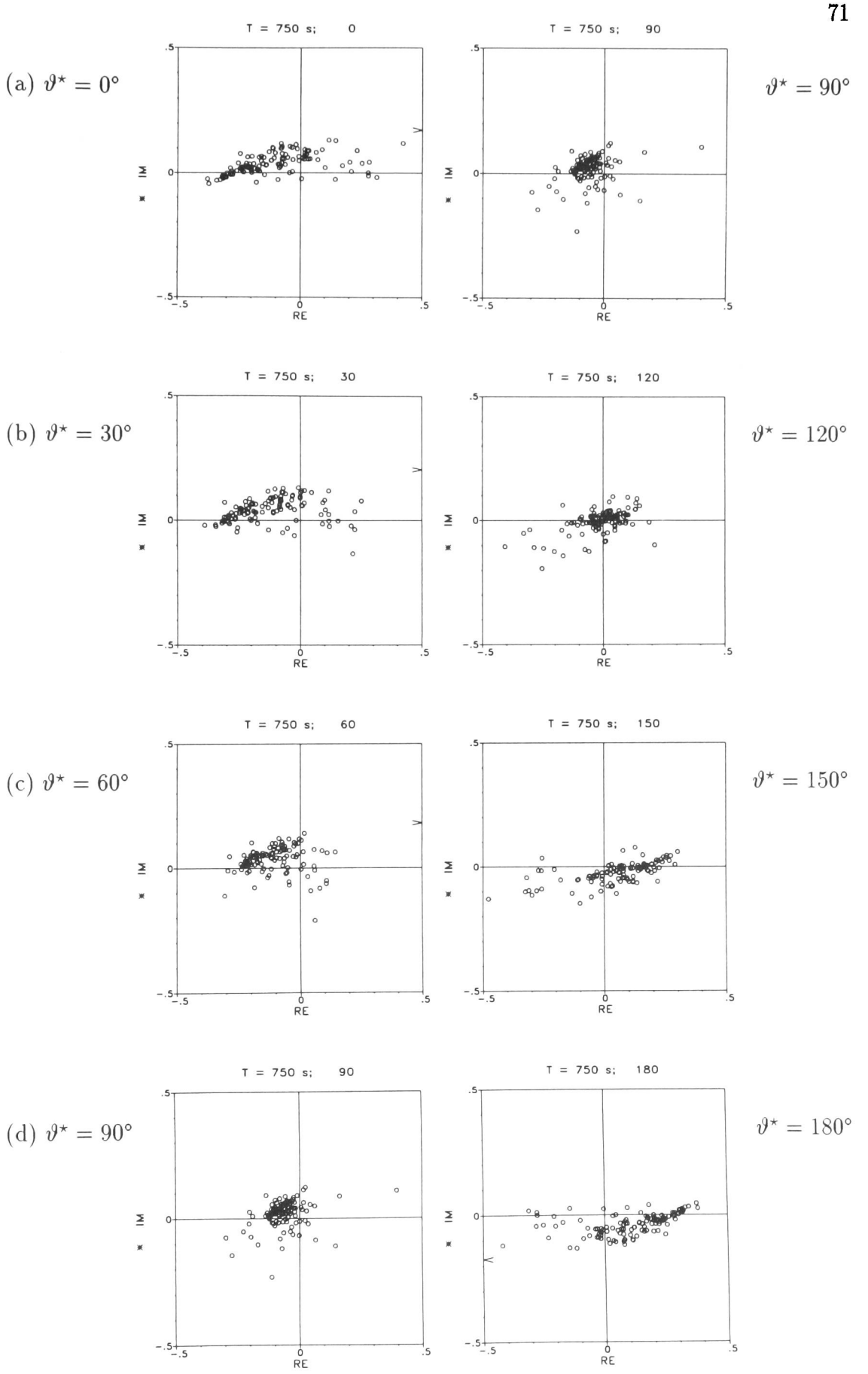

Figure 24: *The Iapetus Dataset: Hypothetical event analysis, all sites, $T = 750s$. Argand diagrams of predicted values $B^p_{z_i}$ that are estimated for polarisations $\vartheta^\star = 0°, 30°, 60°, 90°$ (left column) and perpendicular (right column) to these. The cloud of points passes through the origin at 120°.*

After this visual inspection, it is necessary to use a mathematical method in order to determine the properties of the phase lines in the Argand diagrams more objectively. Obviously, the fitting of regression lines by the least squares method requires a normal linear distribution of the data points. In order to weaken the influence of outliers, robust methods (e.g. Egbert, 1986; Jones et al. 1989; Junge, 1994b) have increasingly been used for all kinds of data processing procedures. However, in our case, most of the points that do not support the general trend do not scatter totally away as individuals, but form a fairly coherent cluster of points in the vicinity of the main distribution. Close inspection of these outliers shows that they belong to sites located in the northern part of the array, where distortion effects are probably produced by differently scaled structures. We can therefore improve the approximation of the phase lines in our diagrams, if we investigate subsets of data according to their geographic locations, rather than applying robust techniques.

5.3.3 Reduced dataset at period T = 750s

In order to improve the linearity of the data distribution and with it the fit of the phase line inferred from the majority of data, the northernmost sites were omitted and hypothetical event analysis was applied to the reduced dataset. The predicted vertical magnetic fields of the remaining sites (all located south of the Southern Upland Fault) are shown in fig. 25. The two diagrams at the top (fig. 25 a) correspond to north- and eastward polarisations, those at the bottom (fig. 25 b) show the data with a minimum offset at polarisation azimuth 123° and perpendicular, at 33°.

Each graph contains the two regression lines computed for the x- and y - distribution of the data (see section 4.2.2). In this notation, x and y refer to real (Re) and imaginary (Im) parts, respectively. The solid line is calculated for the distribution of y - values ($y_i = x_i\, m_y + c_y$), whereas the dashed line is determined for the distribution of x - values ($x_i = y_i\, m_x + c_x$). The gradients m_x and m_y determine the phase angles of the regional impedance. The intercepts (or offsets) c_x and c_y represent the shift of the lines along the real and imaginary axis, respectively. Their crossing point marks the centre of gravity of the data distribution.

The first impression is that the reduced dataset is better suited for the fitting procedure than the complete dataset. As expected, the remaining 95 data points (out of 113) are less widely scattered when compared with the diagrams in fig. 24 (all sites). At northward polarisation (0°), the y - line has a slope of 13.8° ± 1.4°. Compared to the x - line with a gradient of 25.5° ± 11.9°, the y - line represents the better fit. At polarisation azimuth 33°, the y - line has a slope of 14.6° ± 1.6°.

The two regression lines differ in accordance with the degree of linearity of the data. In our case, the x - lines (dashed) have steeper gradients than the y - lines (solid) and their offsets are larger. The only objective criterion to choose between the x- and y - lines is the standard deviation. The regression line properties for both lines are shown in fig. 26 a-d for data distributions at varying polarisation azimuths in the range 0°... 180° (estimated at steps of 5°). The remaining two quadrants 180°... 360° provide equivalent results. From top to bottom the diagrams of fig. 26 show (a) the linear correlation coefficients r and r_{max}, (b) the standard deviations of the gradients S_x and S_y, (c) the offsets c_x and c_y, and (d) the phase angles inferred from the gradients of the two lines, m_x and m_y.

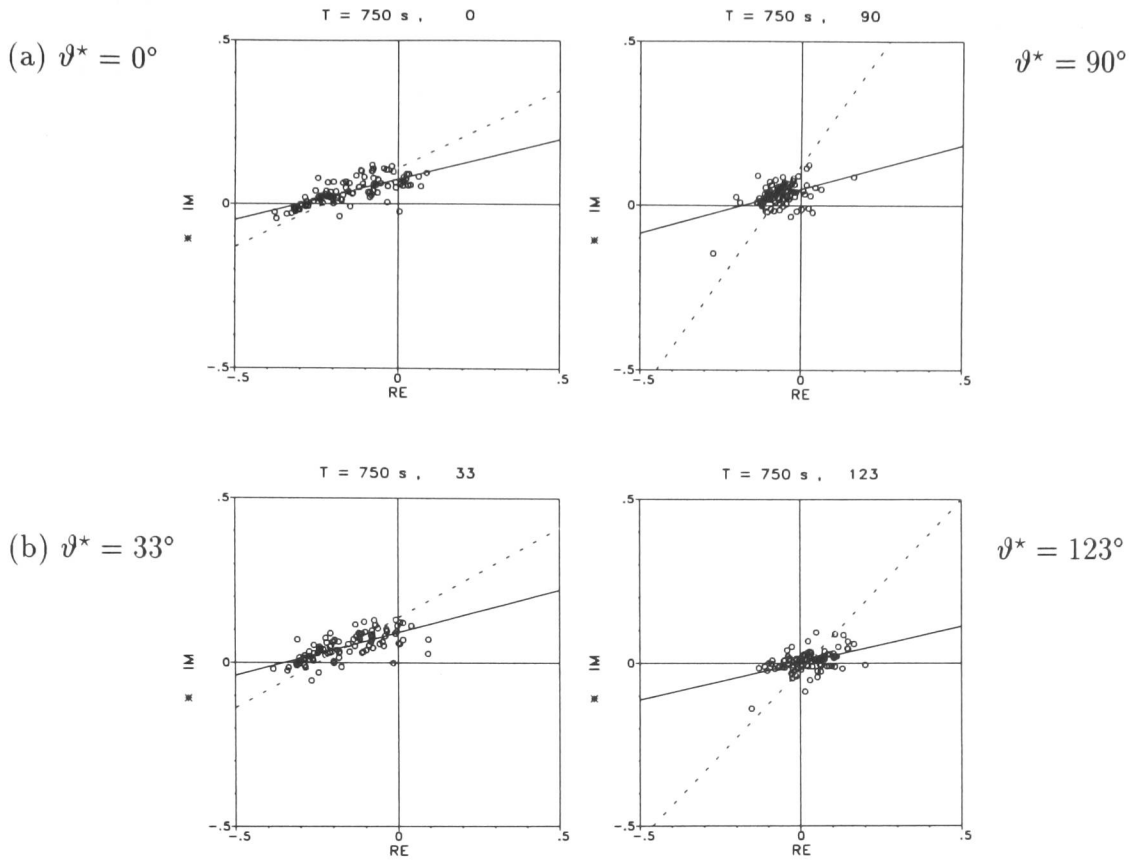

Figure 25: *The Iapetus Dataset: Hypothetical event analysis, reduced dataset (95 sites), T = 750s. All sites are located south of the Southern Upland Fault. Argand diagrams of predicted values $B^p_{z_i}$ at north- and eastward polarisations (a), and at polarisations of minimum offset, 123°, and perpendicular to it 33° (b). Regression lines: dashed = x - line; solid = y - line. The linearity of the data distribution is improved compared to that of the original dataset (113 sites).*

The correlation coefficient r is a measure of the degree of linearity of the data: perfect linear correlation yields $r = 1$, very poor correlation yields $r = 0$. The estimation of r is highly dependent on the orientation of the cloud of points in the coordinate system. Therefore, a more objective *maximum* value r_{max} was computed by rotating the data through the quadrants of the complex plane (see section 4.2.2). For the reduced dataset, both coefficients (fig. 26 a) run in almost parallel curves and indicate high linear correlation at most polarisations, except for a minimum in the range around 100°. At azimuth 120°, at which the cloud of points passes the origin, the more significant r_{max} has recovered to values > 0.7.

The standard deviation of the gradient of the x - line shows values around 10° (fig. 26 b). The y - line deviation takes small values around 2° - 3°. Characteristically, the y - line has its biggest deviations at polarisations around 100° (lowest r). In this range, the x - line gradient is determined best, although its minimum is still more than three times as large as the maximum deviation of the y - line gradient.

Generally, the slope of the y - line varies only little, between 12° and 15°, over the whole azimuth range (fig. 26 d), whereas the gradient curve of the x - line shows fairly strong variations. The x - line is steepest at polarisations of around 95°. It

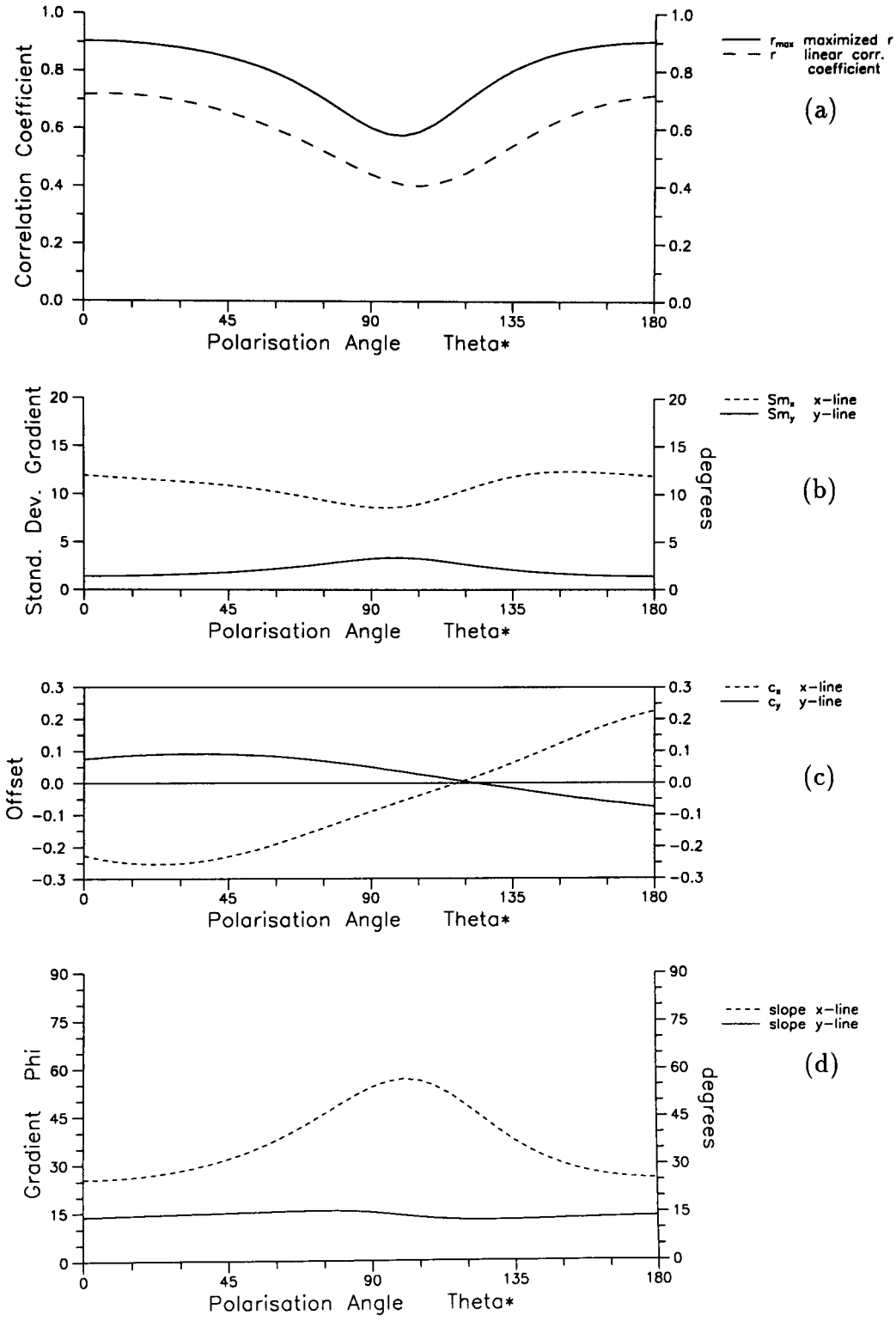

Figure 26: *The Iapetus Dataset: Hypothetical event analysis, reduced dataset (95 sites), T = 750s, polarisations:* 0°... 180°. *Regression line parameters:*
a) Linear correlation coefficients $|r|$ *(dashed line) and* $|r_{max}|$ *(solid line);*
b) Standard deviations of the gradients of the x - line (dashed) and y - line (solid).
c) Intercepts of the x - line (dashed) and y - line (solid);
d) Phase angles inferred from the gradients of the x - line (dashed) and y - line (solid). The phase angles inferred from the y - line are ca. 15° *at all polarisations.*

coincides with the position of the minimum of the linear correlation coefficient. The less dramatic fluctuations of the characteristics of the y - line and its lower errors at all polarisations make this regression line the better representative of the trend observed in the dataset.

The offset of the y - regression line (fig. 26 c) is distinctly smaller than that of the x - line. The polarisation, for which the y - line passes through the origin, is slightly higher than for the complete dataset: 123° compared to 120° before. This polarisation azimuth is assumed to parallel the regional strike direction. Here, the line indicates a phase angle of $12.6° \pm 2.5°$, thus representing one of the two principal impedance phases. The offset is at a maximum at polarisation 35° (i.e. perpendicular to the minimum offset) with a phase angle of $14.7° \pm 1.7°$ for the second impedance.

The presence of distinct maximum and minimum offsets of the phase lines at perpendicular polarisations of the hypothetical magnetic field reinforces the earlier conclusion, that the dataset contains information on a regional two-dimensional structure. Since the results of the reduced dataset are based on a considerably improved linear distribution, the strike direction of the regional structure has to be amended slightly towards 125°. The impedance phase angles at both polarisations are very similar, overlapping within their confidence limits at an angle of ca. 13.5°.

The offsets of the regression lines of both the complete and the reduced datasets suggest that a regional vertical magnetic component B_z^o is superimposed on the local anomalous component B_z^ℓ. Since the dataset covers such a large region, it is likely that this regional component is not laterally uniform over the whole area. In particular, data from sites situated north of the Southern Uplands in the complete dataset do not follow the expected pattern of maximum and minimum values. It is interesting, though, that their inclusion does not influence the estimation of the regression line (y - line) at 120°/123° substantially. The gradient of $12.6° \pm 2.5°$ for the reduced dataset compares well to $16.1° \pm 2.0°$ for the complete dataset in fig. 27 (see also fig. 72, appendix C). In order to minimize the possible effects of a non-uniform regional vertical component at sites south of the Southern Upland Fault, in the next step an even smaller dataset, where even smaller lateral variations of the regional component at long periods can be expected, will be investigated.

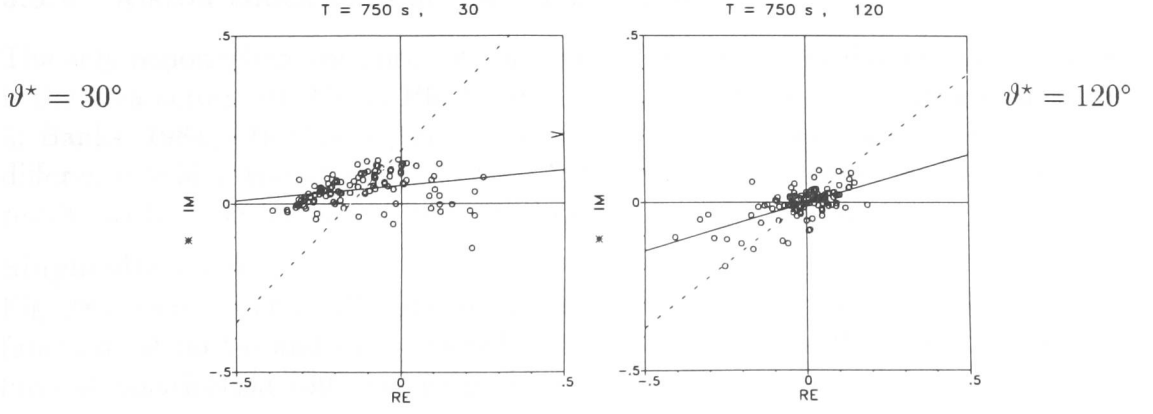

Figure 27: *The Iapetus Dataset: Hypothetical event analysis, all sites, T = 750s. Argand diagrams of predicted values $B_{z_i}^p$ at polarisations* 30° *and* 120°. *The y - line (solid) gradients are:* $5.1° \pm 1.6°$ *at* 30° *and* $16.1° \pm 2.0°$ *at* 120°.

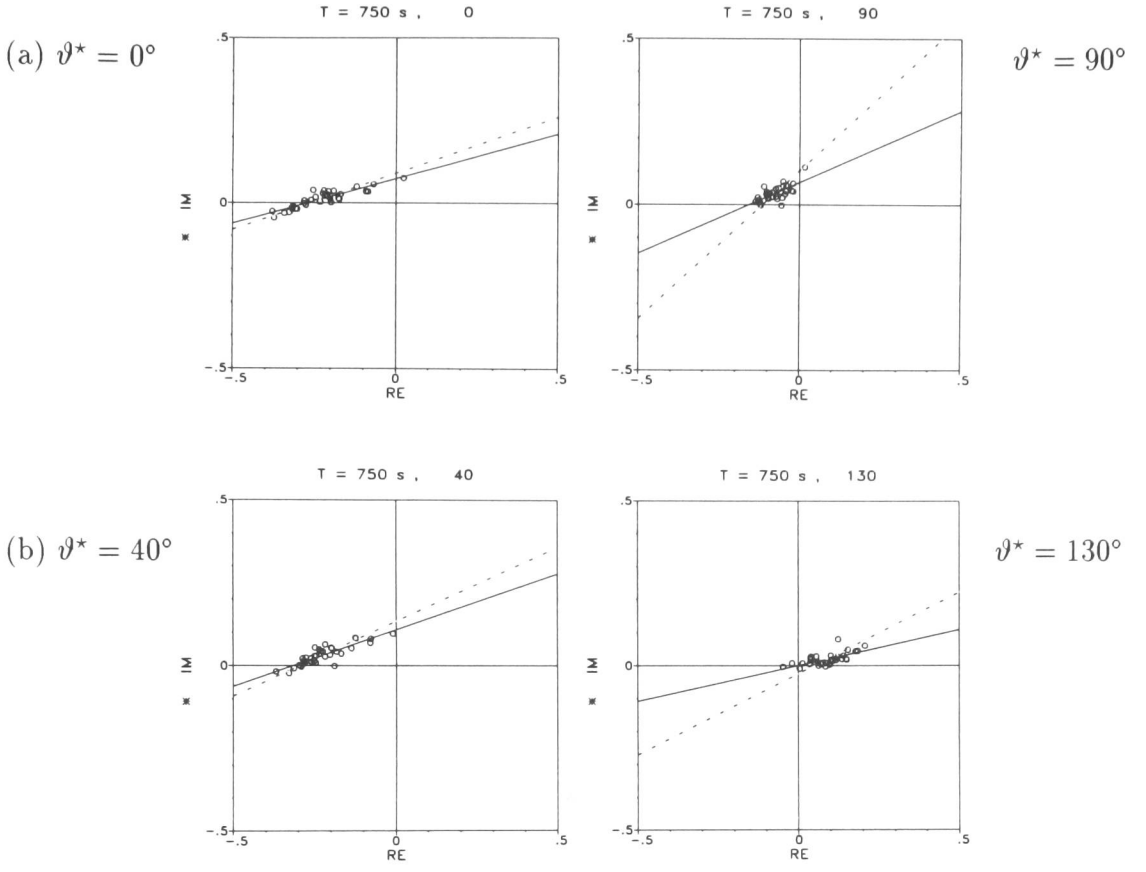

Figure 28: *The Iapetus Dataset: Hypothetical event analysis, Alston Block dataset (35 sites), T = 750s. The sites are located directly south of the Northumberland Trough. Argand diagrams of predicted values* $B^p_{z_i}$ *at north- and eastward polarisations (a), and at polarisations of minimum offset,* 130°, *and perpendicular to it, at* 40° *(b). The azimuth of minimum offset yields the regional strike direction. The fitting of the regression lines has improved considerably compared to the larger datasets (113 sites and 95 sites). Regression lines: dashed = x - line; solid = y - line.*

5.3.4 Alston Block data at period T = 750s

The only region where the horizontal magnetic field was assessed to be quasi-uniform is the area across the Alston Block with less than 20 % lateral variations (Beamish & Banks, 1984). In this region, we have *local* response functions (estimated from difference fields) available at 35 sites. This allows a comparison of the single site results with those calculated from the *local* response functions.

Single site data

Fig. 28 (a) shows the predicted vertical fields calculated from the single site response functions at north- and eastward polarisations. Diagrams with minimum offset (y-line) at polarisation 130° and perpendicular, at 40°, are shown in fig. 28 (b). The regression line characteristics are shown in fig. 73 in appendix C. The phase line indicated by the data points in fig. 28 is clearer than in the larger datasets, especially in the azimuth range, where the line passes through the origin. Due to the improved linearity of the data distribution the x- and y - lines are in better agreement.

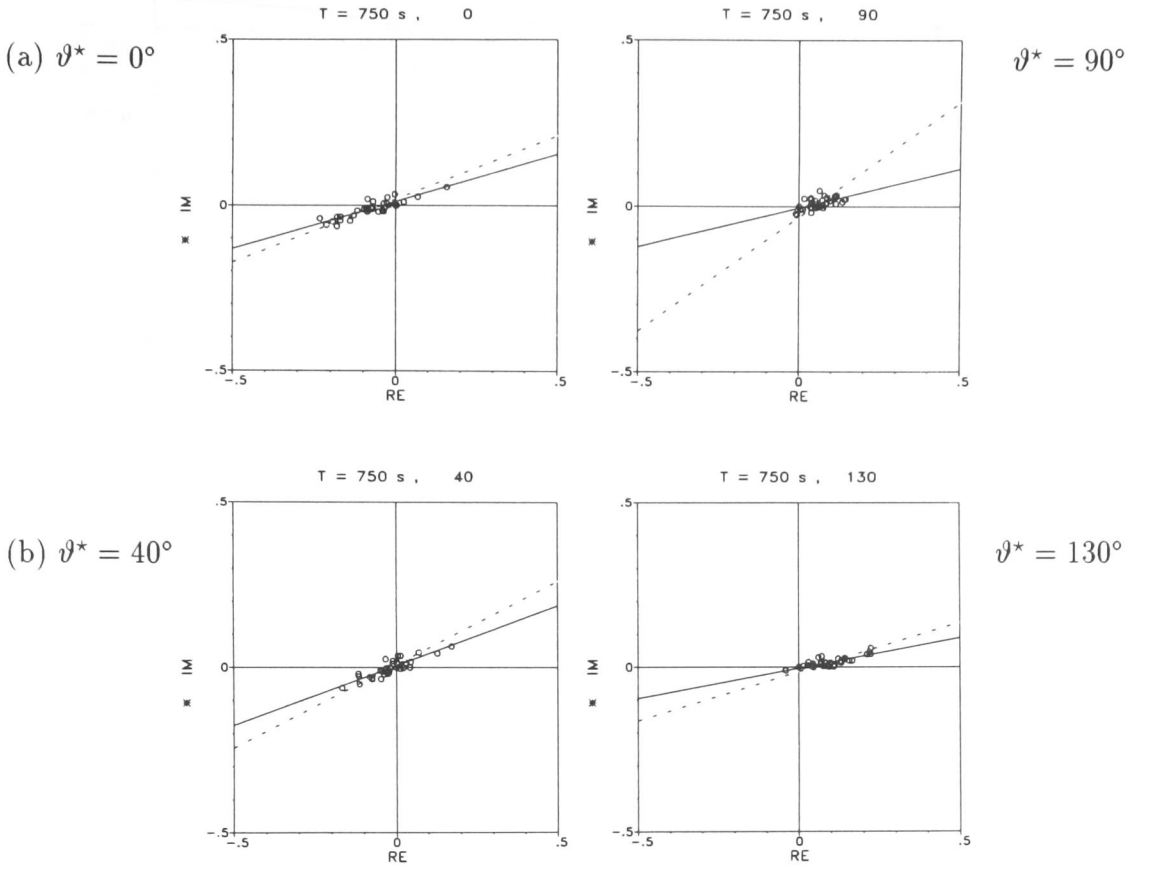

Figure 29: *The Iapetus Dataset: Hypothetical event analysis, Alston Block dataset (35 sites),* **local** *response functions from difference fields, T = 750s.*
Argand diagrams of predicted values $B^p_{z_i}$ at north- and eastward polarisations (a), and at 40° *and* 130° *(b). Regression lines: dashed = x - line; solid = y - line. Since the contribution of the regional vertical component is minimized for the difference field data, all y - lines pass through the origin, and the impedance phases can be determined best.*

Generally, the slope of the y - line, i.e. the impedance phase, takes values between 12° - 24°, which is a stronger variation compared to the flat phase curve of the 95-sites dataset (fig. 26 d). The impedance phases inferred from the regression line gradients (y - lines) for this Alston Block dataset are $18.7° \pm 1.9°$ for Z_E and $12.2° \pm 2.4°$ for Z_B. The phase of Z_B is remarkably similar to the one determined from the 95 - sites dataset ($12.6° \pm 2.5°$), the phase of Z_E is slightly increased ($14.6° \pm 1.6°$, before). The most accurate phase information, however, will result from the difference field data discussed in the following section. The strike direction indicated by the polarisation azimuth of zero-offset of the single site data is 130°.

Difference field data

The predicted values calculated from the *local* magnetic response functions (i.e. difference field response functions) at the same 35 sites are presented in fig. 29. The same polarisation angles were chosen as for the previous diagrams with the single site results. The properties of the regression lines are shown in fig. 30. Since the *local* response functions were obtained by relating the difference of total and reference

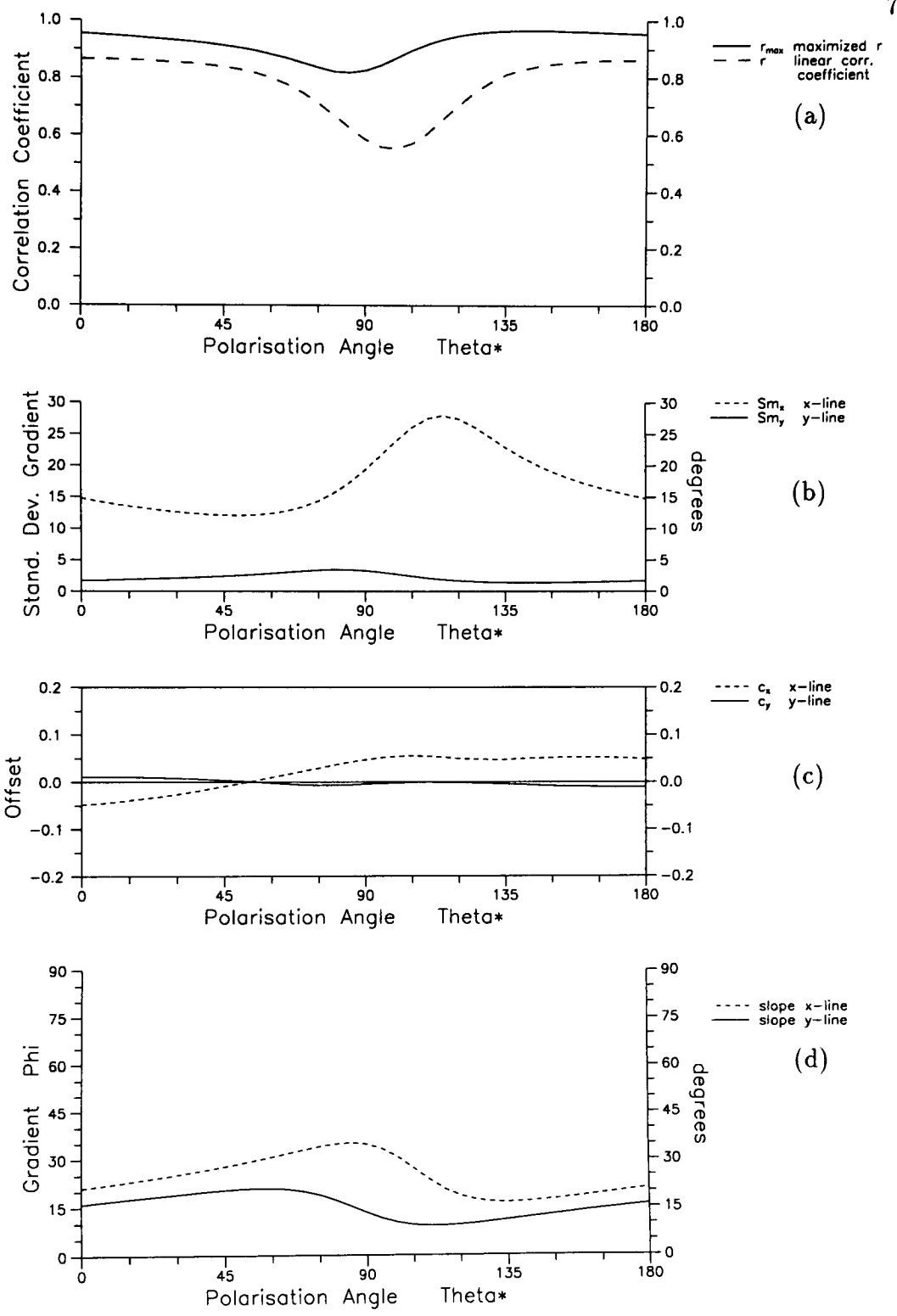

Figure 30: *The Iapetus Dataset: Hypothetical event analysis, Alston Block dataset (35 sites),* **local** *response functions from difference fields, T = 750s, polarisations:* 0°... 180°. *Regression line parameters:*
a) linear correlation coefficients |r| (dashed) and $|r_{max}|$ (solid line);
b) standard deviations of the gradients of the x - line (dashed) and y - line (solid).
c) intercepts of the x - line (dashed) and y - line (solid);
d) phase angles inferred from the gradients of the x - line (dashed) and y - line (solid). Linear correlation is very good throughout the polarisation range. The phase angles (gradients) of the y - line indicate a smaller phase of ca. 10° *at polarisation azimuth* 125° *than at perpendicular polarisation, where the phase angle is ca.* 20°.

vertical magnetic field at each site to the horizontal magnetic field at the common reference site, any contribution of the regional vertical magnetic field should be eliminated. As a consequence, the offset of the regression lines should be reduced considerably.

It is clear from the Argand diagrams that indeed this has been achieved, although the lines still seem to be slightly off-set at polarisations 0° and 40°. But from fig. 30 (c) it becomes obvious that these are only very small variations of only ca. ±0.01 around the origin. They originate probably from contributions of the local anomalous vertical field at the reference site itself. However this slight offset is well within an acceptable limit when compared to the high values of up to 0.1 for the single site data (see fig. 73 c). The general correlation of the data (fig. 29 a) is very good, with values of r_{max} mostly at 0.96, and a minimum at 0.82.

The slopes of the y - regression lines are: 16.0° ± 1.7° at northward polarisation, and 13.3° ± 3.3° at eastward polarisation; 19.9° ± 2.3° at polarisation 40°, and 10.5° ± 1.5° at polarisation 130°. Generally, the variation range of the gradients is slightly lower (9° - 21°, see fig. 30 d) than for the single site regression lines of the same sites (12° - 24°, see fig. 73 d). However, the impedance phase values show very similar tendencies at polarisation azimuths 130° (minimum offset) and 40° (perpendicular): 10° - 12° for Z_B, and 19° - 20° for (Z_E), respectively. Since the contributions of the regional vertical field are virtually eliminated, the gradients of this dataset provide the most reliable values for the regional impedance phase angles.

Because the phase difference between the two impedances is only very small, it cannot be resolved within the larger datasets, where the points scatter more widely. Even more so, since the outliers are clearly not distributed randomly. As a consequence, data points that are either extremely noisy or contain different electromagnetic information due to their geographic location will bias the least squares estimation of the regression lines, i.e. the phase angles. The slopes determined from the 95-sites dataset, for example, showed a coincidence of both impedance phase angles at ca. 13.5°, although the general trend at polarisation 33° seems to suggest a slightly steeper gradient. However, if we omit only a further 4 sites from this dataset, namely ED, HG, LO, TI, which seem to be the most extreme outliers, the slope of the y - line increases to 17.7° ± 1.5° at azimuth 33° (see fig. 31). The gradient of minimum offset at polarisation 123°, on the other hand, is slightly decreased to 11.7° ± 2.6°.

These results obtained from 91 sites (out of originally 113) are very close to the impedance phases determined for the Alston Block difference field data of 35 sites. They confirm the observation, that the two phase angles corresponding to the two principal impedances are indeed slightly different. The agreement of the results of the single site and difference field datasets fits the assumption that the offset observed for the single site data is indeed caused by the the regional vertical component and can be corrected for by hypothetical event analysis.

Regional response function component $\mathcal{B}^o$:

From the offset of each predicted value in the complex plane, an average value for the regional vertical component $\mathcal{B}^o$ at T = 750s can be determined. One method is, to

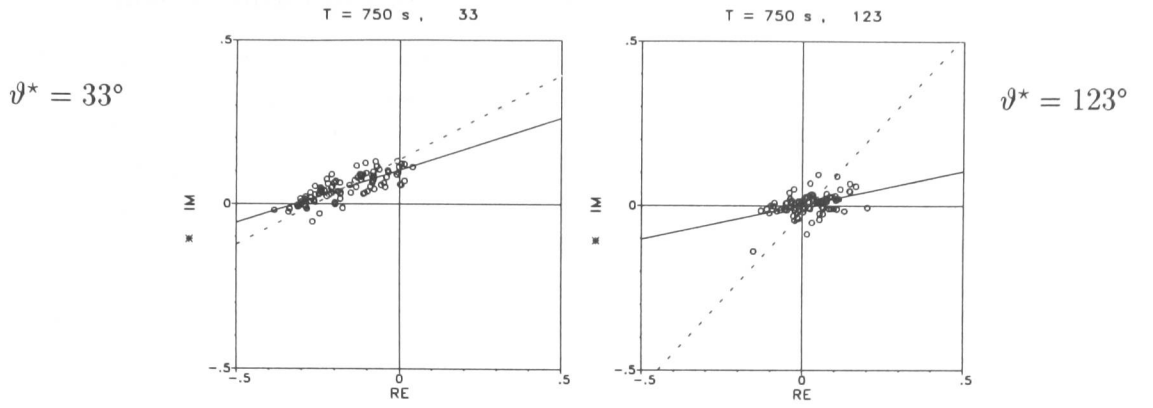

Figure 31: *The Iapetus Dataset: Hypothetical event analysis, 91 sites , T = 750s. All sites are located south of the Southern Upland Fault.*
Argand diagrams of predicted values $B^p_{z_i}$ at north- and eastward polarisations (a), and at polarisations of minimum offset, 123°, *and perpendicular to it* 33° *(b). Different from the 95-sites dataset, the gradients of the y - lines at polarisations* 33° *and* 123°, *i.e. the regional impedance phases, differ slightly (by ca.* 6°*).*

estimate the differences between the predicted values of single site response functions and those of the *local* response functions at polarisation angle 40°, i.e. perpendicular to the azimuth, at which the phase line (single sites) passes through the origin:

$$\mathcal{B}^o = \frac{1}{N}\sum_{i-1}^{N} B^p_z(40°) - B^{lp}_z(40°) \tag{132}$$

The average mean values for real and imaginary parts and their standard deviations are:

$$\mathcal{B}^o = (-0.2120,\, 0.0322) \pm (0.0074,\, 0.0056) \tag{133}$$

The other approach is is to calculate the differences of the predicted values of single site response functions at polarisations 130° and 40°, i.e. at the polarisation azimuths where the phase line (single sites) passes the origin and perpendicular to it:

$$\mathcal{B}^o = \frac{1}{N}\sum_{i-1}^{N} B^p_z(40°) - B^p_z(130°) \tag{134}$$

Since the regression lines at both polarisations have slightly different gradients, the average value of these differences will not be as reliable as the difference estimated above:

$$\mathcal{B}^o = (-0.3192,\, 0.0112) \pm (0.2320,\, 0.0626) \tag{135}$$

Although the latter value has larger errors, it agrees roughly with the first value. This similarity shows that the elimination of the regional vertical component by applying a horizontal magnetic field polarised in regional strike direction is as effective as calculating the difference field response function by common reference processing.

5.3.5 Investigation of the whole period range

In the previous sections I concentrated mainly on the analysis of the dataset at one period (750s). It is now interesting to investigate, whether the observations made for that particular period can be generalized to the whole period range, where distortion is assumed. The distributions of the predicted fields from hypothetical event analysis at 4 chosen periods have already been presented at the beginning of section 5.3 in the Argand diagrams of fig. 23 (a - d). Although the data scatter in different ways, phase lines are conceivable at most periods at north- and eastward polarisations (if only vaguely at T = 70s). At T = 750s, the common regional strike and impedance phases could be determined clearest from predicted vertical fields of the Alston Block dataset of single site and difference field data, respectively. Therefore, the following multi-frequency investigations are focused on these sites. Corresponding diagrams for a larger area including sites south of the Southern Upland Fault are very similar and are shown for comparison in appendix D.

The contour maps of fig. 32 - 34 show the variations of the maximized linear correlation coefficient r_{max}, the slope angle (i.e. impedance phases) of the y - regression lines and those of their offset throughout the period range 30s - 5500s. The polarisation azimuths of the hypothetical horizontal magnetic field vary in the range 0°... 180°. The period axes of the diagrams are scaled as log10(T); a conversion table is given in the appendix (A.5). Due to the very low linear correlation at the longest period at 5500s (band 1, $r_{max} \approx 0.1$), results in this upper period range should not be given too much attention; the same is true for the shortest period at 30s.

(a) Alston Block: single site response functions

The datasets used for the multi-frequency investigations contain 32 stations; only a few sites had to be ruled out for periods T < 500s (listed in appendix A.6.1). Fig. 32 shows the variations of the linear correlation coefficient, while fig. 33 (a,b) show the corresponding variations of offset and phase angles, respectively.

The linear correlation coefficient r_{max} (fig. 32) in the wide range 70s - 1500s follows the pattern already found for period 750s. The minimum occurs generally at polarisation angles in the narrow range of 90° - 105°, whereas the correlation is very good (> 0.95) at the edges at < 45°, and > 135°. At periods exceeding 1000s, the minimum expands towards smaller polarisation azimuths (upper left corner). However, the most important feature is the uniform behaviour of the linear correlation coefficient between 250 s - 1000s, not surprisingly in the same range where galvanic distortion is suspected (400s - 1000s, sections 5.2.1 and 5.2.2).

The offset of the regression line (fig. 33 a) shows an equally constant pattern, but over a more restricted period range. The zero contour line, where the regression line passes through the origin, occurs consistently at polarisation angles between 125° – 135° in the period range 400s - 1500s. The azimuth range of maximum offset (≈ 0.1) at around 45°, i.e. approximately perpendicular to the position of the offset minimum. The contribution of the regional vertical magnetic component, which causes this offset, seems to be stable over this period range. This implies that both the distortion process and the contributions from regional induction contained in the distorted response functions are steady over this period range, and over the area covered by these datasets. At higher and lower periods, the zero-offset line runs fast

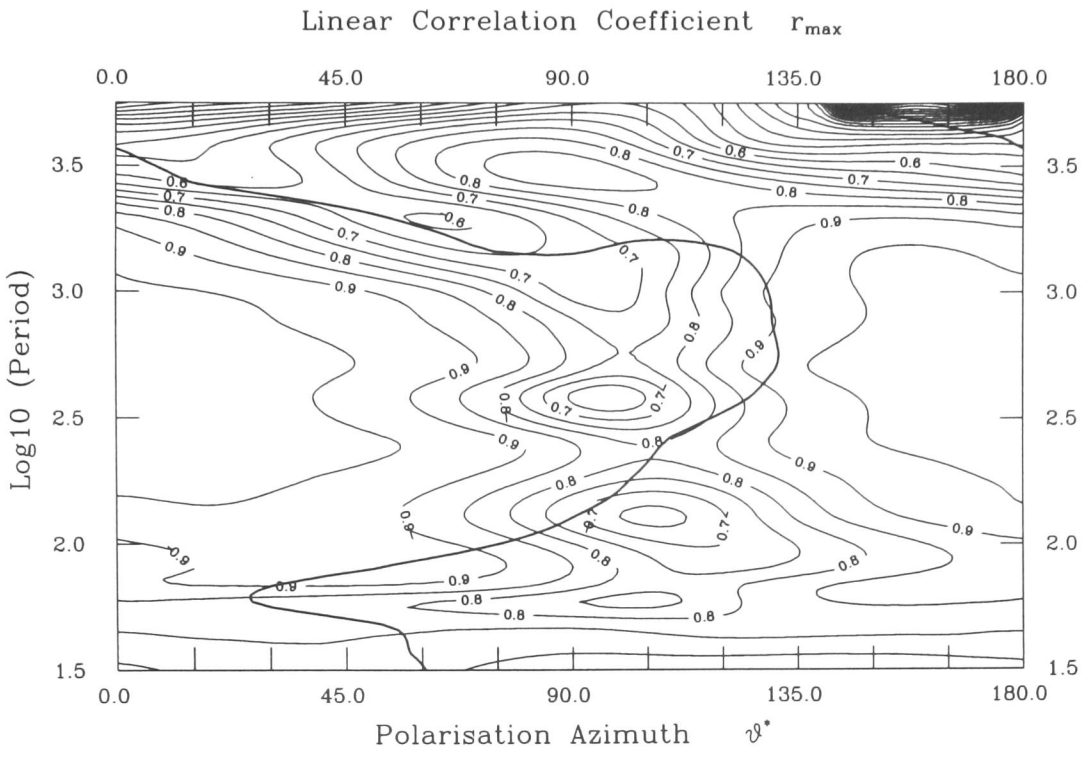

Figure 32: *The Iapetus Dataset: Hypothetical event analysis, all periods, polarisations:* $0° - 180°$. *Contour plot of maximized linear correlation coefficient* $|r_{max}|$: *Alston Block datasets (32 sites).*
The thick line marks the positions of the zero-offset line taken from the associated intercept map (fig. 33 a). The correlation minimum occurs at polarisations 90° - 100° *in the period range < 1000s. At longer periods, the minimum stretches towards smaller polarisation angles. The zero-offset line runs on the right flank of the correlation minimum at periods 400s - 1000s.*
Note that in this and the following maps the period increases from the bottom to the top of each diagram (contrary to the usual convention).

towards smaller polarisation angles.

At periods T < 80s the minimum/maximum pattern of the offset has vanished completely. Interestingly, at long periods (T > 2000s) the maximum values decrease fast and the position of minimum and maximum values are reversed: the zero line runs now towards the upper left corner of fig. 33 (a), and a negative maximum occurs at 135° (upper right corner). This reversal, or rather the position of the zero-offset line, coincides with the extension of the correlation minimum towards smaller polarisation angles (fig. 32). The changes indicate that the processes or structures producing the response functions at these high periods are different from those presumed to operate in the intermediate period range of distortion. The interchange of the polarisation azimuths of maximum and minimum offset hints at a change of strike direction by 90° (see section 4.2.1, 2D).

The variations of the phase angle (slope) in fig. 33 (b) show well defined boundaries between larger and smaller values on the two sides of the linear correlation

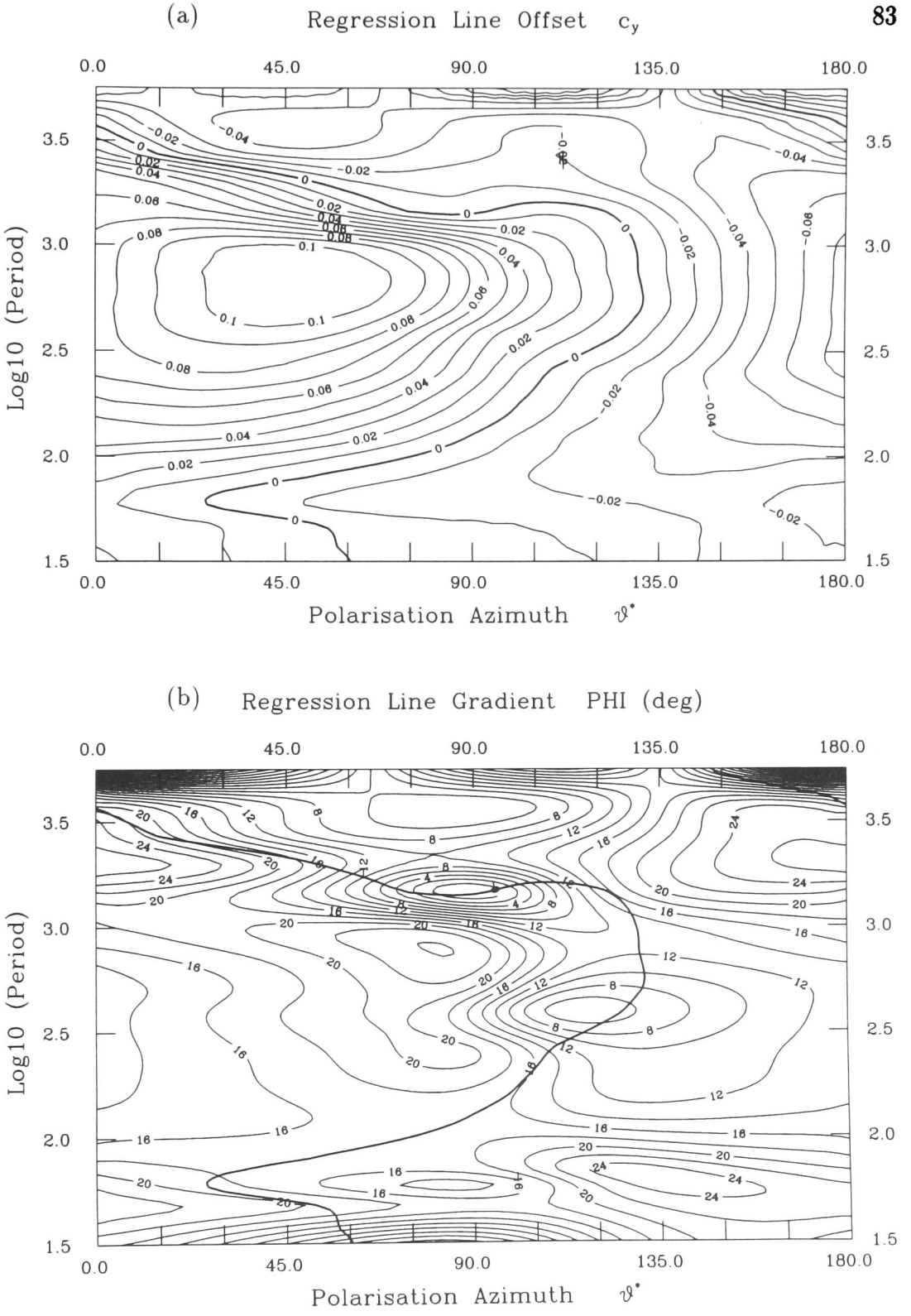

Figure 33: *The Iapetus Dataset: Hypothetical event analysis, Alston Block datasets, all periods, polarisations:* 0° – 180°. *Contour plots of regression line parameters: a) intercepts of y - lines; the zero-line runs in a fairly narrow band of polarisation angles between* 125° - 133° *at periods 400s - 1500s. The zone of maximum offset is located at perpendicular polarisation.*
b) phase angles of the regional impedance derived from gradients of the y - regression lines. The thick line marks the position of the zero-offset line taken from the upper map. It coincides with the position of the phase angle minima.

minimum. The phase angles are slightly higher on the left side of the correlation minimum than on the right. On the right side, two distinct phase minima can be distinguished at periods T = 400s with $\varphi_{min} = 6°$ and at T = 1500s with $\varphi_{min} = 0°$. Their position follows the zero-offset line. These minimum phases therefore correspond to the regional impedance Z_B. In between those minima the phase takes values around 10° - 12°. Across the region of maximum offset (left side) the phase angle is ca. 18° for Z_E.

The contour maps of the single site datasets indicate clearly and consistently that the regional structure is of a two-dimensional nature and strikes N130°E. For the best determination of the regional impedance phases we examine the predicted vertical fields of the *local* response functions in the following subsection (b).

(b) Alston Block: local response functions

The single site results of the previous subsection (a) may be compared with those estimated at the same sites from *local* response functions (i.e. from difference fields). All 35 stations of the Alston Block dataset could be used for hypothetical event analysis, except for two sites at a few periods (see appendix A.6.2). Fig. 34 comprises contour maps of the linear correlation coefficient (a) and of the slope angle of the y - regression line (b). Since the line offset is already eliminated from these data, the variations of the intercepts are not shown.

The linear correlation map (a) reveals distinctly different features only in the long and short period range. At periods T < 200s, the contour lines are mainly horizontal, i.e. the linear correlation is constant with changing polarisation azimuth. At periods T > 200s, however, the familiar minimum occurs. The values of r_{max} jump from less than 0.8 at periods below 200s to values > 0.8 or even > 0.9 for all longer periods. Between 200s and 1000s, the correlation minimum occurs, as in the previous investigations, at polarisations of 90° - 100°, and at slightly smaller polarisation angles around 70° at periods exceeding 1000s.

Because the contribution of the regional vertical field is eliminated when computing the difference fields, the *local* response functions are estimated from virtually pure anomalous vertical fields generated by galvanic distortion. The predicted vertical fields should therefore reveal the common information on the regional impedance phases best. In the phase map (fig. 34 b), we can recognize again the pattern of larger angles on the left flank and minimum values on the right flank of the correlation minimum in the period range 200s - 2000 s. The minimum phase angles are slightly higher than for the single site results: ca. 8° for Z_B, with values up to 16° in between the minima. Values on the left side range from 4° up to 30° for Z_E with increasing periods. Below 1000s, the Z_E-phases are restricted to angles smaller than 22°. Since we cannot determine the regional strike direction from the *local* response functions, the phase angles of Z_E and Z_B are taken at polarisations azimuths of maximum/minimum offset of the single site data, i.e. at polarisations 40° and 130°, respectively (see previous subsection a).

The hypothetical event analysis of the *local* response functions at all periods supports the results from single site data. The period range of distortion, identified by a particularly uniform behaviour of the data, could again be restricted to periods between 200s and 2000s. In this range the phase of Z_E varies continuously from

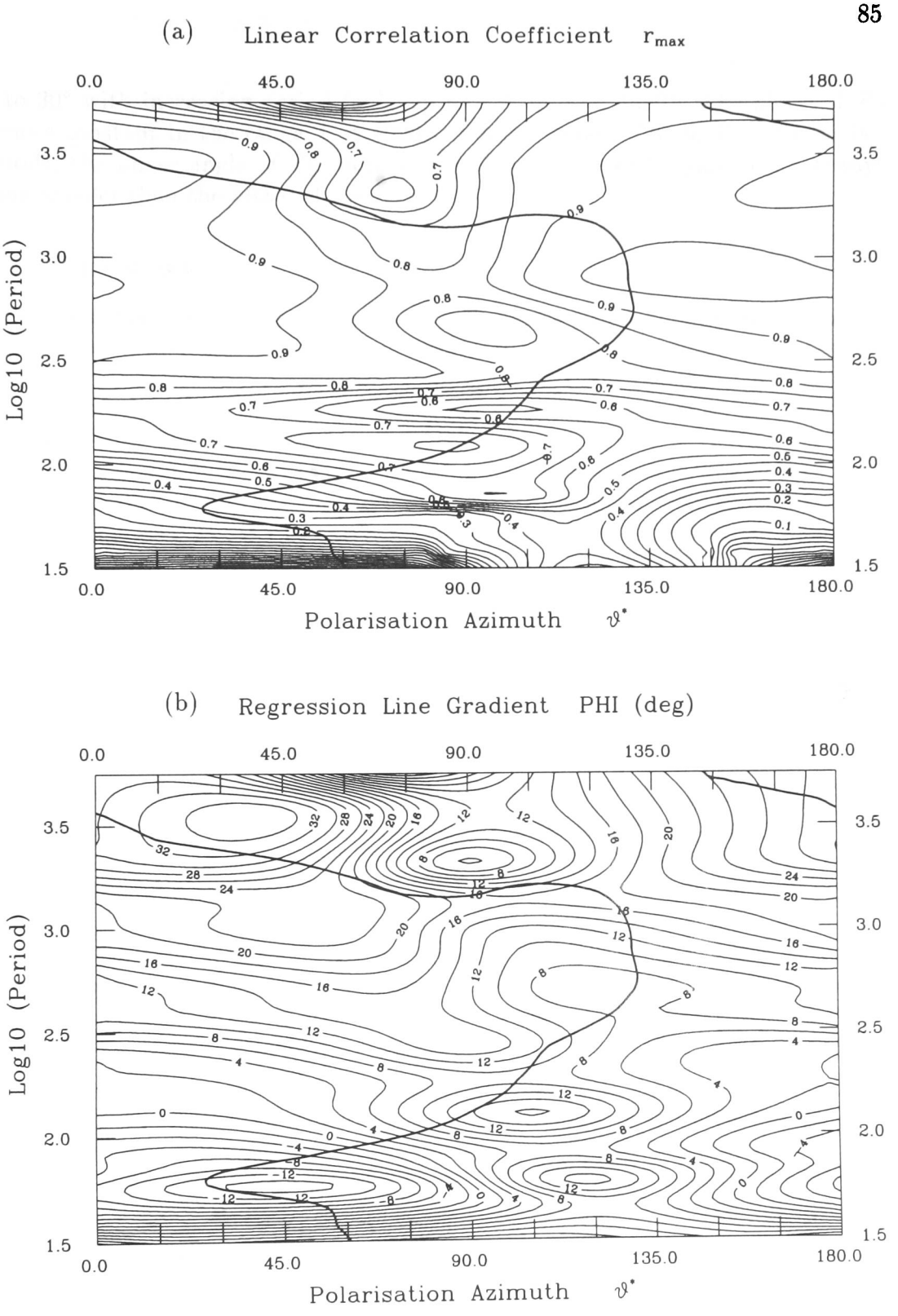

Figure 34: *The Iapetus Dataset: Hypothetical event analysis, reduced datasets,* local *response functions, all periods, polarisations:* $0° - 180°$. *Contour plots of regression line parameters:*
a) linear correlation coefficients $|r_{max}|$*; at periods 200s - 1000s the correlation minimum is located at* $90° - 100°$. *b) phase angles of the regional impedance inferred from gradients of the y - regression lines. The thick lines in both maps mark the position of the zero-offset line taken from the single site intercept map (fig. 33a). It runs on the right flank of the correlation minimum at periods 400s - 1000s. In that range, phases are distinctly smaller along the zero -line than at perpendicular polarisations.*

4° to 30° with increasing period (only up to 22° for T < 1000). The phase of Z_B is more constant in the range T < 1000s: it takes values of 8° to 12°. For higher periods, the phase angle of Z_B increases to 16° and descends again to 8°, always being smaller than the phase of Z_E.

5.4 Summary

It has been shown in the previous chapter that conductivity inhomogeneities of any size can distort the regional magnetic response functions. As a consequence, induction arrows may not provide reliable information on the regional strike directions, but may be dominated by such local anomalies. The real induction arrows of the Iapetus dataset (127 sites at 20s - 7000s covering 200 km E/W × 300 km N/S) indicate the presence of two conductive structures in the middle/lower crust. One is located to the north of the mapped region and is associated with the NE-striking Southern Upland Fault. The other one coincides with the E-W extension of the Northumberland Trough. Both features are well-documented in the electromagnetic literature.

For the Northumberland Trough conductor, the induction regime is clearly delimited to periods < 100s (i.e. middle crust). At periods 400s - 1500s, however, large real induction arrows still indicate a strong current concentration in E-W direction. For sites associated with the conductor beneath the Southern Uplands, induction processes can be identified for T < 500s. The distortion regime is consequently shifted to longer period ranges, i.e. for T > 800s. These longer periods agree with the assumption that the conductive structure reaches greater depths than the one underneath the Northumberland Trough. Information on the regional induction may be suppressed in both cases by the anomalous magnetic fields of current concentrations in these mid/deep-crustal conductors. At longer periods (> 2000s) the real arrows of the whole array vary considerably between areas, whereas imaginary arrows reflect a more consistent behaviour. Common information on regional induction processes may therefore be present in the data at these longest periods, but it might also be affected by galvanic distortion in the complex structure of the crust.

The components of the magnetic response functions ($\mathcal{A}_i, \mathcal{B}_i$) of sites located south of the Southern Upland Fault are very similar over most of the period range. The values of $\mathcal{A}_i$ and $\mathcal{B}_i$ of different sites, and their ratios (distortion test in fig. 22), run in smooth, parallel curves in the range 400s - 2000s, as expected for the case of distortion. A small bump of real and imaginary parts at around 70s indicates induction in a conductive feature, which is probably situated in the middle crust. North of the Southern Upland Fault, the variations of the components show a much different picture. Although different sites still have comparable components, the curves of the two components $\mathcal{A}$ and $\mathcal{B}$ differ considerably. The imaginary parts have generally larger amplitudes and change their sign in the intermediate period range (400s - 800s), thus delimiting the range of induction to shorter periods.

Hypothetical event analysis was applied to all data and to several subsets with the aim of revealing hidden, common information on the regional structure from the distorted response functions. The predicted vertical magnetic fields were calculated

from the measured components $\mathcal{A}_i$ and $\mathcal{B}_i$ for certain polarisations of the horizontal magnetic field. The values of all sites are presented in Argand diagrams in order to assess the common phase content. At northward polarisation (fig. 23), the predicted values for periods T < 2000s scatter roughly around lines with gradients (i.e. phases) of 15° - 20°. Most of the outliers belong to sites located north of the Southern Upland Fault. The best linear correlation is found in the period range 400s - 1000s. At periods T > 2000s, the data are less focused. In the intermediate period range, the lines indicated by the data distribution do not pass through the origin. This offset implies the presence of a regional vertical component in the data, i.e. the regional conductivity distribution must be more than one-dimensional.

In order to compute the common phase information objectively, the data distributions were fitted by regression lines (fig. 26). At T = 750s, a period representing the period range where distortion is presumed and linear correlation seems best, the offset of the regression line can be eliminated, when the hypothetical event is polarised at a direction of 120° - 130°. This azimuth range could be found consistently with datasets containing all sites, only sites south of the Southern Upland Fault or only sites across the Alston Block. As a result we can assume that the regional vertical component B_z^o is generated by a structure striking 120° - 130° from north. The phase angles at this and the perpendicular polarisation azimuth correspond to the regional impedance phases of Z_B and Z_E.

The most reliable estimations for the regional impedance phase angles are obtained from the predicted values of the *local* response functions (Alston Block sites, fig. 34): $10.5° \pm 1.5°$ for Z_B and $19.9° \pm 2.3°$ for Z_E. Since the local response functions are determined using difference fields, they do not contain contributions from a regional vertical magnetic field. Nevertheless, the impedance phases determined from single site data are in very good agreement with those of difference field data across the Alston Block. This similarity underlines the capability of the method and shows that the assumptions of uniformity of the fields are clearly met across this area. Comparison of the predicted vertical fields of single site with *local* response functions at polarisation 40° provide an average value for the regional vertical response function component: $\mathcal{B}^o = (-0.2120, 0.0322) \pm (0.0074, 0.0056)$.

The phase information obtained from datasets covering larger areas differ slightly from the Alston Block results. In particular, they do not resolve the small but distinct phase difference between the two impedances. This is probably due to the fact that the fields are not necessarily uniform over the whole area. In this period range, the induction radius is of the order of 100 - 300 km, depending on the assumptions made for the integrated conductivity of the crust and upper mantle. That implies that the regional phase might not be stable across the whole mapped area. Furthermore, major elongated structures like the Southern Upland conductor are bound to modify the regional response of the host to some extent.

Summarizing the results of the different datasets, at period 750s the regional strike angle can be assumed with some certainty at ca. 125°. The phase angles range at 17° - 20° for Z_E and slightly smaller, at 10° - 12°, for Z_B. Hypothetical event analysis at *all* available periods show that these results are representative for the period range of distortion at sites south of the Southern Upland Fault. This study confirms the range 400s - 1500s to be the period range affected by galvanic

distortion. The impedance phases at these periods are 12° - 24° for Z_E and 8° - 16° for Z_B (with increasing period, fig. 34b). Unfortunately, no equivalent investigations could be carried out for sites further north due the small number of sites and limited data quality at the time when the dataset was analyzed. New long period data in the area north of the Southern Uplands have been recorded and processed by Junge (1995), but the magnetic response functions have yet to be incorporated into the database.

The regional phases are in general agreement, but slightly lower than, recent MT results in this area. Banks et al. (1993, 1996) and Junge (1995) determined the impedance phases in the period range 400s - 2000s at ca. 25° (for direction 50° - 90°) and ca. 40° (for direction −40° - 0°). These low phase values determine the boundary separating the mid- or lower crustal conductor from the more resistive basement in the 2D inversions. Regional strike directions in this period range were determined from MT data at 50° (Banks et al. 1996) or 65° (Junge, 1995) for the northern part of the array (Southern Uplands and north), and at 90° (Banks et al. 1995) for the southern area (Northumberland Trough and south). However, applying hypothetical event analysis we were able to show that the regional strike direction for sites situated south of the Southern Upland Fault must rather be assumed at 125° - 130°.

6 The BC87 Dataset

The second dataset I tested using hypothetical event analysis for distortion elimination is the BC87 dataset. It consists of MT and GDS data in the period range 0.0026s - 1820s from 27 sites along a 150 km profile in British Columbia. The profile was part of the multidisciplinary LITHOPROBE Southern Cordilleran Transect investigations and runs across the eastern part of the southern Canadian Cordillera. The data were made available by D. W. Oldenburg (LITHOPROBE) and A. G. Jones (Geological Survey of Canada), in advance of the MT interpretation workshops MT-DIW1 in Wellington (prior to the 11. Workshop on Electromagnetic Induction in the Earth in Wellington, 1992) and MT-DIW2 in Cambridge (prior to the 12. Workshop on Electromagnetic Induction in the Earth in Brest, 1994). The purpose of these 'pre-workshop' workshops is to compare the results of different interpretation schemes. I chose to include this dataset in my studies for several reasons:

- The data were available at a time when I had formulated the theoretical capability of hypothetical event analysis to recover regional information from distorted response functions. Apart from the Iapetus data I was looking for another dataset from a well-documented region to test the technique.

- Interpretations presented at MT-DIW1 (Jones et al. 1993; Eisel & Bahr, 1993; Lilley, 1993) and other research papers on the same dataset (Groom & Bahr, 1992; Groom et al. 1993; Jones & Groom, 1993; DeGroot-Hedlin, 1995) suggest uniformly that the MT data of the BC87 dataset are strongly affected by 3D induction and galvanic distortion at all scales. Therefore magnetic distortion has to be considered for the interpretation of the GDS response functions.

- Apart from a preliminary study by Jones et al. (1988), the GDS response functions had not been investigated further. Clearly one of the reasons for this is the limited data quality, especially at long periods. Would hypothetical event analysis reveal common information content in the dataset despite the large errors?

- In contrast to the Iapetus dataset, the BC87 sites are arranged along a profile. It seemed interesting to test whether hypothetical event analysis can also be applied successfully in this situation.

- The general structural situation of the investigated region shows certain similarities to the Iapetus Suture Zone, as it features a major terrain boundary (Foreland and Omineca belts) and granitic intrusions (e.g. Valhalla gneiss dome, Nelson Batholith).

It must be stated in advance, that the BC87 dataset is well-suited for this technique. The predicted vertical fields of all sites revealed common features at a certain polarisation range at longer periods. However, the analysis of the magnetic response functions indicates a certain departure from the original distortion model, as the common phase is found in a negative quadrant. Before showing the results of this investigation, it is necessary to give some details of the tectonic setting and the previous electromagnetic results. A good description of the crustal structure and geophysical studies in the region of the BC87 profile can be found in Jones (1993).

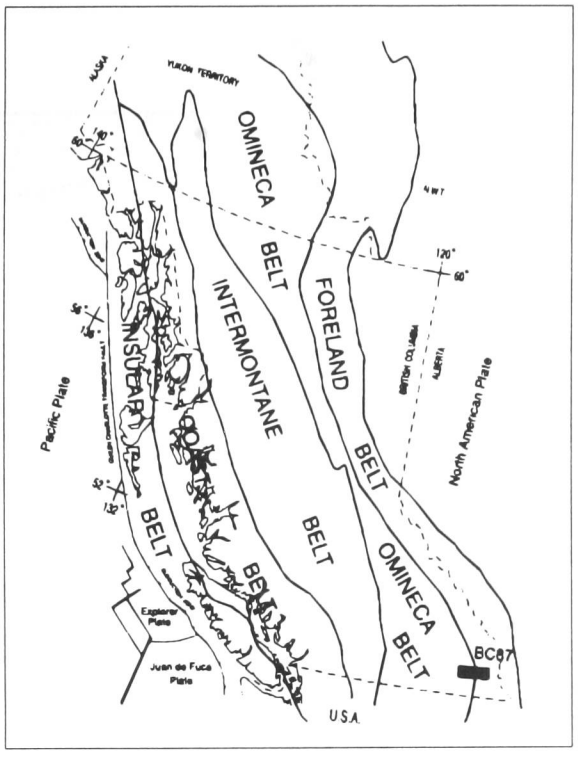

Figure 35: *The BC87 Dataset: Summary map of the Canadian Cordillera showing the 5 morphogeological belts and the location of the BC87 profile (from Jones, 1993).*

6.1 Tectonic setting and previous EM results

The BC87 profile extends in an east-west direction from the Rocky Mountain Trench on the ancestral North American basement to the Valhalla gneiss complex in the Omineca Crystalline Belt (see figures 35 and 36; both from Jones, 1993). From east to west it traverses the Mid-Proterozoic sediments of the Purcell Anticlinorium, the Tertiary intrusives of the Kootenay Arc, and crosses the Mid-Jurassic Nelson Batholith. The Rocky Mountain Belt to the east is of Devonian to Upper Cretaceous age. The Valhalla gneiss to the west is of Cretaceous to Early Tertiary age.

The junction between the Foreland and the Omineca Belt is coincident with a major terrain boundary. To the east, the structures of the Foreland Belt are deformed, brittle, thin-skinned sediment wedges which developed on the western margin of ancient North America. To the west, the Omineca Belt is characterized by penetratively deformed rocks underlain by metamorphic and granitic rocks (e.g. the Valhalla gneiss dome). The Omineca Belt can be seen as the transition zone from the eastern Foreland Belt rocks to the western accreted terrain structures. Seismic reflection data indicate an extension of the ancient North American basement beneath the accretion complex to the west (Cook et al. 1988, 1991).

The Slocan Lake Fault (see fig. 37), which surfaces to the west of the Nelson Batholith, separates the eastern Foreland Belt rocks from the western accreted terrains. It is seen as a dipping boundary reaching into the upper mantle beneath the Purcell Anticlinorium. The Kootenay Arc, which is defined as the boundary between the Foreland Belt and the Omineca Belt (Jones, 1993), runs as a major

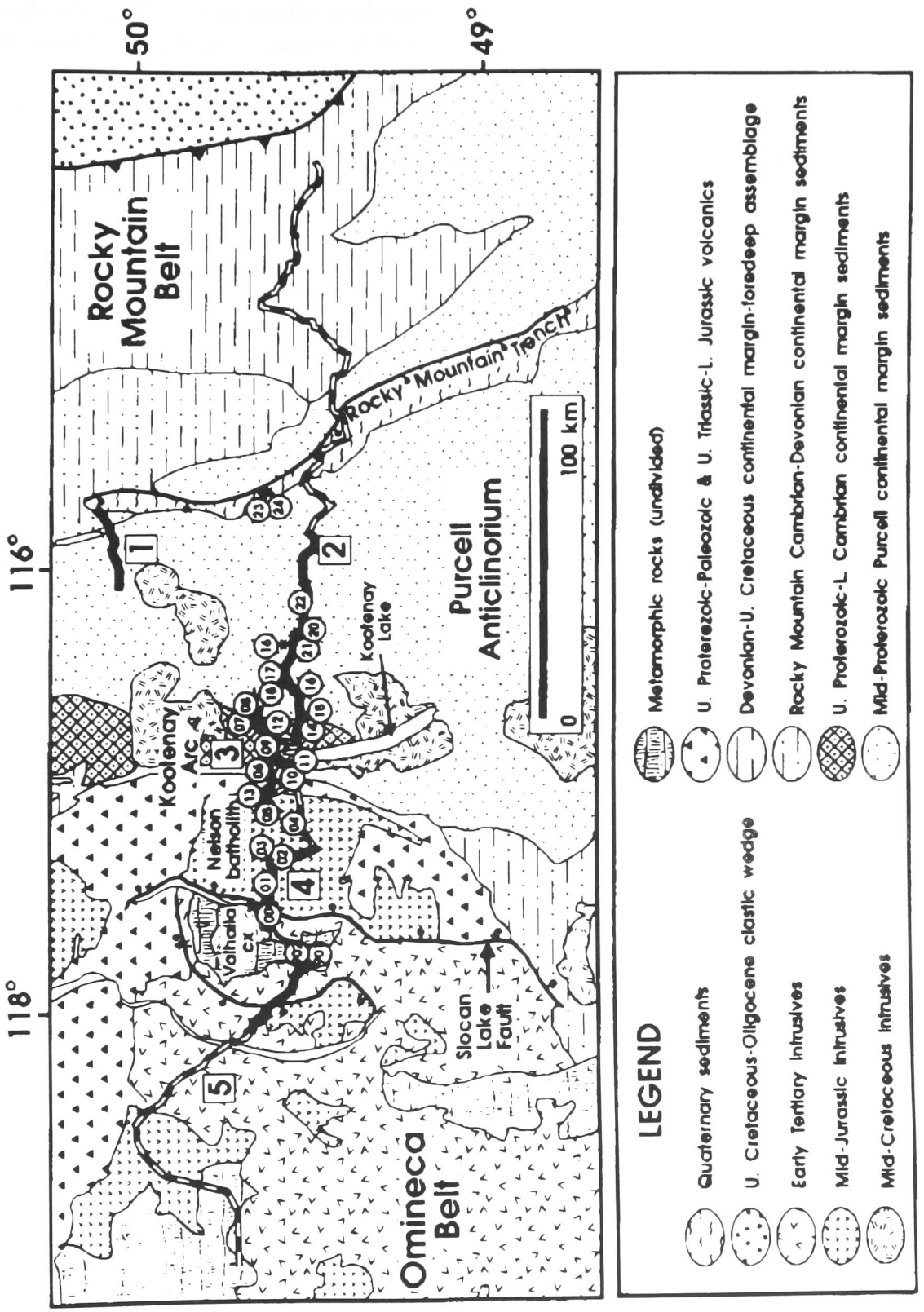

Figure 36: *The BC87 Dataset: Simplified geology map with 27 EM site locations (circles), seismic reflection (solid lines) and refraction (dashed lines) profiles (from Jones, 1993).*

extensional fault in a north-south direction between the two terrains. It is characterized by significant changes of Moho temperature, lower-crustal velocity, crustal thickness, rock age, structure and rheology. It also marks the eastern boundary of Eocene magmatism (see fig. 36)

The Kootenay Arc has also been identified as a boundary in electrical resistivity by a number of MT and GDS interpretations. Hyndman (1963) and Caner et al. (1967) noted an amplitude change in the magnetic response functions, from high values to the east to low values to the west of the arc. This was interpreted as due to a conductive lower crust (10 ± 5 Ωm) at a depth of 15 ± 5 km with a thickness of 20 - 40 km on the western side compared with a resistive crust (> 250 Ωm) reaching down to 30 - 35 km on the eastern side (Caner et al. 1969). However, in this part of the Cordillera, a conductivity contrast was not only found in an east-west direction, but also extending southwards from the BC87 profile (Lajoie & Caner, 1970). The transition from resistive to conductive material is gradual from east to west, but fairly abrupt from north to south (see fig. 38).

As a consequence, the structural models suggested for the region (Caner et al. 1971) feature a deep L-shaped conductive region. The north-south striking part is placed in the lower crust to the west of Kootenay Lake, and the east-west striking part is placed in the lower crust / upper mantle to the south of the BC87 profile. Caner's L-shaped models were challenged by the studies of Dragert & Clarke (1977) and Gough et al. (1982), who suggested that the southern conductor (the so-called SABC conductor) was detached from and at an oblique angle (ca. 45°) to the north-south striking one.

Although seismic reflection and refraction results indicate a 2D geometry for the region, the EM studies show emphatically that the deep-crustal geology is three-dimensional (Jones, 1993). The complex structure of the middle to lower crust is overlain by an equally complex composition of the upper crust, which consists of juxtaposed, laterally bounded features of varying conductivity. Therefore, 3D induction and galvanic distortion effects are liable to occur throughout the whole period range.

Due to software-limitations, the most recent interpretations of the BC87 profile are based on 2D inversions of the *decomposed* MT impedances. Jones et al. (1993) used Groom/Bailey's method (Bailey & Groom, 1989) whereas Eisel & Bahr (1993) used Bahr's modified decomposition technique (Bahr, 1991) to correct the MT data for electrical distortion effects (both procedures are described in detail in chapter 3). Both interpretations confirm the middle/lower-crustal conductivity change beneath the area of Kootenay Lake. However, as a new feature, they suggest consistently that a continuous zone in the deep crust or upper mantle is electrically anisotropic. The minimum resistivity was modelled at $5-10$ Ωm for an azimuth of N60°E (Jones et al. 1993) or N45°E (Eisel & Bahr, 1993), compared with a maximum resistivity in perpendicular directions of 300 Ωm (Eisel & Bahr, 1993) or 1000 Ωm (Jones et al. 1993).

The regional strike direction found by MT decomposition (45° - 60°) is distinctly different from the 'traditional' Swift angle determined at ca. 90°. In a similar way, the strike directions inferred from distorted magnetic response functions may be

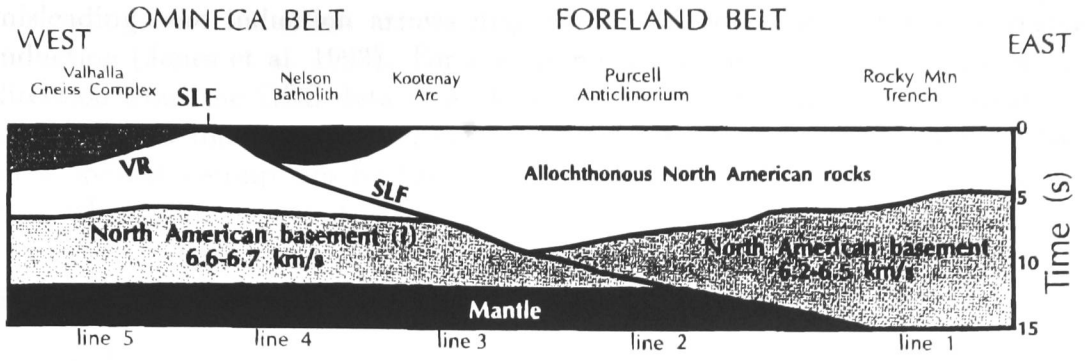

Figure 37: *The BC87 Dataset: Interpreted geological cross section from the seismic reflection studies (based on Cook et al, 1988). Line numbers refer to reflection profiles on fig. 36.* SLF *Slogan Lake Fault;* VR *Valhalla Reflector. Figure taken from Jones (1993).*

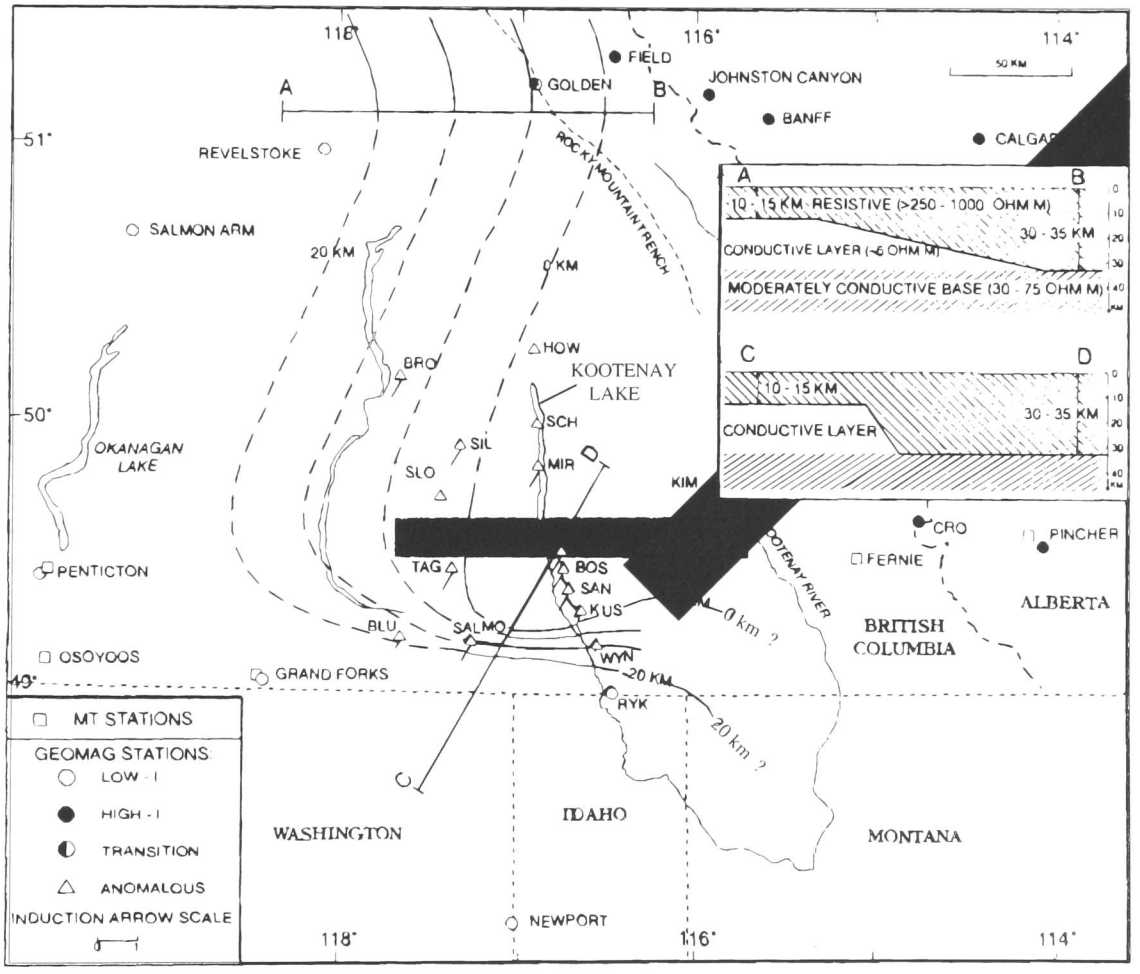

Figure 38: *The BC87 Dataset: Sketch of 3D situation of the southern Canadian Cordillera (based on Jones, 1993). The location of the BC87 profile is marked by the black shaded area. The oblique, grey box gives the presumed position of the SABC conductor (after Gough et al. 1982). The contour lines mark the thickness of the L-shaped conductor (0 km - 20 km). The two sections sketch the different widths of the transition zone to the west (A-B) and to the south (C-D) of the profile (after Lajoie & Caner, 1970). Induction arrows are drawn for the period band 60s – 360s.*

misleading, and induction arrows may not be interpretable in terms of regional induction (Jones et al. 1993). For a more reliable estimation of the regional strike direction from the GDS data it is therefore essential to apply hypothetical event analysis in the manner proposed in this thesis. However, since the technique is based on simplified assumptions for the underlying physical model (e.g. quasi-uniformity, regional two-dimensionality), the results must be treated with some care.

6.2 Vertical magnetic response functions

The quality of the magnetic response functions is generally not as good as for the previously examined dataset, probably due to the choice of sensors. For the BC87 profile, the magnetic field was measured with coils for the horizontal components, and a horizontal air loop for the vertical component (Jones, 1993). The signal-to-noise ratio of the air loop is worse than for the fluxgate magnetometers (normally used for the Iapetus surveys). Apart from external interferences (e.g. weather), the horizontal loop sensor response falls for periods in excess of 100s, making the long period estimates unreliable (Jones, 1993). However, the data are relatively consistent. In the following diagrams, the error bars or ellipses are not shown for clarity, because of their large magnitudes.

6.2.1 Induction arrows

In the short and intermediate period range ($T < 10$s, not shown) the angular distribution of the azimuths of the real arrows is very scattered along the profile. The orientations of the arrows reflect the diversity of the local structures within the area covered by the profile. At longer periods ($T > 10$s), however, the induction arrows at most sites seem to follow an overall trend. They change smoothly from $-90°$ (W) to directions around $0° (\pm 30°)$ with increasing periods, while the imaginary arrows point approximately $-180°$. The lengths and azimuths of the induction arrows for periods 450s and 910s are shown in fig. 39 in the Wiese convention.

The arrow directions suggest an east-west striking structure at some depth to the south of the profile. However, this direction does not coincide with the strike azimuth estimated from decompositions of the MT impedances, which is 45° (Eisel & Bahr, 1993) or 60° (Jones et al, 1993). Both MT interpretations associate this period range with an upper mantle anisotropy, and attribute the estimated strike to the direction of the minimum resistivity: 5 Ωm - 10 Ωm.

Since the strike direction found by MT decomposition methods corresponds to the regional structure, we can assume that the directions inferred from the induction arrows are more likely to be due to local galvanic distortion rather than regional induction. The arrows at periods > 10s may be influenced by current concentrations due to induction in the lower-crustal conductor in the south and, less strongly, to the west (according to the L-shaped conductivity model by Caner et al. 1971). In addition, current deflections around the resistive Nelson Batholith may contribute locally to the distortion of the vertical magnetic response functions. In the following section, the frequency response curves of all sites are investigated in order to identify the period range of distortion.

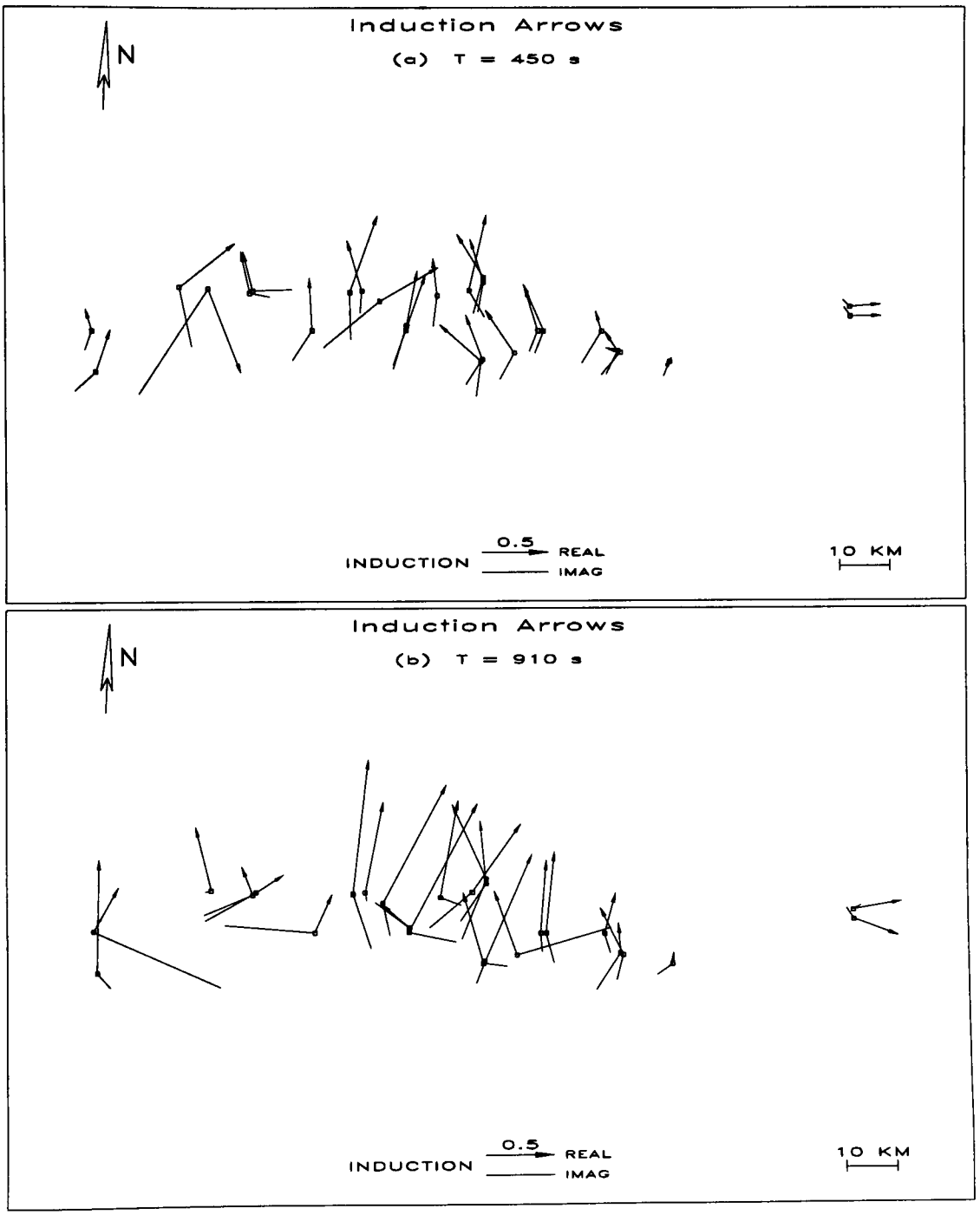

Figure 39: *The BC87 Dataset: Induction Arrows (Wiese convention) of all 27 sites at (a) 450s and (b) 910s; REAL: real arrows, IMAG: imaginary arrows. The corresponding error ellipses are large.*

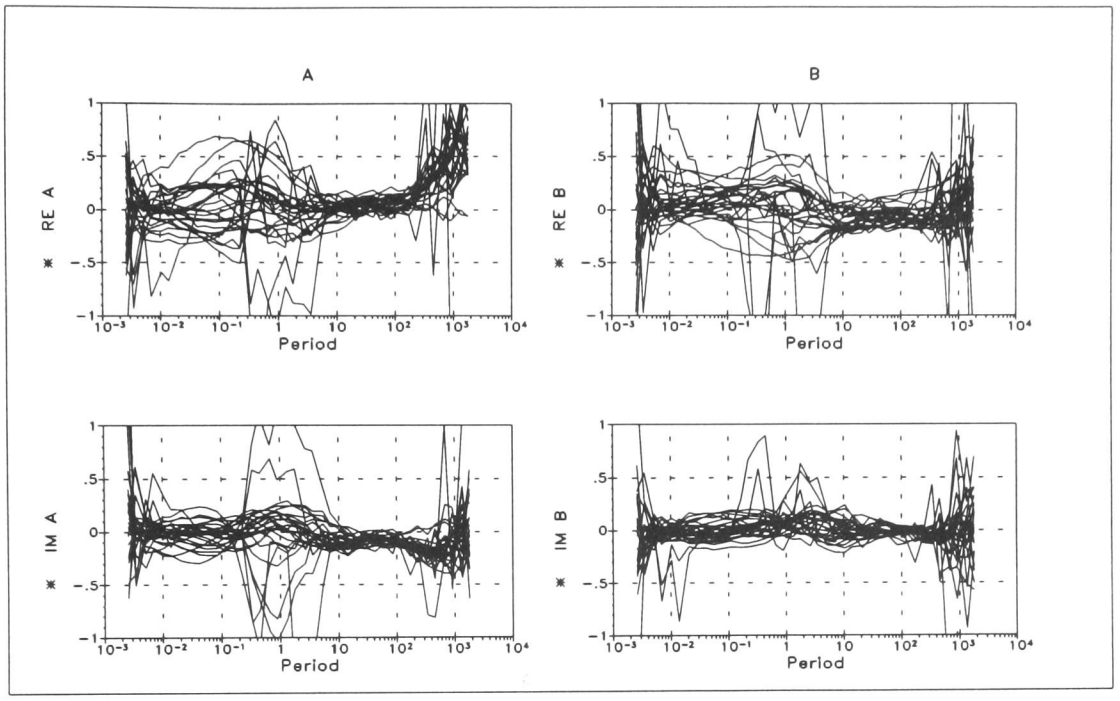

Figure 40: *The BC87 Dataset: Magnetic response functions ($\mathcal{A}, \mathcal{B}$) of all 27 sites over the whole period range; RE: real parts, IM: imaginary parts.*

6.2.2 Period dependency and distortion test

Fig. 40 shows the real and imaginary frequency response curves of all 27 sites. The amplitudes of the response functions show a distinct maximum in the intermediate period range between 0.1s and 10s at all sites. They indicate induction processes in the corresponding upper parts of the crust, e.g. the conductor at the eastern edge of the resistive Nelson Batholith (Jones, 1993). In the adjacent longer period range (10s - 100s), amplitudes are smaller and the curves run in parallel. The real and imaginary parts of component $\mathcal{A}$ increase from ca. 100s towards longer periods, whereas the $\mathcal{B}_i$ curves tend to rise later, approximately from 500s. Here, the curves of most sites are still fairly parallel. However, for periods in excess of 1000s, the data are very scattered.

The distortion test was carried out by estimating the ratios of the components $\mathcal{A}$ or $\mathcal{B}$ at all sites with respect to one site situated in the centre of the profile (ST14). Fig. 41 shows relatively stable and parallel curves for the ratios of the real parts of $\mathcal{A}$ for periods from ca. 70s. A few curves can be singled out as outliers in this period range. Curves showing smaller ratios belong to sites ST00 and ST01, which have extremely large errors. Curves with higher ratios belong to sites ST23 and ST24, both located in the easternmost part of the profile (Rocky Mountain Trench). Since the ratios of most sites are fairly constant over these long periods, we can assume that frequency-independent contributions due to galvanic distortion are present in the data across the profile.

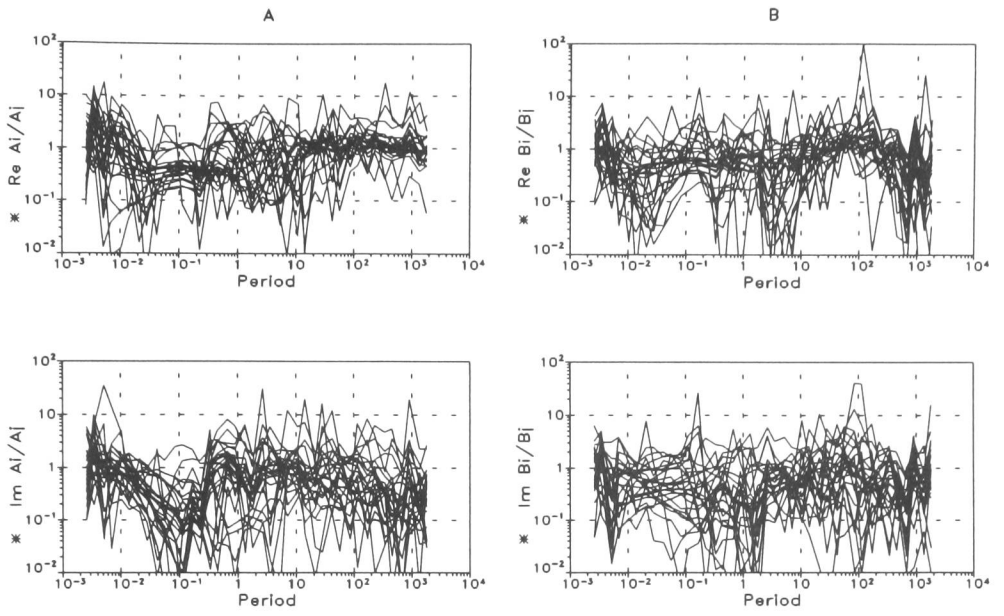

Figure 41: *The BC87 Dataset: Distortion Test: ratios of the components $\mathcal{A}_i$ and $\mathcal{B}_i$ of all sites with respect to the values at site* ST14 *at the centre of the profile; RE: real parts, IM: imaginary parts.*

The ratio curves of $Re\mathcal{B}$ are less smooth in the long period range. They are relatively constant in a range of approximately 50s - 500s. At longer periods, the ratios vary strongly, but most curves still run in parallel. Due to the smaller amplitudes of the imaginary parts, the ratios of both components are fairly scattered and no uniform behaviour can be recognized. On the basis of the observations made for the ratios of the real parts, it seems reasonable to search the period range from 50s onwards for common regional information using hypothetical event analysis. Given the rising error levels with increasing periods, the upper period limit is set to 1000s.

6.3 Hypothetical event analysis

Hypothetical event analysis was applied to all observed magnetic response functions in the range 50s - 1000s in order to reveal the regional strike direction and impedance phase that must be common to all sites. However, since no distinct common features could be found at periods T < 100s, I concentrated the investigations mainly in the decade 100s - 1000s. The real and imaginary parts of the predicted vertical fields B_z^p of all sites at periods 230s and 910s are presented in the Argand diagrams of (fig.42). The data are shown at 4 different polarisations of the hypothetical horizontal magnetic field: at 0° (N), 90° (E), −35° and 55°.

At north- and eastward polarisation, the distribution of the data points is strongly non-linear, particularly at 910s. However, at a polarisation azimuth of about −35° the predicted vertical fields can be fit a line through the origin. Theory (chapter 4) predicts that this happens when the hypothetical magnetic field is polarised parallel

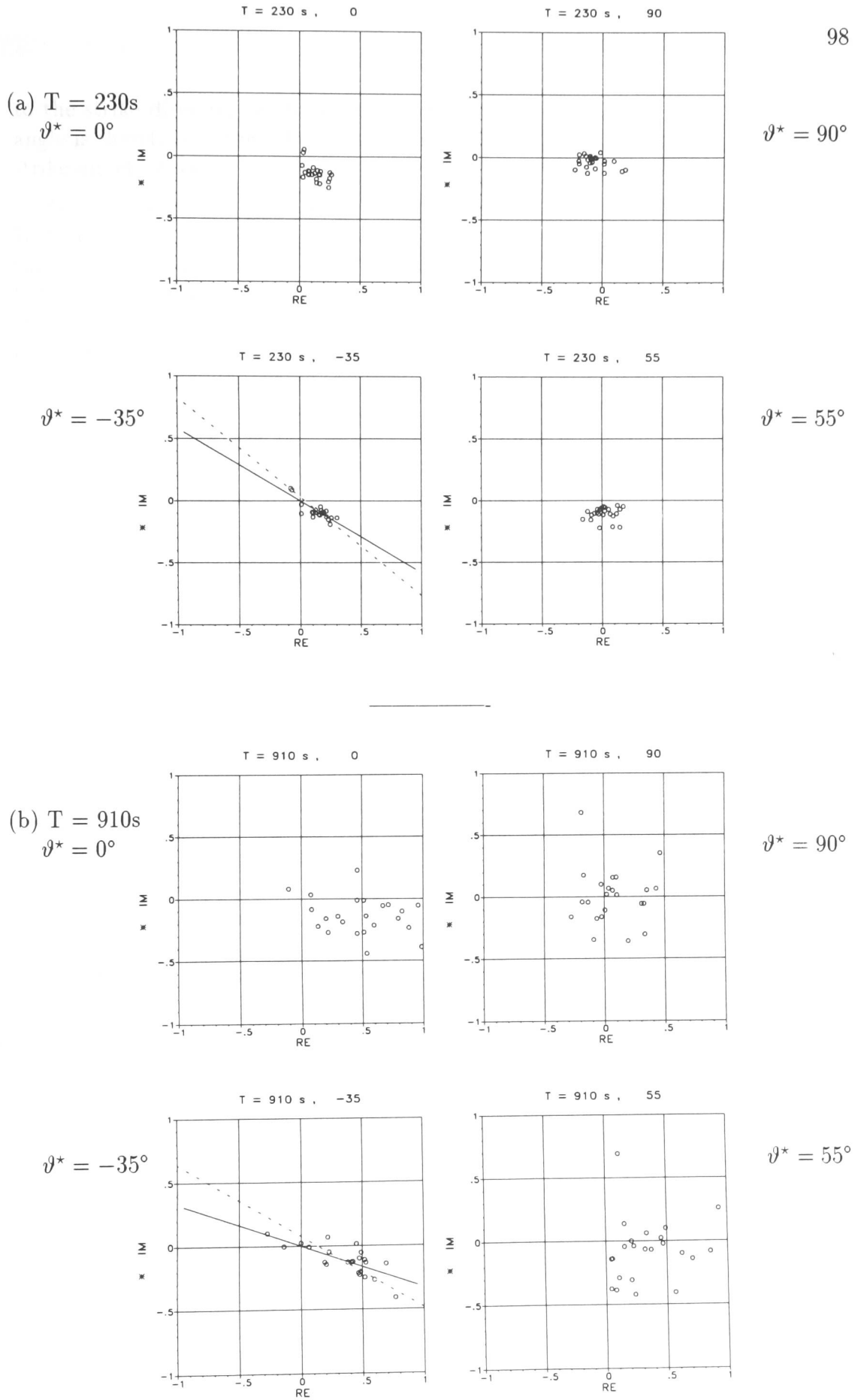

Figure 42: *The BC87 Dataset: Hypothetical event analysis, T = 230s(a) and 910s(b). Argand diagrams of the predicted vertical fields $B^p_{z_i}$ at polarisation azimuths $\vartheta^\star = 0°$, 90°, −35°, 55° of the horizontal magnetic field. At both periods, the linear distribution is best at $\vartheta^\star = -35°$. The solid and dashed lines are the regression lines for y- and x distribution, respectively (see sections 4.2.2 and 5.3.3).*

to the strike direction of the regional structure or perpendicular to it. The strike angle is therefore either $-35°$ or 55°. The latter corresponds well with the regional strike direction found by MT decomposition methods (45° or 60°).

In contrast to the previously examined Iapetus dataset, the phase line of the BC87 dataset is not off-set from the origin at the polarisation azimuth that is presumably perpendicular to the regional strike direction. This implies that the contribution of a regional vertical component is very small or zero. Since the regional structure cannot necessarily be assumed to be exactly 1D, one may conclude that the regional vertical field is attenuated either because of the long distance from the regional 2D structure, or because the conductive structure of the lower crust/upper mantle is laterally anisotropic (Jones et al. 1993). The latter explanation was pursued consistently in the MT interpretations. Eisel & Bahr (1993) and Jones et al. (1993) attributed their regional strike directions to the direction of minimum resistivity (5 - 10 Ωm).

The data distributions were fitted with regression lines by the least squares method as for the Iapetus dataset (see sections 4.2.2 and 5.3.3). The properties of the regression lines for T = 230s are shown in fig. 43 a-d. The linear correlation coefficients r and r_{max} have a distinct maximum at a polarisation azimuth of $-35°$ (fig. 43 a). At this azimuth, the standard deviations for x- and y - distributions are at their lowest levels (fig. 43 b). Due to its smaller error, the y - line approximates the data distribution better than the x - line. At $-35°$, the y - line passes through the origin (fig. 43 c). The offset values at other polarisations are meaningless because the data distribution is strongly non-linear.

The gradient of the y - line for a polarisation azimuth of $-35°$ is $-30.2° \pm 4.7°$ at 230s and $-18.1° \pm 3.2°$ at 910s. In the whole decade 100s - 1000s the phase angles change gradually from $-30°$ to $-18°$ with increasing periods. The phase angles found by hypothetical event analysis should represent one of the regional impedance phases. However, the phases determined by MT decompositions at these long periods are 45° - 60° for Z_B and distinctly higher, ca. 70° - 80°, for Z_E (for strike directions 45° or 60°). The negative common phase cannot be correlated with the impedance phases at all. They must therefore be understood as an indication that the general conductivity distribution does not concur without restrictions with the assumed distortion model.

The values of the maximized linear correlation coefficients of the period range 1s - 1000s are shown in fig. 44. The 3D presentation (graph b) underlines the distinct maximum located in the upper left part of the contour map (graph a). The polarisation azimuth for the optimum linear distribution of the predicted vertical magnetic fields is consistently found at $-35°$ throughout the decade 100s - 1000s. Although r_{max} reaches high values (> 0.8) also at various polarisations at shorter periods, the maximum at 100s - 1000s is the only one occurring consistently at a constant polarisation azimuth over several periods. At the perpendicular polarisation azimuth (55°), no phase line for the second impedance can be fitted as the data points scatter widely.

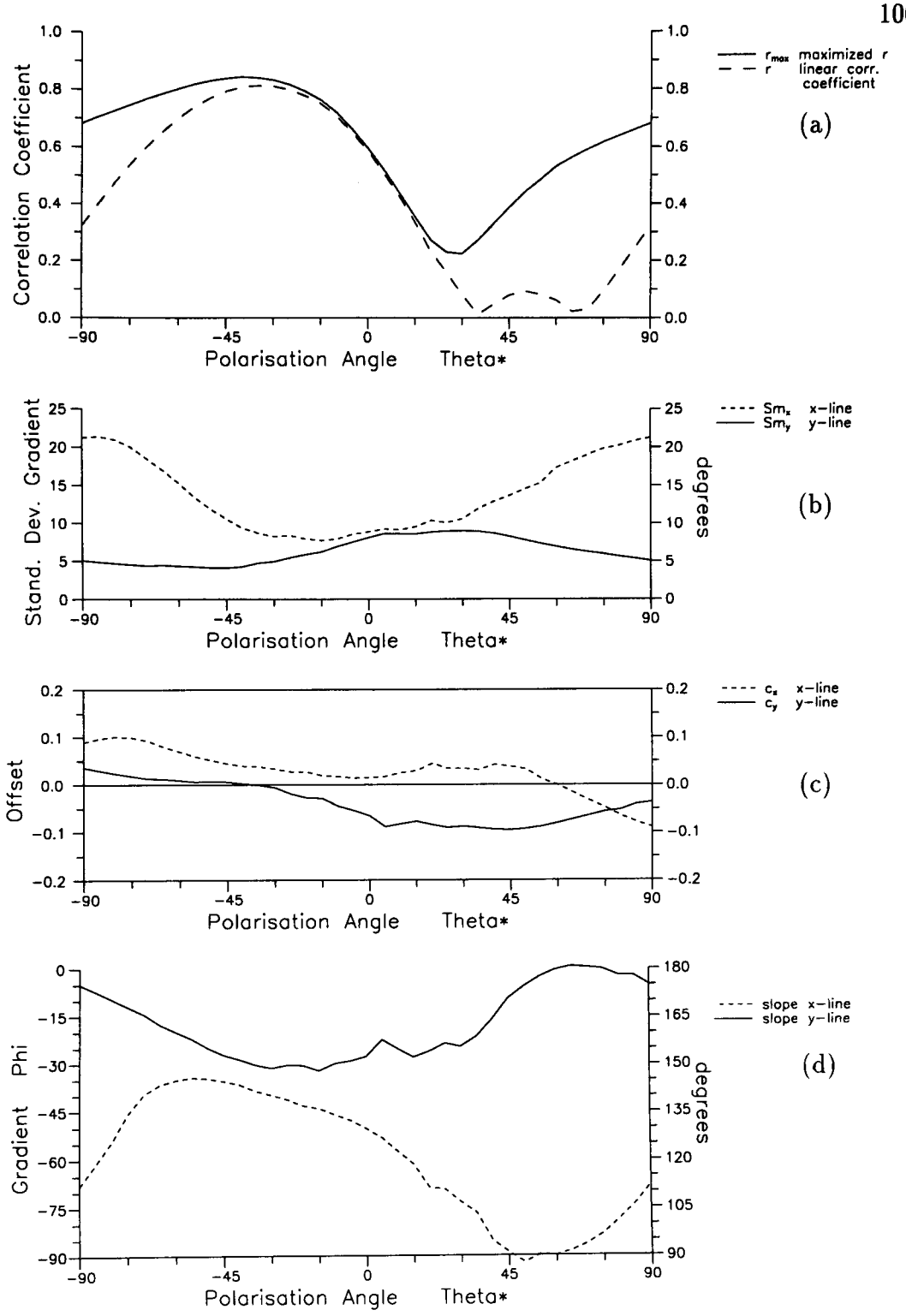

Figure 43: *The BC87 Dataset: Hypothetical event analysis, all sites, T = 230s, polarisations: −90°...90°. Regression line parameters:*
a) Linear correlation coefficients $|r|$ (dashed line) and $|r_{max}|$ (solid line); Both have a distinct maximum at a polarisation azimuth of −35°
b) Standard deviations of the gradients of the x - line (finely dashed) and y - line (solid). The error of the y - line is smaller than that of the x - line.
c) Intercepts of the x - line (dashed) and y - line (solid); at polarisation azimuth −35° the y - line passes through the origin.
d) Phase angles inferred from the gradients of the x - line (dashed) and y - line (solid).

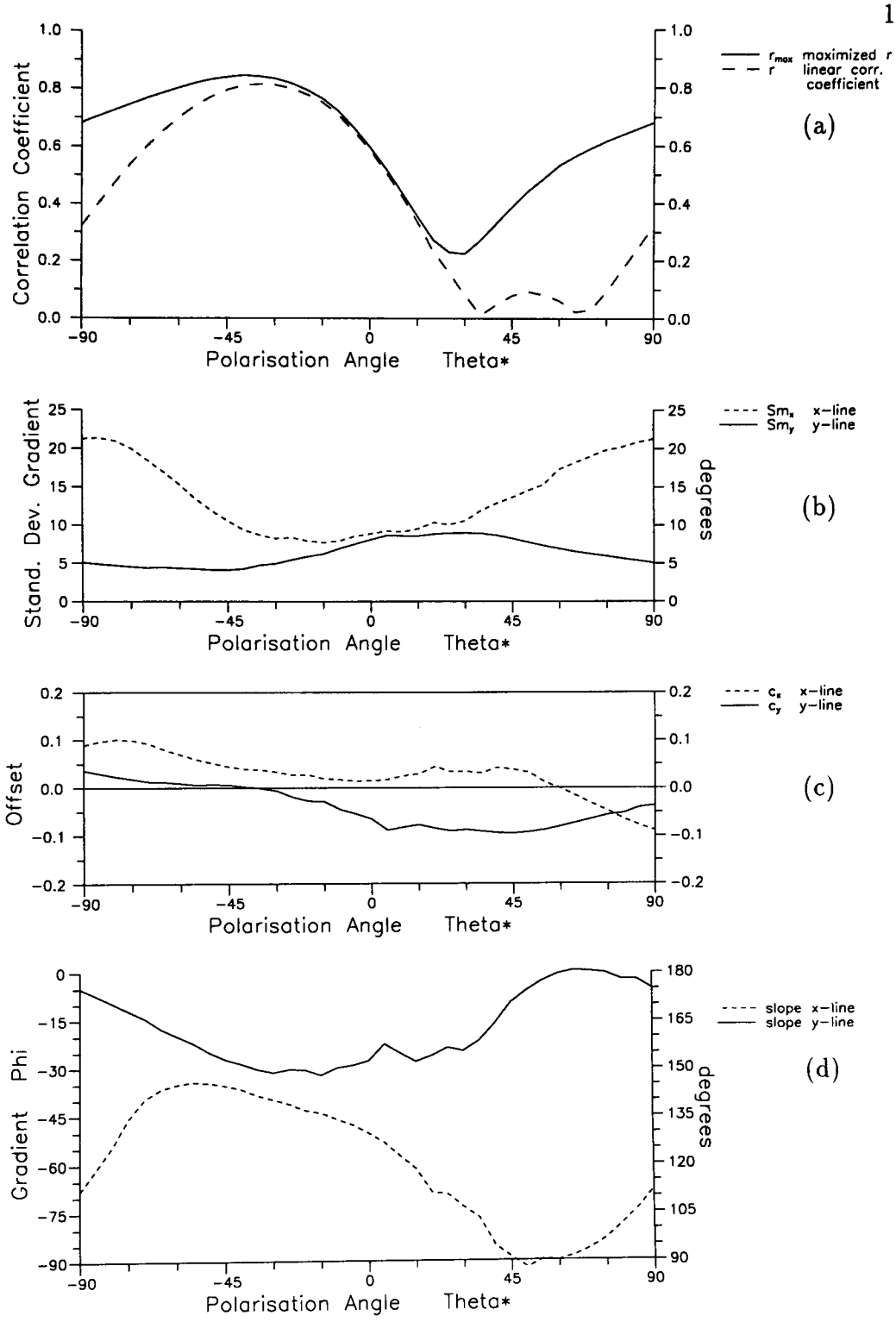

Figure 43: *The BC87 Dataset: Hypothetical event analysis, all sites, T = 230s, polarisations: −90°...90°. Regression line parameters:*
a) Linear correlation coefficients |r| (dashed line) and $|r_{max}|$ (solid line); Both have a distinct maximum at a polarisation azimuth of −35°
b) Standard deviations of the gradients of the x - line (finely dashed) and y - line (solid). The error of the y - line is smaller than that of the x - line.
c) Intercepts of the x - line (dashed) and y - line (solid); at polarisation azimuth −35° the y - line passes through the origin.
d) Phase angles inferred from the gradients of the x - line (dashed) and y - line (solid).

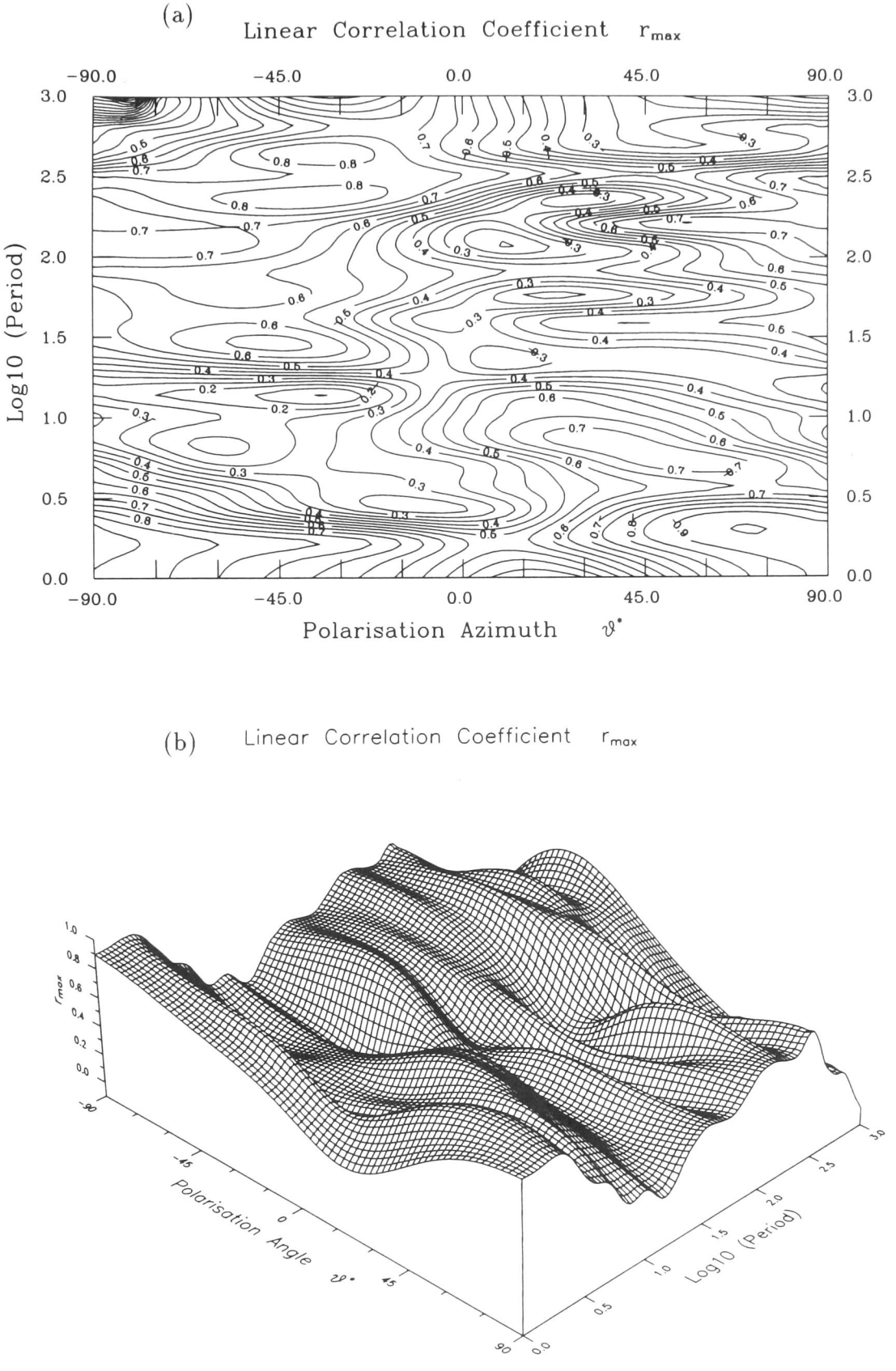

Figure 44: *The BC87 Dataset: Hypothetical event analysis, all periods, polarisations:* $-90°$... $90°$.
a) Contour plot of the linear correlation coefficient r_{max}.
b) 3D presentation of r_{max}.

6.4 Summary

The GDS response functions of the BC87 dataset at long periods (100s - 1000s) are affected by complex 3D induction processes. Since the directions of induction arrows are inconsistent with the regional strike directions found by MT decomposition methods((Eisel & Bahr, 1993; Jones et al. 1993), we applied hypothetical event analysis to the magnetic response functions in order to recover information that is common to all sites. Although a better data quality in the examined period range (100 s - 1000 s) would be desirable, the predicted vertical magnetic fields at all sites reveal common phase angles for polarisations azimuths of the horizontal magnetic field of ca. $-35°$. In this case, the azimuth corresponds to a direction perpendicular to the strike of a the regional conductivity structure. The regional strike is therefore assumed to be 55°.

Since the common phase angles are negative they cannot be correlated with the regional impedance phases. Instead, they imply that the dataset represents a three-dimensional conductivity structure. Contributions from large scale local structures, which may be associated with the resistive Nelson Batholith region, are therefore presumably of a more inductive than galvanic origin in this period range (see also chapter 7).

Due to the geological complexity of the region, the limited spatial coverage, and the deficient data quality at long periods, this dataset might not be appropriate to show the full capability of the method. However the strike direction found is in good agreement with the strike direction determined by decomposition of the MT impedances: 45° (Eisel & Bahr, 1993) or 60° (Jones et al. 1993). They recognized the regional structure as a conductivity anisotropy of the lower crust or upper mantle and correlated the regional strike with the direction of the minor resistivity. The absence of a regional vertical field component in the dataset (i.e. no offset of the phase line) supports this hypothesis.

Thinsheet modelling studies (Ritter & Ritter, 1996; see Appendix E) of the deep crustal conductor (mentioned in section 6.1) at 1000 s confirmed that the induction arrows along the BC87 profile may generally be produced by current deviations around the area that is associated with the resistive Nelson Batholith. Only sites in the (south-) eastern part of the batholith are affected by the form of the deep crustal conductor (L-shaped or oblique). The azimuth distributions and the length variations of the real arrows in the area of the profile indicate that the observed data may rather represent the oblique model (SABC conductor). Also, the direction of the oblique SABC conductor could possibly explain the azimuth of the regional strike found by hypothetical event analysis.

7 3D Modelling of Galvanic Distortion

In the following chapter I investigate the effects of magnetic distortion on vertical magnetic response functions as discussed in theory in chapter 4. The basic physical model is a local 3D conductive anomaly above a regional one- or two-dimensional earth. I will show how the hypothetical event analysis can recover the regional strike direction and at least one of the regional impedance phases. I will also show that elongated anomalies produce a partly galvanic response in the period range, for which their length is of the order of the skin depth of the host material or smaller.

I computed all 3D models with R.L. Mackie's 3D code (Mackie et al. 1994) which uses finite differences and is based on the integral forms of Maxwell's equation. As a part of the Geotools magnetotelluric interpretation package this program is reasonably manageable in terms of model input, computing time and displaying results. In view of the Iapetus dataset in chapter 5, the distorting body was attributed considerable horizontal dimensions and placed in the upper crust. Consequently, the period range studied is between 1s and 10000s. However, it is not the purpose of this chapter to simulate the complex geology of the Iapetus Suture Zone nor to fit the observed magnetic response functions.

The model input consists of 3 parts: (i) a model core containing the 3D structure with a constant horizontal gridsize and layers of increasing thickness (the thickness is always tripled after three layers, see right side of fig. 45); (ii) an expanding outer frame of 2D structures, which should be reasonable continuations of the edge zones of the 3D core (with the same layer thicknesses); and (iii) a layered 1D structure underlying the entire model. To allow for the large scale of the structures involved I chose squares of 10 km $\times$ 10 km for the inner horizontal grid and an initial layer thickness of 1 km (i). For a 3D core of 10 layers a total thickness of 66 km[14] is reached (see fig. 45, right sketch). In order to keep the overall conductivity structure as simple as possible, the 3D core and 2D extension are underlain by a homogenous halfspace of 200 Ωm, as a continuation of the host resistivity of the crust.

I computed three basic regional models: a regional homogenous halfspace, a regional layered earth and a regional two-dimensional earth. In all models, the distorting conductive body is embedded in a more resistive upper crustal host.

For the regional one-dimensional models, I partitioned the 3D core (i) into a 20 $\times$ 20 grid, resulting in a 200 km $\times$ 200 km horizontal plane. In model H (see fig. 45), the resistivity structure of the host does not change with depth. It represents the regional homogenous halfspace model. In model L, a conductive layer of 5 Ωm is emplaced at a depth of 21 km - 39 km in the lower crust in order to generate variations of the impedance phase at long periods. For models H and L the resistive material of the 3D core (i) is continued into the outer 2D extension (ii) in all four directions.

The regional two-dimensional models require a rectangle of 34 $\times$ 50 cells (340 km $\times$ 500 km) for the 3D core (i) in order to construct a regional strike azimuth of ca. N125°E. (see fig. 46, left). A regional conductive structure of 5 Ωm is placed at a depth of 21 km - 39 km on the southern side of the 125°-striking boundary.

[14] (3 $\times$ 1 km) + (3 $\times$ 3 km) + (3 $\times$ 9 km) + 27 km

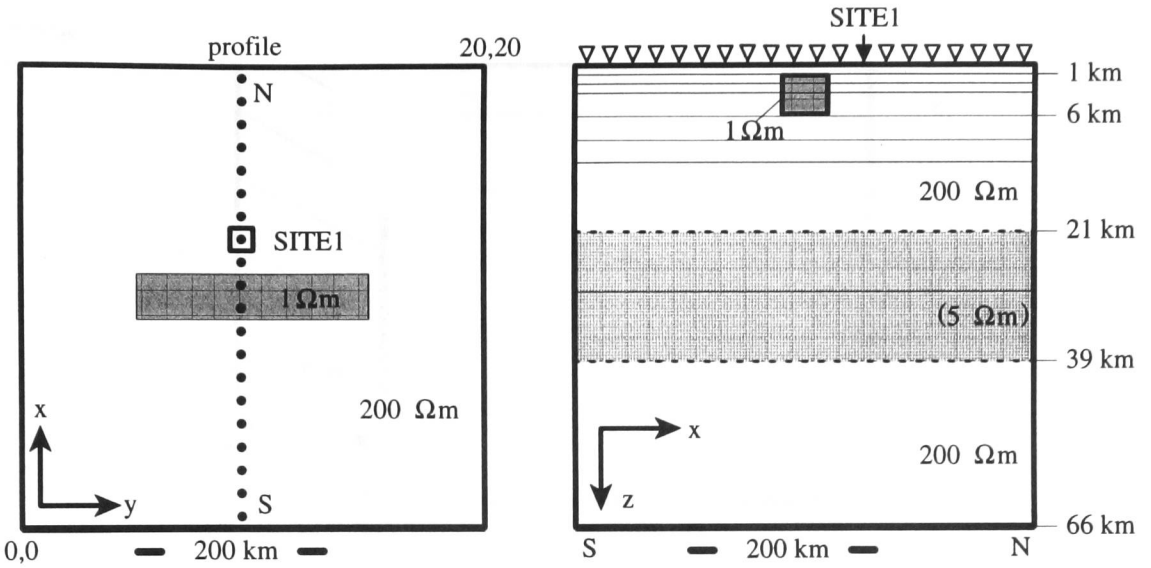

Figure 45: *3D model for a regional homogenous 1D earth with an embedded local conductive anomaly (model H). The dimensions of the local anomaly (grey box) are: 100 km (y) × 20 km (x) × 5 km (z). The dashed layer indicates the position of the lower crustal conductor (layers 8,9) used in model L.*

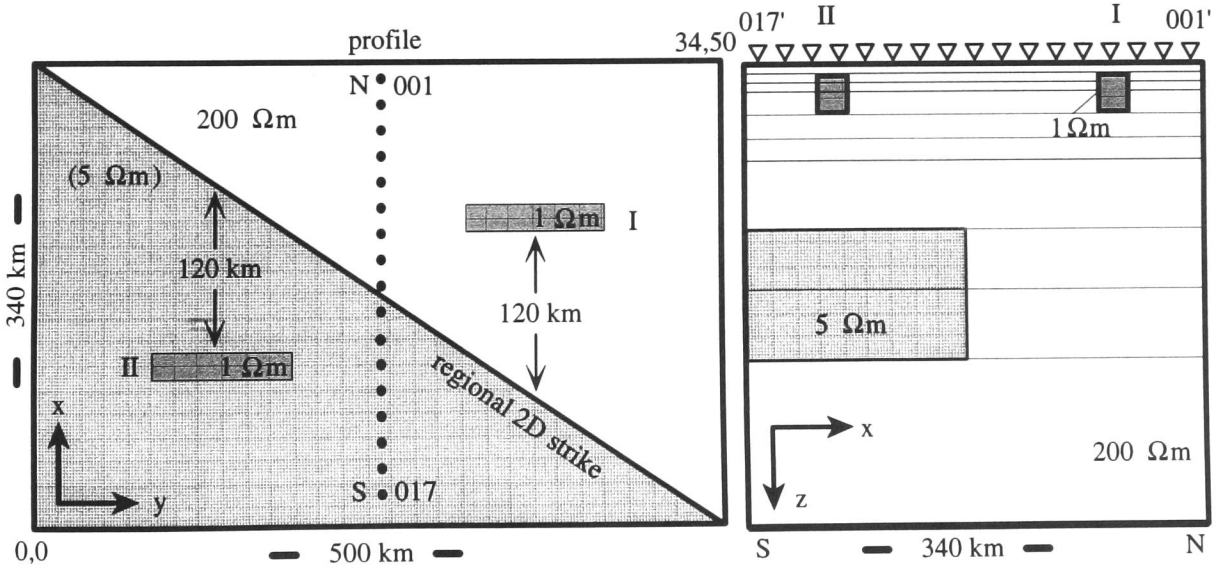

Figure 46: *3D model for a regional 2D earth with an embedded local anomaly. The regional lower crustal structure (5 Ωm) is located south of the diagonal line in the left sketch at a depth of 21km (layers 8,9). The local anomaly has the same properties as in the above regional one-dimensional model. The top view on the left side shows the horizontal positions of the local anomaly (1 Ωm) north (body I) and south (body II) of the regional 2D contact (section 7.2). The diagram on the right side is not a proper cross-section in x-direction, but shows the relative vertical positions of the local anomalies with respect to the deep 2D conductor. The primed site numbers on the right sketch (001' - 017') mark the projected position of the central profile. The strike direction of the local anomalies is 90°, the regional strike is 125°.*

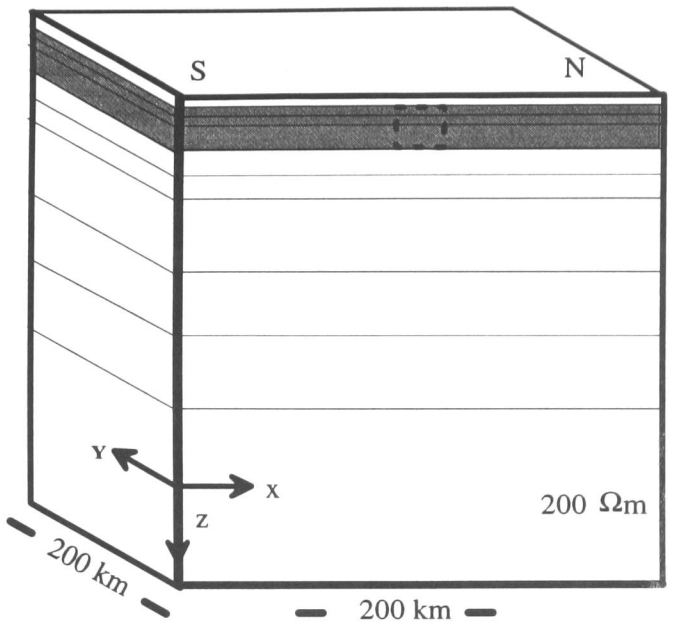

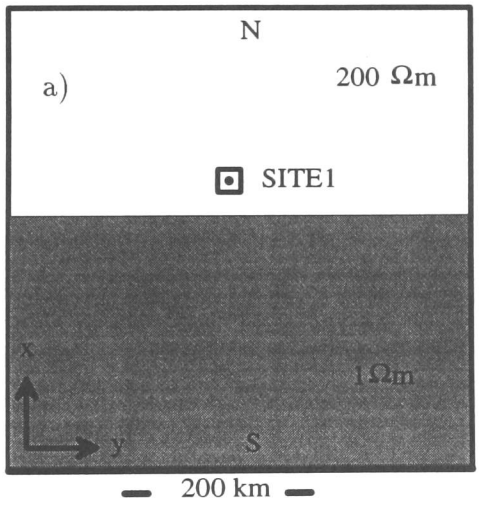

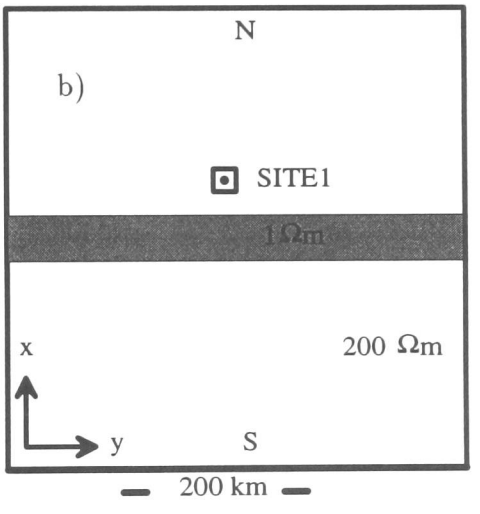

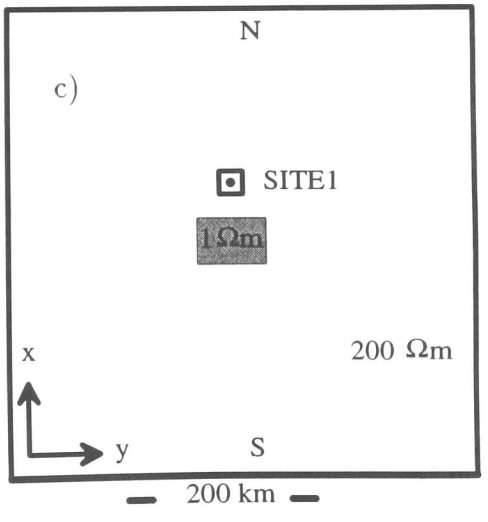

shapes of local anomalies:

a) 1/2 sheet

b) channel

c) short body: 20 km × 30km

Figure 47: *Modelling series (section 7.1.1): regional 1D model and various forms of the upper crustal anomaly (a - c). The vertical position of the anomaly is the same for each model. It is marked in the top figure: 1 km - 6 km (layers 2,3,4).*

In order to concentrate on a clear regional two-dimensional response, I omitted any deeper structures (mantle), i.e. the regional two-dimensional structure is embedded in a halfspace of 200 Ωm. The grid geometry also facilitates a simple 2D extension (ii) of the 3D core (i): the homogenous resistive host is continued to the north and east, while the conductive deep structure is continued to the south and west.

The 3D local anomaly in the principal models presented in figures 45 and 46 is an elongated body of very low resistivity (1 Ωm) with the dimensions: 100 km (y) × 20 km (x) × 5 km(z). It is buried at a depth of 1 km - 6 km and strikes eastwards (in the y - direction). The distorting body is positioned either above the regional one-dimensional earth (model H and L in fig. 45) or, for the regional two-dimensional models, at variable distances on either side of the 2D contact (fig. 46, left). Note that the areas north and south of the regional 2D boundary have the same variation of conductivity with depth as the regional one-dimensional models H and L (right diagrams of figures 45 and 46).

The variety of models was necessary to understand and distinguish induction and distortion processes in the magnetic response functions. The following sections examine the dependency of the vertical magnetic response function on the size of the conductive body, show the effects of distortion on induction arrows, investigate the magnetic phase, and demonstrate the results of hypothetical event analysis.

7.1 Regional 1D models

The simplest model involves the upper crustal conductivity anomaly (1 Ωm) embedded in a homogenous halfspace of resistivity 200 Ωm (model H). We expect that galvanic distortion occurs at periods, at which the skin depths reach well below the local body. However, in practice we cannot be sure what *'well below'* really means. Since the rules to determine the skin depth (eqn. 19) are based on a homogenous halfspace model, they might not be applicable in for laterally bounded 3D structures. Before discussing model H (and L) in detail in section 7.1.2, I investigate the relation between the size of an anomaly and the period range where distortion dominates the magnetic response functions. This study involves three differently shaped conductive bodies.

7.1.1 Three variations of the upper crustal anomaly

I modified the basic model H in such a way that the upper crustal anomaly has different horizontal extensions. In all three variations (see fig. 47), the anomaly has a fixed vertical thickness of 5 km and a resistivity of 1 Ωm, and it is placed at a depth of 1km. The strike direction is east-west. The local anomaly takes the following forms :

a) laterally bounded 2D sheet (*1/2 sheet*);
b) *quasi* - infinite channel of 20 km width and 200 km length;
c) *short* 3D body of 30 km length and 20 km width;

The first two models represent *local* 2D structures, whereas in the third model the local anomaly is truly 3D. The impedance phases, the magnetic phase and the

magnetic response functions for a location 15 km from the centre of the northern lateral boundary (SITE1) are shown in figures 48 (a,b,c).

Before we look at the phases and response curves, it is useful to gain a general idea of the period range, for which the source field diffuses below the bottom interface of the local anomaly. The approximate skin depths of a homogenous halfspace with a resistivity of 200 Ωm are:

0.1s	~	2.2 km	100s	~	70 km
1s	~	7 km	1000s	~	225 km
10s	~	22 km	10,000s	~	700 km

For the host material, a depth of 1 km is reached at a period of T = 0.02s, while 6 km is reached at T = 0.72s. These two depths correspond to the top and the bottom interfaces of the local anomaly. The conductivity-thickness product at a depth of 6 km is 0.03 S. The inclusion of a low-resistivity *layer* of 1 Ωm between 1km and 6km increases the conductance to 5.005 S. This value corresponds to an equivalent surface layer of 6 km thickness with an integrated resistivity of 1.2 Ωm. Hence, if we substitute the local anomaly by a layer, the bottom interface of this layer is actually reached at a period of T_s = 120s (instead of 0.72s for the host). This implies that an inductive response of the local anomaly might be observed up to this period, whereas distortion effects are likely to become dominant in the longer period range. The question arises, whether this particular period T_s can be traced in the magnetic data and if so, how it changes if we alter the shape of the local anomaly.

With this question in mind, we can now start to discuss the curves in fig. 48. The model types in the first, middle and bottom row are stated above each of the graphs; they are the same as already introduced in fig. 47 (a,b,c). The diagrams on the left side of fig. 48 show the impedance phases (φ_E and φ_B), and the magnetic phase φ_m, whereas the diagrams on the right side present the real and imaginary parts of the $\mathcal{A}$-component of the magnetic response function. As the vertical magnetic field is generated by the current flow along the strike direction of the conductive structure (E_y due to B_x), the $\mathcal{B}$ component accounting for the parallel magnetic field (B_y) equals zero. Hence, φ_m actually represents the phase of $\mathcal{A}$.

A comparison of the curves on the right side reveals that the real and imaginary parts of $\mathcal{A}$ have generally the same form for all three local anomalies: The negative minimum of the imaginary parts precedes the positive maximum of the real parts, and the imaginary parts cross the zero-line at the same period, at which the maximum of the real parts occurs. Then, the imaginary parts approach the positive amplitudes of the real parts and at longer periods, both parts converge towards zero.

However, the amplitudes of $\mathcal{A}$ vary considerably between the local 2D anomalies (i.e. the 1/2 sheet (a) and the channel (b)) and the local 3D structure (c). While the local 2D anomalies (a) and (b) have both very similar and strong magnetic response functions with amplitudes over 0.5, we can observe only a weak response for the short 3D body (maximum of the real part: 0.1). Furthermore, in the diagrams of both local 2D anomalies, the imaginary parts of $\mathcal{A}$ cross the zero-line close to T_s, at ca. 120s. As a consequence, the magnetic phase also passes the 0°-line at this period. However, for the short 3D body (c), φ_m equals 0° at a distinctly shorter period (at ca. 10s).

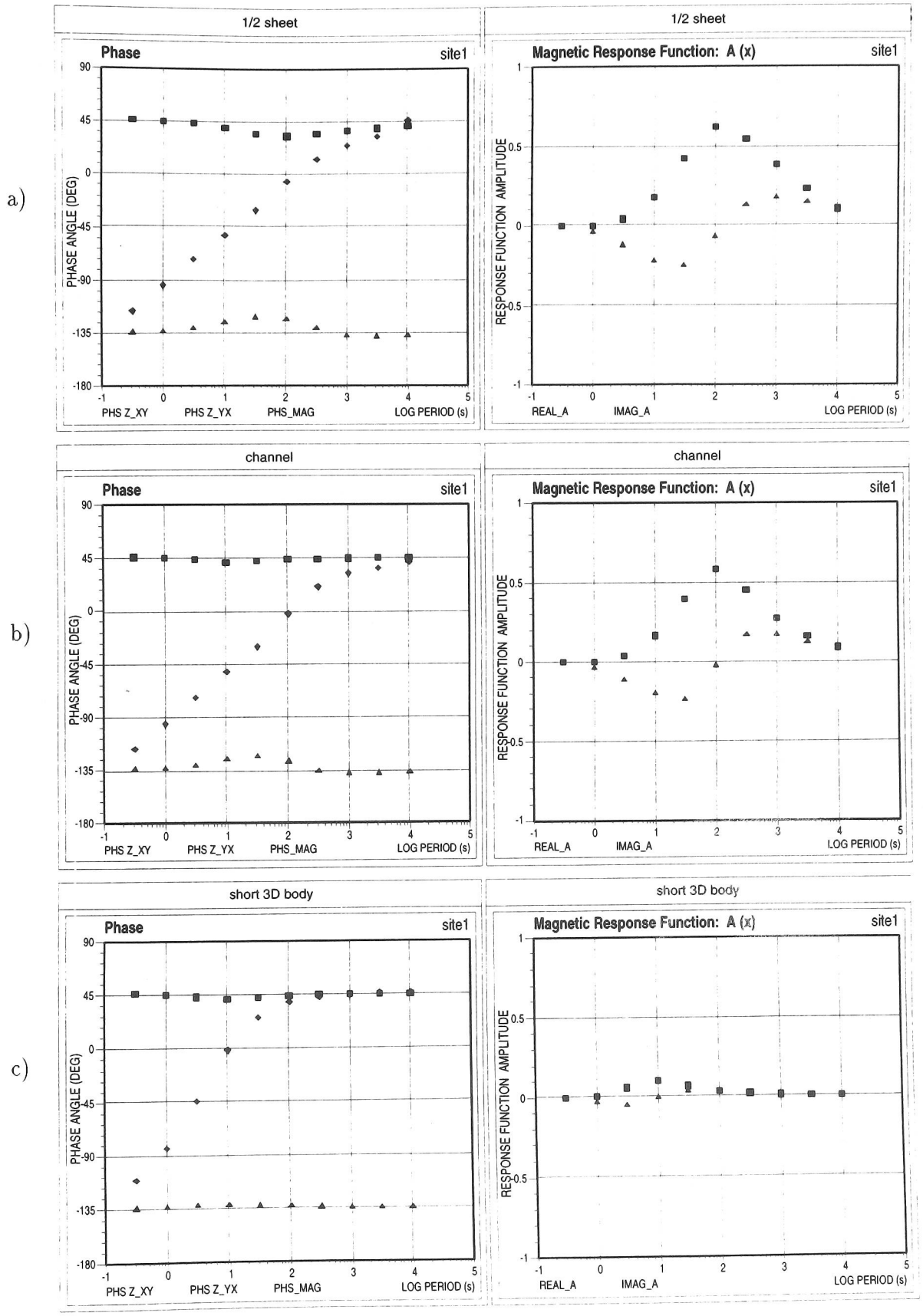

Figure 48: *Three variations of the upper crustal anomaly (see fig. 47): Impedance and magnetic phases (left); magnetic response functions, $\mathcal{A}$-components (right).* Note that on the phase plots, the squares mark the phases of the B-polarisation impedances (here: xy - components) while the triangles represent the phases of the E-polarisation impedances (here: yx - components). The magnetic phases (of $\mathcal{A}$) are printed as diamonds. On the magnetic response function plots, the squares mark the real parts of $\mathcal{A}$ whereas the triangles mark the imaginary parts. The conductive anomaly strikes in y - direction.

Obviously, the period at which the magnetic phase passes through 0° is controlled by the size of the anomaly; I call this particular period T_o. As T_o is very similar for both local 2D anomalies and because it coincides with T_s (which was calculated originally for the equivalent surface layer) we may assume that T_o marks the period of maximum induction in the conductive body of any size.

For periods $< T_o$, the magnetic phase is negative. From values $< -90°$ at the shortest periods (before the fields 'see' the anomaly), φ_m increases continuously as the period increases towards T_o. In this period range, induction inside the local anomaly is the dominant process. As a consequence, a phase difference emerges between the electric and the induced anomalous magnetic field. This phase difference can take values in the order of the impedance phase (i.e. the phase difference between the magnetic source field and the induced electric field) and eventually compensates it at T_o, where we observe $\varphi_m = 0$.

At longer periods $> T_o$, when increasingly more currents are induced in the surrounding homogenous halfspace, the electrostatic field between the local interfaces causes a spatial deviation of these *regional* currents towards and into the local anomaly. The phase difference between the regional electric field and its anomalous magnetic field vanishes and therefore, the magnetic phase takes positive values. φ_m gradually approaches the regional impedance phase φ_Z in this period range of *transition*. Although the skin depths of the host material at these longer periods reach well below the Earth's crust, we can still observe significant amplitudes of the magnetic response functions due to the upper crustal structure. As the anomalous magnetic field caused by galvanic effects is in-phase with the regional electric field (see chapters 3 and 4), the magnetic phase eventually equals the impedance phase of 45°, in the period range where distortion is the predominant process.

In contrast to the 1/2 sheet anomaly (a), the channel (b) is sensed solely by the data of the E-polarisation response (φ_E and $\mathcal{A}$ due to E_y, B_x, B_z), due to its extreme extension as a conductor in one direction. Because this E-polarisation response differs only slightly from that of the 1/2 sheet anomaly (a), we may conclude that the magnetic response (E-polarisation) depends only little on the horizontal width of the 2D structure. Instead, it seems to depend strongly on the length of the structure, as T_o is much smaller for the short 3D body (c). Also, the period range of induction and the period range of distortion are shortened considerably (fig. 48c), and the amplitudes of $\mathcal{A}$ are very small.

As expected, the length of the body strongly controls the period range in which we can see its inductive response. We should therefore be able to make conclusions on the size of the scattering body with respect to the skin depth of the host medium from the period, at which $\varphi_m \approx \varphi_Z$. For the short 3D body (c) this is the case at ca. T = 100s. At this period, the skin depth is 70 km, which is more than twice the length of the short body (30 km). The question arises, whether generally a 3D body needs to be shorter than half the skin depth of the host medium to produce a galvanic response at a given period, and whether this assumption holds also for a *layered* regional conductivity distribution. Does φ_m still approach the regional impedance phase, which for a layered earth would be different from 45° ? In the following section, I compare the responses of an elongated anomaly of 100 km length in a homogenous halfspace and over a layered lower crust (models H and L).

7.1.2 Model H and model L

Fig. 49 shows the results of an elongated 3D anomaly of 100 km length and 20 km width for SITE1. As sketched in fig. 45, the anomaly is buried in a homogenous halfspace (model H) or over a layered lower crust (model L). Compared to the local 2D and 3D anomalies discussed in the previous section 7.1.1 (fig. 48), the magnetic response of model H on the right side of fig. 49 lies in an intermediate period range, somewhere between the channel model (fig. 48b) and the short body model (fig. 48c). Its amplitudes are smaller than for the channel, and T_o is shifted to shorter periods (ca. 50s). For T $\geq$ 100s, the magnetic phase φ_m approaches 45°. At 300s it has already reached ca. 35°, at 1000s it equals the regional impedance phase.

The skin depth of the homogenous host for a period of 300s is 122 km and for 1000s it is 225 km. This implies that the body produces a partly galvanic response ($\varphi_m \longrightarrow \varphi_Z$) from a period, at which its scale length is of the order of the skin depth of the host medium. This estimation does not apply strictly for the short body in the previous section due to its almost square extension. But if we consider an elongated, *quasi* - 2D structure to be the cause for magnetic distortion at long periods, this structure may have an extension of 100 km or more.

Model L on the left side diagrams of fig. 49 shows that the magnetic response is strongly affected by the lower crustal conductor. Not only are the amplitudes of real and imaginary parts smaller than for the halfspace model H, but also the induction range of the 3D body shortens to periods below 30s. The magnetic phase passes the 0° - line at ca. 20s (T_o). Towards longer periods, φ_m approaches the impedance phases with values below 45°. The regional impedance phase is actually reached at 3000s, but the amplitudes of the magnetic response functions are very small at these long periods. As a consequence, we may conclude that, although the period range of induction is shortened considerably, the transition range of mixed induction and galvanic distortion is extended due to the increased integrated conductivity of the host medium. The shape of the magnetic phase curve at periods $> T_o$ clearly indicates that the regional impedance phase is not 45°, i.e. the regional structure is not a homogenous halfspace. From 3000s on, we can observe a purely galvanic response. At this period, the skin depth of the combined host and lower crustal resistivity (10.5 Ωm) is 90 km, which is of the order of the length of the upper crustal body.

Until now, I have only presented the data at a single site. We still need to examine the spatial variations of the magnetic phase. How does φ_m change if we look at more sites located at different distances and angles to the 3D body? Fig. 50 shows the magnetic phase curves of 20 sites on a **profile** in the x-direction across the centre of the anomaly. The diagrams on the left and right side refer to the models L and H, respectively (as in fig.49). The site spacing is 10 km. The profile extends 100 km to the north and south of the elongated body (see fig. 45).

We can observe two groups of data points in each diagram. For one group, the data converge to angles around 45°. They belong to the set of 10 sites located north of the centre of the body. The other group consists of the 10 sites south of the anomaly. Their phases converge towards the $-135°$ - line. This difference of 180° is due to the opposite signs of B_z on either side of the anomaly. For T $<$ 3s, the

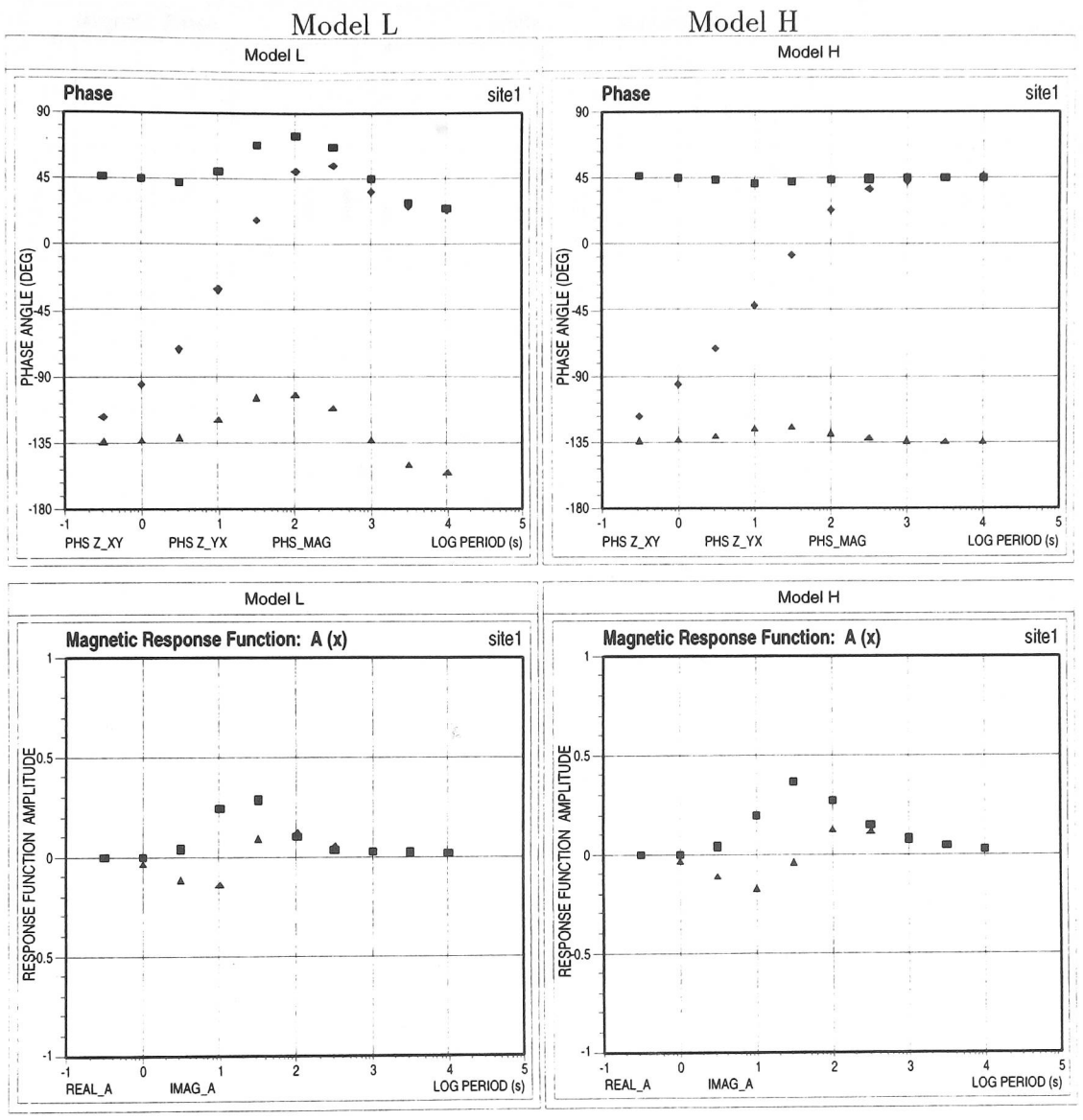

Figure 49: *Impedance and magnetic phases (top) and magnetic response functions $\mathcal{A}$ (bottom) for Model L (left side) and model H (right side):*
The inductive response of the elongated body in model H lies in an intermediate period range, somewhere between the channel (fig. 48b) and short body (fig. 48c) responses. Its magnetic phase shows a galvanic response for $T \geq 300s$. In model L, we observe a shortened period range for the magnetic response function (compared to model H). The magnetic phase approaches the impedance phase for $T \geq 100s$. These two and the previous local 3D structures (fig. 48c) produce a galvanic response as part of the magnetic response from a period, at which the skin depth of the host is of the order of the scale length of the anomaly.

The models L and H are shown in this particular sequence, because the left and the right side can then be compared directly to sites on the south and north side of the later regional 2D model, e.g. fig.56. (For marker conventions see fig. 48)

Model L Model H

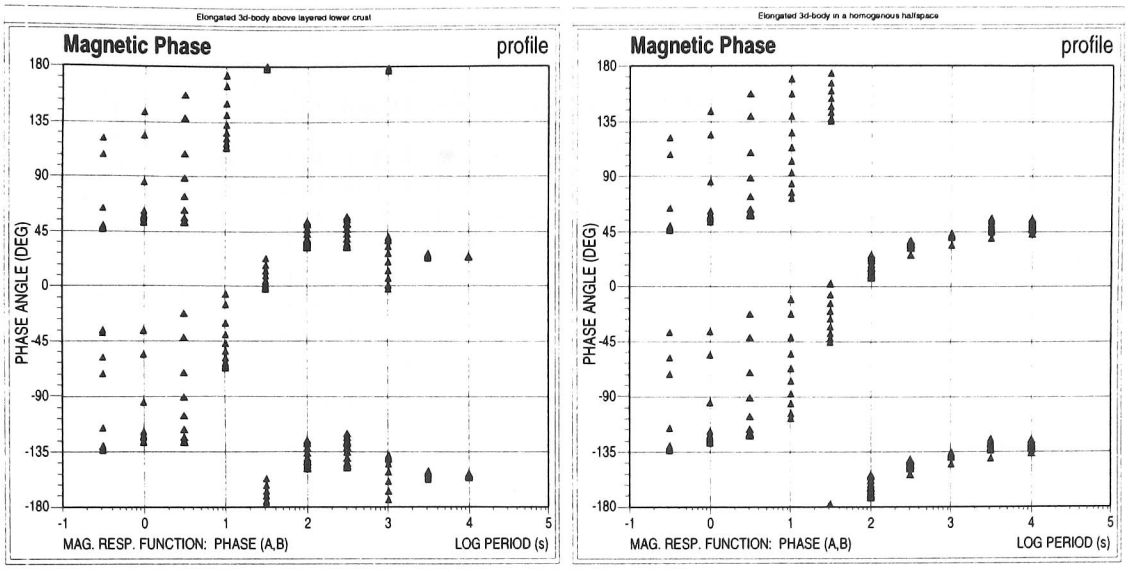

Figure 50: *left side: model L ; right side: model H The points correspond to 20 sites on a profile across the center of the anomaly (see fig.45). Magnetic phases north of the body converge towards* 45°, *phases sites south of the body converge towards* $-135°$. *The data show no differences between the models up to 3s. From 30s (left) or 100s (right) the phases of all sites converge and approach the respective impedance phases. The phases differ significantly between sites only in the range of maximum induction (3-30s).* **(For marker conventions see fig. 48)**

magnetic phases are obviously independent of the regional model because the phases on both diagrams are very similar. The phases along the profile are uniform at these short periods, apart from the 2-3 sites that are closest to the boundaries and show higher phase angles. The phases scatter considerably stronger in the period range 3s - 30s, the period range of maximum induction (SITE1, fig. 49).

In both models, the phases of all sites converge after having passed the 0° - line (T_o). On the left side, the phases are more scattered in the transition range where φ_m approaches 45° ($-135°$) at 100s - 300s. Interestingly, the data scatter even more at T=1000s, before they collapse to show one very distinct phase value of ca. 25° (or $-165°$) at the longest periods. For the homogenous halfspace on the right side, the data converge more steadily towards phase angles around 45° ($-135°$). In both models, the magnetic phases of all sites on the profile approximate the respective regional impedances uniformly in the period range T > 100s, where distortion is thought to be the dominant process.

The results of models H, L and the previous three models (section 7.1.1) suggest that a body causing a galvanic response at long periods may be as large as the skin depth in the host medium. If we consider that distortion starts to affect the magnetic response function for periods slightly longer than T_o (i.e. as soon as φ_m approaches the impedance phase in the transition range), we can assume that the body's extension can be even larger than the skin depth. Even a partly galvanic response allows us to make assumptions on the regional resistivity distribution from the phase angle indicated by φ_m.

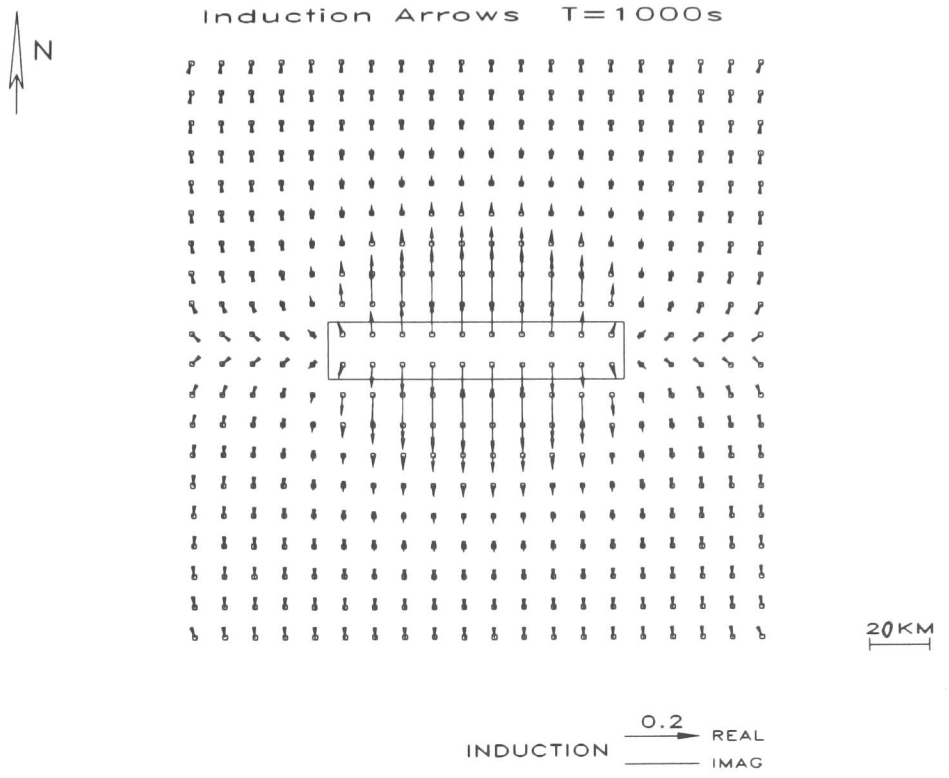

Figure 51: *Model H: Induction arrows of 400 sites due to the 3D body at 1000s. Its position is marked by the box in the centre of the figure. The imaginary arrows are of the same length and direction as the real arrows, therefore they cannot be distinguished in this figure. The area has an extension of 200 km × 200 km.*

7.1.3 Array data - Hypothetical event analysis

In this section, I investigate the magnetic response functions of models H and L at an array of 400 sites located in an area of 200 km × 200 km. The site spacing is given by the horizontal cell size of the 3D core (i): 10 km (see fig. 45). Fig. 51 shows the real and imaginary arrows of model H at a period of 1000s (skin depth in the host: 225 km). Since the magnetic phase is close to 45° at this period, the real and imaginary arrows are of similar length and direction. The arrows point perpendicular to and away from the current flow in the strike direction of the anomaly. Their amplitudes decrease with increasing distance. The arrows are longest for sites parallel to the centre part the anomaly, because in this area, they sense it as a *quasi*-2D structure. At the left and right ends of the body, the induction arrows are smaller and their directions tend to point away from the boundaries in x - direction.

The results in the previous sections led to the assumption that the magnetic response functions in this period range are dominated by galvanic distortion due to the local body. The regional currents are induced in the more resistive host (homogenous halfspace) and concentrated inside and near the local, upper crustal anomaly.

Model H

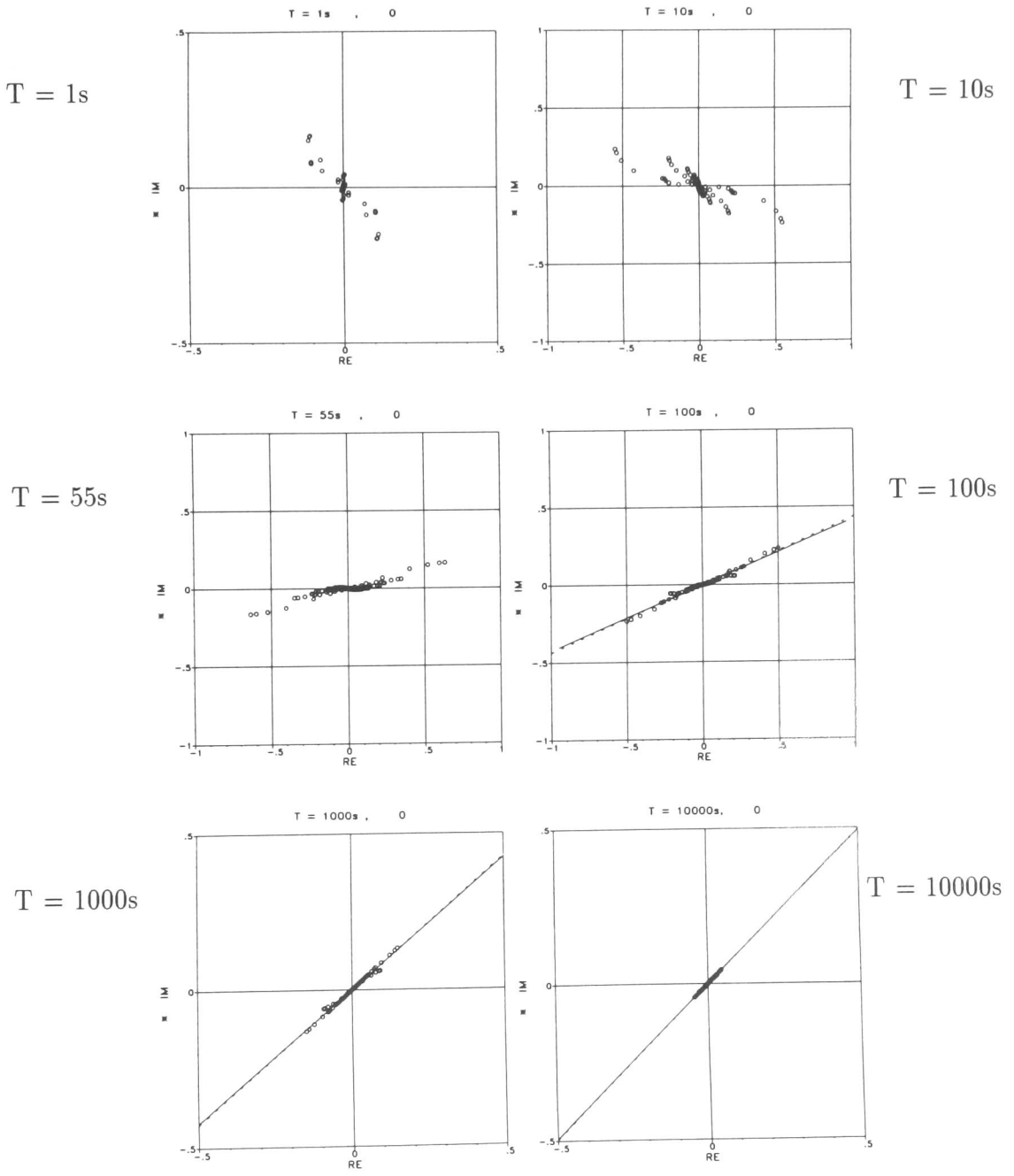

Figure 52: *Array data (model H): Hypothetical event analysis at 6 periods, the polarisation azimuth of the horizontal magnetic field is $\vartheta^{\star} = 0°$ in all diagrams. The elongated, conductive anomaly is embedded in the homogenous halfspace (model H). For $T \geq 100s$, the predicted vertical fields arrange on a phase line which plots closer to the regional impedance phase (45°) as the period increases and the galvanic response becomes more dominant.*

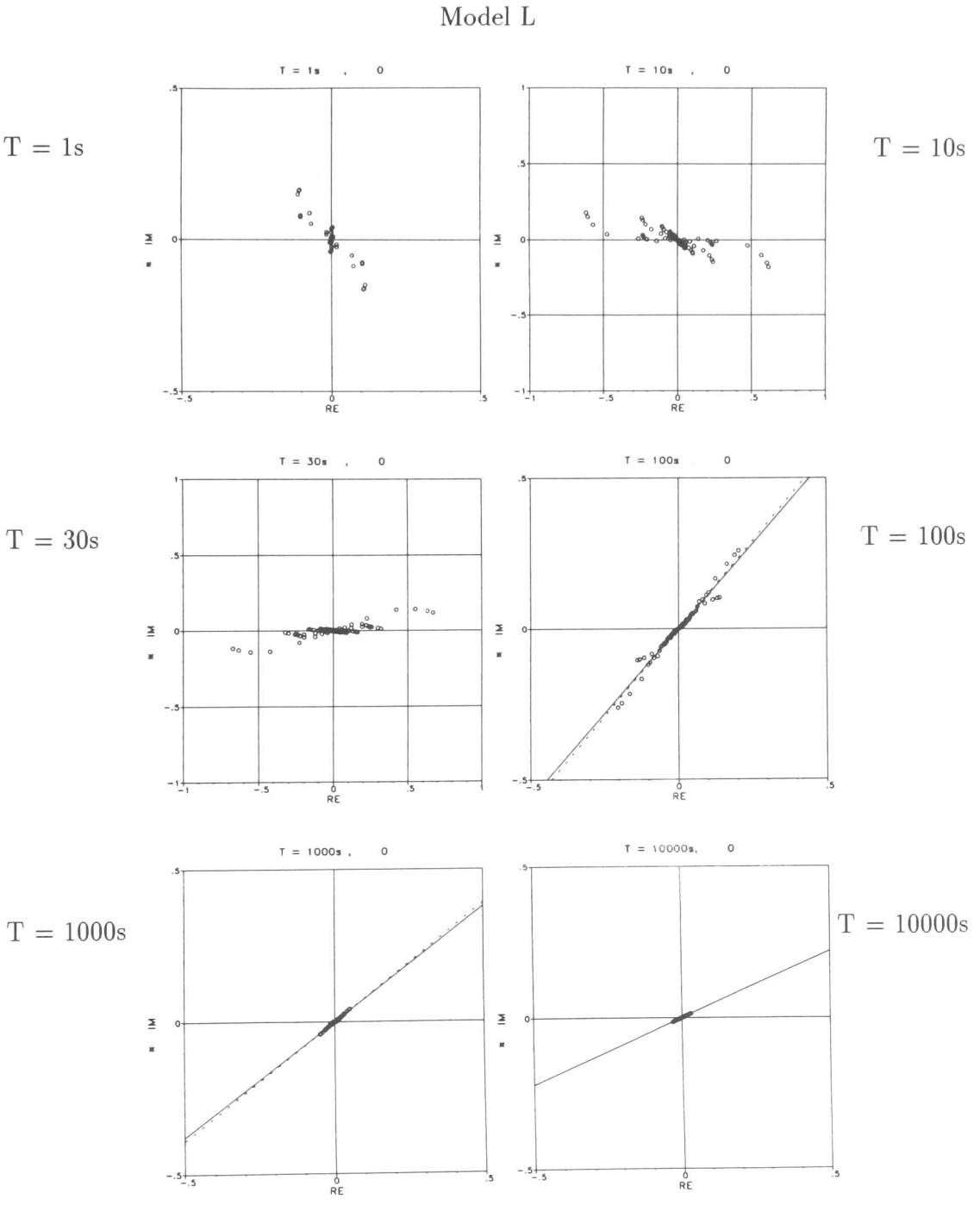

Figure 53: *Array data (model L): Hypothetical event analysis at 6 periods, the polarisation of the horizontal magnetic field is $\vartheta^* = 0°$ in all diagrams. The elongated, conductive anomaly is located above a layered lower crust (model L). For $T \geq 100s$, the predicted vertical fields plot on a phase line which approximates the regional impedance phase of the layered model, as the galvanic response becomes more dominant in the period range of transition. For the actual impedance phase of this model refer to fig. 49*

In order to extract the phase information contained in the magnetic response functions of the array I applied hypothetical event analysis. We have already seen in the previous section (7.1.2, fig. 50) that the sites on a profile show remarkably uniform phases in the period range where distortion processes dominate the data. The Argand diagrams of fig. 52 (model H) and fig. 53 (model L) show the predicted vertical magnetic fields B_z^p of all sites for a northward polarisation ($\vartheta^\star = 0°$) of the horizontal magnetic field for 6 chosen periods. Since the data are given in xy - coordinates (which is also the coordinate system of the anomaly) and the hypothetical event has unit amplitude, the predicted values B_z^p at this polarisation are identical to the $\mathcal{A}$ - component of the magnetic response functions. The phases of B_z^p are therefore directly comparable to the magnetic phases shown in the previous section (fig. 50). Common phases can be recognized when the data points plot along lines in the complex plane of the Argand diagrams. For the respective impedance phases refer to fig. 49.

One period is chosen for each decade and additionally, the period at which most data show phases around 0°, i.e. T=30s for model L and T=55s for model H. As already discussed for the profile data (fig. 50), we can see no differences between the two regional models at T = 1s. At this period, the magnetic response functions are caused by the onset of induction inside the anomaly and their amplitudes are still very small at most sites. At T = 10s, a difference between the two regional models can be observed in the inclination of the clusters of points near the origin (0,0). These points belong to the sites furthest away from the anomaly (i.e. the majority of data). They are the least influenced by the 3D anomaly. The data with the largest amplitudes, on the other hand, are from sites located closer than ca. 20 km to the boundaries. Their scatter reflects the induction process within the anomaly.

The data distribution becomes more linear around the period at which the phases cross the 0° - line (real axis). For periods $\geq$ 100s, the data arrange clearly on lines showing the common phase, as we enter the period range where distortion plays an increasing role. The high degree of linearity can be assessed from the minute difference of the two regression lines. In this period range of *transition*, the gradient of the common phase line approaches the regional impedance phase. For model H (fig. 52), the halfspace phase of 45° is almost reached at 1000s. The phase line has an inclination of 40.3° $\pm$ 0.2°. At T = 10000s, the gradient eventually equals the impedance phase, even though the amplitudes of B_z^p (or $\mathcal{A}$) are small (< 0.1).

For model L (fig. 53), the gradient of the common phase line at 100s (*transition* phase) is already significantly steeper than the gradient of model H. The line indicates an angle of 48.9° $\pm$ 0.5° at this period, but has not yet reached the high regional impedance phase of 80° (top interface of deep conductor). However, for longer periods, the phase line of model L falls distinctly below 45°, due to the bottom interface of the deep conductive layer. At T = 10000s, the amplitudes are even smaller than those of model H, but the linear distribution is perfect and the phase line (23.8°) is very close to the regional impedance phase of $\sim$ 25° (see fig.49).

Until now, we have only considered the northward polarisation (i.e. the $\mathcal{A}$ component), since the response to the eastward polarisation ($\mathcal{B}$ component) is zero at most observation points. Only at sites located at the eastern and western limits of

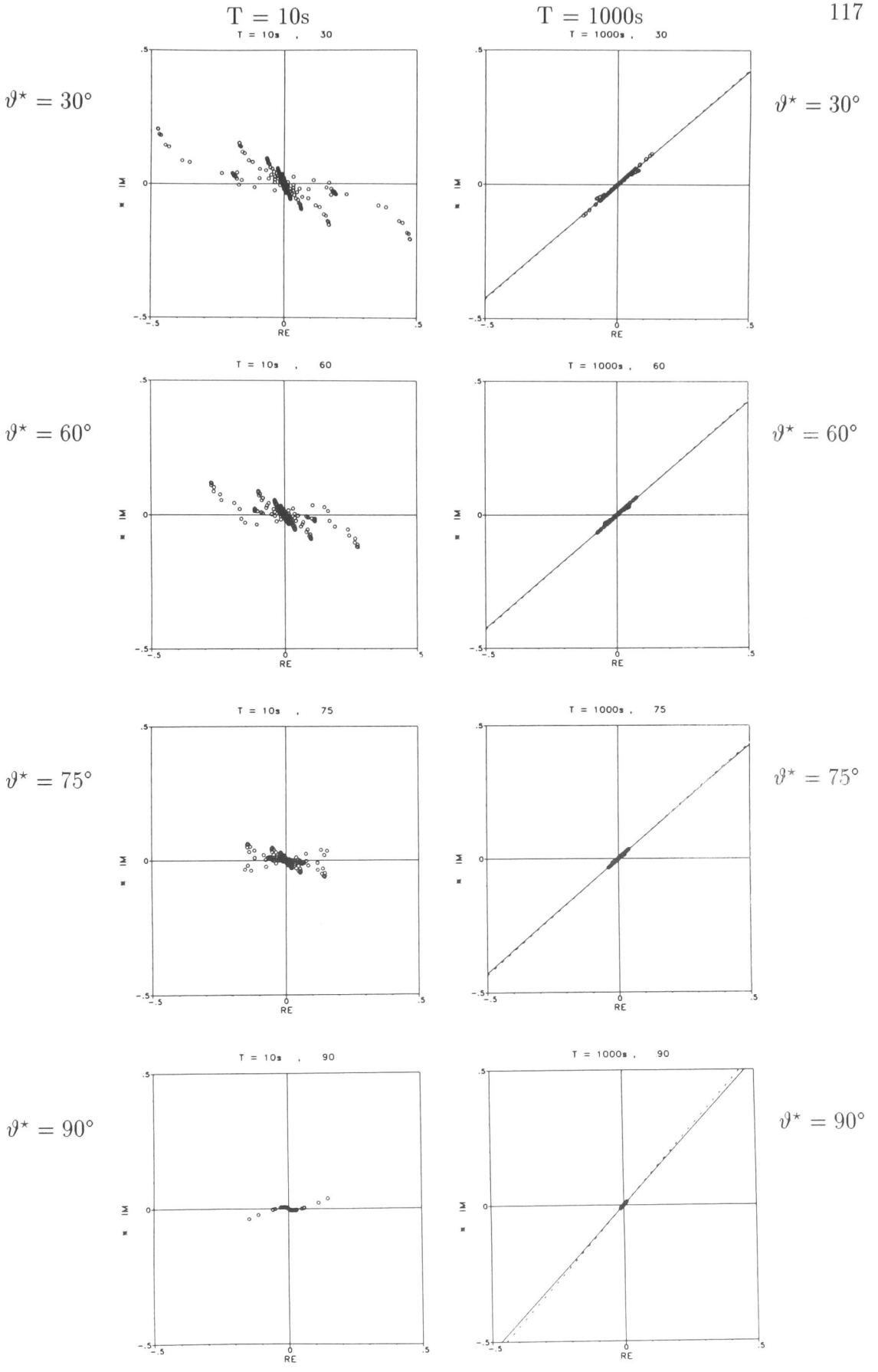

Figure 54: *Array data (model H): Hypothetical event analysis at T=10s (left) and T=1000s (right), the polarisation azimuth of the horizontal magnetic field $\vartheta^\star$ increases from top to bottom. For $\vartheta^\star = 0°$ refer to fig. 52. In the period range of distortion (right side), the fitted phase line is independent of the polarisation azimuth, except for directions very close to the local strike (90°).*

the 3D body, does the parallel magnetic field contribute to the generation of a vertical magnetic field. Therefore we observe a $\mathcal{B}$ component of the magnetic response functions in that area, though with a small amplitude due to the small width of the anomaly. If we change the polarisation azimuth gradually from 0° (x - direction) to 90° (y - direction), the contribution of the $\mathcal{B}$ component to the resulting predicted vertical field should increase, while $\mathcal{A}$ decreases, until eventually B_z^p equals $\mathcal{B}$ at $\vartheta^\star = 90°$.

Fig.54 shows this for periods 10s and 1000s. The resulting predicted values are shown at polarisations 30°, 60°, 75° and 90° of the horizontal magnetic field. Because $\mathcal{B}$ is so small, the amplitudes of the data points decrease with increasing polarisation angle. The general distribution, however, does not change dramatically for $\vartheta^\star < 60°$. At T = 10s, where the inductive response of the body is strong, the contribution of the $\mathcal{A}$ - component gradually decreases for $\vartheta^\star \geq 60°$. When the horizontal magnetic field is directed parallel to the strike of the body ($\vartheta^\star = 90°$), the distribution of the predicted vertical field (now equivalent to $\mathcal{B}$) is distinctly different from that at a perpendicular azimuth ($\mathcal{A}$ - component) at the same period.

For T = 1000s, where the galvanic response strongly outweighs the inductive response, we expect the resulting phases to be the same for all polarisations of the horizontal magnetic field (chapter 4). Indeed, the gradient remains virtually unchanged (around 40°) up to a polarisation azimuth of 75°. Only for polarisations near 90° (±10°) does the phase line change its gradient to values slightly above 45°. At the same time, the linear correlation is slightly decreased, and the amplitudes of the predicted values are very small. This is due to the fact that only a fraction of the regional current is forced to the x - direction (i.e. perpendicular to the local strike).

For conductivity anomalies, which are not so elongate in one direction, e.g. the short body discussed in section 7.1.1, the amplitude of the $\mathcal{B}$ component (not shown in fig. 48c) is almost the same as the $\mathcal{A}$ component. Therefore, B_z^p does not vanish for any azimuth $\vartheta^\star$ and the phase is found - independent of the polarisation - close to the impedance phase in the period range of distortion (T = 100s, fig. 55).

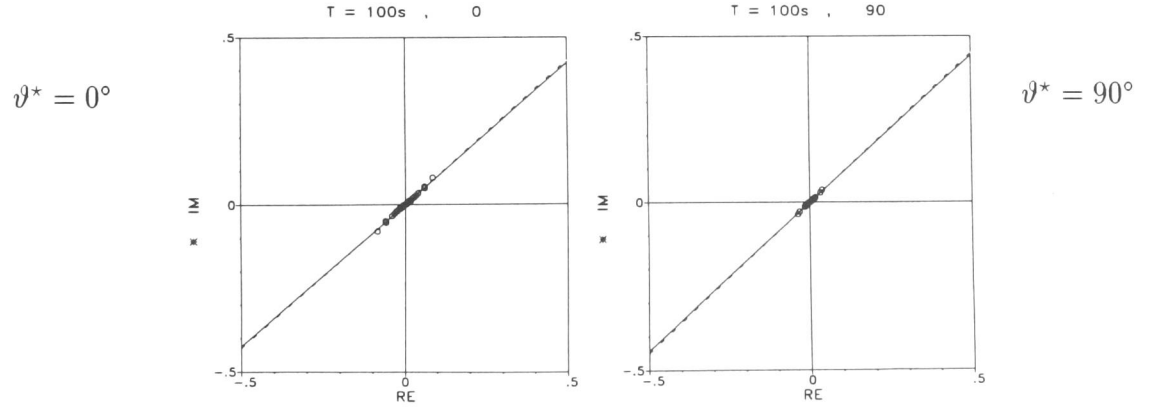

Figure 55: *Array data (short 3D body, see section7.1.1): Hypothetical event analysis for T = 100s at perpendicular polarisations ($\vartheta^\star = 0°, 90°$). $\varphi_Z \approx 45°$.*

7.2 Regional 2D models

The modelling studies in the previous sections show that the magnetic response of the upper crustal anomaly depends strongly on the conductance of the surrounding medium, the regional structure. In this section, I investigate the regional two-dimensional model presented in fig. 46. Fig. 56 shows the phases and magnetic response function component $\mathcal{A}$ of two sites located 35 km to the north and south of the regional 2D contact. The data for these two diagrams were obtained from a model featuring only the 2D regional structure of the lower crust, *without* including an upper crustal 3D body.

At the site north of the contact, the lateral 2D boundary can be detected by the difference of the two impedance phases in a period range 20s - 2000s. At longer periods, the two impedance phases are equivalent (ca. 40°, −140°). For the southern site, we can observe an impedance phase difference at all periods > 500s ($\varphi_B \sim 40°$, $\varphi_E \sim -150°$). The lateral conductivity contact produces a magnetic response for periods > 10s on both sides. On the more resistive northern side, the magnetic phase passes the 0° - line at slightly shorter periods ($T_o = 2000$s) than on the southern side ($T_o = 3000$s). At the longest periods, distortion due to the deep 2D structure becomes visible, as the magnetic phase approximates the regional impedance phases on both sides. On the northern side, this transition phase reaches slightly larger angles according to the higher phase of φ_E.

The different phases of the regional impedances are an indication for a regional two-dimensional conductivity distribution. For our regional 2D model, the northern and the southern 2D period ranges, where we can actually see phase differences, overlap at 500s - 2000s. If we aim to detect the phase difference from the distorted magnetic response functions with hypothetical event analysis, we have to make sure that the upper crustal anomaly produces a galvanic response in the interesting period range. The elongated conductive anomaly discussed in the previous sections 7.1.2 and 7.1.3 was found to generate a galvanic response for periods ≥ 100s for both regional one-dimensional models (model H and L). Since models H and L have the same conductivity distribution at depth as the areas north and south of the regional 2D contact, the results can be applied to the regional 2D problem in this section. We can therefore employ the same type of local anomaly (100km long) in order to investigate the interesting period range.

At the same time we have to place the anomaly fairly close to the 2D boundary or the regional impedance phase will be one-dimensional (see fig. 57, upper profile). For T = 1000s, the two impedance phases differ within a distance of 100 km -120 km to the 2D contact, i.e. between sites 011 - 015 in the south, and between sites 004 - 008 in the north. Close to the boundary, on the other hand, we can observe a very strong and spatially varying regional vertical field B_z^o, which might inhibit the detection of a common phase in the Argand diagrams at this period.

One can try to overcome this problem, by selecting an array of sites which are located on lines parallel to the regional boundary. For such a dataset, the regional vertical magnetic field is similar at each site and therefore produces a certain offset of the regional phase line in the Argand diagram, but the gradient may still indicate

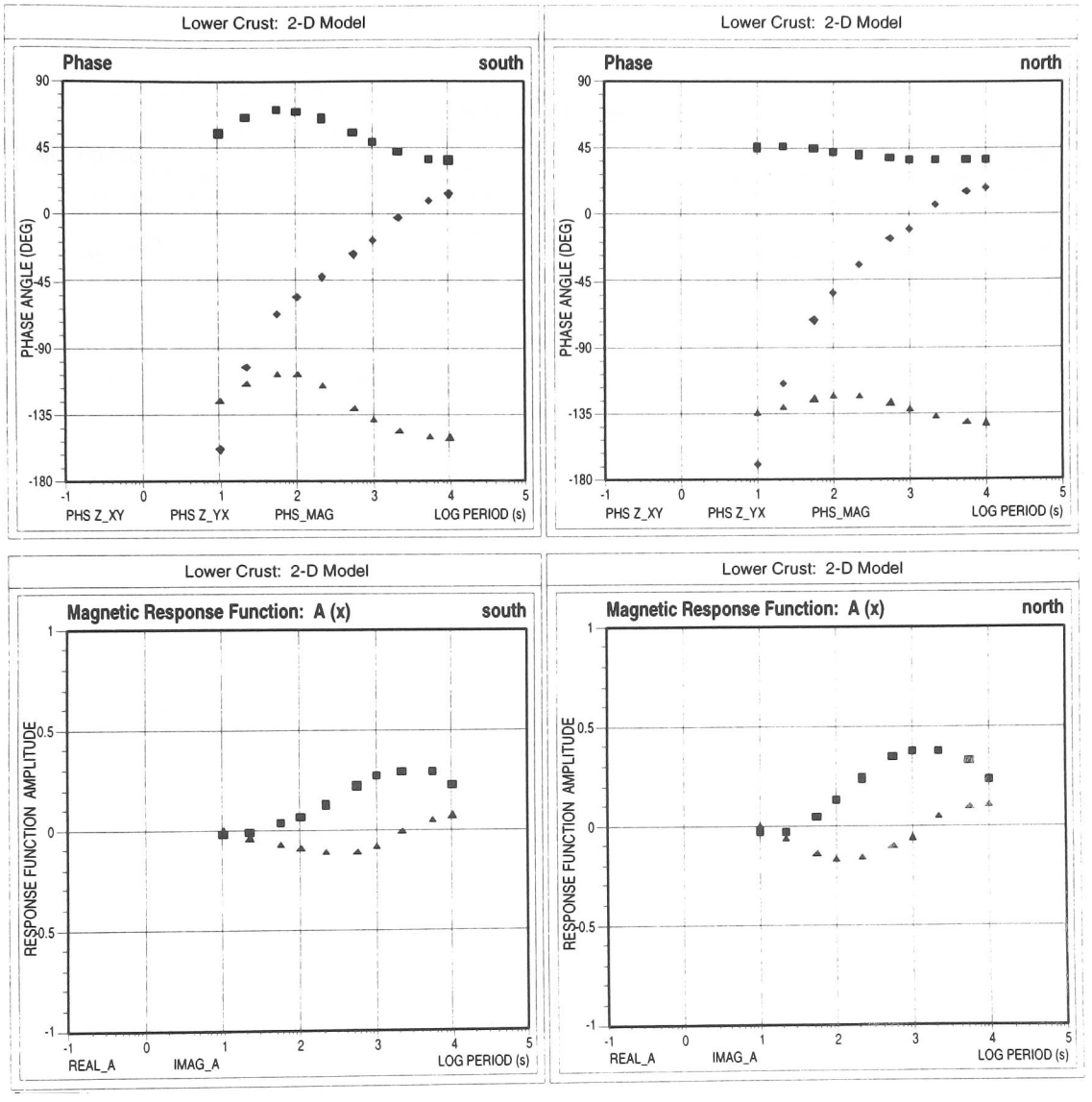

Figure 56: *The regional 2D model,* without *a local 3D body in the upper crust.*
left side: site 45 km **south** *of the regional contact;*
right side: site 45 km **north** *of the regional contact.*
The impedance phases of E- and B-polarisation differ in the ranges > 500s at the southern site and 20s - 2000s at the northern site. The magnetic phase approaches the regional impedance phase for periods > 2000s at both sites. The data are rotated into a coordinate system of 35°, *perpendicular to the regional strike direction.*
As before, the squares mark the phases of the B-polarisation impedances (here: xy - components) while the triangles represent the phases of the E-polarisation impedances (here: yx - components). The magnetic phases (of $\mathcal{A}$) are printed as diamonds. On the magnetic response function plots, the squares mark the real parts of $\mathcal{A}$ whereas the triangles mark the imaginary parts. The conductive anomaly strikes in y - direction.

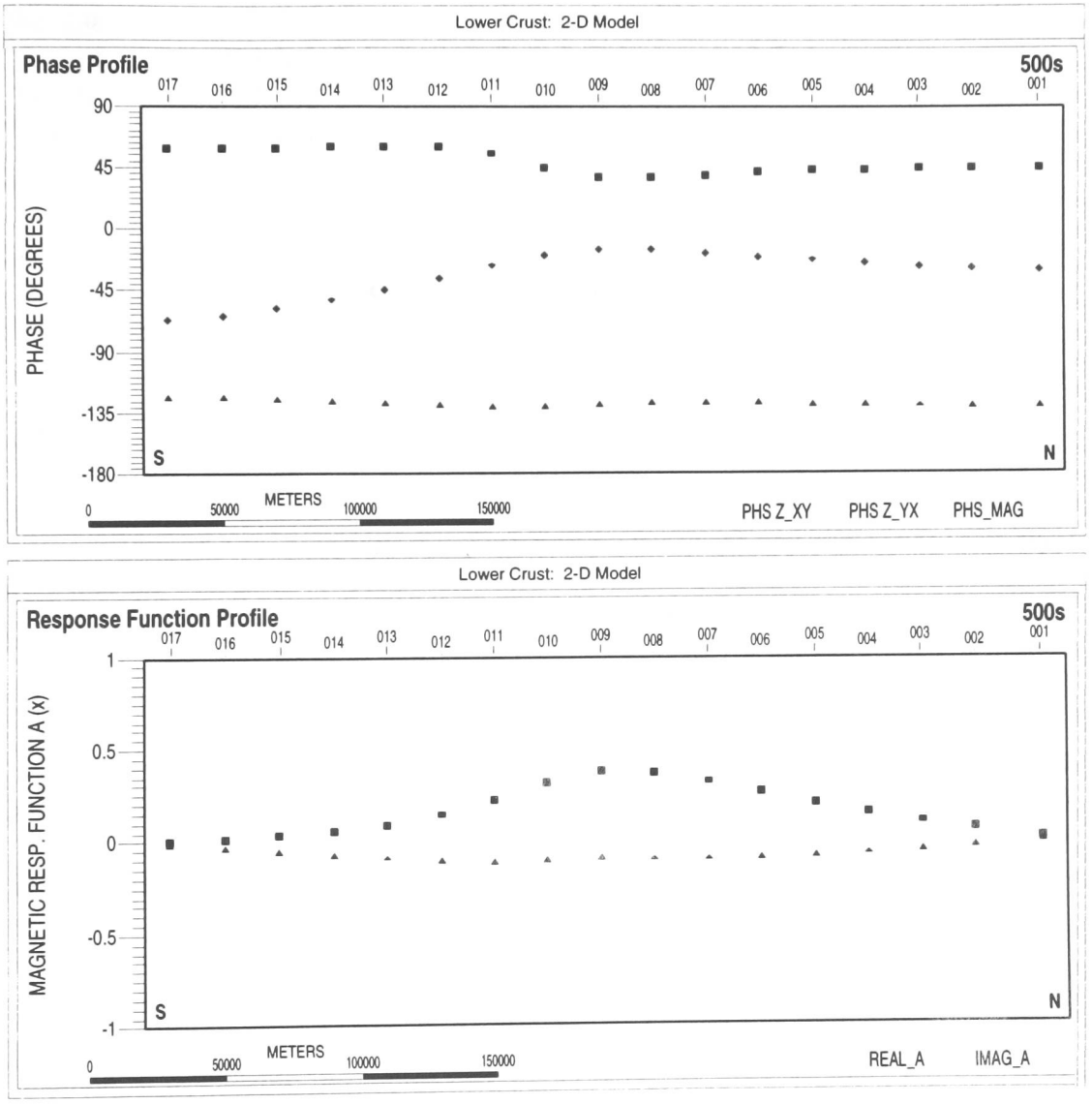

Figure 57: *The regional 2D model,* without *a local 3D body in the upper crust. Profiles of the impedance and magnetic phases (upper diagram), and of the magnetic response function component $\mathcal{A}$ (bottom diagram) at $T = 1000s$. The site spacing is 20 km. The regional 2D contact is located just south of site 009. Sites 011 and 007 on the profile correspond to sites NORTH and SOUTH in the previous figure 56. The data are rotated into a coordinate system of* 35°, *perpendicular to the regional strike direction.* (Marker conventions as for fig. 56)

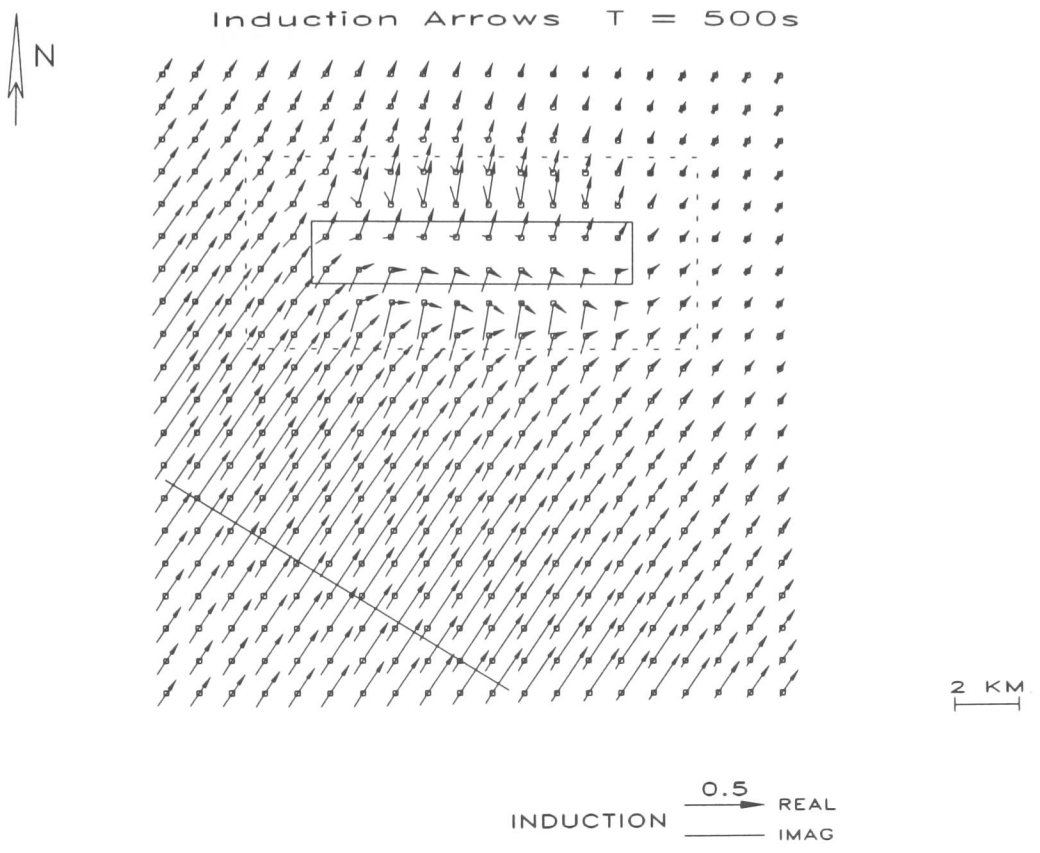

Figure 58: *Induction arrows of 400 sites at 500s. The model includes the local 3D anomaly (solid box) and the regional 2D structure (oblique line). The dotted box marks the array of 6 × 14 sites which is used for hypothetical event analysis in the following section. The elongated, conductive anomaly is embedded ca. 120 km north of the 2D contact.*

the correct impedance phase φ_E. The offset can be eliminated if the hypothetical event is polarised parallel to the regional strike direction. It is therefore always possible to determine the impedance phase of φ_B and the regional strike direction. On the other hand, if it is not possible to find a distinct phase line corresponding to φ_E due to spatially varying regional vertical fields, this behaviour can at least be taken as an indication that the regional structure features lateral conductivity boundaries.

Initially, the elongated body was placed at a distance of 120 km (centre of the body) north of the 2D boundary (anomaly I in fig. 46). Its strike direction is, as before, in east-west direction (y). Fig. 58 shows the induction arrows at a period of 500s. Well away from the local anomaly, the real and imaginary arrows generally indicate the correct strike of the regional 2D structure of N125°E. However, at a radius of ca. 40 km around the 3D body, the direction and length of the regional arrows are distorted, particularly in the areas south and north of the local anomaly and directly above it.

7.2.1 Hypothetical event analysis at various periods

In order to recover the regional information from the distorted magnetic response functions of sites in the vicinity of the anomaly, hypothetical event analysis is applied to an array of 6 × 14 observation points at an interval of 10 km. The sites cover the anomaly symmetrically (see fig. 58, dotted box). In this region, the regional vertical magnetic field is already attenuated, but still decreasing with distance from the 2D contact (see sites 001 - 005 in fig. 57). The resulting impedance phases can be expected to be close to 45°, as on this side of the 2D contact the conductivity does not change with depth.

Fig. 59 shows the predicted vertical fields of the 84 sites at polarisations of 35° (left) and 125° (right) at four different periods: 100s, 500s, 2000s, and 10000s. The periods were selected to demonstrate the gradual change of the phase content of the dataset with increasing skin depth. The polarisation azimuths are perpendicular and parallel to the regional strike. We can therefore observe a maximum contribution from the regional vertical field due to the regional 2D boundary (B_z^o) on the left side (E-polarisation, $B_z^p = \mathcal{A}$), while on the right side, B_z^o is eliminated (B-polarisation, $B_z^p = \mathcal{B}$). Consequently, the right side diagrams show the predicted vertical field components which are solely due to the upper crustal anomaly. The distribution of the data points is therefore very similar to the diagrams of fig. 52 (model H), for which the regional structure is a homogenous halfspace. In the chosen period range, we can observe that the common phase line indeed approaches the impedance phase of 45° with increasing periods. At the same time, the amplitudes of the predicted values become smaller, as the anomalous vertical field due to the local anomaly decreases.

On the left side, the influence of the regional vertical field builds up with increasing periods and, as a result, the data distribution is clearly less linear than on the right side. Although the array sites are at some distance from the regional 2D contact, the superposition of the regional response causes the data points to scatter away from the common phase lines produced by the local distortion field. At T = 100s, the data points are only slightly shifted, and can still be represented by the regression lines. At T=500s, however, the distribution is more elliptical and the regression lines do not fit the data at all. The cloud of points is distinctly offset from the origin, but its direction indicates a phase angle similar to the phase line on the corresponding right side diagram ($38.0° \pm 1.1°$ at $\vartheta^\star = 125°$). Observation points that are closest to the 2D boundary (south-western sites) scatter in a second peculiar shape on the right side of the elliptical cloud of points. This cluster reflects even more clearly the presence of a magnetic phase due to the 2D contact (see fig. 60). For those sites, the anomalous magnetic fields due to induction in the regional deep structure outweigh the fields caused by increasing current concentrations inside the upper crustal anomaly.

For comparison, the predicted vertical fields of the same 84 sites of the regional 2D model *without* the local anomaly are shown in fig. 60. The distributions of these regional data help us to understand their effects in the corresponding diagrams of the combined model in fig. 59 (left), especially at 500s and at 10000s. Obviously, at the longest period, the data near the local anomaly are influenced mainly by the

(a) T = 100s

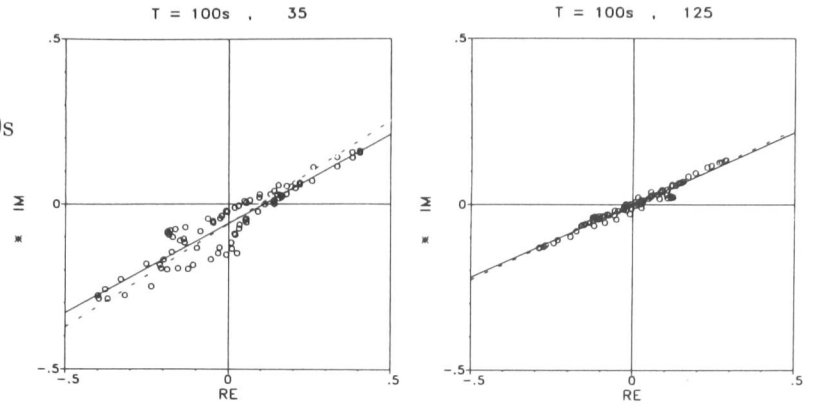

(b) T = 500s

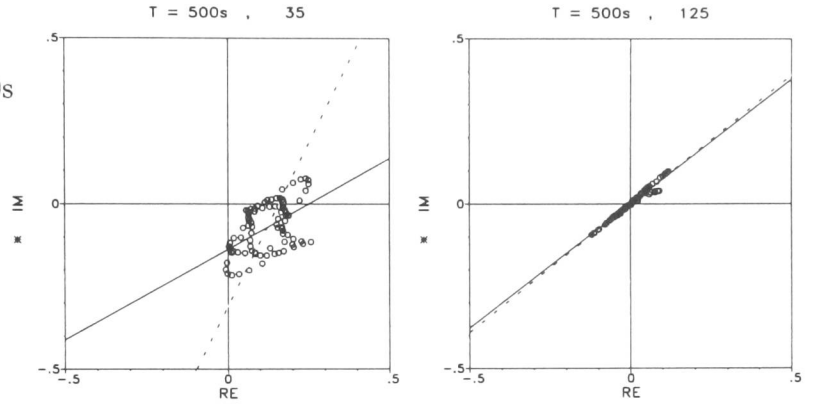

(c) T = 2000s

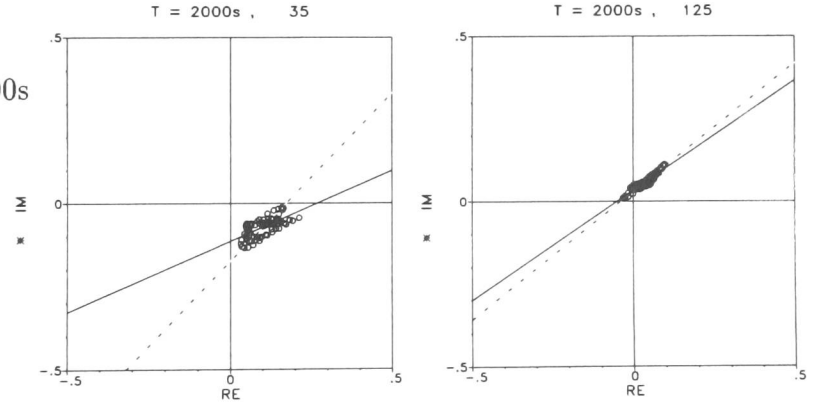

(d) T = 10000s

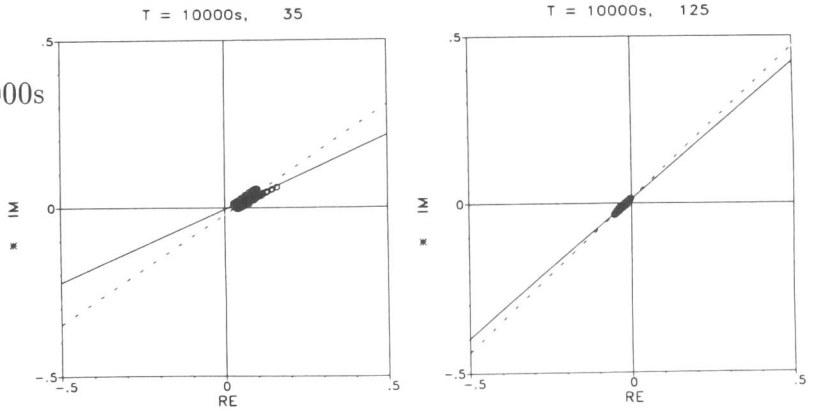

Figure 59: *Hypothetical event analysis at T=100s, 500s, 2000s, and 10000s. The Argand diagrams show the predicted vertical fields of 6 × 14 sites on an array of 60 km × 140 km. The polarisation of the horizontal magnetic field is 35° on the left side, and $\vartheta^{\star}$ = 125° on the right side, i.e. perpendicular and parallel to the strike direction of the regional 2D structure. The elongated, conductive anomaly is embedded ca. 120 km north of the 2D contact.*

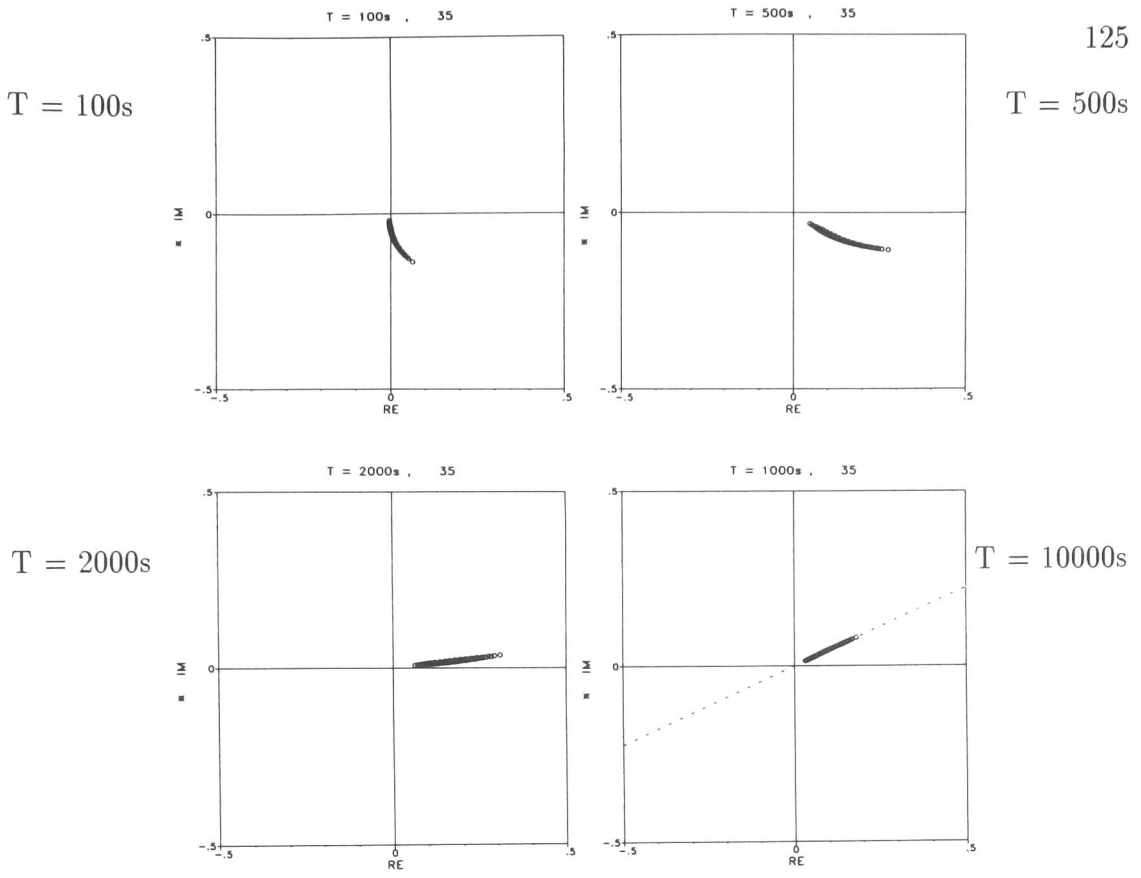

Figure 60: *Hypothetical event analysis at T = 100s, 500s, 2000s, and 10000s for the regional 2D model, without the upper crustal anomaly. The sites are the same as in the previous figure 59.*

vertical field due to the regional 2D contact. The regional field however, must be partly produced by the onset of distortion effects due to the lower crustal structure, as the common phase in fig. 60 at 10000s is positive (24.2°). This *transition* phase is already approaching the regional impedance phase (ca. 45°). The local anomaly in the combined model (fig. 59, $\vartheta^{\star} = 125°$), on the other hand, generates a phase of (40.8° ± 2.0°) at this period. This is in agreement with the impedance phase computed for the regional 2D model in fig. 56 (top right): ~ 40°. Obviously we can see the distant lower crustal conductor at this polarisation in the locally distorted magnetic response functions, even at this long period.

7.2.2 Hypothetical event analysis at various polarisations

The data distributions of the predicted vertical fields at perpendicular polarisations (35° and 125°) differ strongly (see fig. 59). Obviously, the contribution of the regional vertical field increases, as the polarisation of the hypothetical event approaches an azimuth that is perpendicular to the 2D strike direction (35°). In order to obtain a more complete picture, fig. 61 shows the data at 8 polarisations for T = 500s. The linearity of the data can be assessed by the difference of the two regression lines. Clearly, the distribution is linear only in an azimuth range close to the strike of the regional structure (125°). Because the regional vertical field is eliminated at this polarisation azimuth (B-polarisation), the common phase line also passes through the origin.

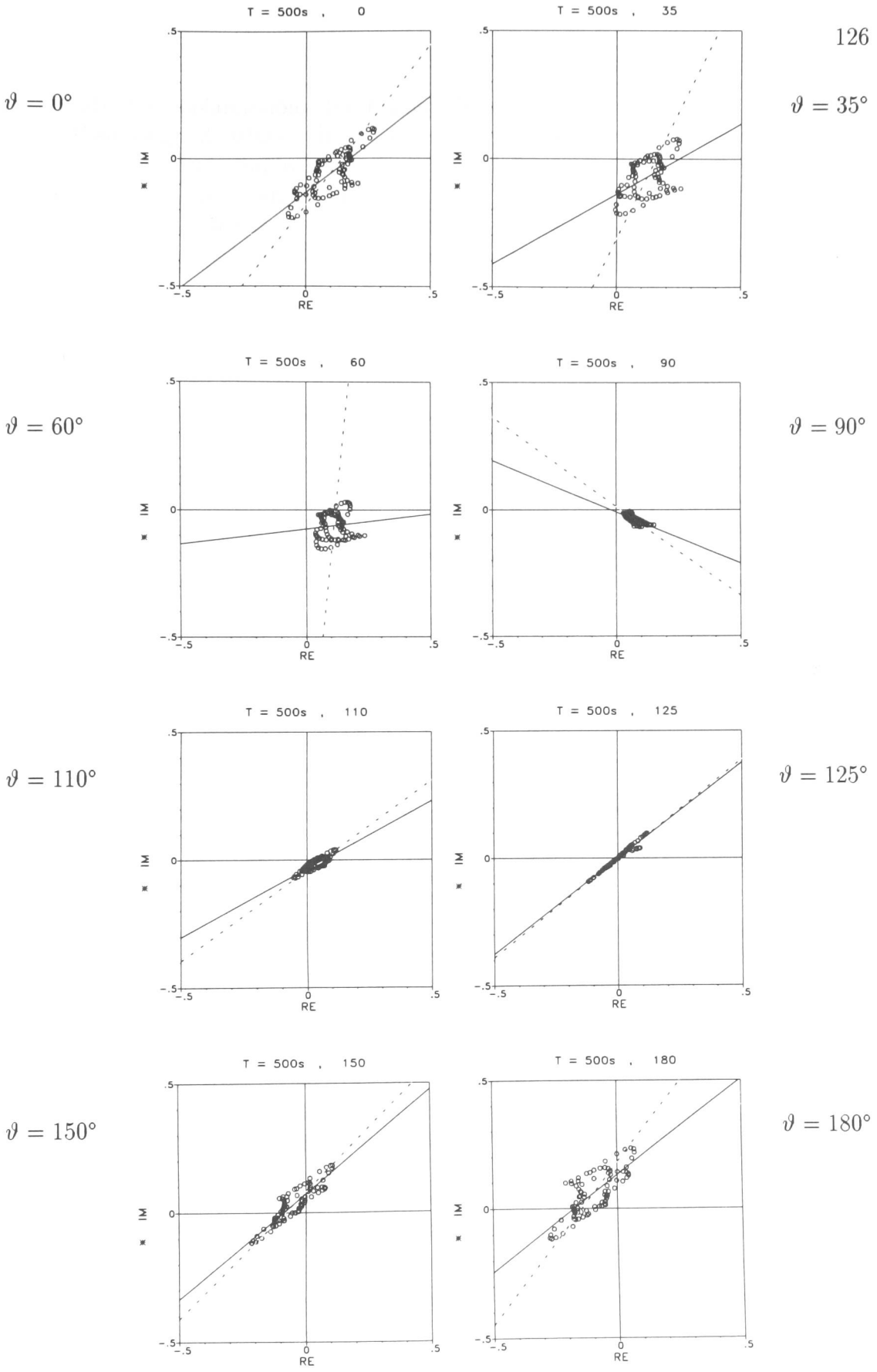

Figure 61: *Hypothetical event analysis at T=500s. The Argand diagrams show the predicted vertical fields of 6 × 14 sites spaced at 10 km. The polarisation of the horizontal magnetic field increases from top to bottom. At $\vartheta = 125°$ the data scatter linearly on a line through the origin, because the contribution of the regional vertical field is eliminated. The elongated, conductive anomaly is embedded ca. 120 km north of the 2D contact (striking N125° E).*

At all other polarisations, the regional field causes the data points to be shifted from their original values. If the regional vertical field was homogenous across the array, the phase line would only be off-set from the origin, but still retain its linear shape, as each point is shifted by the same amount. However, for sites close to a regional lateral structure the spatial variations of B_z^o cause individual shifts. Therefore the shape of the data distribution is altered and the linearity decreased.

Another special case is given, when the polarisation of the hypothetical event parallels the local strike direction of the upper crustal anomaly at $\vartheta^\star = 90°$. Then, most of the anomalous field due to the upper crustal body is eliminated and we observe mainly the regional part (compare to fig. 60) with only small local contributions from sites located at the extremes of the anomaly. On the other hand, at a polarisation azimuth perpendicular to the local strike direction (0°), the contribution of the anomalous vertical field due to the local anomaly is maximal. The largest values which determine the elliptical shape of the data distribution are obtained from the sites located parallel to the long sides of the anomaly at a distance of 10 - 20 km. Despite the regional vertical field, which is present also at this polarisation azimuth, this data distribution provides probably the most reliable phase angle of the regional E-polarisation impedance. The inclination of the elliptical cloud of points is ca. 46°, a slightly higher angle than for the B-polarisation phase of 40° (at $\vartheta^\star = 125°$). This phase difference is also indicated by the magnetotelluric impedance phases in the upper profile of fig. 57.

7.2.3 The 3D anomaly at various distances to the 2D contact

Two further models were computed in order to investigate the influence of the regional vertical field at varying distances to the regional 2D contact. The predicted vertical fields of the hypothetical event analyses of these models at T = 500s are shown at polarisations 35° and 125° in fig. 62, left and right side diagrams, respectively. In the top Argand diagrams (a), the position of the upper crustal body was shifted 60 km further north. Its center is now placed at a distance of 180 km from the 2D contact. The diagrams (b) repeat the results of the previous section, with the body placed at 120 km from the 2D boundary. In the lower diagrams (c) and (d), the position of the upper crustal body was shifted 80 km further south; its centre is placed at a distance of 40 km north of the 2D contact. Except for the bottom diagrams, the data represent an array of 6 × 14 sites which are arranged symmetrically above the 3D anomaly. The datapoints of diagrams (d) belong to 24 sites on 3 parallel profiles that are placed across the centre of the body and run parallel to the regional 2D boundary at a distance of 30 km - 50 km. These sites were chosen to minimize the considerable spatial variations of the regional component.

From the top to the bottom, the distribution at $\vartheta^\star = 125°$ (right side diagrams) is highly linear, because the regional vertical field is eliminated at this polarisation azimuth. The phase angles indicated by the regression lines are the same for the long distances of 180 km and 120 km (ca. 40°). However, for the close anomaly in diagrams (c) and (d), the common phase is distinctly lower, indicating an angle of ca. 30°. This is in agreement with the decrease of the magnetotelluric impedance phase when the 2D contact is approached (see upper profile, fig. 57).

(a) $\hat{d} = 180$km

(b) $\hat{d} = 120$km

(c) $\hat{d} = 40$km

(d) $\hat{d} = 40$km
parallel profile

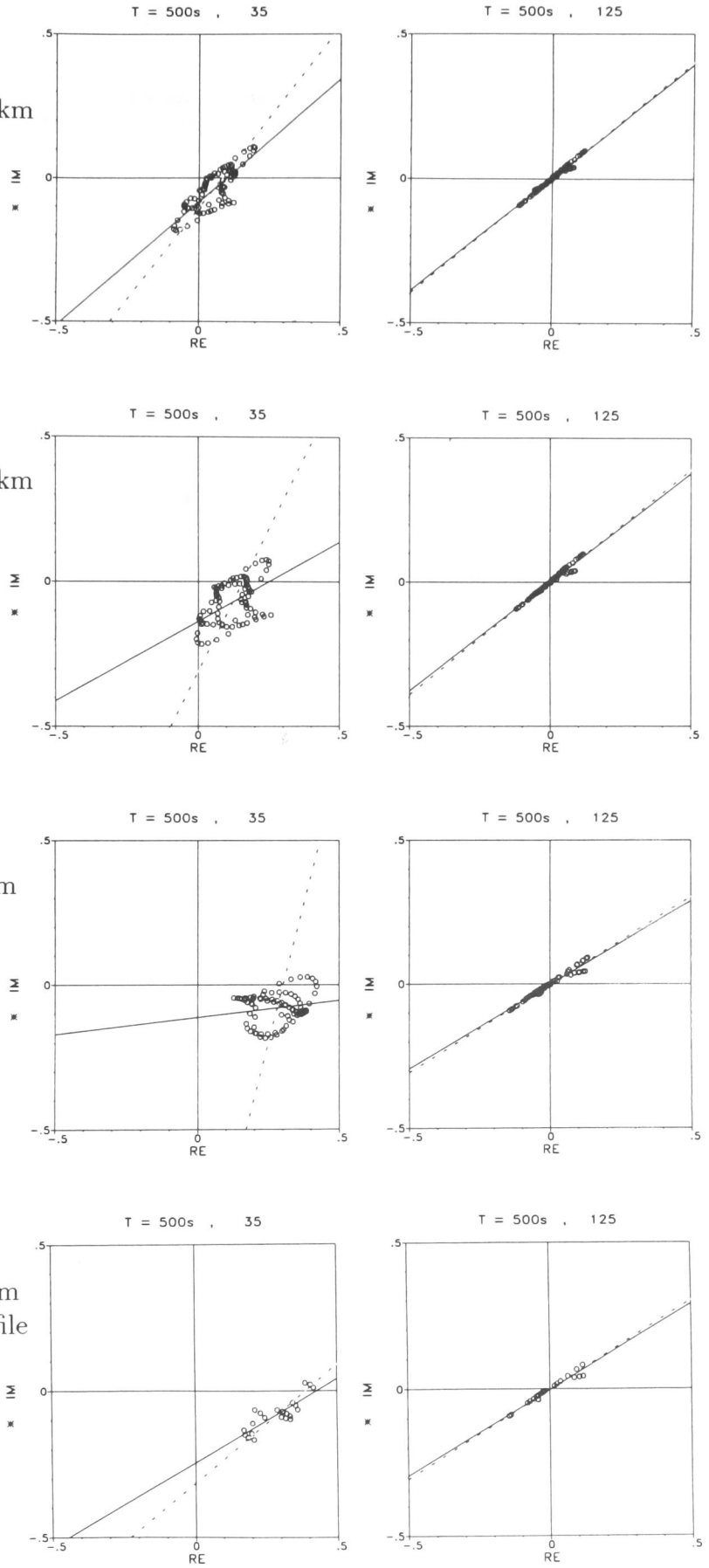

Figure 62: *Hypothetical event analysis at T=500s, the body is buried at various distances from the regional contact. The Argand diagrams show the predicted vertical fields of 6 × 14 sites spaced 10 km, except for the bottom diagrams. The polarisation of the horizontal magnetic field is 35° on the left side, and $\vartheta^\star = 125°$ on the right side, i.e. perpendicular and parallel to the strike direction of the regional 2D structure. The distances $\hat{d}$ are measured to the centre of the body.*

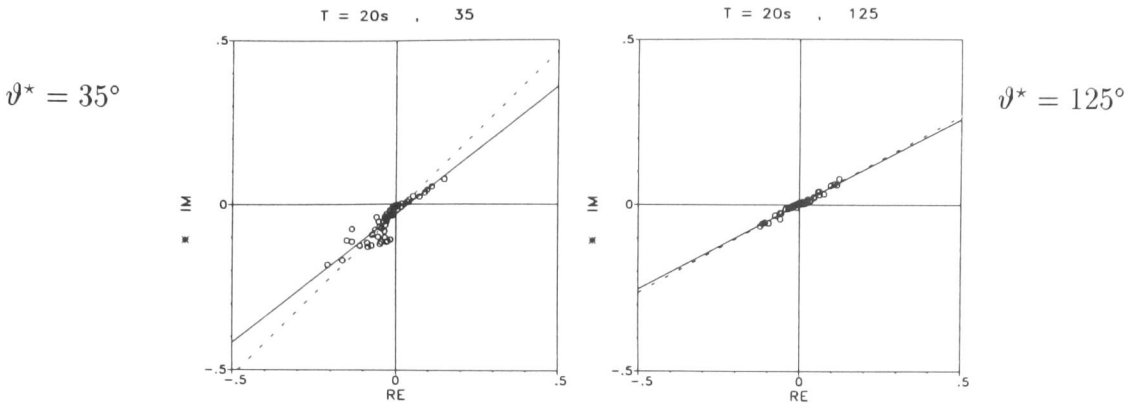

Figure 63: *Hypothetical event analysis for 6 × 9 sites above the short body, which is buried 40 km north of the regional 2D contact. Polarisations are perpendicular and parallel to the 2D boundary. T = 20s. The regression lines are approximations of the regional impedance phases and their different gradients imply that the regional structure is laterally bounded.*

On the left hand diagrams, the linear distribution of the predicted vertical fields at a polarisation azimuth of 35° clearly decreases as the body and the sites are moved towards the 2D boundary (diagrams a-c). This effect is caused by the increasing amplitude and spatial variation of the regional field as the lateral contact is approached (see fig. 57, bottom profile). Only the data of the parallel profiles (d) plot more linearly. Although the linear correlation is not as good as for polarisation 125°, the regression lines could be fitted. Their gradients indicate an average phase angle of ca. 35°. However, from the phase profile of fig. 57 we would expect φ_E to be larger than 45° (or −135°; site 007). The reason for this discrepancy is the scatter due to non-uniformity of the regional vertical field, even on these parallel profiles. Furthermore, the electrical field due to the 2D contact cannot be assumed uniform across the area where the body is buried. This implies that the basic conditions of the distortion model are not met for this extreme situation and the results of the E-polarisation must be treated carefully.

In order to move away from the period range where the amplitudes of the regional vertical component are large, I shortened the upper crustal anomaly to the size 20 km × 30 km. This shape has been studied already in section 7.1.1 (fig. 48c) with respect to the regional one-dimensional model H. I examined the predicted vertical field values at T = 20s, because at this period, the amplitude of the response functions due to the local anomaly is larger than that of the regional structure. At a period of 20s, the magnetic phase due to the short body has already passed the 0° - line and is approaching the regional impedance phase (fig. 48c). Since the phase difference due to the regional 2D contact is already visible at 20s ($\varphi_B = 45°, \varphi_E = -130°$, see fig. 56), we should see different magnetic phases for the polarisations perpendicular and parallel to the regional boundary.

The predicted vertical fields of 6 × 9 sites (located symmetrically above the short body) are shown in fig. 63 at polarisations azimuths of 35° and 125°. In fact, the

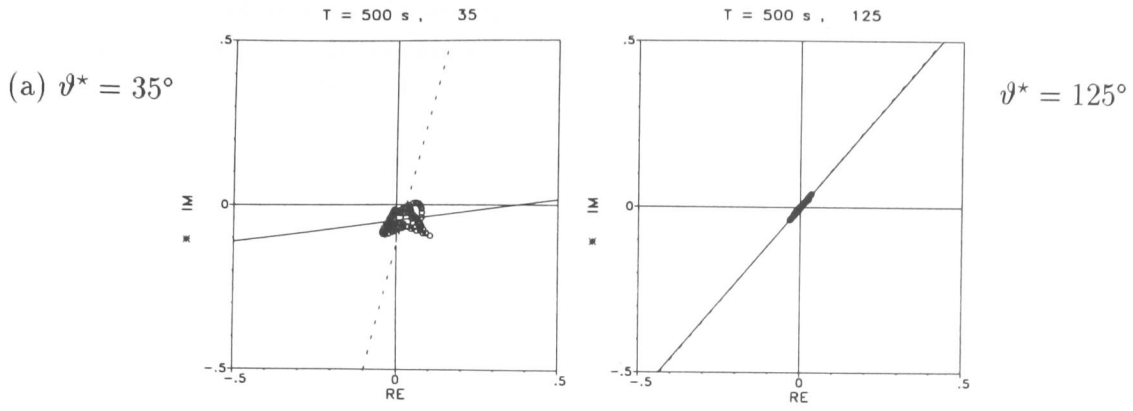

Figure 64: *Hypothetical event analysis for 6 × 14 sites above the anomaly, which is buried 120 km* **south** *of the regional 2D contact. Polarisations are perpendicular and parallel to the 2D boundary. T = 500s. The inclination of the left cloud of points is less steep than the gradient of the regression lines on the right. The implied phase difference and the obvious scatter due to the regional vertical field at 35° indicate that the regional structure is multidimensional.*

regression lines of the two diagrams indicate different phase angles, as the gradient on the left side (37.8° ± 3.2°, E-polarisation) is steeper than that on the right side (27.1° ± 0.8°, B-polarisation). The common phase angles, however, do not equal the regional impedance phase angles taken from fig. 56, probably because the anomalous vertical field is not caused by galvanic distortion alone at this period. Therefore, the magnetic phase is a transition phase, which is only approaching the regional impedance. The data of (fig. 48c) show, that the impedance phase is reached only at ca. 100s. At this period, however, the amplitude of the vertical field of the 2D structure outweighs that of the local anomaly so that no phase line can be detected for the E-polarisation case. Although the common magnetic phases do not coincide with the true impedance phases, we can conclude from their different gradients, that the regional conductivity structure cannot be one-dimensional.

7.2.4 Local anomaly south of the contact

To complete the series, one further model was computed, where the upper crustal anomaly was placed above the conductive lower crust on the south side of the regional 2D contact (fig. 46, body II). The horizontal distance to the boundary is the same as for the model described at the beginning of this section: 120 km. The predicted vertical fields at T = 500s for polarisations 35° and 125° are shown in fig. 64. At this period, the regional impedances on the south side are beginning to show different phases due to the 2D structure (see left side of fig. 56). On the other hand, the magnetic phase of the upper crustal body is approaching the regional impedance phase (see left side of fig. 49 and fig. 53, model L). As the lower crust is more conductive, the respective regional impedance phases at 500s are higher than on the north side of the 2D contact. They are $\varphi_E \sim -132°$ and $\varphi_B \sim 55°$ (fig. 56).

The results of this model are generally comparable to those of the northern anomaly (fig. 59, same distance), only the amplitudes of the predicted vertical fields are smaller due to the lower resistivity of the deep crust. For the same reason, the gradient of the common phase line is steeper, which accounts for the higher impedance phases. The data distribution is strongly linear at a polarisation azimuth of 125° on the right side of fig. 64 and the regression lines indicate a common phase angle of 48.8° ± 0.7°. At the perpendicular polarisation on the left side, however, the linear distribution is decreased considerably due to the strong regional vertical field. However, the elliptical cloud of points has an inclination of ca. 40°, which corresponds to a phase difference between the 2D impedance phases of ca. 10°. Although the phase angles indicated by the predicted vertical fields are only transition phases at this period, the phase difference is clearly visible and implies a multi-dimensional conductivity distribution. This finding is supported by the obvious presence of a regional vertical field, and by the fact, that it can be eliminated at a certain polarisation azimuth.

In order to enlarge the local amplitude relative to the regional field, I re-computed the model for a longer anomaly (160 km, not shown). The predicted vertical fields at 35° then form a more elongated elliptical shape. The common phases, however, are smaller, i.e. further from the true impedance phase angles, as T_o, the transition range, and accordingly the range of distortion, are shifted to slightly longer periods.

7.3 Summary

The aim of the 3D modelling studies was to investigate the behaviour of the regional magnetic response functions of an array of sites in the presence of a local anomaly. Investigations of a series of regional one-dimensional models with local structures of varying sizes showed, that

- a three-dimensional conductive body produces an inductive response in a period range which depends more on its elongation than on its width and thickness (as well as on the resistivity contrast to the host material).
- the local distortion of regional currents begins to affect the magnetic response functions at a period for which the skin depth of the host material is of the same size as the body.

The anomalous magnetic field generated by this process is *in-phase* with the regional electric field. It is therefore crucial to monitor the period dependency of the magnetic phase. The magnetic phase represents the phase shift of the vertical anomalous field of a structure relative to the horizontal source field. For the various local bodies studied in section 7.1.1, the magnetic phase is 0° at T_o, the period of maximum induction, because here, the phase shifts of primary and secondary induction are compensated. T_o also marks the onset of distortion processes. For periods at which the skin depth of the host medium is larger than twice the length of the anomaly, the galvanic response outweighs the inductive response and hence the magnetic phase corresponds to the regional impedance phase (e.g. 45° for a homogenous halfspace). In the intermediate period range of *transition*, where both processes affect the data, the magnetic phase is positive and *approaches* the regional impedance phase.

This phase behaviour can be observed clearly in the predicted vertical magnetic fields obtained by hypothetical event analysis. For different regional one-dimensional settings (homogenous halfspace and layered earth), the data of a large array of sites indicate the 1D impedance phase or the transition phase very *uniformly* in the period range where distortion affects the magnetic response functions. As expected from the theoretical distortion model (chapter 4), the predicted vertical fields arrange *linearly* on common phase lines if they are displayed in Argand diagrams. Local 2D and 3D structures can be distinguished by the reaction of the predicted fields to variations of the polarisation azimuth of the horizontal magnetic field: For a local 3D anomaly, the common phase line can be observed *independently* from the polarisation azimuth, whereas for an elongated, *quasi* - 2D local anomaly, the predicted vertical fields *disappear* for a polarisation azimuth parallel to the local strike direction.

If the regional structure is two-dimensional, the distribution of the phases of the predicted vertical fields of a data array depends strongly on the polarisation azimuth of the horizontal magnetic field. The presence of a regional vertical component, whether small or large, makes it more difficult to determine the regional impedance phases. Only if the polarisation is *parallel* to the regional 2D strike direction, we can observe that the data plot on a line indicating the phase of the B-polarisation impedance. As in the 1D case, this common phase may only be a transition phase (i.e. an approximate value of the impedance phase) if the anomalous magnetic field is produced by both induction and distortion at the local anomaly.

The phase of the E-polarisation impedance can be determined at a *perpendicular* polarisation only if the regional vertical field does not vary too strongly between sites. If the array is located too close to the regional 2D contact we can not recover the impedance phase correctly, even if the sites are arranged on profiles running parallel to that boundary. However, at some distance from the 2D boundary, ca. 100 km in the model investigated, the data plot on an elliptical cloud of points. The inclination of this cloud of points gives at least an approximate value of the E-polarisation phase. A phase difference of the recovered (approximate) impedance phases or transition phases can help to support the assumption of a regional 2D structure. This assumption is justified if the predicted vertical fields reveal a distinct regional strike direction.

If the period investigated with hypothetical event analysis is not in the period range in which distortion processes influence the magnetic response functions (for $T < T_o$), the magnetic phases found in the Argand diagrams are *negative*. They indicate a phase difference between the anomalous magnetic field and the regional electric field due to induction inside the anomaly. In this case, a regional strike direction of a larger scale structure can still be detected if its influence can be minimized clearly for a certain polarisation azimuth, and the predicted vertical fields collapse on a line through the origin with a negative gradient.

From the whole series of models we can draw the following conclusions:

- A local conductivity anomaly does not prohibit the estimation of the true dimension of the regional structure.
- Induction and distortion processes may be distinguished by the sign of the magnetic phase.
- If we have magnetic response functions available that were measured at an array of sites, we can recover the concealed regional information with hypothetical event analysis.
- For a regional two-dimensional setting, we can find the correct regional strike direction plus at least an approximate value of the B-polarisation impedance phase.
- If the extension of the local anomaly is large enough to produce an anomalous vertical field of a similar magnitude to the regional vertical field, we can also obtain an (approximate) phase for the E-polarisation impedance.

8 Conclusions

Magnetic distortion is a problem in GDS, because the usual interpretation of the magnetic response functions by induction arrows allows only the inference of the location of current concentrations, but not whether these currents are caused by inductive or galvanic processes. In the presence of distortion effects due to local conductivity anomalies, essential information on the inductive process, such as the regional strike direction, may be concealed. In contrast with earlier publications on magnetic distortion, which analyse the GDS response functions at single sites using MT impedances as additional information (Zhang et al. 1993, 1995 and Chave & Smith, 1994), I use spatially distributed magneto-variational measurements to extract the 'hidden' regional information with the help of hypothetical event analysis.

The proposed technique is based on the physical distortion model, as it is employed for decomposition methods in MT: a distorting 3D local anomaly is situated above a 2D regional earth (Bahr, 1985; and Groom & Bailey,1989). The distortion model has been examined in theory and the findings are tested against both real data and synthetic data from 3D modelling.

As the regional information can be assumed to be contained in the magnetic data of a number of sites, it can be accessed, if the more site-dependent distortion parameters are eliminated, e.g. by investigating the phase of the magnetic response functions. As shown in theory in chapter 4, the common phase content of the data of an array of sites holds the key to recovering the regional strike direction, and additionally the regional impedance phases.

The results of the 3D modelling studies confirm the assumption, that induction and distortion processes can be distinguished by the phase behaviour of the array data. Response functions originating from induction processes have negative phases and the angles differ between sites. If the magnetic response functions are caused by distortion processes, the phase angles at all sites are uniformly positive and they are equal to the regional impedance phase, as predicted in theory. This is a consequence of the fact that the observed vertical field is generated by local deflections of the regional currents and, hence, is in phase with the regional electric field.

Models with varying anomaly sizes show that the period T_o, at which the magnetic phase changes from negative to positive angles, depends strongly on the length of the body. An anomaly produces a partly galvanic response from a period, at which its length is of the order of the skin depth of the host medium. In the period range of transition (close to T_o), distortion gains influence as increasingly more currents are induced in the host material. Here, the magnetic phase is not yet equivalent to the regional impedance phase. Instead, with increasing periods, it approaches the regional phase angle and therefore provides only an 'approximate' regional phase.

This transition phase of the magnetic response functions, however, can be determined uniformly across the array of sites. To assess the common phase content of an array at a certain period, the complex data of all sites are displayed in Argand diagrams (complex plane). In the period range, where distortion affects the data, the response function components plot on a line through the origin indicating the regional impedance phase or the transition phase.

Since the electrical properties of a regional 2D structure are described by two impedances, Z_E (tangential E-field), and Z_B (tangential B-field), the magnetic response functions must be investigated with respect to the polarisation azimuth of the horizontal magnetic field. This can be done by applying hypothetical event analysis. If the horizontal field is polarised in the regional strike direction, the resulting predicted vertical fields reveal the phase of the B-polarisation impedance. For a perpendicular polarisation, the common line shows a different gradient indicating the phase of the E-polarisation impedance.

However, in an area, where we observe a 2D impedance phase difference, the measured vertical magnetic field also contains a vertical component due to the regional 2D structure. This regional part can make it very difficult to recover the phase of Z_E, especially if it varies strongly across the array. In this case, the predicted vertical fields scatter in the Argand diagram and no regression lines can be fitted. However, if difference field response functions are available, they can be used to determine φ_E, because common reference processing eliminates the spatial variations of the regional vertical component.

Nevertheless, the regional part of the vertical magnetic field can be used very effectively to find the regional strike direction with hypothetical event analysis. If the horizontal field is polarised parallel to the regional strike, the vertical field due to the regional 2D boundary is zero, because no current is induced perpendicular to that boundary (B-polarisation). As a consequence, the predicted vertical fields of all sites show a highly linear distribution, as no scatter due to the regional magnetic field occurs at this polarisation, and the phase of Z_B is indicated clearly.

Two datasets have been investigated to test the application of hypothetical event analysis for extracting the regional information from possibly distorted magnetic data at long periods. The 3D modelling studies show that elongated crustal structures of the length scale of 100 km or more may be the cause of distortion at periods in the range 100s - 10000s.

The Iapetus array comprises 127 sites in a region of 200 $\times$ 300 km, covering the Iapetus Suture Zone in S-Scotland / N-England. The magnetic response functions are influenced by crustal structures associated with the Northumberland Trough and the Southern Upland Fault. At sites in the northern part of the array, the large amplitudes of the magnetic response functions at long periods indicate inductive processes probably related to deep reaching structures of the NE-striking Southern Upland Fault. The induction arrows of sites located south of the Southern Upland Fault, however, indicate current concentrations along the east-westerly strike direction of the Northumberland Trough. At periods of around 400s - 1500s, the predicted vertical fields of hypothetical event analysis reveal a common strike direction of ca. N125°E. The uniform behaviour of the magnetic response functions and the presence of a positive common phase in the array indicate that in this period range, the data are affected by distortion processes. According to the distortion model, the recovered strike direction is assumed to be the regional strike.

The common impedance phases determined from the predicted vertical fields are: 12° - 24° for Z_E and 8° - 16° for Z_B (with increasing period). The phase of Z_E was determined from difference field response functions. Although we cannot

be absolutely sure, whether these phase angles are the regional or the transition impedance phases, the distinct phase difference between Z_E and Z_B supports the assumption of a regional 2D structure. The strike of this regional structure can be assumed at 125° – 130°. This direction, however, cannot be correlated with one single crustal feature, but is a result of induction in the complex deep crustal structure of the Iapetus Suture Zone and the deep ocean to the west and southwest of the British Isles.

The BC87 dataset consists of 27 sites along a profile of 150 km in the southern Canadian Cordillera in British Columbia, Canada. Although the magnetic data are very noisy at long periods, this is the only range, where the data exhibit a common feature when hypothetical event analysis is applied. At 100s - 1000s, the predicted vertical fields collapse roughly on a line with a negative gradient. This happens at a polarisation azimuth of ca. −35°. This direction or the perpendicular azimuth corresponds to a regional strike direction. The perpendicular direction, 55°, is in agreement with earlier MT decomposition results by Jones et al. (1993) and Eisel & Bahr (1993). The negative common phase line indicates that the magnetic response functions are produced by inductive rather than galvanic processes in this period range. The crustal structure generating this phase response can probably be associated with the region adjacent and beneath the resistive Nelson Batholith. The regional strike azimuth found by hypothetical event analysis must then be attributed to a larger, possibly deeper feature of the lower crust. Because of the strong indications in MT and GDS data for a 3D conductivity distribution, and the large errors in the long period data, the results have to be interpreted with care.

The fact, that we can determine a common strike azimuth even for the 'complicated' BC87 profile data, should provide encouragement for the improvement of the measurements of the vertical magnetic field in both quality and quantity. As I demonstrated with the Iapetus dataset, we can separate the local from the regional information with a better degree of certainty, if we have good quality data and a good spatial coverage of the investigated region. With hypothetical event analysis we can then extract confidently the regional strike direction and the regional impedances phases (or the transition phases) from the magnetic response functions.

The 3D modelling studies and the two datasets show that the regional strike direction is retrievable reliably even in situations, where the assumptions made for the basic physical distortion model are not met exactly: this is true for inductive processes that cause uniform, but negative phases across the data array, and also for non-uniform regional fields. Furthermore the technique can detect a strike direction in those cases where the two principal impedance phases are very similar which would cause a failure of the phase criterion of the MT decomposition methods (e.g. Bahr, 1988).

I am convinced that further work with the dataset of the Iapetus array is necessary, as - due to its location near the Edinburgh EM research group - more data are likely to be collected in the future. In the area north of the Southern Uplands, for example, new long period data (Junge, 1995) are already available. They are a valuable complement of the existing dataset, as up to now too few sites have been available to apply hypothetical event analysis successfully in this region.

Furthermore, the method should also be used with short period magnetic response functions to recover the regional strike and the regional impedance phases. O.Ritter (1995) showed, that vertical magnetic fields in the AMT frequency range can be used effectively for the dense mapping of more shallow, upper crustal structures. Obviously, in the short period range, distortion effects may be caused by numerous, small-scale inhomogeneities. Since a new AMT instrumentation is now available (S.P.A.M. MkIII), which allows for time-synchronous measurements at several remote sites, difference field response functions can be used to determine also the E-polarisation phase φ_E reliably.

References

Bahr, K. (1985). Magnetotellurische Messungen des Elektrischen Widerstandes der Erdkruste und des oberen Mantels in Gebieten mit Lokalen und Regionalen Leitfähigkeitsanomalien. *Ph.D. thesis, G. August Univ. Göttingen.*

Bahr, K. (1988). Interpretation of the magnetotelluric impedance tensor: regional induction and local telluric distortion. *Journal of Geophysics*, 62:119–127.

Bahr, K. (1991). Geological noise in magnetotelluric data: a classification of distortion types. *Phys. Earth Planet. Int.*, 60:24–38.

Bahr, K. and Groom, R. W. (1990). Corrections for near surface effects: a tutorial. *presented at EM Workshop at Ensenada, Mexico.*

Bailey, R. C., Edwards, R. N., Garland, G. D., Kurz, R., and Pitcher, D. (1974). Electrical conductivity studies over a tectonical active area in Eastern Canada. *J. Geomagn. Geoelectr.*, 26:125–146.

Baird, D. C. (1962). *Experimentation: An Introduction to Measurement theory and Experiment Design.* Prentice Hall, Inc., Englewood Cliffs, New Jersey.

Bamford, D., Nunn, K., Prodehl, C., and Jacob, B. (1978). LISP-IV: Crustal structure of northern Britain. *Geophys. J. R. astr. Soc.*, 54:43–60.

Banks, R. J. (1986). The interpretation of the Northumberland Trough Geomagnetic Variation Anomaly using two-dimensional current models. *Geophys. J. R. astr. Soc.*, 87:595–616.

Banks, R. J. (1994). The origin of high electrical conductivity and seismic reflectivity in the crust. *Final Report to N.E.R.C., Grant GR3/7696.*

Banks, R. J. and Beamish, D. (1984). Local and regional induction in the British Isles. *Geophys. J. R. astr. Soc.*, 79:539–553.

Banks, R. J., Beamish, D., and Geake, M. J. (1983). Magnetic Variation Anomalies in Northern England and Southern Scotland. *Nature*, 303:516–518.

Banks, R. J., Irving, A. A. K., and Livelybrooks, D. W. (1993). The simulation of magnetic variation anomalies using single station data. *Phys. Earth Planet. Int.*, 81:85–98.

Banks, R. J., Livelybrooks, D. W., Jones, P. C., and Longstaff, R. (1996). Causes for high crustal conductivity beneath the Iapetus Suture Zone in Great Britain. *Geophys. J. Int.*, 124:433–455.

Barton, P. J. (1992). A new look under the Caledonides of northern Britain. *Geophys. J. Int.*, 110:371–391.

Beamish, D. and Banks, R. J. (1983). Geomagnetic Variation Anomalies in Northern England: Processing and presentation of data from a non-simultaneous array. *Geophys. J. R. astr. Soc.*, 75:513–539.

Beamish, D. and Smythe, D. K. (1986). Geophysical images of the deep crust: the Iapetus Suture. *J. Geolog. Soc.*, 143:489–497.

Beblo, M. (1982). Die Dielektizitätskonstante ε_r der Minerale und Gesteine. *in Landolt - Börnstein, Zahlenwerte und Funktionen aus Naturwissenschaften und Technik, Neue Serie, (Hg. G. Angenheister), Springer Verlag, Berlin - Heidelberg - New York*, V1b.

Born, M. and Wolf, E. (1980). *Principles of Optics*, page 808. Pergamon, New York.

Bott, M. H. P. (1967). Geophysical investigations of the northern Pennine basement rocks. *Proc. Yorks. Geol. Soc.*, 36:139–168.

Bott, M. H. P., Long, R. E., Green, A. S. P., Lewis, A. H. J., and Sinha, M. C. (1985). Crustal structure south of the Iapetus Suture beneath northern England. *Nature*, 314:724–727.

Bott, M. H. P., Swinburn, P. M., and Long, R. E. (1984). Deep structure and origin of the Northumberland and Stainmore Troughs. *Proc. Yorks. Geol. Soc.*, 44:479–495.

Brewitt-Taylor, C. R. and Weaver, J. T. (1977). Numerical solutions of two-dimensional induction problems. *Acta Geodaet., Geophys., Montanist. Acad. Sci. Hung.*, 12:241–245.

Bronstein, I. N. and Semendjajev, K. A. (1981). *Taschenbuch der Mathematik.* Verlag H. Deutsch, Thun u. Frankfurt a. M.

Cagniard, L. (1953). Basic theory of the magneto-telluric method of geophysical prospecting. *Geophysics*, 18:605–635.

Caner, B., Auld, D. R., Dragert, H., and Camfield, P. A. (1971). Geomagnetic depth sounding and crustal structure in western Canada. *J. Geophys. Res.*, 76:7181–7201.

Caner, B., Camfield, P. A., Andersen, F., and Niblett, E. R. (1969). A large scale magnetotelluric survey in western Canada. *Can. J. Earth Sciences*, 6:1245–1261.

Caner, B., Cannon, W. H., and Livingstone, C. E. (1967). Geomagnetic depth sounding and upper mantle structure in the Cordillera region of western North America. *J. Geophys. Res.*, 72:6335–6351.

Cevallos, C. (1986). Magnetotelluric interpretation - another approach. *Ph.D. Thesis, Macquary Univ. Sydney.*

Chave, A. D. and Smith, J. T. (1994). On electric and magnetic galvanic distortion tensor decompositions. *J. Geophys. Res.*, 99 B3:4669–4682.

Coggon, J. H. (1971). Electromagnetic and electrical modeling by the finite element method. *Geophysics*, 36:132–155.

Cook, F. A., Green, A. G., Simony, P. S., Price, R. A., Parrish, R. R., Milkereit, B., Gordy, P. L., Brown, R. L., Coflin, K. C., and Patenaude, C. (1988). LITHOPROBE seismic reflection structure of the southeastern Canadian Cordillera: Initial results. *Tectonics*, 7:157–180.

Cook, F. A., Varsek, J. L., and Clowes, R. M. (1991). Lithoprobe reflection transect of southwestern Canada: Mesozoic thrust and fold belt to mid-ocean rigde. *in Continental Lithosphere, Deep Seismic Reflection, Geodynamics series (ed. by R. Meissner, L. Brown , H.-J. Dürrbaum, W. Franke, K. Fuchs and F. Seifert)*, 22:247–255, Amer. Geophys. Union.

DeGroot-Hedlin, C. (1995). Inversion for regional 2-d resistivity structure in the presence of galvanic scatterers. *Geophys. J. Int.*, 122:877–888.

Dragert, H. and Clarke, G. K. C. (1977). A detailed investigation of the Canadian Cordillera geomagnetic transition anomaly. *Journal of Geophysics*, 42:373–390.

Edwards, R. N., Law, L. K., and White, A. (1971). Geomagnetic variations in the British Isles and their relation to electrical currents in the ocean and shallow seas. *Phil. Trans. R. Soc. London*, A270:289–323.

Egbert, G. D. and Booker, J. R. (1986). Robust estimation of geomagnetic transfer functions. *Geophys. J. R. astr. Soc.*, 87:173–194.

Eisel, M. and Bahr, K. (1993). Electrical anisotropy in the lower crust of British-Columbia - an interpretation of a magnetotelluric profile after tensor decomposition. *J. Geomagn. Geoelectr.*, 45(9):1115–1126.

Floyd, J. D. (1994). The derivation and definition of the 'Southern Uplands Fault': a review of the Midland Valley - Southern Uplands terrane boundary. *Scottish Journal of Geology*, 30:51–62.

Fluche, B. (1983). Erdmagnetische Tiefensondierung und Magnetotellurik in der Hessischen Senke. *Dipl. thesis, G. August Univ. Göttingen.*

Freeman, B., Klemperer, S. L., and Hobbs, R. W. (1988). The deep structure of northern England and the Iapetus Suture Zone from BIRPS deep seismic reflection profiles. *J. Geol. Soc. Lond.*, 145:727–740.

Gough, D. I., Bingham, D. K., Ingham, M. R., and Alabi, A. O. (1982). Conductive structures in southern Canada: a regional magnetometer array study. *Can. J. Earth Sciences*, 19:1680–1690.

Gough, D. I. and Ingham, M. R. (1983). Interpretation methods for magnetometer arrays. *Rev. Geoph. Space Phys.*, 21:805–827.

Grimes, D. I. F. (1977). Geomagnetic deep sounding in north-west England. *MSc Thesis, Univ. of Lancaster.*

Groom, R. W. (1988). The effects of inhomogeneities on magnetotellurics. *Ph.D. thesis, Univ. Toronto.*

Groom, R. W. and Bahr, K. (1992). Corrections for near surface effects: Decomposition of the magnetotelluric impedance tensor and scaling corrections for regional resistivities: a tutorial. *Surveys in Geophysics*, 13:341–379.

Groom, R. W. and Bailey, R. C. (1989). Decomposition of magnetotelluric impedance tensors in the presence of local three-dimensional galvanic distortion. *J. Geophys. Res.*, 94:1913–1925.

Groom, R. W. and Bailey, R. C. (1991). Analytic investigation of the effects of near-surface 3D galvanic scatterers on MT tensor decomposition. *Geophysics*, 56:496–518.

Groom, R. W., Kurtz, R. D., Jones, A. G., and Boerner, D. E. (1993). A quantitative methodology to extract regional magnetotelluric impedances and determine the dimension of the conductivity structure. *GJI*, 115:1095 - 1118.

Haak, V. (1978). Interpretationsverfahren für die Magnetotellurik unter besonderer Berücksichtigung lateral variierender Leitfähigkeit im Erdinnern und eines räumlich inhomogenen Magnetfeldes. *Bayer. Akad. Wiss. Math.-Nat. Klasse, München*, 158.

Habashy, T. M., Groom, R. W., and Spies, B. R. (1993). Beyond the Born and Rytov approximations: A nonlinear approach to electromagnetic scattering. *J. Geophys. Res.*, 98(B2):1759–1776.

Hall, J., Brewer, J. A., Mathews, D. H., and Warner, M. (1984). Crustal structure across the Caledonides from the WINCH seismic reflection profile: Influences on the evolution of the Midland Valley. *Trans. R. Soc. Edin.: Earth Sc.*, 75:97–109.

Harinarayana, T. (1987). Lithospheric electrical conductivity structure across southern Scotland and northern England. *Ph.D. Thesis, Univ. of Edinburgh.*

Harinarayana, T., Hutton, V. R. S., and Jones, P. C. (1993). Lateral variations of conductivity structure across Southern Scotland and Northern England. *Phys. Earth Planet. Int.*, 81:25–41.

Hobbs, B. A. (1971). The calculation of geophysical induction effects using surface integrals. *Geophys. J. R. astr. Soc.*, 25:481–509.

Hobbs, B. A. (1992). Terminology and symbols for use in studies of electromagnetic induction in the Earth. *Surveys in Geophysics*, 13:489–515.

Hohmann, G. W. (1975). Three-dimensional induced polarisation and electromagnetic modelling. *Geophysics*, 40:309–324.

Hutton, D. H. W. (1987). Strike - slip terranes and a model for the evolution of the British and Irish Caledonides. *Geol. Mag.*, 124:405–425.

Hutton, V. R. S. and Jones, A. G. (1980). Magnetovariational and magnetotelluric investigations in southern Scotland. *J. Geomagn. Geoelectr.*, 32:141–149.

Hutton, V. R. S., Sik, J. M., and Gough, D. I. (1977). Electrical conductivity and tectonics of Scotland. *Nature*, 266:617–620.

Hyndman, R. D. (1963). Electrical conductivity inhomogeneities in the Earth's upper mantle. *M.Sc. Thesis, Univ. British Columbia, Vancover.*

Ingham, M. R. (1981). Lateral variation of the electrical conductivity structure across southern Scotland. *Ph.D. Thesis, Univ. of Edinburgh.*

Jiracek, G. (1990). Near-surface and topographic distortions in electromagnetic induction. *Surveys in Geophysics*, 11:163–203.

Jones, A. G. (1977). Geomagnetic induction studies in southern Scotland. *Ph.D. Thesis, Univ. of Edinburgh.*

Jones, A. G. (1983). The problem of current channelling: a critical review. *Geophysical Survey*, 6:79–122.

Jones, A. G. (1993). The BC87 dataset - tectonic setting, previous EM results, and recorded MT data. *J. Geomagn. Geoelectr.*, 45(9):1089–1105.

Jones, A. G., Chave, A. D., Egbert, G., Auld, D., and Bahr, K. (1989). A comparison of techniques for magnetotelluric response function estimation. *J. Geophys. Res.*, 94(B10):14201–14213.

Jones, A. G. and Groom, R. W. (1993). Strike-angle determination from the magnetotelluric impedance tensor in the presence of noise and local distortion: rotate at your peril! *Geophys. J. Int.*, 113:524–534.

Jones, A. G., Groom, R. W., and Kurtz, R. D. (1993). Decomposition and modeling of the BC87 dataset. *J. Geomagn. Geoelectr.*, 45(9):1127–1150.

Jones, A. G. and Hutton, V. R. S. (1979). A multi-station magnetotelluric study in southern Scotland - I. Fieldwork, data analysis and results. *Geophys. J. R. astr. Soc.*, 56:329–350.

Jones, A. G., Kurtz, R. D., Oldenburg, D. W., Boerner, D. E., and Ellis, R. (1988). Magnetotelluric observations along the LITHOPROBE southeastern Canadian Cordilleran transect. *Geophys. Res. Lett.*, 15:677–680.

Jones, F. W. (1973). Induction in laterally non-uniform conductors: Theory and numerical models. *Phys. Earth Planet. Int.*, 7:282–293.

Jones, F. W. and Price, A. T. (1970). The perturbations of alternating geomagnetic fields by conductivity anomalies. *Geophys. J. R. astr. Soc.*, 20:317–334.

Junge, A. (1994a). Decomposition considering impedance tensor confidence limits. *Abstract at 12. Workshop EM Induction, Brest*, page 97.

Junge, A. (1994b). Induzierte erdelektrische Felder - neue Beobachtungen in Norddeutschland und im Bramwald. *Habil., math.-nat. Fachb., G. August Univ. Göttingen.*

Junge, A. (1995). Magnetotellurics in the long period range. *Final Report to the EEC, Contract* ERBCHBICT 93 0610.

Kirkwood, S. C., Hutton, V. R. S., and Sik, J. M. (1981). A geomagnetic study of the Great Glen Fault. *Geophys. J. R. astr. Soc.*, 66:481–490.

Klemperer, S. L. and Mathews, D. H. (1987). Iapetus Suture located beneath the North Sea by BIRPS deep seismic profiling. *Geology*, 15:195–198.

Lajoie, J. J. and Caner, B. (1970). Geomagnetic induction anomaly near Kooteney Lake – a strike-slip feature in the lower crust? *Can. J. Earth Sciences*, 7:1568–1579.

Larsen, J. C. (1977). Removal of local surface conductivity effects from low frequency mantle response curves. *Acta Geodaet., Geophys., Montanist. Acad. Sci. Hung.*, 12:183–186.

LaTorraca, G. A., Madden, T. R., and Korringa, J. (1986). An analysis of the magnetotelluric impedance for three-dimensional conductivity structures. *Geophysics*, 51:1819–1829.

Leeder, M. R. (1982). Upper Palaeozoic basins in the British Isles - Caledonide inheritance versus Hercynian plate margin processes. *J. Geol. Soc. Lond.*, 139:479–491.

Leggett, J. K., McKerrow, W. S., and Soper, N. J. (1983). A model for the crustal evolution of Southern Scotland. *Tectonics*, 2:187–210.

Lilley, F. E. M. (1993). 3-Dimensionality of the BC87 magnetotelluric data set studied using Mohr circles. *J. Geomagn. Geoelectr.*, 45(9):1107–1113.

Livelybrooks, D. W., Banks, R. J., Parr, R. S., and Hutton, V. R. S. (1993). Inversion of electromagnetic induction data for the Iapetus Suture Zone in the UK. *Phys. Earth Planet. Int.*, 81:67–84.

Mackie, R. L., Smith, J. T., and Madden, T. R. (1994). Three-dimensional electromagnetic modeling using finite difference equations: The magnetotelluric example. *Radio Science*, 29(4):923–935.

McKerrow, W. S. and Cocks, L. R. M. (1986). Oceans, island arcs and olistostromes: the use of fossils in distinguishing sutures, terranes and environments around the Iapetus Ocean. *J. Geol. Soc. Lond.*, 143:185–191.

Novak, M. (1981). A broadband magnetotelluric study in the north England high heat flow region. *Ph.D. Thesis, Univ. of Edinburgh.*

Parkinson, W. D. (1959). Directions of rapid geomagnetic fluctuations. *Geophys. J.*, 2,No1:1–14.

Parr, R. S. (1991). Development of magnetotelluric processing and modelling procedures - application to northern England. *Ph.D. Thesis, Univ. of Edinburgh.*

Parr, R. S. and Hutton, V. R. S. (1993). Magnetotelluric studies in and adjacent to the Northumberland Basin, Northern England. *Phys. Earth Planet. Int.*, 81:43–66.

Price, A. T. (1973). The theory of geomagnetic induction. *Phys. Earth Planet. Int.*, 7:227–233.

Reddy, I. K. and Rankin, D. (1971). Magnetotelluric effect of dipping anisotropies. *Geophys. Prospecting*, 19:84–97.

Ritter, O. (1995). An audiomagnetotelluric investigation of the Southern Upland Fault: novel instrumentation, field procedures and 3D modelling. *Ph.D. Thesis, Univ. of Edinburgh.*

Ritter, P. and Ritter, O. (1996). The bc87 dataset: Application of hypothetical event analysis on distorted GDS response functions and some thinsheet modelling studies of the deep crustal conductor. *J. Geomagn. Geoelectr.*, in press.

Schmucker, U. (1970). Anomalies of geomagnetic variations in the south-western United States. *Bull. Scripps Inst. Oceanogr.*, 13:1–165.

Schmucker, U. (1986). 2D Modellrechnungen - neue Fassung älterer Programme. *Protokoll Kolloquium Elektromagnetische Tiefenforschung (Hg. V. Haak und H. Homilius)*, Lerbach.

Schmucker, U. (1987). Substitute conductors for electromagnetic response estimates. *Pageoph*, 125.

Schmucker, U. and Weidelt, P. (1975). *Electromagnetic Induction in the Earth.* Lecture Notes (not published), Aarhus.

Siemon, B. (1991). Ein Interpretationsverfahren für induktiv schwach gekoppelte Leitfähigkeitsanomalien, dargestellt am Beispiel des Salzstockes Wesendorf im Giffhorner Trog. *Ph.D. thesis, G. August Univ. Göttingen.*

Sik, J. M. and Hutton, V. R. S. (1977). A magnetometer array study in Scotland. *Acta Geodaet.*, 12:139–143.

Sik, J. M., Hutton, V. R. S., Dawes, G. J. K., and Kirkwood, S. C. (1981). A geomagnetic variation study of Scotland. *Geophys. J. R. astr. Soc.*, 66:491–512.

Smith, J. T. (1995). Understanding telluric distortion matrices. *Geophys. J. Int.*, 122:219–226.

Spiegel, M. R. (1961). *Statistics.* Schaum Publishing Company, New York.

Spitz, S. (1985). The magnetotelluric impedance tensor properties with respect to rotations. *Geophysics*, 50:1610–1617.

Sule, P. O., Hutton, V. R. S., and Dumitrescu, C. (1993). Subsurface structure of SE Scotland from broadband magnetotelluric measurements. *Phys. Earth Planet. Int.*, 81:9–24.

Swift, C. M. (1967). A magnetotelluric investigation of an electrical conductivity anomaly in the southwestern United States. *Ph.D. thesis, M.I.T. Cambridge, Mass.*

Tikhonov, A. N. (1950). On determining electrical characteristics of the deep layers of Earth's crust (in Russian). *Dokl. Akad. Nauk. SSSR*, 73:295 – 297.

Wannamaker, P. E., Stodt, J. A., and Rijo, L. (1987). A stable finite element solution for two-dimensional magnetotelluric modelling. *Geophys. J. R. astr. Soc.*, 51:2131–2144.

Weaver, J. T. (1973). Induction in a layered plane Earth by uniform and non-uniform source fields. *Phys. Earth Planet. Int.*, 7:266–281.

Weaver, J. T. (1990). On the addition of induction vectors. *Protokoll Kolloquium Elektromagnetische Tiefenforschung (Hg. V. Haak und H. Homilius)*, Hornburg.

Weaver, J. T. (1994). *Mathematical Methods for Geo-Electromagnetic Induction.* Research Studies Press, Taunton, England.

Weidelt, P. (1975). Electromagnetic induction in three-dimensional structures. *J. Geophys.*, 41:85–109.

Wiese, H. (1962). Die Streichrichtung der Untergrundstrukturen des elektrischen Widerstandes, erschlossen aus geomagnetischen Variationen. *Pageoph*, 52:83–103.

Xiong, Z., Lou, Y., Wang, S., and Wu, G. (1986). Induced polarisation and electromagnetic modelling of a three-dimensional body in a two-layer anisotropic earth. *Geophysics*, 51:2235–2246.

Yee, E. and Paulson, K. V. (1987). The cannonical decomposition and its relationship to other forms of magnetotelluric impedance tensor analysis. *Journal of Geophysics*, 61:173–189.

Zhang, P., Chouteau, M., Mareschal, M., Kurtz, R., and Hubert, C. (1995). High-frequency magnetotelluric investigation of crustal structure in north-central Abitibi, Quebec, Canada. *Geophys. J. Int.*, 120:406–418.

Zhang, P., Pedersen, L. B., Mareschal, M., and Chouteau, M. (1993). Channelling contribution to tipper vectors: a magnetic equivalent to electrical distortion. *Geophys. J. Int.*, 113:693–700.

Zhang, P., Roberts, R. G., and Pedersen, L. B. (1987). Magnetotelluric strike rules. *Geophysics*, 51:267–278.

Zhang, P., Chouteau, M., Mareschal, M., Kurtz, R., and Hubert, C. (1995). High-frequency magnetotelluric investigation of crustal structure in north-central Abitibi, Quebec, Canada. *Geophys. J. Int.*, 120:406–418.

Zhang, P., Pedersen, L. B., Mareschal, M., and Chouteau, M. (1993). Channelling contribution to tipper vectors: a magnetic equivalent to electrical distortion. *Geophys. J. Int.*, 113:693–700.

Zhang, P., Roberts, R. G., and Pedersen, L. B. (1987). Magnetotelluric strike rules. *Geophysics*, 51:267–278.

Appendix

A The Iapetus Dataset - Coordinates

A.1 GDS Sites - Northern England and Scotland

I.D.	*Station Name*	*Eastings (km)*	*Northings (km)*	*Survey*	*Bands*
AC	Aydon Castle	400.5	566.8	GMU80	1-18
AF	Ashes Farm	377.8	478.2	LAN79	3-9
AL	Alston (AL)	371.5	546.5	ELW71	3-6
AS	Alston	370.0	551.7	GMU80	1-18
BA	Bampton (BAM)	351.6	518.3	LAN75	3-9
BB	Blackburnhead	379.8	595.7	GMU81	1-18
BE	Berwick-on-Twd(BE)	400.0	651.5	ELW71	3-6
BI	Burntisland (BUR)	322.0	688.0	EDU73	1-10
BK	Bankend (BKD)	302.7	568.5	EDU73	1-10
BR	Boreland (BOR)	314.9	592.7	JON75	4-18
BS	Brough Sowerby	380.3	513.1	LAN80	1-18
BU	Burton-in-Kndl(BUR)	352.7	474.8	LAN75	3-9
BW	Borthwickbrae (BOW)	336.6	616.3	ING81	7-16
BZ	Brackenber (BB)	372.4	519.5	LAN80	1-18
CA	Caton	352.9	465.1	LAN79	3-9
CB	Colburn (CO)	420.8	500.8	ELW71	3
CE	Crieff (CRF)	290.4	720.8	ING81	6-17
CF	Chapel Fell	386.9	535.0	GMU80	1-18
CH	Cliffe Hall	421.1	515.4	GMU79	1-18
CK	Craik (CRK)	334.8	608.0	JON75	2-17
CK	Craik	335.2	609.8	GMU81	1-18
CL	Carlisle (CAR)	337.7	564.3	LAN75	3-9
CN	Carsphairn (CPH)	256.5	593.0	EDU73	1-10
CO	Cornhill-on-Tw(COT)	386.3	637.1	EDU73	1-10
CP	Cappercleuch (CAP)	322.6	623.3	JON75	6-18
CR	Cumrew	354.8	550.9	LAN80	1-18
CS	Cauldron Snout	380.5	528.1	GMU80	1-18
CZ	Close House (CH)	411.5	567.3	ELW71	3
DA	Dalton	392.2	559.0	GMU80	1-18
DH	Chapel-le-Dale (CD)	371.4	475.4	LAN85	1-17
DM	Durham	426.6	541.5	GMU79	1-18
DU	Dumfries (DU)	297.0	574.4	ELW71	3-6
DZ	Drumelzier (DZR)	311.5	634.3	JON75	1-17
EB	Earlyburn (EB)	322.8	649.6	ELW71	3-6
EB	Earlyburn (EAR)	322.8	649.6	ING81	12-17
EB	Earlyburn	322.8	649.6	GMU80	1-18
ED	Elsdon (ELS)	394.6	594.2	EDU73	5-10

EG	Edges Green (924)	372.3	568.7	NOV81	6-18
EH	Edge House	393.3	574.0	GMU80	1-18
EL	Elsrickle (ELC)	303.4	641.9	JON75	1-17
ES	Eskdalemuir (ES)	323.5	602.7	ELW71	3-6
ES	Eskdalemuir (ESK)	323.5	602.7	JON75	7-18
ES	Eskdalemuir	323.5	602.7	GMU79	1-18
FY	Fintry (FIN)	258.5	690.0	EDU73	1-10
FT	Forth (FTH)	294.2	655.2	JON75	2-18
GA	Galashiels (GAL)	351.2	639.6	EDU73	1-10
GB	Great Bavington	396.7	580.5	GMU81	1-18
GI	Gisburn (GIS)	383.3	447.7	LAN75	3-9
GO	Gordon (GOR)	366.4	643.6	JON75	1-18
GQ	Glen Quaich (GQU)	288.5	736.6	ING81	7-18
GS	Galston (GST)	250.0	637.0	EDU73	1-10
HB	High Birkhurst	358.0	563.6	LAN80	1-18
HC	Honey Crook	383.0	566.5	GMU80	1-18
HE	Hill End	401.3	535.5	GMU79	1-18
HE	Hill End (925)	401.2	535.5	NOV81	7-18
HF	Hardberry House	393.8	528.0	GMU80	1-18
HG	Hagg Beck (HAG)	345.7	573.8	EDU73	1-10
HH	Herding Hill	371.0	565.4	GMU79	1-18
HK	Hesket (HES)	345.3	546.6	LAN75	3-9
HL	Helensburgh (HEL)	232.0	685.0	EDU73	1-10
HM	Hamsterley Forest	406.5	530.4	GMU79	1-18
HN	Happendon (HN)	284.7	634.9	ELW71	3-6
HO	Hornby	358.2	469.6	LAN79	3-9
HP	Haverah Park (HP)	424.0	452.5	ELW71	3
HR	Lancaster (LA)	349.2	457.9	ELW71	3
HR	Hazelrigg	349.2	457.9	LAN79	3-9
HR	Hazelrigg (HZ)	349.2	457.9	LAN85	1-18
HS	Heysham	342.5	460.9	LAN79	3-9
HW	Hawick (HW)	342.8	615.0	ELW71	3-6
KG	Keverstone Grange	413.8	522.8	GMU79	1-18
KL	Kielder	364.9	598.2	GMU81	1-18
KN	Kinloch Rannoch(KLR)	268.3	758.7	ING81	6-18
KR	Kershope	350.4	579.7	GMU81	1-18
KS	Kinross (KRS)	307.5	700.3	ING81	6-18
LB	Laithbutts	373.6	469.9	LAN79	3-9
LE	Leyland (LEY)	357.3	423.7	LAN75	3-9
LF	Lodge Farm	422.0	531.4	GMU80	1-18
LH	Lesmahagow (LES)	283.1	639.7	EDU73	1-10
LO	Low Oxnop	393.2	497.4	LAN80	1-18

LP	Lampert (927)	368.1	574.4	NOV81	6-18
LS	Lambshield	402.1	549.2	GMU80	1-18
LV		366.0	625.8	GMU81	1-18
MA	Mallerstang	378.3	499.0	LAN80	1-18
MB	Milburn	365.5	529.4	LAN80	1-18
MG	Midgeholme	362.7	558.0	GMU80	1-18
NE	Newcastleton (NEW)	348.9	589.2	JON75	1-18
NH	Nenthead	378.0	543.5	GMU80	1-18
NL	Newlands	408.8	557.2	GMU80	1-18
OI	Old Irvine	334.5	580.1	GMU81	1-18
PB	Peebles (PEE)	327.4	640.5	ING81	6-18
PE	Penrith (PEN)	348.5	532.3	LAN75	3-9
PK	Park Wall	413.6	537.3	GMU80	1-18
PM	Pilling Moss (PM)	339.5	446.7	LAN85	1-18
PN	Penicuik (PEN)	321.7	660.9	ING8	6-18
PR	Preston (PRE)	383.9	660.3	JON75	5-18
PS	Pundershaw	380.0	580.3	GMU81	1-18
PW	Pennine Way	371.7	536.8	GMU80	1-18
RF	Rigfoot	337.2	593.1	GMU81	1-18
RH	Rookhope I (921)	390.3	542.4	NOV81	6-18
RK	Rookhope	393.0	543.5	GMU79	1-18
SA	Little Salkeld	357.1	536.2	LAN80	1-18
SB	Stalling Busk	391.6	485.8	LAN79	3-9
SC	Stobb's Castle	349.9	609.9	GMU81	1-18
SD	Sinderhope	385.3	551.3	GMU79	1-18
SD	SinderhpeShield(923)	385.0	552.0	NOV81	6-18
SE	Sedbergh (SED)	363.2	492.7	LAN75	3-9
SG	Saugh Tree (SGH)	355.2	595.5	EDU73	1-10
SN	Saltoun (SAL)	346.3	668.7	JON75	5-18
SO	Stobo (STB)	315.2	635.8	EDU73	1-10
SP	South Plantation	408.3	544.3	GMU80	1-18
SS	Stripe Sike	365.3	579.6	GMU81	1-18
ST	Stonyhurst (STY)	370.2	439.8	LAN75	3-9
SW	SwinhopeShield(920)	384.4	548.0	NOV81	6-18
SY	Strathyre (STY)	258.0	711.0	ING81	6-18
TD		376.9	610.4	GMU81	1-18
TE	Tebay (TEB)	363.3	505.6	LAN75	3-9
TG	T'head of Greenlaw	274.0	565.0	EDU73	1-10
TH	Thorntonhall (TH)	259.2	655.0	ELW71	3-6
TI	Tinwald (TIN)	299.7	580.4	JON75	1-18
TL	Thornhill (THO)	288.5	595.5	EDU73	1-10

TR	Tranent (TR)	341.8	673.2	ELW71	3-6
TW	Towhouse (TOW)	376.2	563.8	HAJ80	12-14
WC	Cotherstone (Woden Croft)	400.7	520.9	LAN80	1-18
WD	Widdale (WD)	381.0	486.6	LAN85	1-18
WF	Whitfield	378.0	558.5	GMU79	1-18
WH	Whitfield (926)	377.9	560.5	NOV81	6-18
WI	Widdale	382.3	487.9	LAN79	3-9
WK	Wark	378.1	573.9	GMU80	1-18
WR	Wark (WRK)	383.5	576.8	EDU73	1-10
WS	Wileysike	365.6	570.7	GMU79	1-18
WT	Warton (WT)	339.5	428.4	LAN85	1-18
WY	Wray (WR)	360.0	466.4	LAN85	1-18
YO	York	462.2	450.3	GMU79	1-18
YW	Yarrow (YAR)	329.9	624.4	ING81	6-18

All sites are shown on the location map (fig. 10). References for the 12 different surveys can be found in the text (chapter 5).

*

A.2 Sites with common reference processing

The following 35 sites provide response functions estimated with common reference processing:
AC, AS, BS, BZ, CF, CH, CR, CS, DA, EH, HB, HC, HE, HF, HH, HM, KG, LF, LO, LS, MA, MB, MG, NH, NL, PK, PW, RK, SA, SD, SP, WC, WF, WK, WS; all from surveys LAN79 and GMU80.
Common reference site is DM.

*

A.3 Sites omitted in induction arrow maps

The following sites were omitted from datafiles for the induction arrow maps in figures 11 to 14 of section 5.2.1. The respective missing components $\mathcal{A}$ or $\mathcal{B}$ are given in brackets:

fig.11, band 14, real arrows: YW ($\mathcal{B}$)
fig.12, band 10, real arrows: BK ($\mathcal{A}$), RH ($\mathcal{B}$)
imaginary arrows: CN ($\mathcal{B}$), LH, RH ($\mathcal{A},\mathcal{B}$), TL ($\mathcal{B}$)
fig.13, band 7, real arrows: BW ($\mathcal{B}$), RH ($\mathcal{B}$), SO ($\mathcal{B}$)
imaginary arrows: GS ($\mathcal{A}$), LH, TL ($\mathcal{B}$)
fig.14, band 3, real arrows: GS ($\mathcal{B}$), HG ($\mathcal{B}$) , HL ($\mathcal{A}$), SG ($\mathcal{B}$)
imaginary arrows: TH

*

A.4 Sites used in Fig. 18 to 20: variations of $\mathcal{A}$ and $\mathcal{B}$ with period

The following sites were used in the datasets of figures 18, 19, and 20 in section 5.2.2:

top fig. 18:	area a) Askrigg Block & South AF, BU, CA, CB, DH, GI, HO, HP, HR, HS, LB, LE, LO, MA, PM, SB, SE, ST, WD, WI, WT, WY
bottom fig. 18:	area b) Alston Block & Stainmore Trough AS, BA, BS, BZ, CF, CH, CR, CS, HE, HK, HM, KG, LF, LS, MG, NH, NL, PE, PK, PW, RK, SA, SD, SP, TE, WC
top fig. 19:	area c) Northumberland Trough AC, BB, CL, CZ, EH, GB, HB, HC, HG, HH, KL, KR, NE, OI, PS, SG, SS, WK, WR, WS
bottom fig. 19:	area d) Southern Uplands BE, BK, BR, BW, CK, CO, CP, GA, GO, HW, LV, PR, RF, SC, TD, TG, TI
top fig. 20:	area e) Midland Valley CN, DZ, EB, EL, FT, GS, PB, PN, SN, TR
bottom fig. 20:	area f) North BI, CE, FY, HL, KN, KS, GQ, SY

*

A.5 Conversion of log10 (Periods)

log10(period) is used in the contour maps of figures 75 - 34 in section 5.3.5. The corresponding periods for the range 100 s - 1000 s are:

2.0	-	100 s
2.1	-	125 s
2.2	-	150 s
2.3	-	200 s
2.4	-	250 s
2.5	-	300 s
2.6	-	400 s
2.7	-	500 s
2.8	-	650 s
2.9	-	800 s
3.0	-	1000 s

*

A.6 Sites omitted in the datasets for HEA contour plots

A.6.1 Alston Block datasets from single site response functions

The following stations were omitted from the datafiles used to create the contour plots in figures 74 (b) and 33 (a,b) of section 5.3.5:

Band 1,	T = 5454 s :	-
:		
Band 7,	T = 750 s :	-
Band 8,	T = 500 s :	HE, MA
Band 9,	T = 400 s :	MA,SD*
Band 10,	T = 263 s :	HF, MA, SD*
Band 11,	T = 185 s :	HF, MA
Band 12,	T = 125 s :	HF, MA
Band 13,	T = 83 s :	HF, MA, MB
Band 14,	T = 68 s :	MA, MB
Band 15,	T = 58 s :	BZ, HF, MA, MB
Band 16,	T = 48 s :	BZ, HF, MA, MB, SD*
Band 17,	T = 37 s :	BZ, HF, MA, MB
Band 18,	T = 27 s :	SD*, HF

Stations marked * are represented twice in the original dataset, because they were covered by different surveys. However, the results in these cases were so different, that only one point, i.e. the one joining the majority of data, could be used for this study.

*

A.6.2 Alston Block datasets from local response functions

Apart from the following two sites, all 35 sites of the Alston Block dataset could be used to create the contour plots in figure 34 (a,b) of section 5.3.5:

Band 6,	T = 1000 s :	LO
Band 7,	T = 750 s :	LO
Band 8,	T = 500 s :	LO
Band 9,	T = 400 s :	LO
Band 10,	T = 263 s :	MA

*

B Argand Diagrams with Station Identifiers

The following figures 65 - 70 are enlarged reproductions of the diagrams in figures 23 and 24 of sections 5.3.1 and 5.3.2. The associated station names are printed beside the data points. Due to the high density of points, the site names are not always readable. Outliers, however, can be identified in most cases.

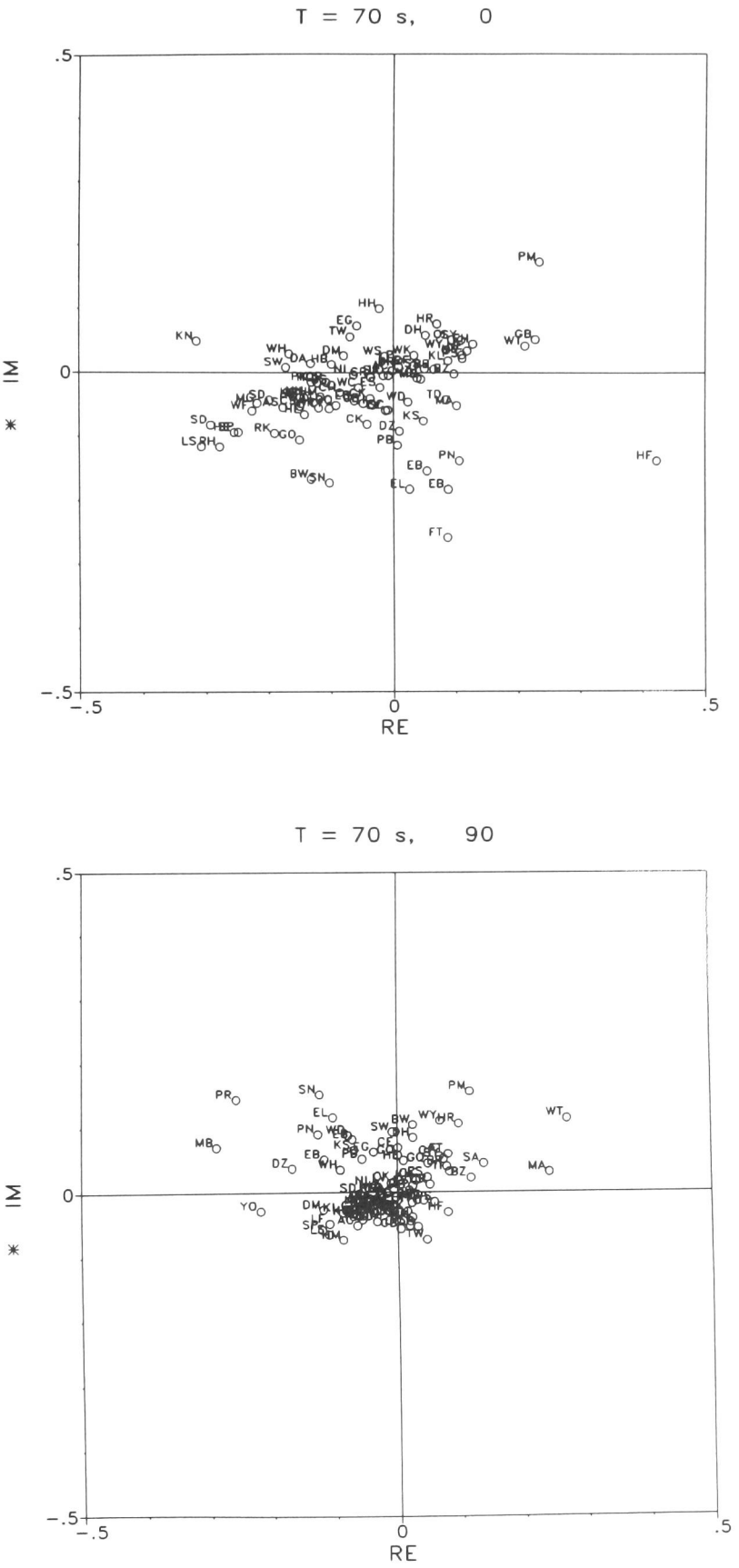

Figure 65: *The Iapetus Dataset: Argand diagrams - site identifiers for fig. 23 (a) of section 5.3.1.*

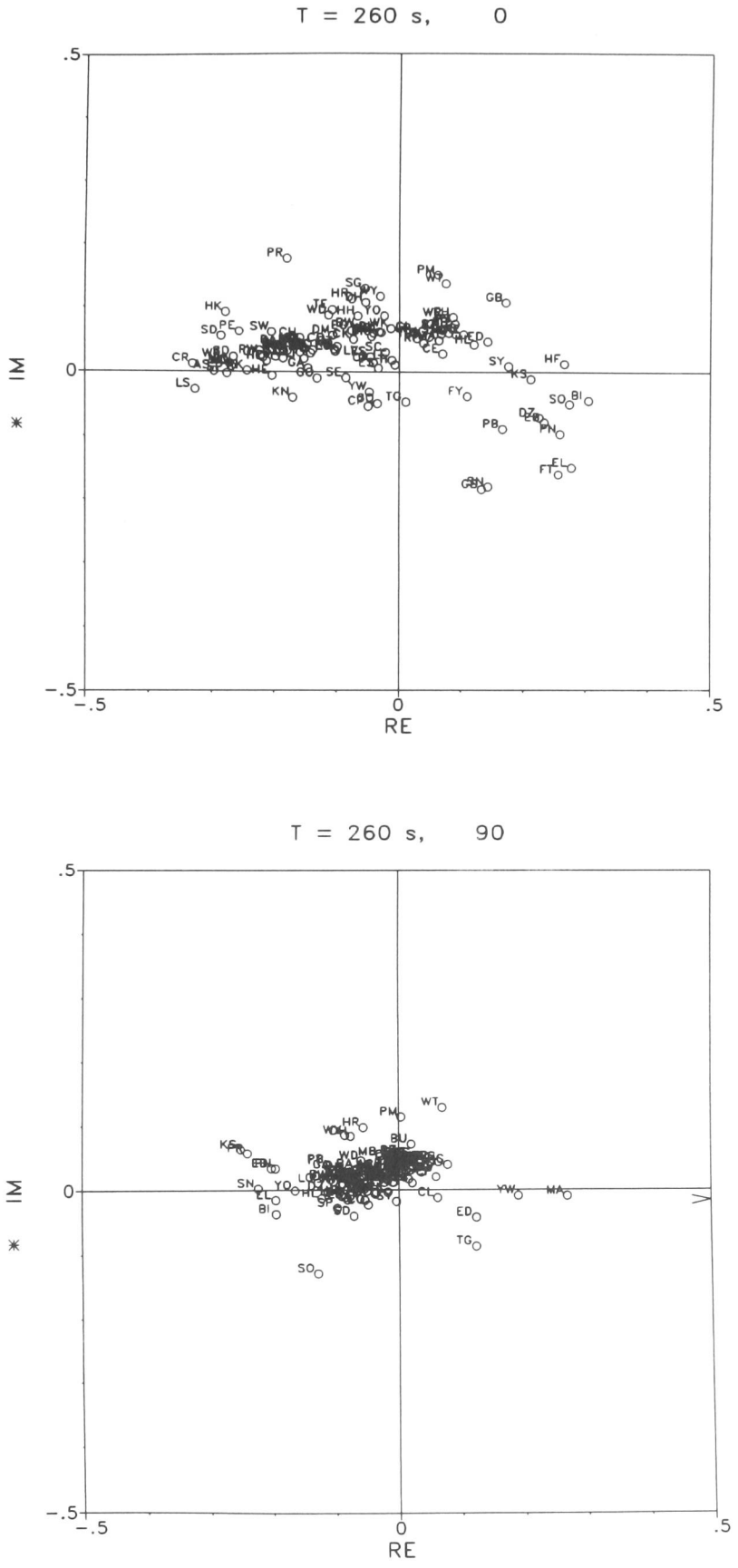

Figure 66: *The Iapetus Dataset: Argand diagrams - site identifiers for fig. 23 (b) of section 5.3.1.*

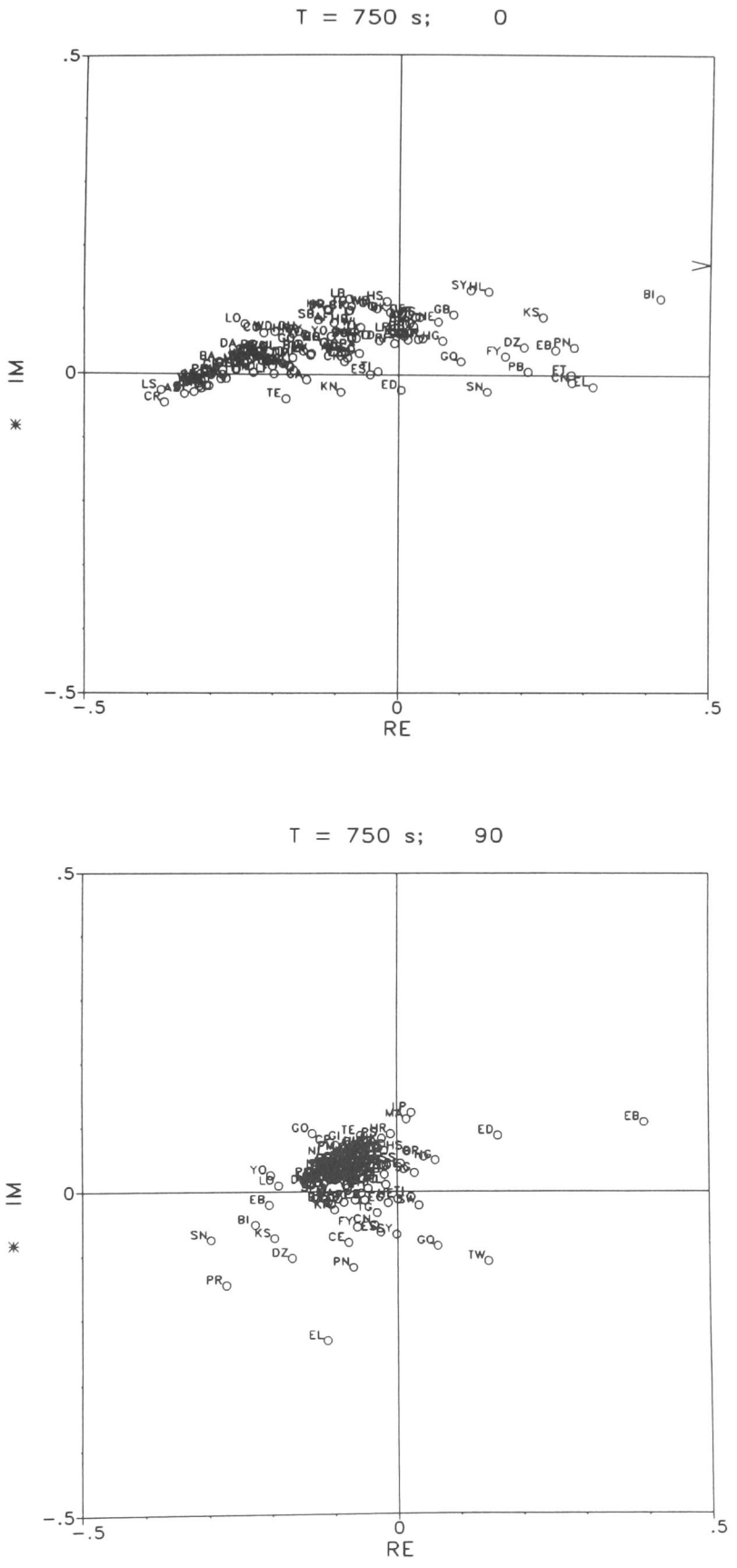

Figure 67: *The Iapetus Dataset: Argand diagrams - site identifiers for fig. 23 (c) and 24 (a) of section 5.3.1.*

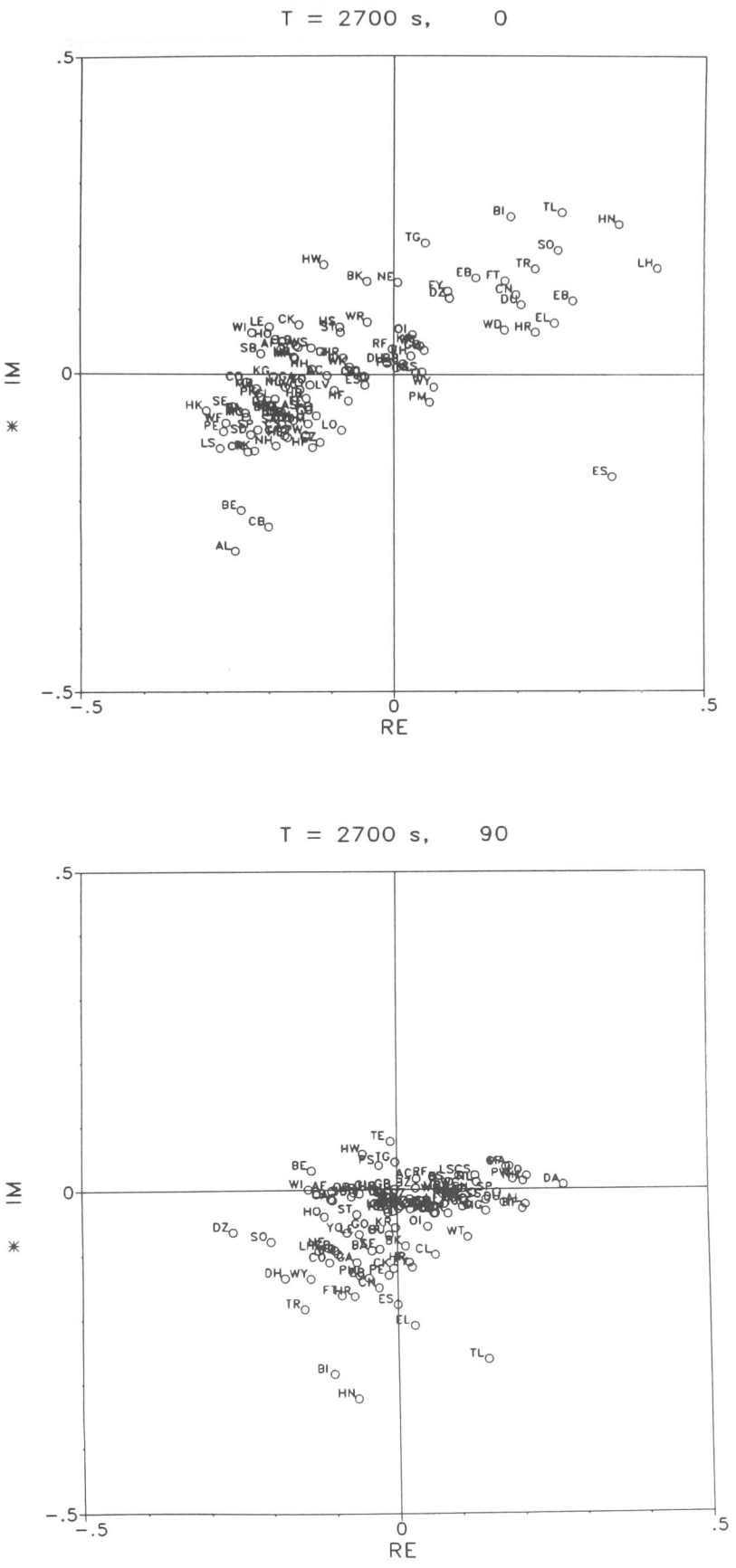

Figure 68: *The Iapetus Dataset: Argand diagrams - site identifiers for fig. 23 (d) of section 5.3.1.*

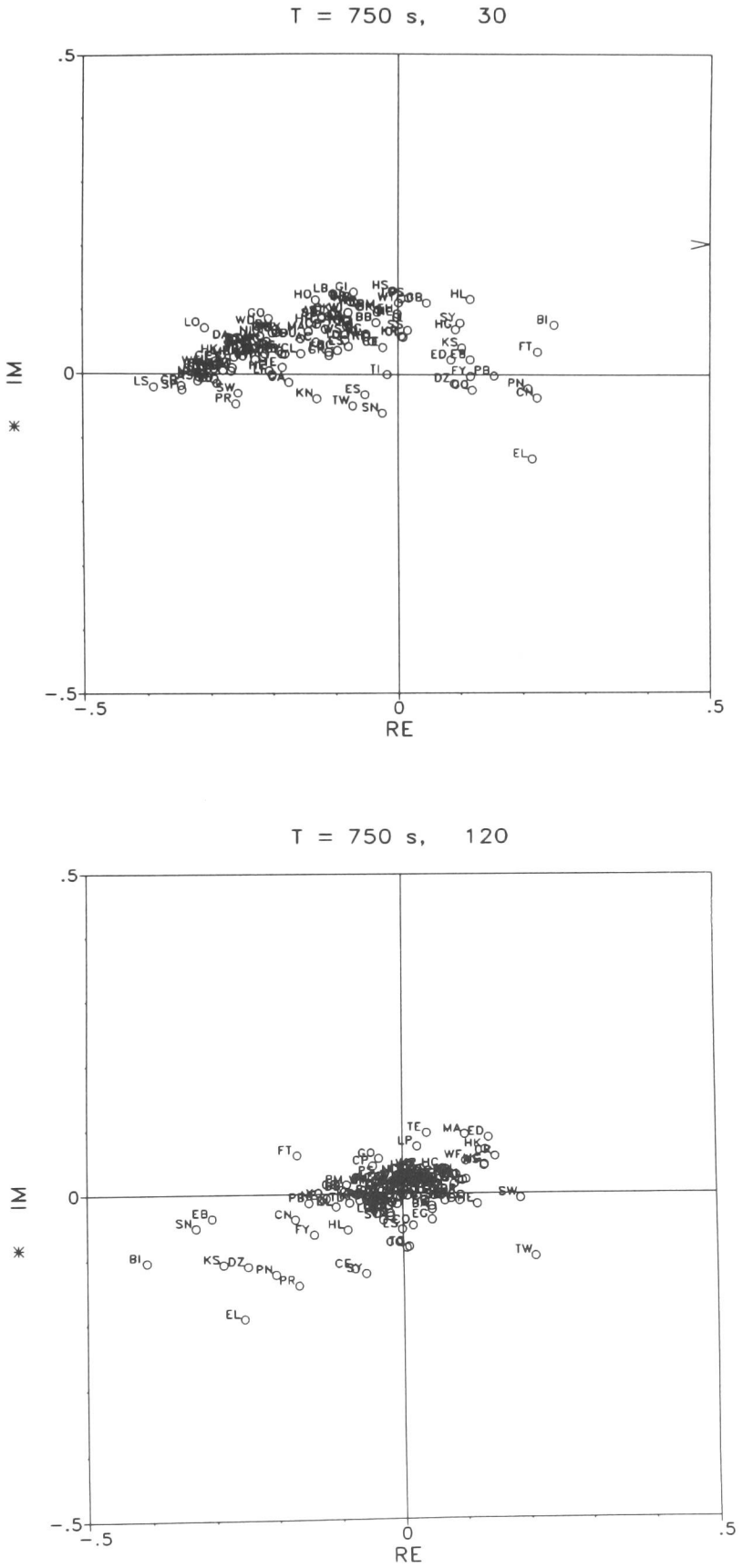

Figure 69: *The Iapetus Dataset: Argand diagrams - site identifiers for fig. 24 (b) of section 5.3.2.*

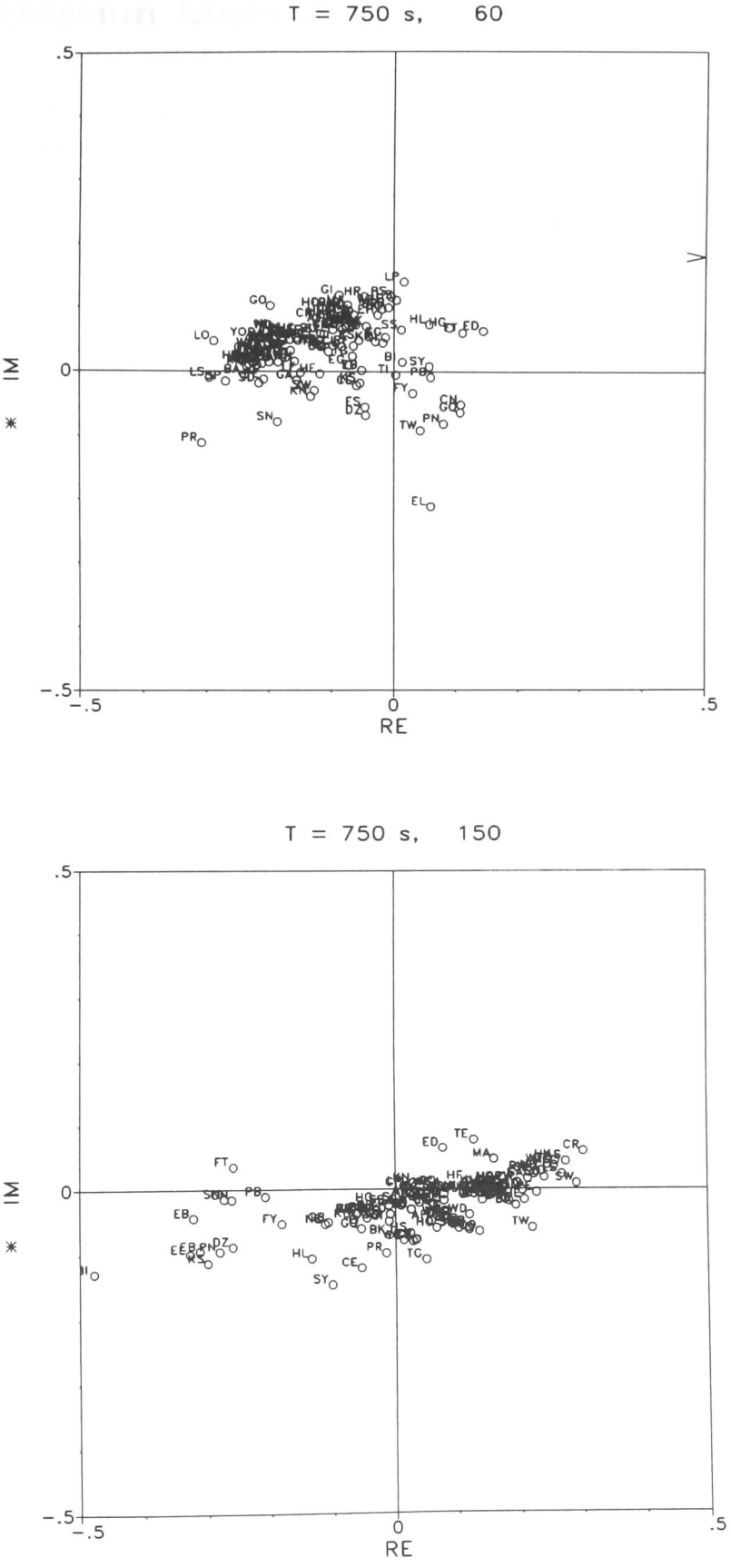

Figure 70: *The Iapetus Dataset: Argand diagrams - site identifiers for fig. 24 (c) of section 5.3.2.*

C Regression Lines

Fig. 71 presents the predicted values of polarisations in the range 90° - 150° in steps of 10°. For comparison, the graph of northward polarisation is repeated in this figure (upper left corner).

Fig. 72 and 73 shows the regression line characteristics of the 95 - sites dataset and the Alston Block dataset.

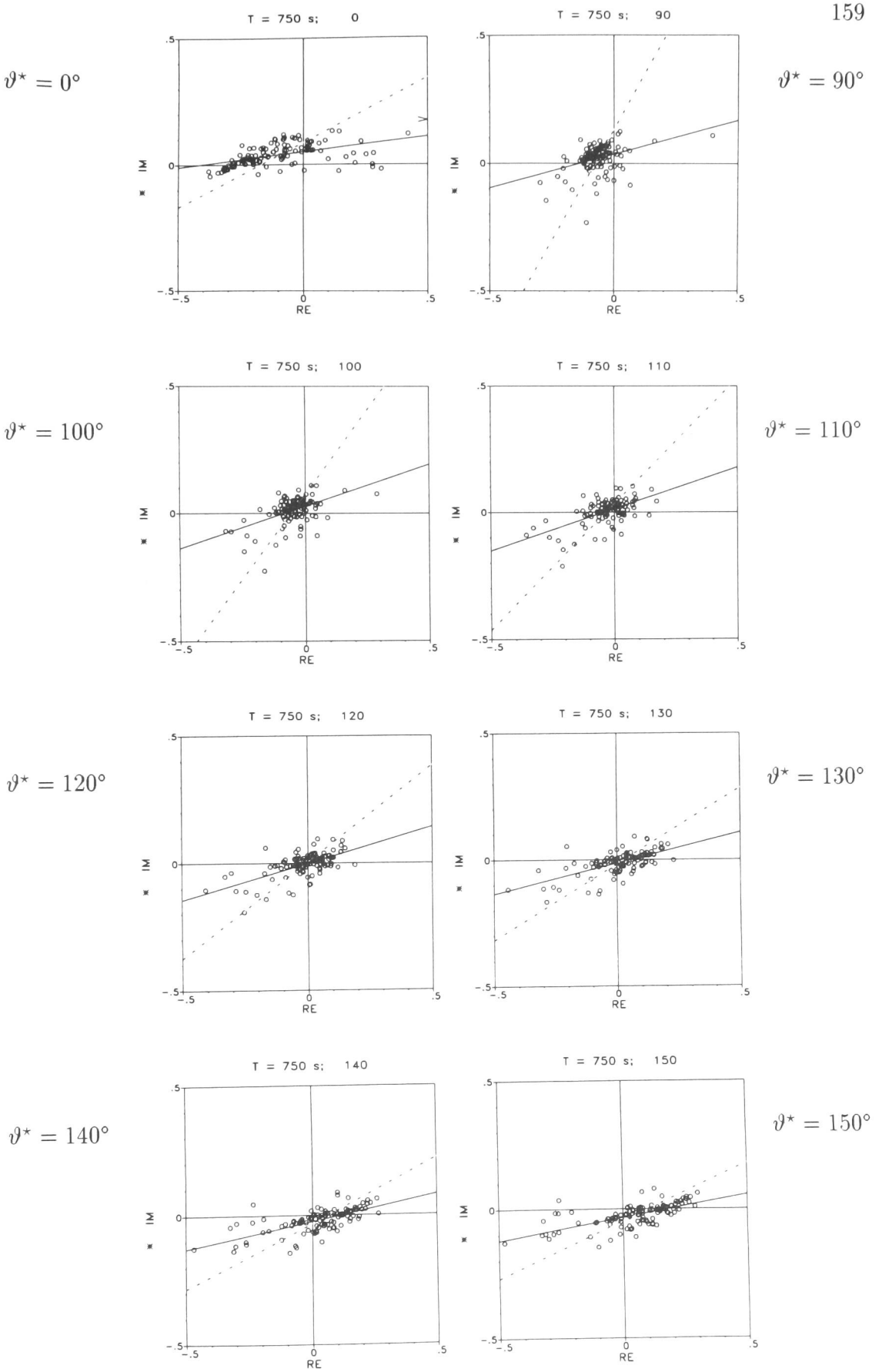

Figure 71: *The Iapetus Dataset: Hypothetical event analysis, all sites, $T = 750s$. Argand diagrams of predicted values $B^p_{z_i}$ at polarisations in the azimuth range where the cloud of points passes the origin, investigated in steps of* 10°. *Regression lines: dashed = x - line (fit of imaginary parts); solid = y - line (fit of real parts). The y - lines fit the data better in most cases.*

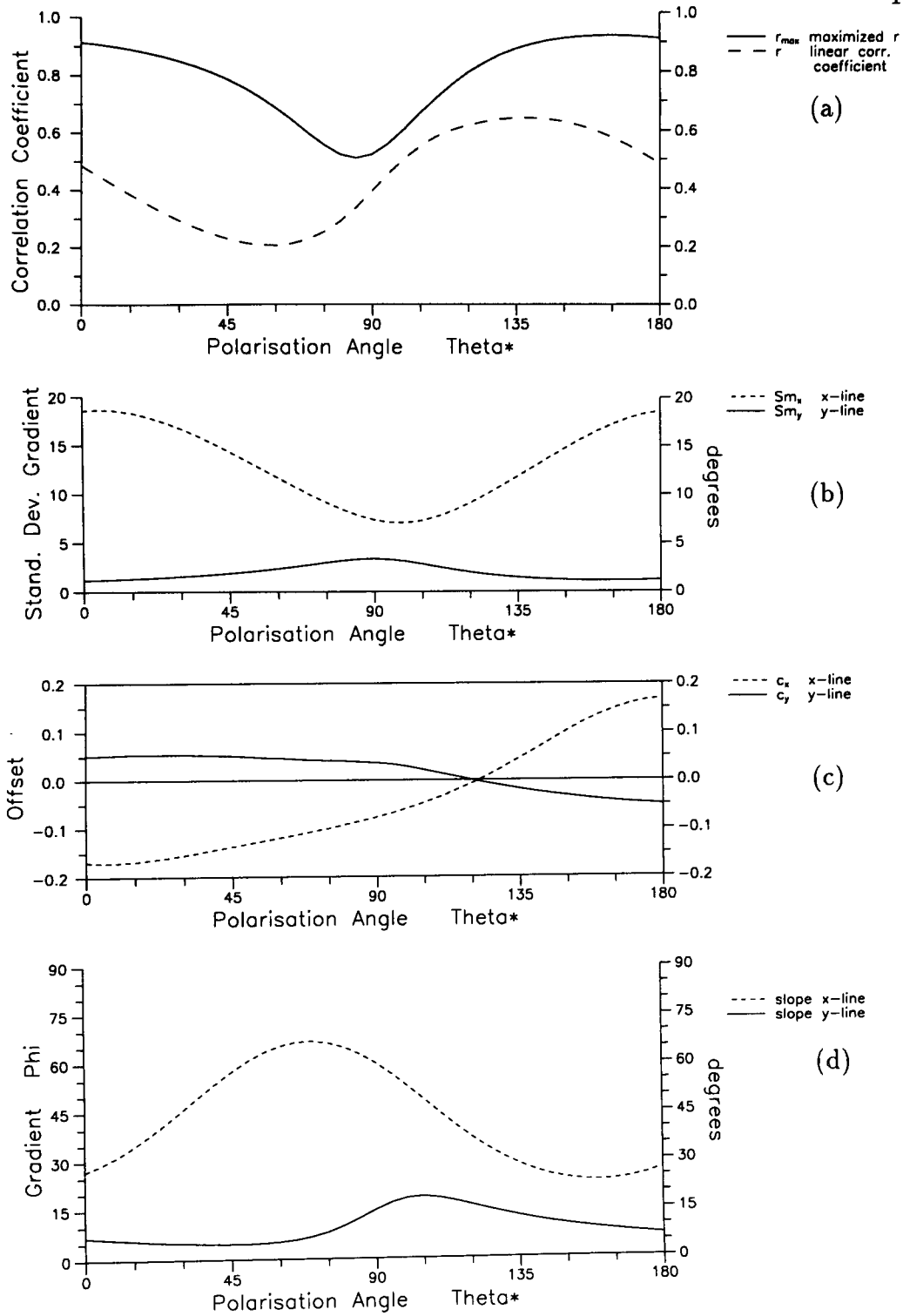

Figure 72: *The Iapetus Dataset: Hypothetical event analysis, all sites, T = 750s, polarisations:* 0° – 180°. *Regression line parameters:*
a) Linear correlation coefficients $|r|$ *(dashed line) and* $|r_{max}|$ *(solid line);*
b) Standard deviations of the gradients of the x - line (finely dashed) and y - line (solid). Generally, the standard deviation of the y - line is much smaller than that of the x - line. Its maximum coincides with the minimum of linear correlation (r_{max}) *at a polarisation of ca.* 90°.
c) Intercepts of the x - line (dashed) and y - line (solid); at polarisation azimuth 120° *both lines pass through the origin. The common regional vertical component is eliminated at this azimuth, which may therefore be interpreted as regional strike.*
d) Phase angles inferred from the gradients of the x - line (dashed) and y - line (solid). Phases of the y - line are generally smaller than 20°.

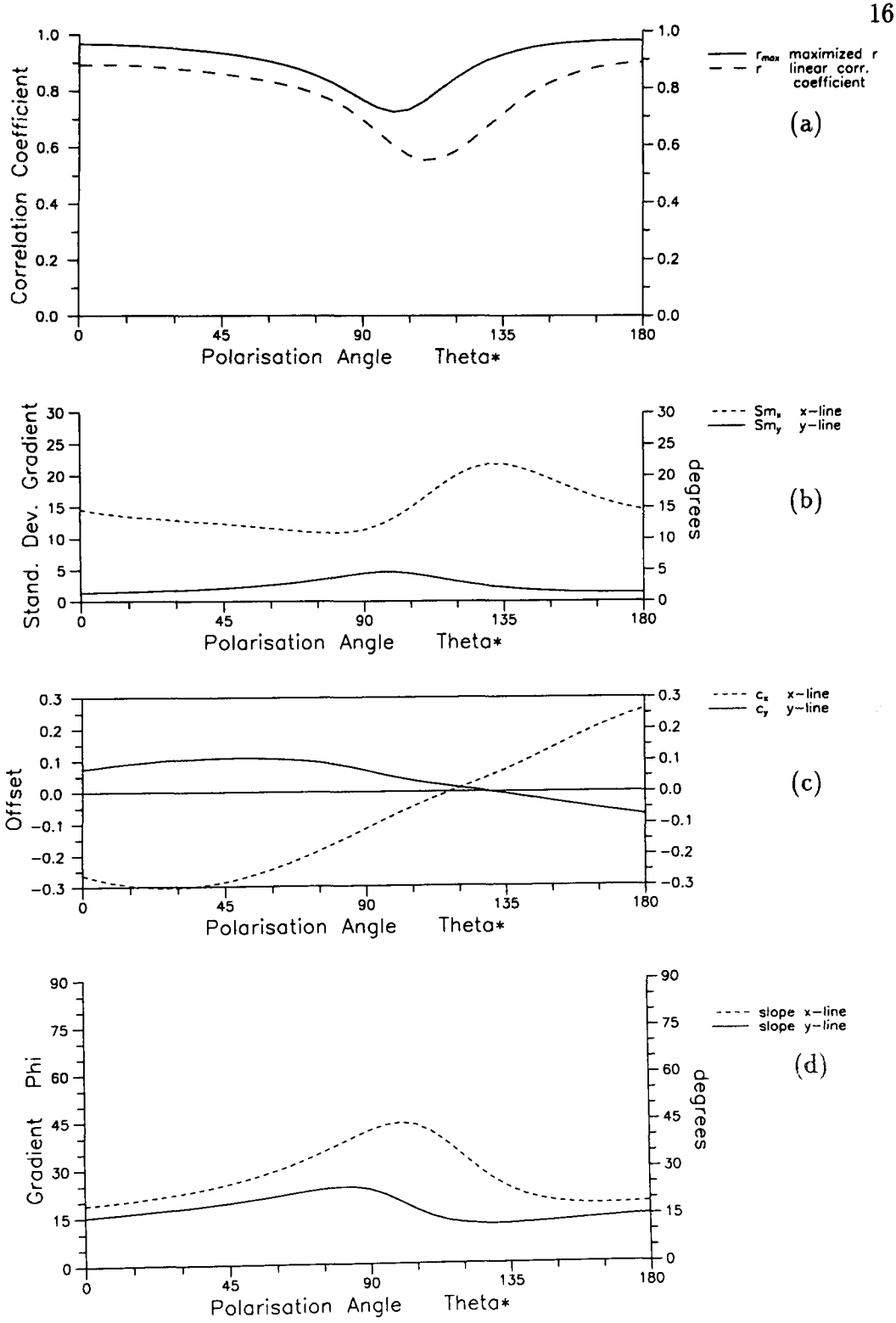

Figure 73: *The Iapetus Dataset: Hypothetical event analysis, Alston Block dataset (35 sites), T = 750s, polarisations: 0° − 180°. Regression line parameters:*
a) linear correlation coefficients |r| (dashed line) and $|r_{max}|$ (solid line);
b) standard deviations of the gradients of the x - line (dashed) and y - line (solid).
c) intercepts of the x - line (dashed) and y - line (solid);
d) phase angles inferred from the gradients of the x - line (dashed) and y - line (solid). Although x- and y - lines have now similar gradients in regions of high linear correlation, the y - line is to be preferred because of its smaller error. It passes through the origin at slightly higher polarisation azimuths than for the larger datasets.

D Contour Maps of the 'Reduced Dataset'

On this basis, the datasets of all other period bands (bands 1 - 18) were reduced to sites located south of the Southern Upland Fault. Apart from the data of the northern sites, few additional data points had to be omitted from the datasets, because they were identified as outliers throughout several or most period bands (for example HF, MA, TL). Dropping those few outliers from the datasets, together with stations that provide only incomplete response functions, is justified in view of the large number of sites available. The sites ruled out are listed below. Since not all sites provide data at all periods, the average number of sites contained in these datasets is 80. They still cover an area of 190 × 230 km.

*

Apart from the 22 northernmost sites, namely

BI, CE, CN, DZ, EB, EL, FT, FY, GQ, GS, HL, HN, KN, KS, LH, PB, PN, SN, SO, SY, TH, TR,

the following were omitted from the datafiles used to create the contour plots in figures 75 (a,b) and 74 (a) of section 5.3.5:

Band 1,	T = 5454 s :	-
Band 2,	T = 4000 s :	BK, CO, GO, HR, MA, NE, PM, PS, WD, WY
Band 3,	T = 2727 s :	ES*, HC, HG, SG, TL
Band 4,	T = 2000 s :	HG, PM, SG, TG, TL, WR, YO
Band 5,	T = 1428 s :	ED, PR, TG
Band 6,	T = 1000 s :	BE, DU, ED, ES*, TG
Band 7,	T = 750 s :	BW, ED, ES*, HG, LO, RH, TI, TL, TW
Band 8,	T = 500 s :	ED, ES*, PM, PR, SD, SG, TI, TL, YW
Band 9,	T = 400 s :	BW, CP, ED, ES*, GA, MA, SW, TI, TL, YW
Band 10,	T = 263 s :	BK, CP, ED, ES*, HF, MA, PR, RH, TG, TL, YW
Band 11,	T = 185 s :	BW, HF, LP, MA, PR
Band 12,	T = 125 s :	HF, MA, PR
Band 13,	T = 83 s :	DZ, EG, HF, KS, MA, SD*, YW
Band 14,	T = 68 s :	HF, MA, MB, PR, TW, YW
Band 15,	T = 58 s :	HF, MA, MB, PR, RH
Band 16,	T = 48 s :	BW, BZ, HF, LO, MA, MB, NE, RH, SD*, WT, WY, YO
Band 17,	T = 37 s :	BW, HF, LP, MB, PR, RH, SD*, YO
Band 18,	T = 27 s :	CK, HF

Stations marked * are represented twice in the original dataset, because they were covered by different surveys. However, the results in these cases were so different, that only one point, i.e. the one joining the majority of data, could be used for this study.

*

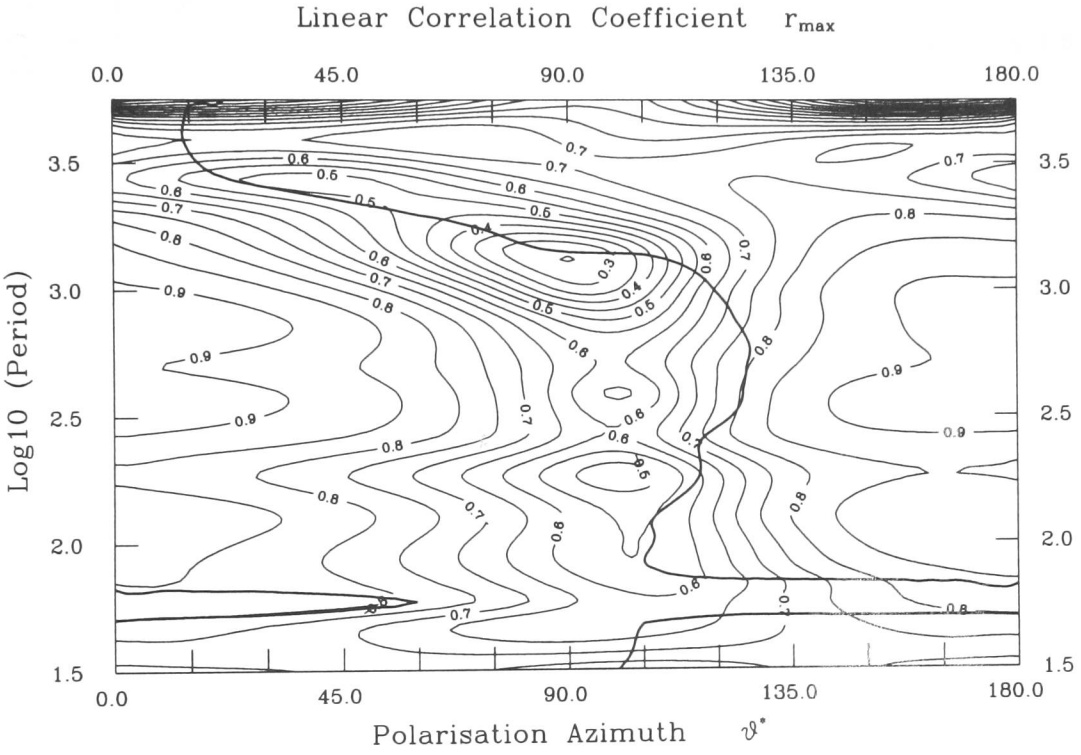

Figure 74: *The Iapetus Dataset: Hypothetical event analysis, all periods, polarisations:* 0° – 180°. *Contour plot of maximized linear correlation coefficient* $|r_{max}|$*: Reduced datasets (sites south of Southern Upland Fault; av. 80sites).*
The thick line marks the positions of the zero-offset line taken from the associated intercept map (fig. 75 a). The correlation minimum occurs at polarisations 90° - 100° *in the period range < 1000s. At longer periods, the minimum stretches towards smaller polarisation angles. The zero-offset line runs on the right flank of the correlation minimum at periods 400s - 1000s.*
Note that in this and the following maps the period increases from the bottom to the top of each diagram (contrary to the usual convention).

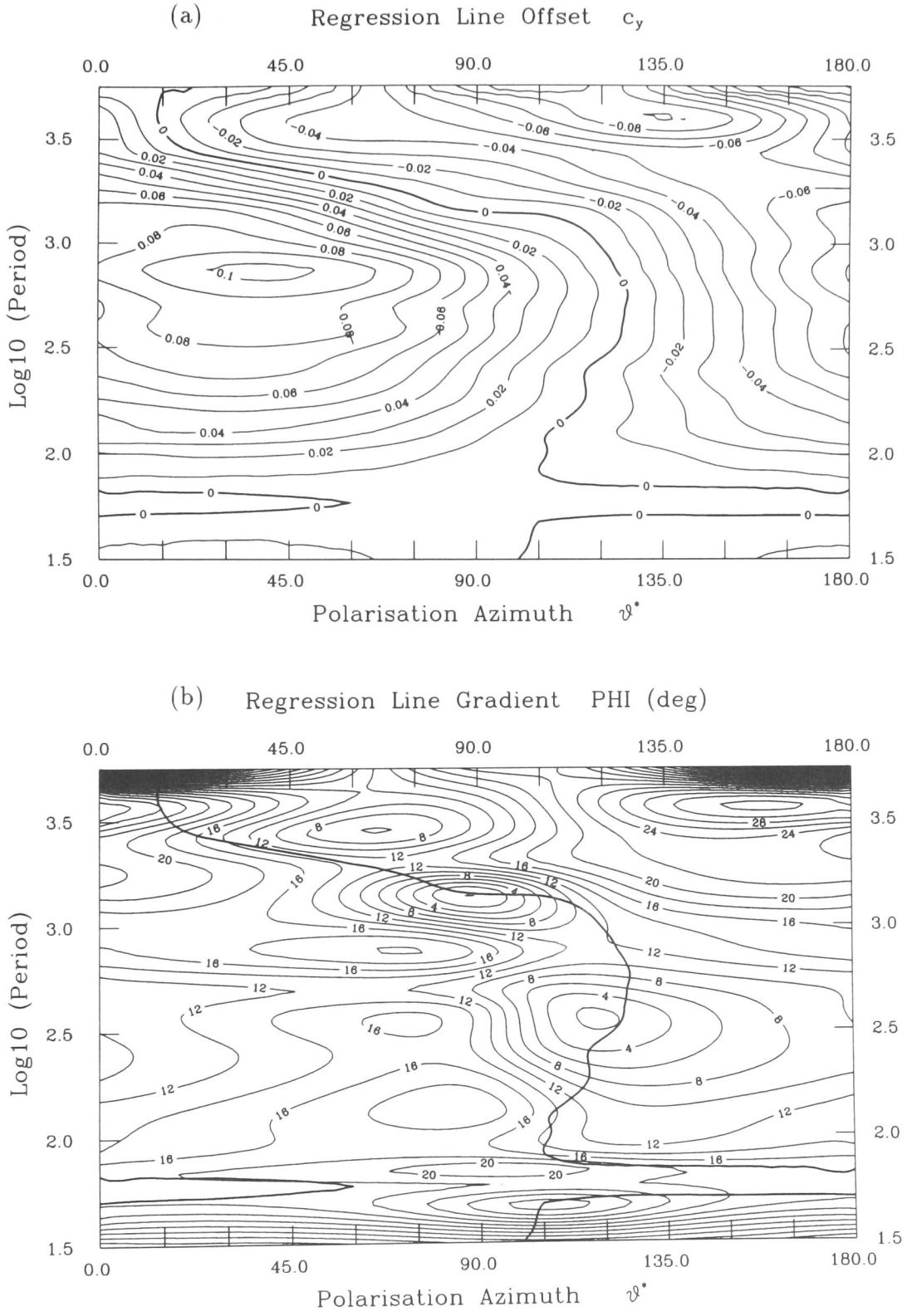

Figure 75: *The Iapetus Dataset: Hypothetical event analysis, reduced datasets, all periods, polarisations:* 0° – 180°. *Contour plots of regression line parameters:*
a) intercepts of the y - lines; the zero-line corresponds to a fairly constant polarisation of 110° - 130° *at periods 200s - 1500s. The zone of maximum offset is located at perpendicular polarisation.*
b) phase angles of the regional impedance inferred from gradients of the y - regression lines. The thick line marks the position of the zero-offset line taken from the upper map. It coincides with the position of the phase angle minima.

E Publications

The following paper has been published during the course of this study:

- P. Ritter and O. Ritter, [accepted Feb 1996], *The BC87 Dataset: Application of Hypothetical Event Analysis on Distorted GDS Response Functions and Some Thinsheet Modelling Studies of the Deep Crustal Conductor*, Journal of Geomagnetism and Geoelectricity.

J. Geomag. Geoelectr., **48**, 000–000, 1996

The BC87 Dataset: Application of Hypothetical Event Analysis on Distorted GDS Response Functions and Some Thin sheet Modelling Studies of the Deep Crustal Conductor

Patricia Ritter and Oliver Ritter

Department of Geology and Geophysics, University of Edinburgh, Edinburgh EH9 3JW, Scotland

(Received: December 23, 1994; Revised: December 15, 1995; Accepted: February 2, 1996)

Galvanic distortion of the regional MT responses was inferred from the analyses of the BC87 dataset presented at the MT-DIW1 in 1992. Since perturbation currents also produce an anomalous magnetic field, the GDS response functions were suspected to be distorted in the long period range. In order to reveal the correct regional strike direction, hypothetical event analysis was applied to the data from all sites. With this technique, common regional information, such as strike and impedance phase, can be recovered from distorted response functions. Although the BC87 GDS data are noisy, and the distortion is more of an inductive than of a purely galvanic nature, the resulting regional strike direction of 60° agrees well with the azimuth suggested from previous MT decomposition methods.

Thin sheet modelling studies of the geometry of the deep crustal conductor (L-shaped or oblique) at 1000 s imply that along the BC87 profile induction arrows are generally produced by current concentrations around a resistive region associated with the Nelson Batholith. Comparison of the model induction arrows with those determined from the BC87 data indicates that the model featuring the oblique, NE striking (SABC) conductor may be favoured.

1. Introduction

At the first Magnetotelluric Data Interpretation Workshop (MT-DIW1) held in Wellington in 1992, interpretation of the BC87 dataset focused mainly on the MT responses, although GDS data are available for all 27 sites in the dataset. This seemed to be for two reasons: 1. GDS data quality is not very good, especially in the long period range; 2. MT observations revealed strong 3-D effects over the whole period range. These effects were interpreted partly as 3-D induction, partly as galvanic distortion, depending on the geometry of the relevant anomalies (EISEL and BAHR, 1993; JONES *et al.*, 1993; DEGROOT-HEDLIN, 1995). Galvanic distortion of the electric field imposes strong effects on the magnetic field components too. Therefore distortion of the magnetic response functions must also be suspected. This phenomenon is well known in GDS, but has been examined with respect to decomposition methods only recently (GROOM, 1988; ZHANG *et al.*, 1993; CHAVE and SMITH, 1994).

Magnetic distortion due to near-surface conductivity heterogeneities becomes particularly evident when the magnetic response functions are presented as induction arrows: lengths and azimuths may entirely be controlled by the local anomalous magnetic field of the shallow deviations of the regional currents. Nevertheless, one would expect that the response functions also contain information on the regional geology. We can assume that this information is common to all sites within a certain area at long periods. On the other hand, distortion is highly site-dependent. Hence the magnetic distortion problem can be formulated as a combination of site-dependent distortion parameters and contributions from site-independent regional induction processes. ZHANG *et al.*, (1993) and CHAVE and SMITH (1994) used these relations to extract distortion parameters and undistorted response functions at individual sites by solving the appropriate equation

systems. The method used in our approach reveals the common, regional information simply by visualizing the whole set of response functions of a surveyed area.

Hypothetical event analysis (HEA), as a method for interpreting the output from magnetometer arrays, treats the dataset as a unit, and therefore it is most effective in recovering the common information content. If the results from HEA are presented in appropriate diagrams, site-dependent parts of the vertical magnetic field can be isolated. RITTER and BANKS (*in prep.*) show that with noise-free data, and good spatial coverage of the area, it is possible to determine the regional strike direction and phases of the principal regional impedances with this technique. The response functions of the BC87 dataset do not quite meet these conditions: they have large error bars at long periods and the sites are arranged along a profile. Nevertheless, all sites were submitted to HEA in the suspected period range of distortion of 100 s - 1000 s. The results are consistent throughout the whole decade, confirming a strike angle in the same range as found in previous MT analyses.

Another unsolved problem of the area is the geometrical nature of the deep crustal conductor (JONES, 1993). For the MT-DIW2 we investigated with 3-D thin sheet modelling at 1000 s, whether the form of the conductor may be determined from the induction arrows; if a resistive structure associated with the Nelson Batholith is also included into the models.

2. Theoretical Background

Magnetic Distortion: Conductivity heterogeneities causing galvanic distortion are generally assumed to be near-surface and much smaller than the skin depth of the host medium. However, any anomaly produces a partly galvanic response from that period on, where the magnetic source field penetrates into the host, and induction inside the anomaly is not the only cause of electric fields. With increasing period, more and more currents that are induced in the host may be deviated into, or towards, a conductive anomaly. If the anomalous magnetic field $\mathbf{B}^a$, due to local deflections of otherwise uniform regional currents, outweights the anomalous magnetic field, due to induction inside the anomaly, $\mathbf{B}^a$ is in phase with the regional electric field $\mathbf{E}^o$. Since this galvanic response is superimposed on the regional magnetic response, it is known as the magnetic distortion effect. Depending on the size and dimension of the body, distortion may occur at periods where the skindepth of the host is of the order of the scale-length of the distorting body (RITTER and BANKS, *in prep.*). The parameters describing magnetic distortion of the regional response function are real, frequency-independent quantities (GROOM, 1988; ZHANG *et al.*, 1993). If the regional structure is 1-D, the vertical magnetic field is due to distortion only:

$$B_z^a = (D_{zx}, D_{zy})\,\mathbf{E}^o = (D_{zx}, D_{zy}) \begin{pmatrix} 0 & Z^o \\ -Z^o & 0 \end{pmatrix} \begin{pmatrix} B_x^o \\ B_y^o \end{pmatrix} \qquad (1)$$

(D_{zx}, D_{zy}) are the vertical magnetic distortion parameters; Z^o is the regional 1-D impedance. The product $(D_{zx}, D_{zy})\,\underline{\mathbf{Z}}^o$ defines the *local* magnetic response function $(\mathcal{A}^\ell, \mathcal{B}^\ell)$, where $\mathcal{A}^\ell$ and $\mathcal{B}^\ell$ denote the components in x- and y-directions, respectively. For a regional two-dimensional structure, the regional vertical magnetic field B_z^o must be considered:

$$B_z = B_z^a + B_z^o = [\,(\mathcal{A}^\ell, \mathcal{B}^\ell) + (\mathcal{A}^o, \mathcal{B}^o)\,]\,\mathbf{B}_h^o = (\mathcal{A}, \mathcal{B})\,\mathbf{B}_h^o \qquad (2)$$

In this case, the observed response function $(\mathcal{A}, \mathcal{B})$ consists of a local and a regional part. The local part $(\mathcal{A}^\ell, \mathcal{B}^\ell)$ contains the regional 2-D impedance tensor. If the observation points are well removed from any regional lateral boundary, the regional contribution can be assumed small and homogenous across a region of considerable extension, especially for long periods.

Hypothetical event analysis: We can calculate a predicted value for the vertical magnetic field B_z^p that is associated with a certain polarisation $\vartheta^\star$ of the horizontal magnetic field from the observed response function $(\mathcal{A}, \mathcal{B})$. The horizontal field $B^\star$ is supposed to be of unit amplitude over the area of investigation. Using the above expressions which include magnetic distortion, the predicted vertical field in observation coordinates is obtained from:

$$B_z^p = \left[(D_{zx}, D_{zy})\, \underline{\mathbf{R}}_{\theta_r}\, \underline{\mathbf{Z}}'^{o}\, \underline{\mathbf{R}}_{\theta_r}^T + (0, \mathcal{B}'^{o})\, \underline{\mathbf{R}}_{\theta_r}^T \right] \begin{pmatrix} 1 \cdot \cos\vartheta^\star \\ 1 \cdot \sin\vartheta^\star \end{pmatrix} \tag{3}$$

The primes denote quantities in regional strike coordinates $(x', y'$ with a strike direction parallel to the x'-axis) and $\underline{\mathbf{R}}_{\theta_r}$ denotes anti-clockwise rotation by the strike angle θ_r. The equation for the predicted value simplifies considerably for two special cases: when the polarisation azimuth equals the regional strike direction, and when it is perpendicular to it.

$$\vartheta^\star = \theta_r : \qquad B_z^p = Z'_{yx}[-D_{zx}\sin\theta_r + D_{zy}\cos\theta_r] \tag{4}$$

$$\vartheta^\star \perp \theta_r : \qquad B_z^p = Z'_{xy}[\ D_{zx}\cos\theta_r + D_{zy}\sin\theta_r] + \mathcal{B}'^{o} \tag{5}$$

In fact, the expression for the predicted vertical magnetic field B_z^p for the first case does not contain any contribution from the regional vertical field at all. This direction corresponds to the B-polarisation, where no vertical field is generated. Note that the predicted fields at both polarisations contain only one of the principal impedances. This is an important aspect, because it implies that their phases are equal to the phases of the respective regional impedances, if the regional contribution to the vertical field is sufficiently small. In this case, the predicted values at all sites representing the same regional geology should show the same phases at a given period.

In practice, one can find the regional strike direction by gradually varying the polarisation azimuth $\vartheta^\star$ and plotting the predicted values of all sites at one given period in the complex plane (Argand diagram). We can determine the regional phase when the data points fall on a line through the origin, indicating the common phase angle. This happens when the magnetic field is polarised in the strike direction of the regional structure, or perpendicular to it. If the common phase falls in the range 0° - 90°, the response is at least partly caused by galvanic distortion, and the phase angle found is close to the respective impedance phase. If the magnetic response functions are not purely galvanic, but contain also a strong contribution from induction inside the anomaly, the distribution of the predicted values is less linear, and the phase determined by this method is negative. In that case, the phase angle found corresponds to the phase difference between the magnetic source field and the anomalous magnetic field induced in a local structure, whereas the vertical field eliminated belongs to a more regional structure. The strike direction of the latter is indicated by the polarisation azimuth.

3. The BC87 Dataset

Induction Arrows (Wiese convention): In the short and intermediate period range (T < 10 s) the angular distribution of the azimuths of the real arrows is very scattered along the profile. At longer periods (T > 10 s), however, arrows at most sites follow an overall trend, changing smoothly from −90° to directions around 0° (±30°) with increasing periods, although in this range magnetic response functions have relatively large errors. At these periods, the imaginary arrows point approximately −180°. Lengths and azimuths of the Wiese arrows are shown in fig.1 for periods 450 s and 910 s. Note that Wiese arrows point away from conductive regions.

The arrow directions suggest an east-west striking structure at some depth to the south of the profile. However, this does not coincide with the strike direction inferred from MT results

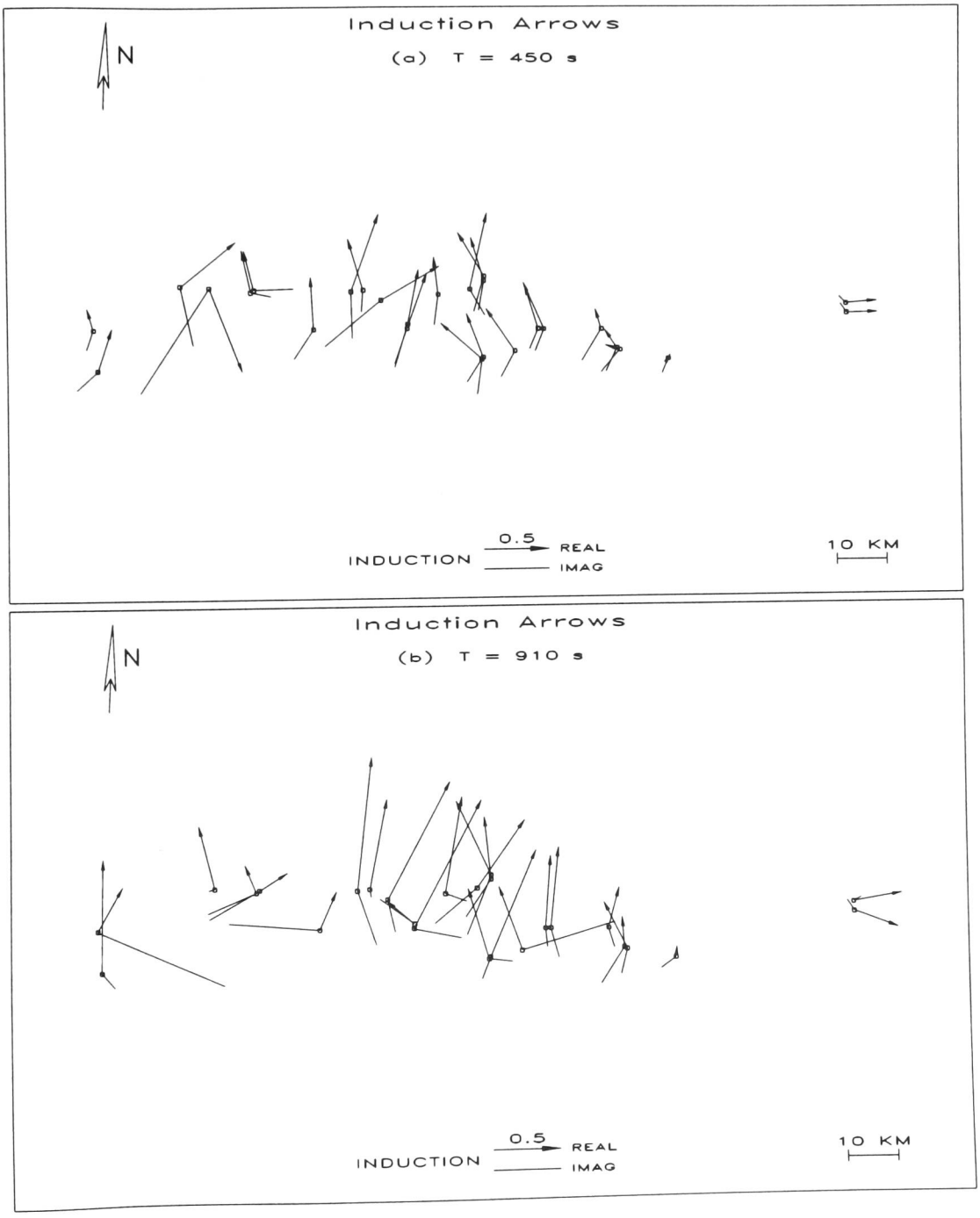

Fig. 1. Induction Arrows (Wiese convention) of all 27 sites at (a) 450 s and (b) 910 s; REAL: real arrows, IMAG: imaginary arrows.

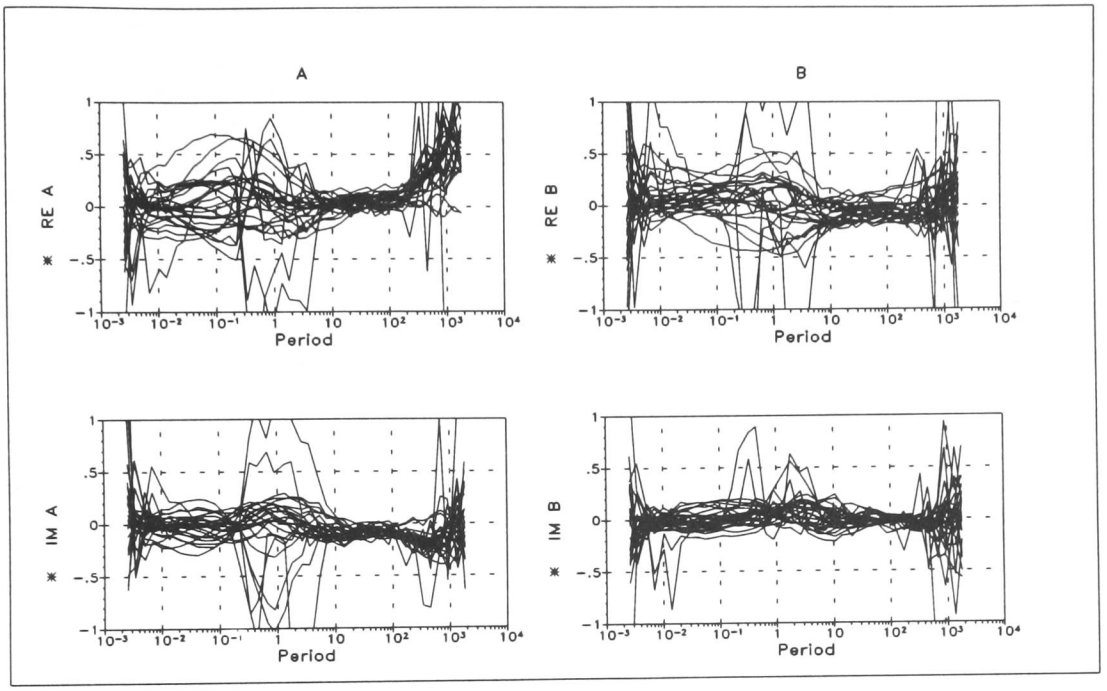

Fig. 2. Magnetic response functions ($\mathcal{A}, \mathcal{B}$) of all sites over the whole period range; RE: real parts, IM: imaginary parts.

at 45° to 60°, associated with the upper mantle anisotropy (EISEL and BAHR, 1993; JONES *et al.*, 1993). Since the amplitudes of the response functions show a definite maximum in the intermediate period range between 0.1 s and 1 s at all sites (fig.2), we can assume that induction takes place in the upper parts of the crust (i.e. the conductor at the eastern edge of the resistive Nelson Batholith, JONES, 1993). The large arrows at longer periods are likely to be produced by currents being deflected by these complex structures and the vertical magnetic field components observed may reflect a mixture of induction and galvanic processes.

Hypothetical Event Analysis: In order to find a more reliable regional strike direction, we applied HEA to all magnetic response functions in the range 10 s - 1000 s. In the case of the BC87 dataset, sites are located along a profile (150 km E-W) with only limited spatial extent (25 km N-S). Hence mapping of the results in contour plots, as it is usually undertaken, may be dominated by interpolation effects rather than providing true images. We found that in this case, a presentation of the values in the complex plane (Argand diagram) is better suited to find common aspects in the data. Since no distinct features could be found in the range 10 s to 100 s, we concentrated our investigations mainly to the decade 100 s to 1000 s. The real and imaginary parts of the predicted values B_z^p of all sites at periods 450 s and 910 s are presented in Argand diagrams (fig.3) for 4 different polarisations of the event.

Varying the polarisation of the hypothetical event moves the points in the complex plane relative to each other, according to the contribution of the regional vertical field. At a polarisation azimuth of about −30° the predicted values calculated from the observed response functions arrange approximately on a line through the origin. This happens when the hypothetic magnetic field is polarised parallel to the strike direction of the regional structure, or is perpendicular to

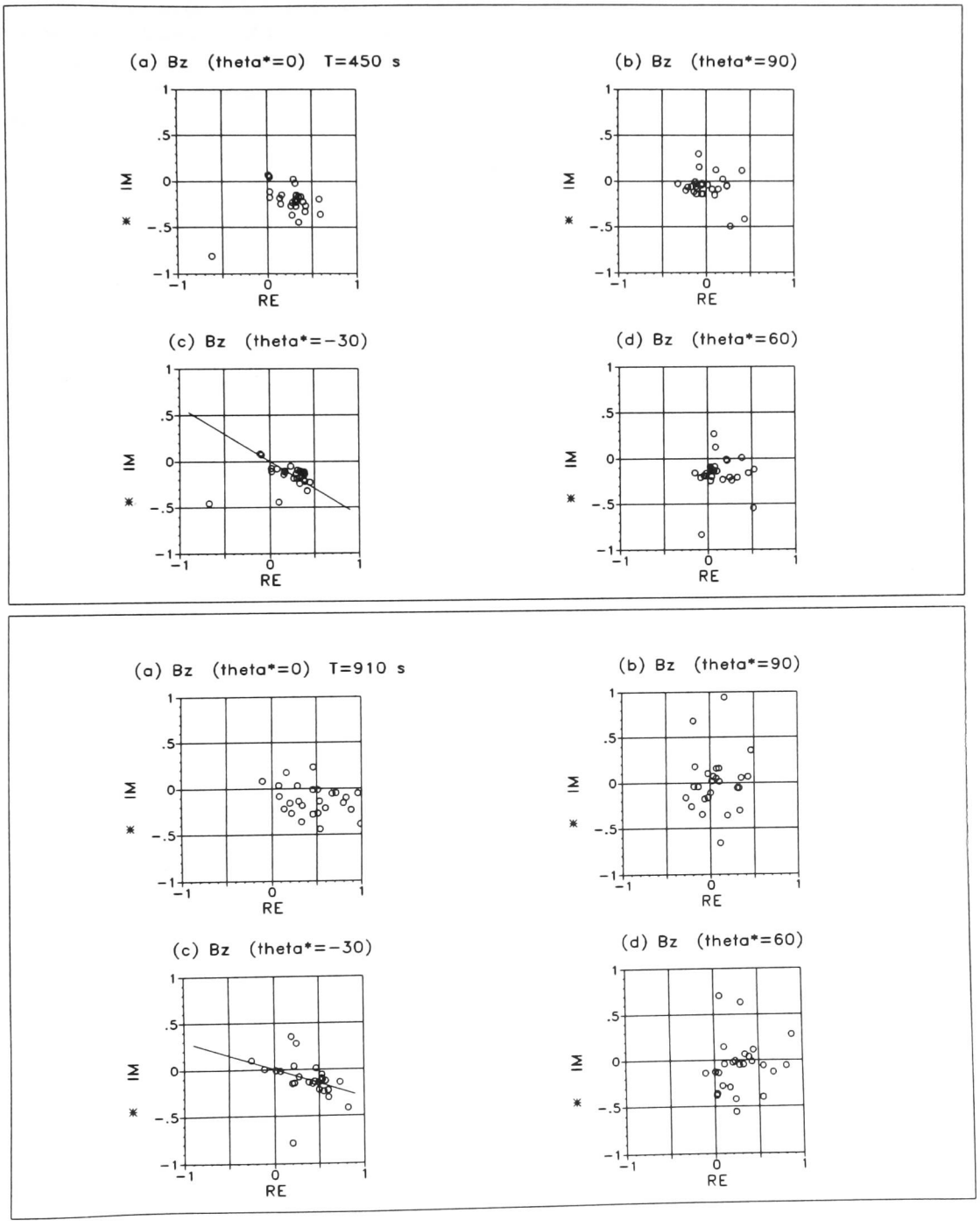

Fig. 3. Hypothetical event analysis, Argand diagrams: Predicted vertical magnetic fields B_z^p of all sites at periods 450 s (upper half) and 910 s (lower half).
RE: real parts, IM: imaginary parts. (a) Polarisation azimuth of the hypothetical magnetic field (with amplitude = 1, phase = 0°) : $\vartheta^* = 0°$, (b) $\vartheta^* = 90°$, (c) $\vartheta^* = -30°$, (d) $\vartheta^* = 60°$.

it. The strike angle can therefore be expected at $-30°$ or at $60°$. The latter corresponds well to the strike found by MT decomposition methods at $45°$ - $60°$. The slope of the line through the origin was determined by weighted least squares fitting; it dips $-30°$ at 450 s and ca. $-20°$ at 910 s. The negative gradients indicate negative common phases, which can only be produced by mainly inductive processes. The phases vary consistently from $-40°$ to $-20°$ from shorter to longer periods. However, the optimum polarisation azimuth is constantly $-30°$ throughout the investigated period range and can therefore be attributed to the strike direction of a more regional structure. Unfortunately, the errors of the response functions increase towards the long period end, so that no reliable results can be obtained from data beyond 1000 s.

4. Thin sheet Modelling - The Deep Crustal Conductor

The method described above aims to recover regional two-dimensional information from an originally three-dimensional problem. It is therefore interesting to expand these investigations by some three-dimensional model calculations. Another question that arose from previous MT and GDS interpretations in the area is whether the deep crustal conductor is L-shaped (striking N/S and E/W), or whether it consists of two separate parts: one situated in the west and striking N/S, the other one located further east and striking NE/SW (the so-called SABC anomaly in Southern Alberta - British Columbia). A detailed description of the general geological situation of the area can be found in JONES (1993). We concentrate our efforts on the investigation of the induction arrows in the region of the BC87 profile (fig.4). The models are calculated with the McKirdy & Weaver thin sheet code (McKIRDY *et al.*, 1985) for a period of 1000s.

The emphasis of such an investigation can only be to study principal effects, as the range of valid thin sheet models is limited by strict requirements for valid cell geometry and conductivity gradients (e.g., WEAVER, 1994). Consequently, resistivity contrasts and sizes in our models are oversimplified. Both models in figure 4 rely on three principal cell resistivities. Cells of $250\Omega m$ generally denote conductive material in a $500\Omega m$ host, resistive cells of $750\Omega m$ represent a more resistive region in association with the Nelson Batholith.

In both models, the magnetic response functions are clearly affected by the resistive complex and their induction arrows are attenuated over its centre. Along the edges of the resistor we find the greatest current concentrations and hence, the largest induction arrows. At the south-eastern part of the resistor, the arrows are also influenced by the form of the conductor. East of the batholith, the real arrows are bent into directions perpendicular to the strike of the 'second' conductor: near the E/W striking structure they point northwards, while arrows near the oblique conductor have a northwest tendency. However, across the southern part of the batholith, and in the vicinity south of it, the arrows point generally towards the northeastern direction in both models, although arrows of the SABC model in the southern area are clearly more inclined to the east. The main difference between the responses from the models is manifested in the lengths of the real arrows in the region east of the resistor. The arrows decrease towards the center of the SABC conductor and also reverse their sign beyond it, whereas they are of constant lengths along the edge of the L-shaped conductor. The imaginary arrows are generally smaller and point at varying, non-parallel angles relative to the real arrows due to the strong three-dimensionality of the studied area.

The azimuthal distribution of the BC87 data along the profile shows a preferred direction of the real arrows of approximately $10°$ to $30°$ from north, although directions of ca $-20°$ occur as well at the more easterly located sites. The lengths of the real arrows decrease towards the east, and at the most eastern sites of the profile they point strictly westwards. Although the observed real arrows are generally longer than the modelled arrows, the general behaviour of arrow directions and magnitudes supports the oblique model.

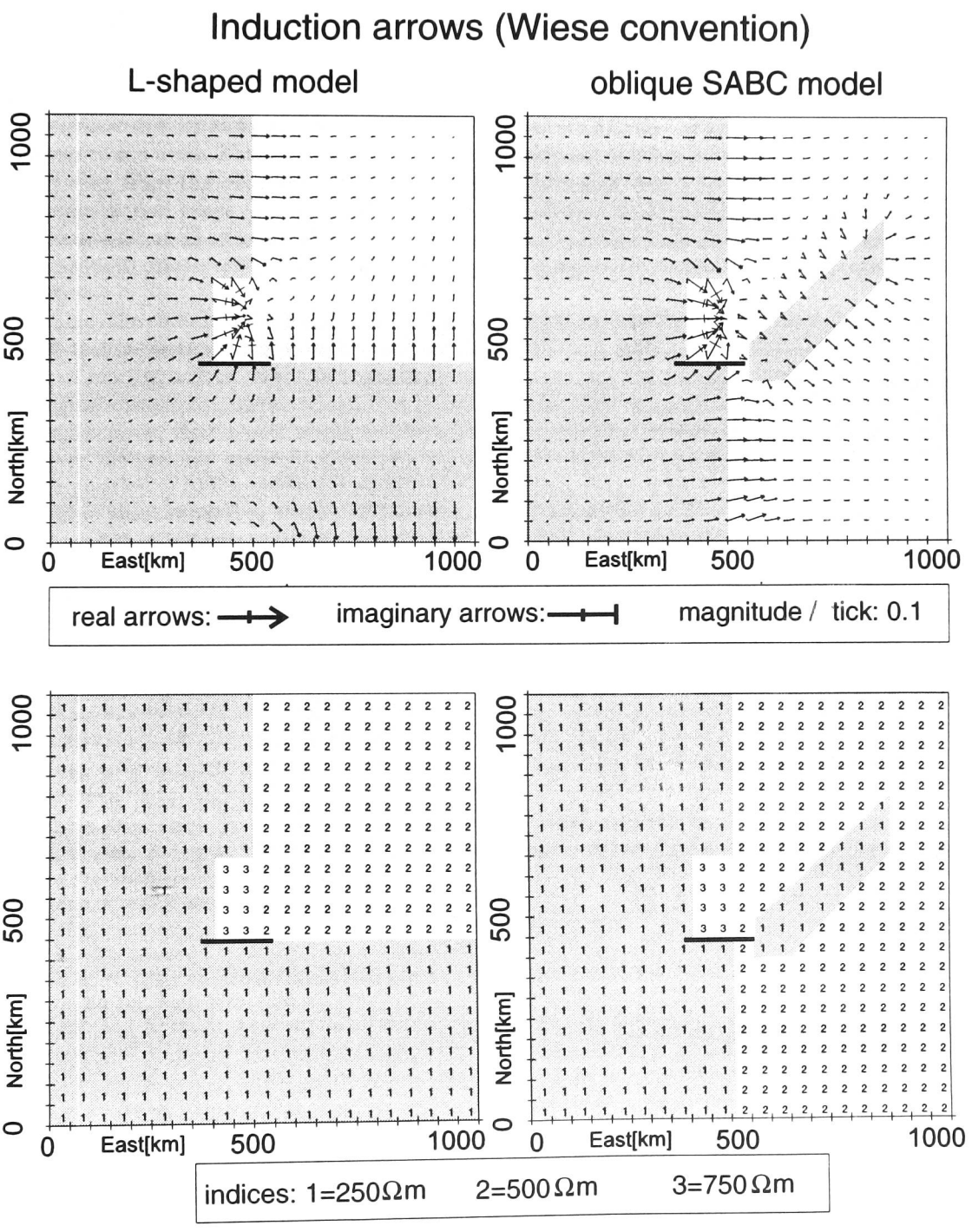

Fig. 4. 3-D thin sheet modelling of the deep crustal conductor: Induction arrows (Wiese convention) for the L-shaped model (left) and the oblique SABC model (right). Marked in the central parts of the figures are the resistor associated with the Nelson Batholith and the approximate location of the BC87 profile (thick line). The sheet cells extend to 50 km in each direction. Beneath the thin sheet we placed a resistive layer of 750 Ωm which is followed by a homogenous halfspace (50 Ωm) at a depth of 400 km.

5. Conclusion

The GDS response functions of the BC87 dataset at long periods are affected by both local and regional induction processes. Since the directions of induction arrows are inconsistent with the regional strike directions found by MT decomposition methods, we applied hypothetical event analysis to the data. This technique is capable of recovering regional information that is common to all sites from the observed response functions. Although better quality of the data in the examined period range (100 s - 1000 s) would be desirable, the predicted values for the vertical magnetic field at all sites reveal common phase angles for polarisations azimuths of around $-30°$. This azimuth corresponds to the strike of the regional conductivity structure or to a perpendicular direction.

Since the common phase angles are negative we must assume that large scale local structures, which may be associated with the resistive Nelson Batholith region, are responsible for contributions of more inductive rather than galvanic origin to the regional response functions. Due to the geological complexity of the region, the limited spatial coverage, and the deficient data quality at long periods, this dataset might not be appropriate to show the full capability of the method; however the regional strike found is in good agreement with the strike direction determined by decomposition of MT impedances at 45° - 60°.

Thin sheet modelling studies of the deep crustal conductor (L-shaped or oblique) at 1000 s confirmed that induction arrows along the BC87 profile may generally be produced by current concentrations around the area that is associated with the resistive Nelson Batholith. Only sites in the (south-) eastern part of the batholith are affected by the form of the deep crustal conductor. The azimuth distributions and the length variations of the real arrows in the area of the profile indicate that the observed data may rather represent the oblique model (SABC conductor). Also, the direction of the SABC conductor could possibly explain the azimuth of the regional strike found by hypothetical event analysis.

The BC87 dataset was made available by D. W. Oldenburg (LITHOPROBE) and A. G. Jones (GSC). This paper was prepared for the second Magnetotelluric Data Interpretation Workshop (MT-DIW2) in Cambridge, preceding the 12th Workshop of Electromagnetic Induction in the Earth held in Brest, France, in August 1994. Alan Jones and Adam Schultz are thanked for their excellent organisation of the pre-workshop workshop, that truly deserved its name. We also thank Alan Jones and the two anonymous reviewers for their very useful comments. LITHOPROBE Publication number 731.

REFERENCES

CHAVE, A. D. and J. T. SMITH, On electric and magnetic galvanic distortion tensor decompositions, *J. Geophys. Res.*, **99 B3**, 4669–4682, 1994.

EISEL, M. and K. BAHR, Electrical anisotropy in the lower crust of British-Columbia - an interpretation of a magnetotelluric profile after tensor decomposition, *J. Geomagn. Geoelectr.*, **45** no.9, 1115–1126, 1993.

DEGROOT-HEDLIN, C., Inversion for regional 2-D resistivity structure in the presence of galvanic scatterers, *Geophys. J. Int.*, **122**, 877–888, 1995.

GROOM, R. W., The effects of inhomogeneities on magnetotellurics, *PhD thesis, Univ. Toronto*, 1988.

JONES, A. G., The BC87 dataset - tectonic setting, previous EM results, and recorded MT data, *J. Geomagn. Geoelectr.*, **45** no.9, 1089–1105, 1993.

JONES, A. G., R. W. GROOM and R. D. KURTZ, Decomposition and modelling of the BC87 dataset, *J. Geomagn. Geoelectr.*, **45** no.9, 1127–1150, 1993.

MCKIRDY, D. M., J. T. WEAVER and T. W. DAWSON, Induction in a thin sheet of variable conductance at the surface of a stratified Earth - II. Three-dimensional theory, *Geophys. J. R. astr. Soc.*, **80**, 177–194, 1985.

RITTER, P. and R. J. BANKS, Separation of local and regional information in the Iapetus dataset with the help of hypothetical event analysis, *in preparation.*

WEAVER, J. T., Mathematical methods for geo-electromagnetic induction, Research Studies Press, Taunton, England, 1994.

ZHANG, P., L. B. PEDERSEN, M. MARESCHAL and M. CHOUTEAU, Channelling contribution to tipper vectors: a magnetic equivalent to electrical distortion, *Geophys. J. Int.*, **113**, 693–700, 1993.